Mitigating Ballast Fouling Impact and Enhancing Rail Freight Capacity

CFIRE

CFIRE 04-07
November 2012

National Center for Freight & Infrastructure Research & Education
Department of Civil and Environmental Engineering
College of Engineering
University of Wisconsin–Madison

Authors:

Andrew Keene, Tuncer B. Edil, and James M. Tinjum
University of Wisconsin–Madison

Principal Investigator:

Tuncer Edil, Ph.D., P.E., D.GE and James M. Tinjum, PhD., P.E.
National Center for Freight & Infrastructure Research & Education
University of Wisconsin–Madison

Technical Report Documentation Page

1. Report No. CFIRE 04-07	2. Government Accession No.	3. Recipient's Catalog No. **CFDA 20.701**
4. Title and Subtitle **Mitigating Ballast Fouling and Enhancing Rail Freight Capacity**		5. Report Date **November 2012** 6. Performing Organization Code
7. Author/s Andrew Keene, Tuncer Edil and James Tinjum, UW-Madison		8. Performing Organization Report No.
9. Performing Organization Name and Address National Center for Freight and Infrastructure Research and Education (CFIRE) University of Wisconsin-Madison 1415 Engineering Drive, 2205 EH Madison, WI 53706		10. Work Unit No. (TRAIS) 11. Contract or Grant No. **DTRT06-G-0020**
12. Sponsoring Organization Name and Address Research and Innovative Technology Administration U.S. Department of Transportation 1200 New Jersey Ave, SE Washington, DC 20590		13. Type of Report and Period Covered **Final Report [11/1/10 – 10/31/12]** 14. Sponsoring Agency Code
15. Supplementary Notes **Project completed by CFIRE for RITA of the USDOT.**		

16. Abstract

In this report, an application using polyurethane void filling and particle bonding technology for stabilizing ballast is evaluated. Application of rigid-polyurethane foam (RPF) as an *in situ* stabilization method does not require premixing with aggregates, soil, or with water, would not require track shutdown, and reaches 90% full strength in 15 minutes after application. PSB is found to have suitable mechanical properties for use as a material in track-substructure. Ease of injection and negligible curing period for PSB makes it an attractive option for railway maintenance, especially for time-sensitive maintenance activities, such as intersections and bridge approaches. Use of PSB stemming from the research presented in this report can serve as an economically feasible/favorable maintenance approach compared with traditional methods, such as undercutting, track raising and ballast addition, tamping, etc.; especially for preserving uninterrupted track operations during track stabilization/enhancement.

17. Key Words polyurethane-stabilized ballast, ballast, rigid-polyurethane foam, rail infrastructure	18. Distribution Statement **No restrictions. This report is available through the Transportation Research Information Services of the National Transportation Library.**		
19. Security Classification (of this report) **Unclassified**	20. Security Classification (of this page) **Unclassified**	21. No. Of Pages 255	22. Price **-0-**

Form DOT F 1700.7 (8-72) **Reproduction of form and completed page is authorized.**

DISCLAIMER

This research was funded by the National Center for Freight and Infrastructure Research and Education. The contents of this report reflect the views of the authors, who are responsible for the facts and the accuracy of the information presented herein. This document is disseminated under the sponsorship of the Department of Transportation, University Transportation Centers Program, in the interest of information exchange. The U.S. Government assumes no liability for the contents or use thereof. The contents do not necessarily reflect the official views of the National Center for Freight and Infrastructure Research and Education, the University of Wisconsin, the Wisconsin Department of Transportation, or the USDOT's RITA at the time of publication.

EXECUTIVE SUMMARY

Between 1980 and 2008, traffic on Class 1 railroads has increased 93% and total track length has decreased 42%, leading to a substantial increase in traffic density and maintenance requirements. These increasing volumes, tonnage, and speeds on our nation's rail system are stressing rail substructure to levels never before evaluated or considered in depth. To improve maintenance techniques for problematic railway elements (i.e., bolted rail joints, intersections, bridge approaches, etc.), an *in situ* method involving ballast layer reinforcement with polyurethane is proposed.

Ballast is crucial for the structural support of the rail superstructure. The structural integrity of fouled ballast (i.e., containing fine particles) can be compromised leading to track instability and, ultimately, train derailments. Thus, prevention or mitigation of fouling would greatly reduce costs for railway track and ballast maintenance. Non-expanding polyurethane has been used in rail infrastructure. However, very few experimental and analytical methods have been developed to determine mechanical properties of materials (i.e., course aggregates) stabilized with polyurethane, behavior of stabilized track-substructure, and subsequent railway lifecycle characteristics. Furthermore, research into injection of expanding polyurethane, herein referred to as rigid-polyurethane foam (RPF), into rail substructure is unprecedented.

Injection protocols developed herein (e.g., percolation and subsurface injection) create stabilized formations that can possess targeted mechanical properties and occupy specified areas within the ballast layer. Percolation injections create unconnected monolithic formations of polyurethane-stabilized ballast (PSB) extending from the bearing surface of the tie (tie/ballast interface) down to the base of the ballast layer. These areas beneath the ties are the primary loading areas in the ballast layer. The purpose of stabilizing these areas is to arrest permanent deformation of the ballast layer and prevent further infiltration of fouling. When the subsurface-

injection technique was employed, a layer of PSB was formed at the base of the ballast layer (i.e., *in situ* PSB trackbed). The benefits of this approach are that RPF spreads easy along the base of the ballast layer and involves quick (short curing time) implementation, prevents water infiltration into moisture-sensitive layers (i.e., subballast and subgrade layers), and prevents subgrade intrusion into the ballast layer.

Implementation of PSB is proposed as more sustainable maintenance approach for problematic railway elements such as intersections, bridge approaches, bolted rail joints, etc. Track substructure materials (e.g., clean ballast, fouled ballast, recycled ballast, etc.) when stabilized with RPF have superior resistance to accumulation of plastic strain during cyclic loading and much greater compressive strength compared to untreated substructure material, as discussed further herein. Thus, RPF stabilization is an applicable tool for maintaining track geometry and preventing ballast layer settlement thereby reducing maintenance cycles associated with plastic deformation of the ballast layer.

From evaluation of the elastic deformational behavior of PSB, the compressive moduli (i.e., Young's and Resilient Modulus) of PSB are typically less than clean ballast. Since PSB has far lower accumulation of plastic strain than the clean ballast, PSB elastic deformational behavior becomes a primary focus for PSB. Increased elasticity of the ballast layer can be ideal for dynamic loading conditions and in high-speed rail applications where impact loading can cause accelerated substructure deterioration. Consistency in track modulus can be established in bridge approach sections with a ballasted bridge-deck and in areas of the track where differential settlement in the ballast layer threatens rider comfort and freight-transport operations.

The benefits of stabilizing fouled ballast with RPF include correction of already fouled ballast substructure and arresting permanent deformation in the track. After injection into fouled

ballast, RPF was observed to encapsulate fine-grained fouling while forming a solid geocomposite, which would prevent further infiltration of fouling material or water. When 'highly fouled ballast' was stabilized with RPF there was a large reduction of cumulative plastic strain during cyclic loading in polyurethane-stabilized fouled ballast compared to untreated fouled ballast, results of which are presented in this thesis. RPF stabilization of the ballast layer has the potential to mitigate impacts of ballast fouling thereby enhancing rail freight capacity (i.e., operational speeds) and improve track-substructure maintenance efficiencies.

In this thesis, an application using polyurethane void filling and particle bonding technology for stabilizing ballast is evaluated. Application of RPF as an *in situ* stabilization method does not require premixing with aggregates, soil, or with water, would not require track shutdown, and reaches 90% full strength in 15 minutes after application. PSB is found to have suitable mechanical properties for use as a material in track-substructure. Ease of injection and negligible curing period for PSB makes it an attractive option for railway maintenance, especially for time-sensitive maintenance activities, such as intersections and bridge approaches. Use of PSB stemming from the research presented in this thesis can serve as an economically feasible/favorable maintenance approach compared with traditional methods, such as undercutting, track raising and ballast addition, tamping, etc.; especially for preserving uninterrupted track operations during track stabilization/enhancement.

TABLE OF CONTENTS

LIST OF TABLES

LIST OF FIGURES

1 INTRODUCTION AND SCOPE

1.1 MOTIVATION AND PROBLEM STATEMENT

In 2000, Class 1 rail operators in the United States (US) spent $500 million each year on ballast maintenance for 150,000 km of Class 1 track (Chrismer and Davis 2000). Ballast serves two essential roles in rail substructure, to distribute loads from the track into the lower substructure layers and to maintain drainage. With repeated loading, ballast breaks and rearranges into a more graded continuum that retains more water, a process termed as 'fouling'. Other sources of fouling come from sleeper (tie) wear, infiltration from underlying granular and subgrade layers, and spillage from passing trains (Selig and Waters 1994). Ebrahimi (2011) found that the permanent deformational behavior of fouled ballast is a function of the amount of fouling present, the type of fouling, and the moisture content of the material. For each type of fouling material present, as the amount of fouling and moisture increase the rate of plastic deformation increases and strength decreases, leading to higher rates of track deformation, deterioration, and eventual failure (Ebrahimi and Keene 2011). Track superstructure (i.e., rails, ties, and fastening system) typically has much longer lifecycle than the substructure (i.e., ballast, subballast, and subgrade); however, the superstructure lifecycle is dependent upon substructure conditions and substructure maintenance intervals (Huang 2004). Thus, prevention or mitigation of fouling in the ballast layer would greatly reduce costs for railway track and ballast maintenance.

National initiatives on sustainability, safety, and infrastructure rehabilitation are underway in the US. These "hot-topics" have inspired a multitude of novel and innovative ideas for meeting future societal demands. Injection of polyurethane into substrates is a new and growing stabilization technology. The process of injecting expanding polyurethane that forms into rigid-foam polyurethane (RPF) is unique due to rapid polyurethane curing (90% cured in 15

min, 100% in 24 h), material resilience against hydro and chemical weathering, and ability to stabilize substructures with polyurethane injections where conventional methods would be expensive and disruptive.

Rigid-polyurethane foam applied to coarse-grained materials, after injection and solidification, improves the strength and protection by occupying the pore space and cementing the particles together. Due to expansive properties of the foam, RPF has also found applications in foundation engineering to support footings and slabs. Due to these advantages, there have been efforts to expand the applicability of RPF to other infrastructure settings, including the rail industry. Currently, no standards exist for conducting engineering tests on polyurethane-fortified materials, such as stabilized soils and aggregates. Many methods are available for the mechanical analysis of polymeric cellular foams or for engineering properties of granular materials; however, little is understood about the behavior of the combination of an expanding polymer with granular material and effects on the mechanical properties of foundations, embankments, substructures. Concurrently, mechanical properties of geomaterials (i.e., soils and coarse aggregates) stabilized with RPF are not well documented. To determine the applicability of RPF injections into rail infrastructure, laboratory testing protocols and equipment are required, mechanical properties of polyurethane-stabilized ballast must be evaluated, and influence on track elastic and plastic deformational behavior needs to be considered.

1.2 RESEARCH OBJECTIVES

The objectives of the research presented in this thesis are the following: (1) develop protocols and guidelines for use of rigid-polyurethane foam and fabrication of specimens in a laboratory setting. (2) develop testing procedures for characterizing the mechanistic behavior of railway ballast and infrastructure materials stabilized with polyurethane. (3) describe mechanisms controlling behavior of polyurethane stabilized materials. (4) develop a track model using finite

element analysis tools for studying track mechanistic response to strategic polyurethane injections. (5) integrate injection protocols, mechanistic characteristics of PSB, and track modeling outcomes to provide guidance for a new maintenance approach.

The goals of using RPF for reinforcing ballast in the railway substructure include: (1) reducing particle breakage and fines intrusion, thus mitigating fouling generation, (2) correcting already fouled ballast substructure and arresting permanent deformation in the track, (3) improving substructure performance and preserving track geometry thereby enhancing rail-freight capacity and rider-comfort, and (4) providing a cost and time-effective maintenance tool to supplement rail maintenance capabilities. Development of techniques that would enable strategic polyurethane injection into a defective substructure would be, in essence, a surgical tool to enhance strength and performance of problematic infrastructure elements, thus avoiding disruptive and expensive maintenance activities and lengthening structural and infrastructure lifecycle.

1.3 THESIS OUTLINE

This thesis is written into several chapters that address the development and implementation of the research. Several appendices are included regarding details of the research and other testing conducted to supplement research results.

Chapter 2: A review of problems facing the rail industry and current aspects of railway maintenance are introduced. The contents of Chapter 2 provide an introduction into the composition and behavior of polyurethanes, uses of polyurethane in civil engineering applications, uses of polyurethanes in rail infrastructure, and areas for improvement of polyurethane use in rail infrastructure and the purpose of fostering the maintenance approach presented herein.

Chapter 3: Observations and results of the PSB fabrication process are presented. Two phases of specimen fabrication involved: (1) injection of numerous ballast samples for observing the reaction of compacted ballast to polyurethane expansion and bonding and (2) creation of specimens for mechanistic testing and analysis of PSB.

Chapter 4: Methods developed in Chapter 3 were used to determine plastic and elastic deformational behavior, flexural strength and fatigue, unconfined compressive strength, and Young's modulus. The mechanical properties of RPF, ballast, and PSB are compared and compared to other materials commonly used in transportation infrastructure (e.g., natural aggregates, cement-stabilized soil, etc.).

Chapter 5: Two analytical and constitutive models are presented: (1) a model for predicting elastic and plastic deformational behavior under cyclic compressive loading, which is important for use of PSB in forming stabilized zones in the ballast layer and (2) a model for predicting flexural strength and fatigue characteristics, which is important for use of forming PSB stabilized layers.

Chapter 6: A 3-dimensional model is presented using finite element analysis (FEA) to study track elastic response to strategic injection and establishment of PSB within the ballast layer. The effect on individual substructure layers and overall track response due to localized areas of differing modulus (PSB formation) in the ballast layer is investigated.

Chapter 7: Conclusions and recommendations for the new maintenance approach developed herein are presented. Discussion of the PSB maintenance approach and other potential maintenance alternatives are also addressed.

Chapter 8: Future work regarding rail research is presented. Methods and different types of rigid-polyurethane foam for ballast stabilization, further laboratory testing of polyurethane-stabilized ballast compositions (i.e., fouled ballast), alternative constitutive and numerical

modeling approaches, full-scale model and field implementation, and field evaluation and monitoring are discussed.

Appendix A: Procedures are presented for RPF injection and PSB specimen fabrication and for potential field injection procedures. Details regarding PSB composition, phase properties, flow behavior of RPF (i.e., rheological properties), and characteristics of RPF flow in ballast (i.e., pores space properties) are included.

Appendix B: RPF was tested in this study and compared to RPF tested in several other studies at varying RPF densities and with different testing modes (tension and flexural). The constituents of RPF mechanical properties (i.e., closed-cell content, temperature effects, and cell elongation and size) are also introduced.

Appendix C: An elastic-wave based (seismic) testing procedure was developed and used to correlate seismic results with damage occurring within PSB between intervals of loading repetitions applied. The seismic testing method can also be used in durability testing (e.g., freeze-thaw cycles, wet-dry, cycles, etc.) of PSB materials.

Appendix D: Background of asphalt trackbed layers used in railway infrastructure is presented. Aspects of stabilized trackbed layers and applicability a PSB trackbed are included.

Appendix E: Details regarding numerical model construction is included. These details are important when constructing a numerical model for evaluating track mechanical behavior.

Appendix F: Supplementary pictures are included.

Appendix G: Tables of PSB index properties are included. Table of modeling values from other studies is also included.

2 BACKGROUND AND CONCEPT DEVELOPMENT

In this Chapter, problems facing the rail industry and current aspects of railway maintenance are introduced. An introduction into the composition and behavior of polyurethanes, uses of polyurethane in civil engineering applications, and uses of polyurethanes in rail infrastructure is provided. Areas for improvement in polyurethane/infrastructure research and implementation for railway infrastructure are detailed and a new maintenance procedure is advanced.

2.1 INTRODUCTION

Ever increasing volume, tonnage, and speeds on our nation's rail system are stressing rail substructure to levels never before evaluated or considered in depth. According to the Federal Railroad Administration, between 1980 and 2008 traffic on Class 1 railroads increased 93% while the length of total track owned decreased 42%, thus leading to a large increase in traffic density. Ballast provides structural support of rail tracks and trains and fast drainage. Ballast performance degrades during its service life due to deterioration caused by cyclic loading of passing trains and chemical and environmental weathering, thus creating 'fouled ballast'. Despite numerous advancements in maintenance technology within the rail industry, railroads annually invest billions of dollars in maintenance activities, including the removal and replacement of ballast. Because demand for railway transportation (freight and passenger) is increasing, new methods of rail substructure maintenance and improvement must be adopted.

Due to frequent use and high loads experienced, railroad ballast and substructure undergo rigorous and continuous maintenance and renewal. Renewing and resurfacing railroads has become an expensive process. North American railroads spend about $3.4 billion every year on track maintenance and renewal due to track-component degradation (Li et al. 2004). In Canadian Northern's (CN) eastern region, which serves the eastern United States from New York to Maine and the Canadian provinces of Ontario and Quebec, the length of track

is approximately 7,258 route-km. An Austrian network, similar in length to the track that CN operates, generates 400,000 tonnes of excavated material from track work and the amount of new ballast required each year ranges from 500,000 tonnes to 700,000 tonnes (Rudolf et al. 2005). For Burlington Northern Santa Fe (BNSF), from 1983-2002 an annual average of 50.8 m^3 of ballast was replaced per km of track (107 cubic yards/mile, CY/mi) (Stefani 2003). BNSF currently has 51,499 track-km (32,000 mi), which calculates out to an annual average replacement of 28,178,150 m^3 of ballast (3,424,000 CY). The costs and frequency of track maintenance has greatly increased due to increasing volume, tonnage, and speeds on our nation's rail system. From 1995 to 2001, Wisconsin & Southern Railroad (WSOR) experienced an increase of 30,372 to 44,405 carloads and an increase of 2,212,210 tonnes to 3,424,080 tonnes. In 2002, WSOR operated its track at maximum weight capacity of 129,700 kg per car and the freight haul industry is pushed to allow 142,880 kg cars on these tracks (WSOR 2002). With similar occurrences happening around the US, track construction and maintenance must meet the increase in weight and frequency of travel demand, which will need economical and environmentally stable methods of ballast recycling, renewal, and strengthening.

2.2 RAILWAY MAINTENANCE AND BALLAST FOULING

A railway consists of a superstructure and substructure. As defined in Selig and Waters (1994), the superstructure and substructure are separated by the sleeper-ballast interface. Therefore, the superstructure consists of the rails carrying the carloads, which are attached by a fastening system to the railroad sleepers (ties) typically made of wood or reinforced concrete. The superstructure is supported by a substructure of ballast, subballast, and subgrade layers (Figure 2.2.1). The superstructure typically has much longer lifecycle than the substructure; however, the superstructure lifecycle is dependent upon substructure conditions and substructure maintenance intervals (Huang 2004). The ballast layer is responsible for drainage after rain events and distributing the loads from the superstructure down into the substructure layers. As the extent of ballast fouling increases, the capacity of the ballast layer for supporting the superstructure decreases. Certain railway components (e.g., bolted rail joints, intersections, bridge approaches) require maintenance more frequently due to unpredicted or accelerated substructure deterioration. The structural integrity of 'seriously fouled ballast' (defined in Ebrahimi (2011) as fouling index of 25% and moisture content of 15%) can be compromised leading to track instability and ultimately, train derailments. Because of this serious consequence, ballast maintenance activities, such as undercutting, tamping, and shoulder cleaning, are routinely performed by railroads, especially on tracks serving the heavy axle load unit trains.

Fouled ballast is defined in a variety of ways. The primary definition pertains to the quantity and size of particles within the ballast, often through a “fouling index.” Fouling index (FI), as defined by Selig and Waters (1994), is calculated by summing percent particles passing 4.75 mm (P4) and percent particles passing 0.075 mm (P200); hence, (FI=P4+P200). Ballast with an index between 20% and 39% is considered highly fouled. The second parameter involves the rate at which water can flow through the ballast, which is characterized by hydraulic

conductivity. Since one of the essential roles of ballast is maximizing drainage of water, ballast failing to have a high hydraulic conductivity is considered fouled. The hydraulic conductivity of fouled ballast typically has flow rates between $5 \cdot 10^{-6}$ m/s and $1.5 \cdot 10^{-3}$ m/s (Shukla 2002). Properties of fouled ballast such as fouling index and hydraulic conductivity can be very difficult to determine visually; therefore, fouled ballast identification methods are critical for successful railway maintenance programs.

Ballast fouling is generated from several common sources: (1) mineral fouling from breakage of ballast particles due to loading, (2) spillage of materials into the track from car loads (e.g., coal fouling), and (3) clay fouling due to mud-pumping of the subgrade or subballast into the ballast layer. The primary contributor to deterioration of track geometry is ballast fouling (Indraratna 2012). Higher fouling and water contents lead to higher rates of plastic strain in fouled ballast. As the amount of fouling increases, the strength of the ballast layer decreases, leading to higher rates of track deformation (Ebrahimi 2011).

Fouled ballast removal and ballast resurfacing processes can be disruptive to railway traffic, necessitating efficient fouled ballast removal, separation, cleaning, and resurfacing. The use of off-track undercutting operations leads to traffic interruption, transportation and delivery costs, and environmental impacts. Areas of track that encounter ballast fouling frequently are subject to more unscheduled maintenance. Routine maintenance, which occurs over several year increments, is based on the type of track and loading capacities. Canadian Pacific Railroad (CPR) reported that they had a 7-year plan for continuous welded rail and a 3-year plan for jointed rail. Swiss Federal Railways (SBB) renews approximately 2% of their tracks yearly. Ballast renewal consists of 40% of track renewal each year, which consists of 595,000 tonnes of ballast renewed (Becker and Patrick 2005). The renewal process involves extensive removal of the ballast structure, which is an expensive procedure, potentially hazardous to other railway components, and disruptive to railway traffic.

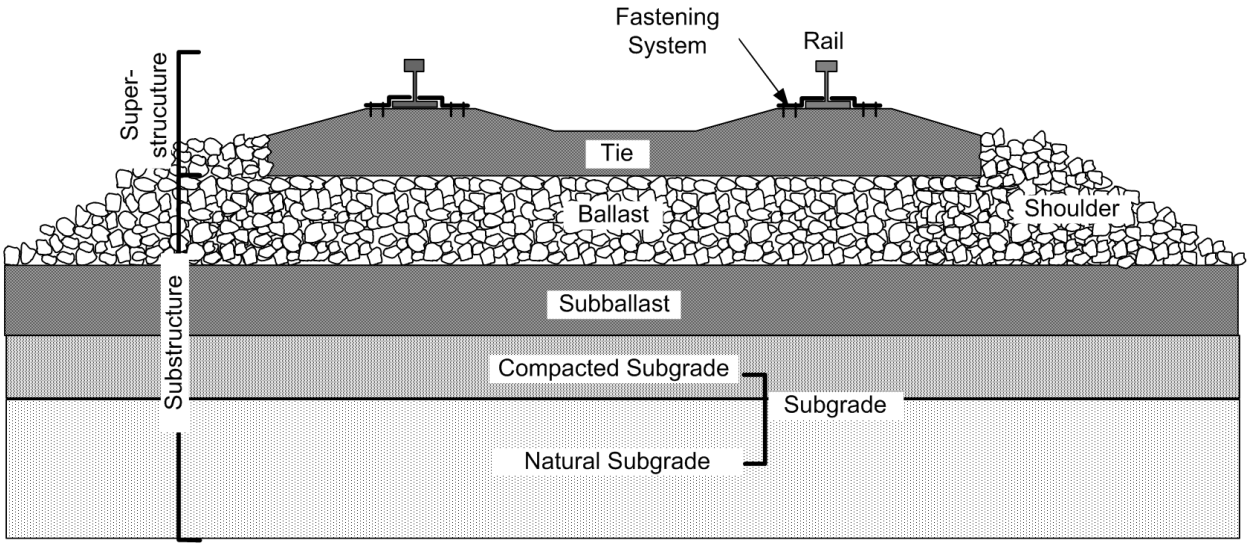

Figure 2.2.1: Typical Components of Superstructure and Substructure in a Railway Track.

2.3 PRODUCTION AND PROPERTIES OF POLYURETHANE

Polyurethane materials are hydrophobic polymers formed in an exothermic chemical reaction of specific chemical components that lead to a product designed to be either foamed or compact and soft (cushiony), semi-rigid (flexible), or rigid (stiff) (Oertel 1985). The chemical mix consists of molecules containing two or more isocyanate groups and polyol molecules containing two or more hydroxyl groups (Randall and Lee 2002). The polyols involved in the formation of polyurethane are usually either polyether or polyester, which are typical polymers used in many manufactured products. Each compound involved in the reaction can be adjusted so that variation in the exothermic reaction and physical outcome can be targeted. Randall and Lee (2002) indicate that wide varieties of polyurethanes are formulated from only a few basic isocyanate compounds and a much larger number of polyols that possess several molecular weights and functionalities. The isocyanates are responsible for the highly reactive process that takes place, but selection from the wide varieties of polyols available dictates the resulting polyurethane.

For synthesis of rigid-foam polyurethanes or “thermoset polyurethane-resin foams” two liquid components, a polyester or polyether polyol and an organic polyisocyanate, are proportionately mixed in the presence of a catalyst (Szycher 1999; Randall and Lee 2002). The foam structure is the result of gas bubbles formed during the polyurethane polymerization process, known as ‘blowing’. Gas bubble formation is the result of introducing a chemical ingredient known as a ‘blowing agent’ (Szycher 1999). When allowed to rise freely, the volume of the mixed ingredients can expand up to 30 times that of their original volume.

The setting phases for the reaction times are similar for both foam and compact polyurethanes. For foam polyurethanes, the foaming process occurs during one of the setting phases (i.e., cream phase), the reaction timing is described in Randall and Lee (2002). The

cream phase is identified when the mix begins to foam (blowing); the phase typically initiates after 5 s. The early stages of the cream phase consist of foaming and lead to the gel phase where the mix is no longer liquid. Considerable material expansion occurs during the cream phase, which typically lasts 30 s. Transition into the gel phase is identified when the foam begins sticking to objects. The transition from gel to tack-free can be characterized as a molten resin or foam flow (Mitani and Hamada 2003); the gel phase typically lasts less that 30 s. Expansion of the material continues into the tack-free phase, which begins when the foam is no longer tacky (i.e, sticky) to the touch. From initialization of the tack-free phase, rate of expansion lessens and decays until expansion has reached the maximum amount, at which point the material is considered at the end-of-rise phase. End-of-rise occurs up to 60–90 s after mixing.

The cellular structure of the rigid-foam polyurethanes, when reacted properly, have a largely closed-foam structure (Szycher (1999); Randall and Lee (2002), Oertel 1985). Typically, for closed-cell polyurethanes the percent of the closed cells and open cells are determined per ASTM D6226. In the case where the formation of RPF is the target, the strength, hardness, and resistance to fatigue are controlled by several outcomes. In Randall and Lee (2002), the mechanical characteristics are explained as dependent on the quality of the foam, which is evidenced by the closed-cell content. The higher the open-cell content (i.e., inverse of closed-cell content), the more the foam acts like a semi-rigid (flexible) foam. In the case of rigid-foam, where mechanical properties such as high strength and stiffness are intended, highly closed-cell foam is ideal. However, the density of the polyurethane is also important for the mechanical characteristics of the foam, as the density of the foam increases the strength, hardness, and resistance to fatigue all increase (Randall and Lee 2002; Oertel 1985). Consequently, polyurethane may possess a density that would be sufficient in the case of rigid-foam, but high open-cell content would result in mechanical properties that are substandard for the intended design of a rigid-foam.

2.4 POLYURETHANE IN INFRASTRUCTURE

Polyurethane markets of the 21st century have predominantly consisted of five industries. In the automotive industry, soft-foams and semi-rigid-foams have been used for seating and padding, rigid foams for door panels (i.e., for impact performance), and many polyurethane varieties for other vehicle components. The furniture industry uses soft-foams for cushioning and rigid-compact polyurethane where tough decorative exteriors may be needed. The construction industry uses a variation of a semi-rigid-foam polyurethane (i.e., thermoset foam) for insulation properties due to the closed-cell, low thermal conductivity, and lightweight properties. Other rigid and compact polyurethanes can be used to support strength of other construction materials and composites and to replace some conventional materials such as brick, concrete, wood, or metal. The consumer appliance industry also uses rigid foams for their lightweight and low-volume thermal insulation properties; a common domestic appliance utilizing this type of foam is a refrigerator. Finally, the footwear industry replaces materials traditionally used for shoe manufacturing, such as leather and padding, with polyurethane for wear resistant characteristics (Randall and Lee 2002).

Because of the high strength and lightweight properties of rigid-compact polyurethanes, the unique expansive and quick-setting processes of RPF, and improvements in the technology and affordability of manufacturing polyurethane, the applications in structural engineering, transportation geotechnics, and geotechnical engineering are increasing. Freitas et al. (2010) conducted a parametric study on the use of rigid-foam polyurethane in an experimental orthotropic steel bridge deck for reducing bridge weight for long span and movable bridge applications. Polyurethane foams of varying density (closed-cell) were sandwiched between a top plate and a deck plate supported by a typical bridge deck made of longitudinal stiffeners (steel decking) and steel girders. In Freitas et al. (2012), the objective was to study the reduction in the direct stress carried to the top plate from vertical loading and increase in the

stiffness of the bridge section. In their findings, they determined that the system was a promising alternative to conventional bridge decks.

A case study by Monaghan and Trevits (2004) for the National Institute for Occupational Safety and Health (NIOSH) looked into the use of a type of rigid-compact polyurethane known as a polyurethane grout for bonding and strengthening the rock layers making up the walls for mine roof control. A Federal Highway Administration technical report indicated that polyurethane grout has been used for mine roof control for over three decades, but also that injection for pavement and subgrade improvement has also been done extensively in the U.S.

Erdemgil et al. (2007) investigated the effect of injecting rigid-foam polyurethane beneath a building for mitigating seismic foundation failure from earthquakes. The purpose of the injection was to increase the bearing capacity of the foundation so that, in an event of an earthquake, the seismic forces generated would not be in excess of capacity or strength of the bearing soils. Erdemgil et al. (2007) reported that the SPT blow count before the subsurface injections were 10–25 for the clayey-sand and 8–14 for the silty-sand layer; after the subsurface treatment, the SPT counts for the improved zone were 2–3 times greater.

2.5 POLYURETHANE IN RAIL INFRASTRUCTURE

A small number of investigations have been conducted concerning the use of polyurethane in ballast layer stabilization or reinforcing for rail infrastructure. In Dersch et al. (2010) and Boler (2012), the material used for reinforcement is known as Elastrotrack®, a rigid-compact type of polyurethane used to coat the ballast particles. Using a direct-shear box test, the shear strength of the reinforced ballast was measured under varying confining stresses and polyurethane curing times (up to 14 days). In the study, the shear strength of the treated ballast specimen was 40-60% greater than uncoated clean ballast. After each of the direct shear tests, a powdering test was conducted where the amount of breakage was measured by percent particles passing a 13-mm sieve, the treated ballast samples had 3-5% less breakage than untreated ballast. Therefore, Dersch et al. (2010) identified that polyurethane treatment greatly increases shear strength of ballast and reduces breakage of ballast particles under loading.

Kennedy et al. (2009) led a study where a full-scale model test was assembled and tested to determine the deformational characteristics of the ballast layer with and without polyurethane reinforcement. The full-scale model consisted of a superstructure system of several rails and ties and substructure layer with a subgrade and a ballast layer. The polyurethane was similar to the type in Dersch et al. (2010), but supplied in the United Kingdom (UK) from XiTrack™. Unlike the coating of the ballast particles in Dersch et al. (2010), the rigid-compact polyurethane was injected on and into the ballast layer; the resulting bonding with the ballast particles formed a semi-continuous geocomposite. In their investigation, the accumulation of plastic strain in their full-scale model over 500,000 loading repetitions was measured. The tests were conducted in the GRAFT facility, where loading repetitions applied to the full-scale model simulate railway traffic loading conditions on the substructure. Kennedy et al. (2009) found that settlement of the ballast layer in the model was 95-98% less for the treated

substructure than untreated substructure modeled at their facility as well as other tests on untreated substructure at other test facilities.

There have been a couple of instances where polyurethane has been implemented in track maintenance operations. In the UK, a company called XiTrack™ has used rigid-compact polyurethane for stabilizing railway ballast in numerous infrastructure applications. In a case study by Woodward et al. (2007), polyurethane was injected on, into, and beneath the ballast layer at a rail crossing in a tidal floodplain. The rail line supports both passenger trains and heavy rail freight operated by Network Rail. The choice and need for the XiTrack™ reinforcement was due to heavy maintenance required on the particular railway segment, concerns over track stability, and inability to close the tracks for reconstruction. The polyurethane reinforcement was considered over several alternatives due to problematic geotechnical conditions and potential loss in revenue due to track closure/reconstruction. Concerns over constructing a concrete slab-track involved potential water pressure developing underneath the slab under cyclic loading conditions and creating a foundation transition, which can be problematic at bridge approaches. Concrete pile installation would have come at high cost and generated foundation transition problems. In the study, the XiTrack™ technique enhanced the vertical stiffness of the track, which reduced vertical bearing pressure on the foundation soils that made up the subgrade foundation. Accelerometer sensors in the substructure were used to measure vertical accelerations due to passing loads. Woodward et al. (2007) reported that this reduction in vertical acceleration could be correlated to lessening of the bearing pressure on the subgrade and therefore reduction in the subgrade permanent deformation (i.e., settlement).

In a study by Thomson and Woodward (2004), the XiTrack™ method was implemented at a bridge approach (i.e., railway track segment approaching a railway bridge) on the West Coast Main Line in the UK. The method was chosen due to the high level of maintenance

required for that particular track segment. The aspects of the track that were the focus of their investigation included the segment of track before the bridge and the length of track that transitions from the ballasted track to the fixed foundation on the bridge. As indicated in their study, bridge approaches are commonly problematic track segments that routinely require maintenance and cause track instability. Problems that occur in bridge approaches are typically associated with the rigid transition from the rigid concrete foundation that the bridge provides to a flexible and more deformable foundation of the ballasted track. Thomson and Woodward (2004) found that due to the polyurethane stabilization method chosen, several track stability issues were mitigated. These included prevention of differential settlement under sleepers due to inconsistent substructure degradation, preservation of track geometry in segments that undergo localized overstresses (e.g., at bridge approaches and rail joints), and more consistency in foundation stiffness where the track transitioned from ballast to a fixed foundation. Laboratory tests were also conducted to gain insight into the compression and flexural capabilities of the composite material including compression and flexural beam testing. In their conclusions, Thomson and Woodward (2004) referred to a previous railway site that had required 3 to 4 maintenance cycles a year. After implementation of the XiTRACK^{TM} technology, the site had not required any maintenance to the date of their publication, which was 4 years thereafter.

2.6 A NEW MAINTENANCE APPROACH

While rigid-compact polyurethane in rail infrastructure has been used, very few experimental and empirical methods have been developed for ascertaining mechanical properties and lifecycle characteristics of rail substructure stabilized with polyurethane. Thomson and Woodward (2004), Kennedy et al. (2009), Dersch et al. (2010), and Boler (2012) are studies that involved basic laboratory investigations of strength characteristics of polyurethane coating and reinforcement of ballast. In case studies involving use of XiTRACK^{TM} technology, rough guidelines were developed that outline objectives polyurethane stabilization should meet when used in rail infrastructure. Development of laboratory methods for mechanical analysis of PSB and other aggregates is crucial for understanding the geomechanical implications of stabilization, providing parameters for good engineering practice, and for developing cost-effective approaches for engineering design.

Investigation into injection of an expanding polyurethane (rigid-foam polyurethane) into rail substructure is an uncharted area. Development of standard laboratory tests for fabrication and characterization of PSB is aimed at contributing to research infrastructure and state of practice for methods of geotechnical stabilization. Presented herein are methods for experimental testing and for determination of the mechanical properties of polyurethane stabilization. An investigation into the feasibility of strategically injecting polyurethane within the ballast substructure is conducted for the purpose of mitigating ballast fouling and fines intrusion. The overall objective is to reduce maintenance life cycle costs, increase rail freight load capacity, and provide maintenance techniques undisruptive to railroad traffic.

3 MATERIALS AND DEVELOPMENT OF MECHANICAL PROPERTY TESTING METHODS

3.1 INTRODUCTION

In this study, the mechanical properties of polyurethane improved ballast layer is evaluated by considering: (1) the extent to which the void space of ballast is filled by the RPF, (2) the strength and degree of bonding that occurs between the ballast particles and RPF, and (3) the degree to which volumetric expansion of ballast during RPF injection is limited. Due to the large particle size and resulting aperture of the pore space within ballast, the hydraulic conductivity, K, of ballast (K = 0.025–0.050 m/s) is much greater than that of a typical clay (K = 10^{-10} m/s – Buzzi et al. (2010)). Fluids would flow more easily through ballast than typical clay and thus the geometry of the ballast pore space conveniently allows injection of polyurethane. This geometry allows room for expansion of the RPF and ability to meet target volume and density. In contrast, the highly porous ballast layer has the potential to inhibit low viscosity or liquid-phase (non-expanding) polyurethanes foams from reaching targeted areas and having the intended effect. This chapter evaluates the properties of ballast stabilized with RPF and presents polyurethane injection procedures, laboratory methods for geotechnical and mechanistic characterization of polyurethane-stabilized ballast (PSB), and processes for determining the mechanical properties of PSB for design purposes.

3.2 MATERIALS

3.2.1 Ballast

The ballast used in this investigation was provided by the BNSF Railway Company from a quarry near Cheyenne, Wyoming (Figure 3.2.2). The ballast is the same granitic ballast characterized by Ebrahimi (2011), where the particle size distribution (ASTM D6913) showed particle sizes of 25–63 mm and conformed to the AREMA N0. 24 ballast gradation specification (Figure 3.2.1). Maximum dry density was achieved using the procedure developed in Ebrahimi (2011), resulting in a clean ballast void ratio, e_b, of 0.62. Corresponding clean ballast dry unit weight (γ_d) and density (ρ_d) were 15.8 kN/m^3 and 1,611 kg/m^3, respectively. These compaction characteristics were targeted for fabrication of each specimen of clean ballast in this study.

3.2.2 Fouled Ballast

Fouled ballast was mixed in the same manner as outlined in Ebrahimi (2011). Used ballast was obtained from Wisconsin Southern and Railroad (WSOR) and repartitioned into a mixture with specific fouling index (FI) and moisture content (MC) as defined by Selig and Waters (1994). The fouling index consists of summing the percent of particles passing through a 4.75-mm (P4) sieve with the percent of particles passing a 0.075-mm (P200) sieve (Figure 3.2.1). Ballast with an index between 20% and 39% is considered highly fouled. The fouling mixture was reconstituted from 80% P4 and 20% P200 (based on WSOR fouled ballast removed from service), mixed with water to create the chosen moisture content, mixed with clean ballast, and compacted to make the fouled ballast continuum. This mixture was used to observe the effect of injecting RPF into fouled ballast; the resulting composite specimens were later used for cyclic triaxial tests.

3.2.3 Recycled Ballast

Recycled ballast was sieved from ballast taken out of service by WSOR, which was characterized in Ebrahimi (2011). For obtaining recycled ballast, 19–53 mm particle sizes used were partitioned out of the WSOR fouled ballast (Figure 3.2.1). Similar to the use of the fouled ballast, the recycled ballast was created for observing injection into recycled ballast.

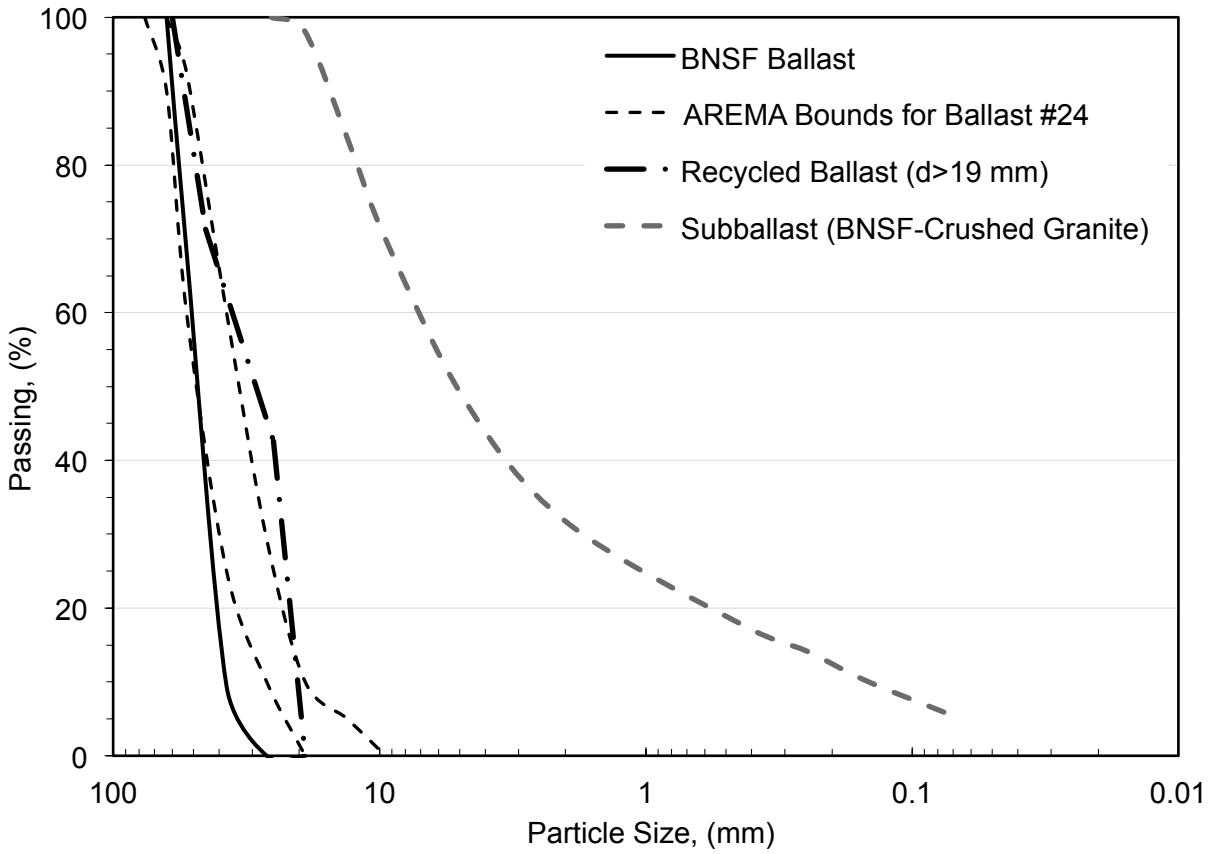

Figure 3.2.1: Particle size distribution of clean, fouled, and recycled ballast from Ebrahimi (2011).

3.2.4 Rigid-Polyurethane Foam (RPF) – (486STAR-4 BD)

The 486STAR-4 BD, referred to as rigid-polyurethane foam, is a two-component, high-density, expanding, thermoset, polyurethane-resin system. The 486STAR-4 BD was formulated by Bayer Material Science for different applications including void filling and sealing. The specific elastomer system was developed in partnership with Uretek USA Inc. Uretek USA Inc. supplied material in this study and assisted with specimen fabrication.

There are two primary chemical components that are required prior to mixing and application of RPF. As defined in a technical data sheet from Bayer Material Science (2010), the liquid components are defined as “A” component and “B” component. For synthesis of thermoset polyurethane-resin foams, the two components (polyester or polyether polyol and organic polyisocyanate) are proportionately mixed in the presence of a catalyst (Szycher 1999). The foam structure results from of gas bubble formation during the polyurethane polymerization process, known as *blowing*. Gas bubble formation is the result of introducing the *blowing agent* (Szycher 1999).

The cellular structure of the RPF is a closed-cell structure as defined by Szycher (1999). For closed-cell polyurethanes, the percent of closed cells and open cells are determined per ASTM D6226, which was used in the technical data sheet produced by Bayer Material Science (2010). The 486STAR-4 BD possesses a closed-cell content of 90%. A picture of the 486STAR-4 BD RPF used in this study is shown in Figure 3.2.3. Further investigation and techniques are needed for determining the closed-cell content of the RPF within the PSB composite. Closed-cell content may provide further understanding of overall RPF bonding properties and mechanical behavior.

3.2.5 Polyurethane-Stabilized Ballast (PSB)

In this study, the injection of RPF was observed to fill the voids of the ballast. After injection, the RPF would expand and flow through the pore space in ballast, which involved expansive forces and dynamic interactions discussed in Section 3.4.3. While the RPF transitions through the gel phase into the tack-free phase, RPF establishes bonds with materials in contact with the reacting RPF. In the case of the injected ballast samples, the bonding was considerable and the samples of ballast injected with RPF formed a bonded geocomposite discussed herein as polyurethane-stabilized ballast (PSB) (see Figure 3.2.4). The bonding of RPF with the ballast particles is a critical interaction that takes place during the polyurethane foaming process, which is important for the PSB formation process (see Appendix A) and for the mechanistic testing conducted (see Chapter 4). Materials such as PVC, vinyl plastic, and materials coated with oil and water-based lubricants did not bond with RPF during the polyurethane reaction. The bonding properties were unique due to the interaction of the polyurethane with the aggregates. The bonding of RPF with ballast is attributed to rough surfaces of the ballast particles and intermolecular bonds formed during the polyurethane reaction due to aggregate mineralogy, which are also the common characteristics that control strength in asphalt and concrete, discussed in detail in Chapter 4.

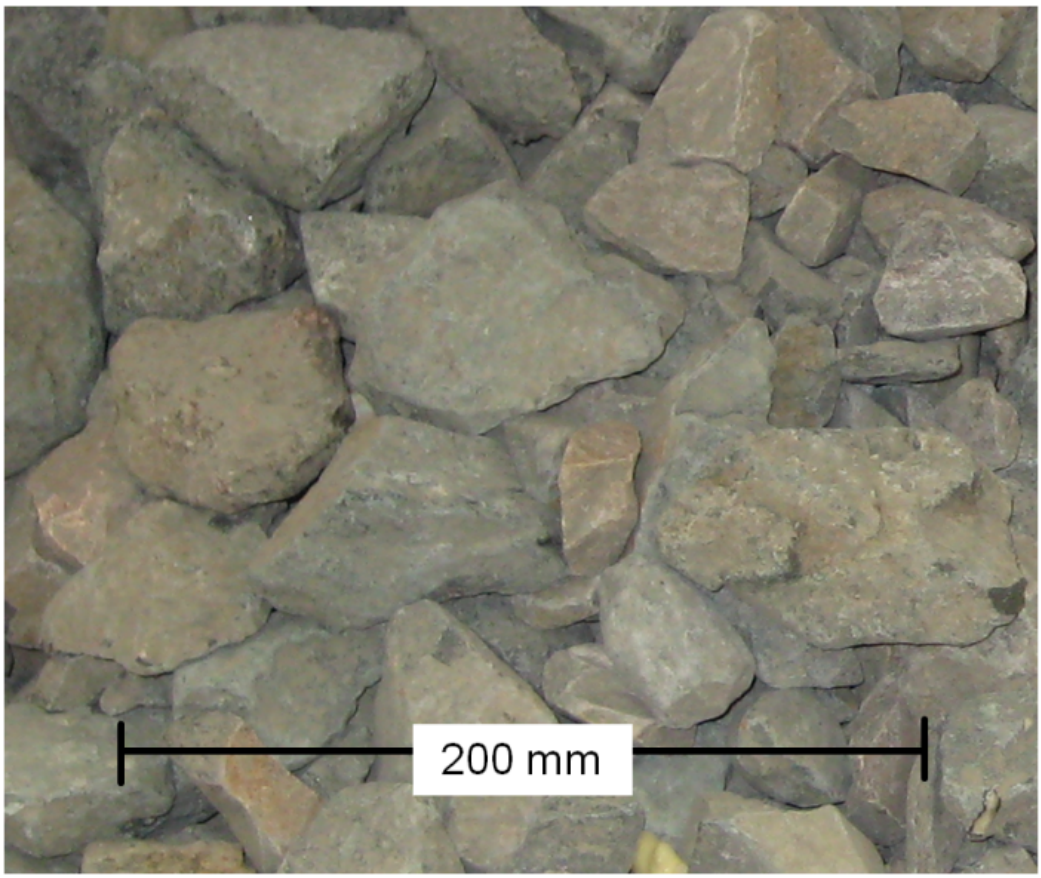

Figure 3.2.2: Picture of granitic ballast provided by the BNSF Railway Company from a quarry near Cheyenne, Wyoming.

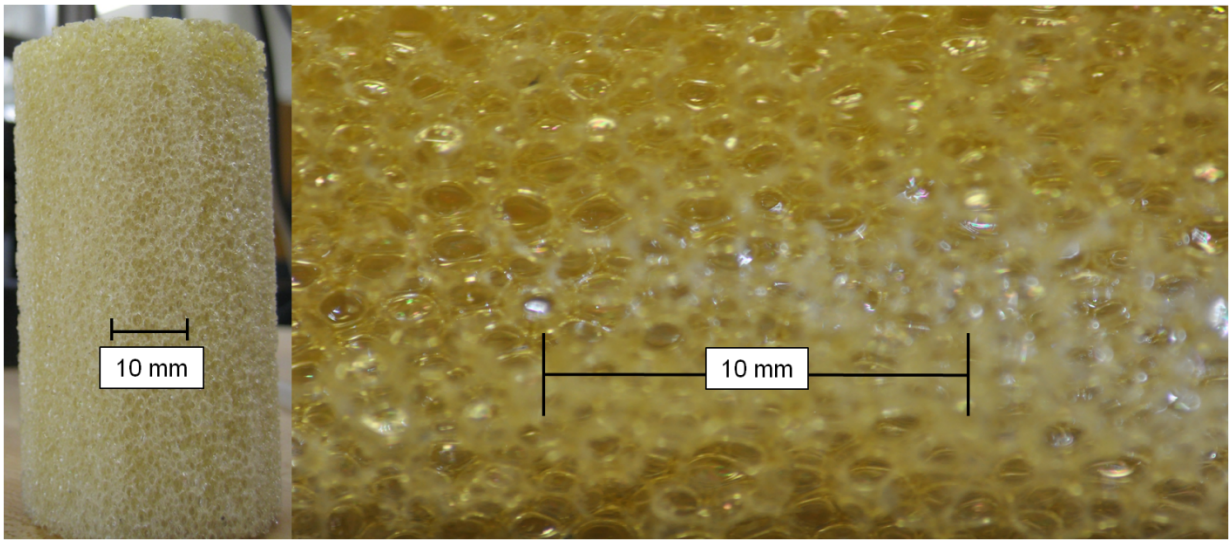

Figure 3.2.3: Pictures of RPF foam created during this study.

Figure 3.2.4: A PSB specimen cut in half shows complete void filling by the expanding foam and coherence of the two materials after concrete masonry saw was used for cutting.

3.3 MECHANICAL PROPERTY TESTING METHODS FOR PSB

3.3.1 General Testing Considerations

The specimen fabrication molds were designed to create PSB samples that could be tested for mechanical properties using customary material testing protocols. The objective was to create cylindrical specimens for cyclic triaxial compression testing, beam specimens for flexural and fatigue testing, half-beam specimens for unconfined compressive strength tests, and ballast layer prototypes and a full-scale-track-model-experiment for observation of RPF-injection integration. The values obtained from each testing procedure are used as input for numerical modeling to guide field implementation.

As detailed in Appendix A, the injection procedures developed for specimen fabrication involved successive injections where timing between injections were 45 s ± 15 s. A 30 s minimum injection interval was established to ensure that there was not too much reacting RPF within the specimens and so successive injections could be done. Two specimen fabrication stages were conducted in this study. In Phase I, the goal during injections was to achieve higher post injection RPF densities for evaluating the effect of increasing density on the mechanical properties of PSB. In Phase II, the goal during injections was to generate little to no expansion force and to target RPF densities that would likely occur with *in situ* stabilization.

3.3.2 Cyclic Triaxial Compression Testing on PSB Cylinders

3.3.2.1 Methodology

An investigation conducted by Kennedy et al. (2009) involved cyclic loading on rail ballast stabilized with non-expanding polyurethane "XiTRACK™." The study involved testing on a full-scale track model to determine the cyclic response of the stabilized layer. Ebrahimi (2011) used a triaxial cell to determine the response of clean and fouled ballast to cyclic loading; in the

study, the results of cyclic triaxial testing were correlated to a full-scale model to validate use of a triaxial cell for ballast testing. Cyclic triaxial testing of ballast and railway materials has been used in several studies (Ebrahimi 2011; Aursudkij et al. 2009; Skoglund 2002; Anderson and Fair 2008). Based on these studies, a cyclic triaxial testing method was chosen for cyclic triaxial compression testing of PSB. This type of laboratory test method was chosen to represent rail traffic loading on the substructure that occurs in the field; the purpose of these tests is to measure the plastic and elastic deformational behavior of materials under cyclic compressive loading. A typical triaxial cell used in this study is illustrated in Figure 3.3.1.

Cylindrical specimens with a minimum diameter (D) of 254 mm maintained an appropriate ratio of ballast particle diameter to specimen diameter; these dimensions were reasonable base on a study by Anderson and Fair (2008) on triaxial testing of railway ballast. The specimens with 304-mm diameter were acceptable based on Skoglund (2002), which presented a minimum ratio (1:6) of particle-size diameter to specimen diameter. A 1:6 ratio is also specified for load controlled cyclic triaxial strength of soil in ASTM D 5311. Clean ballast specimens were tested in each triaxial cell and the corresponding results were validated with the data found in Ebrahimi (2011), the data validation for the clean ballast test results are shown in Figure 4.2.1. Therefore, each triaxial cell and cyclic triaxial compression method were deemed appropriate for testing on the PSB cylinders.

Load was applied to the cylinders through a servo-hydraulic system (MTS®, loading capacity of ~98 kN). Vertical deflection of the specimens was measured using two (for redundancy) linear variable differential transducers, LVDTs, (Omega, 10±0.005-mm, Model AX/5/S) during cyclic loading. LVDTs were mounted to the loading piston extending into the triaxial chamber through the top plate.

3.3.2.2 Specimen Fabrication

Fabrication of cylindrical specimens involved drilling an injection rod to the bottom of a pre-compacted ballast specimen that was contained within a cylindrical mold (Figure 3.3.2). Typical RPF injections consisted of injecting a specified quantity of liquid RPF every 154 mm of height (H) within the specimen. For example, a specimen with dimensions D254 mm x H508 mm would have a specified injection quantity at the base, at 154 mm from the base, at 305 mm from the base, and 457 mm from the base. The nominal dimensions for the other PSB cylinders are presented in Figure 3.3.1.

Typical injection quantities for PSB cylinders are shown in Table 6.2.1. During Phase I, five 254-mm-tall PSB cylinders were made, two were allowed free-rise expansion (vertically), one was injected with enough RPF to generate no expansion force, and three were injected with excess quantities and sealed to allow measurement of the force of expansion (i.e., vertical force), shown in Appendix A.

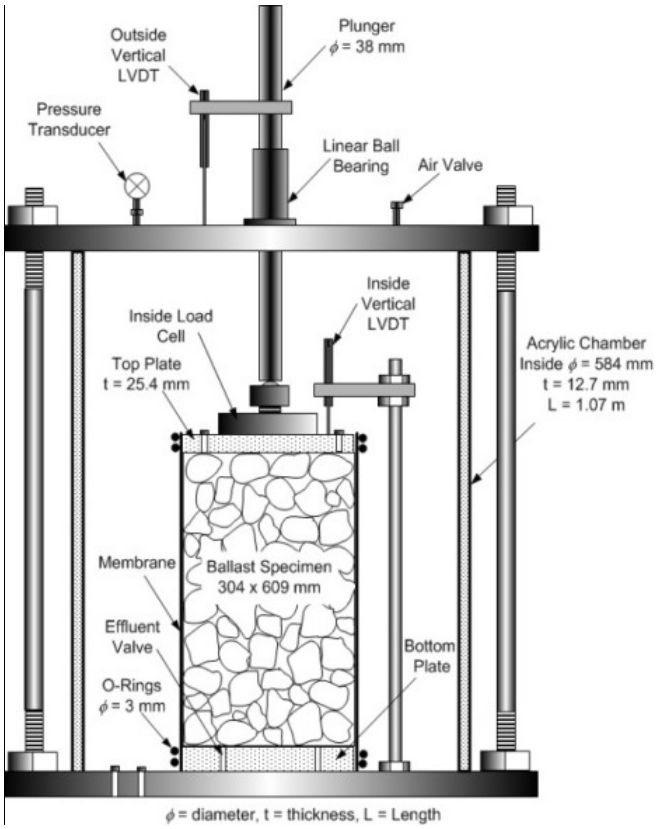

Figure 3.3.1: Triaxial chamber used for testing specimens with nominal dimensions of 254-mm diameter x 279-mm height, 254-mm diameter x 506-mm height, or 304-mm diameter x 609-mm height (right).

Figure 3.3.2: Diagram of injection mold (left), picture of specimen fabrication molds (middle), picture of PSB cylindrical specimen (right).

3.3.2.3 Analysis of Cyclic Triaxial Compression Tests

The cyclic triaxial compression test consists of applying a constant confining pressure (σ_3) to a specimen that is contained within a membrane and sealed in a triaxial chamber. A plunger or piston that extends through a seal in the top plate of the triaxial cell applies the cyclic load. The cyclic load is applied as a 5-Hz haversine, bell-shaped loading pulse with peak and rest loads as used in Ebrahimi 2011. A typical deviator stress at peak (300 kPa) and during the rest (17.6 kPa) period is given by

$$\sigma_p = \sigma_r = \frac{F_P}{A_P} \tag{3.3.1}$$

where the load from the piston (F_P) is applied through the area of the plate on top of the specimen (A_P). After each loading cycle, a non-recoverable deformation (plastic deformation, δ_P) is measured and plastic strain ε_P calculated from

$$\varepsilon_P = \frac{\delta_P}{L} \tag{3.3.2}$$

where L is the original length of the specimen. Throughout the cyclic triaxial test, plastic strain accumulates, which provides the deformational behavior of a material over the life cycle of loading cycles. The recoverable deformation (elastic deformation, δ_E) is found by subtracting δ_P from the measured total deformation (δ_T) in each load pulse, and the elastic strain ε_E is calculated from

$$\varepsilon_E = \frac{\delta_E}{L} \tag{3.3.3}$$

with peak stress (σ_P), rest stress (σ_R), and ε_E, the resilient modulus (M_R) calculated from

$$M_R = \frac{\sigma_P - \sigma_R}{\varepsilon_E} \tag{3.3.4}$$

The resilient modulus is an estimate of the Young's modulus and quantifies the stiffness of a material. In the cyclic triaxial tests, the calculation of the resilient modulus over many loading cycles reveals how the stiffness changes over the life cycle of the material or reaches a constant value after numerous loading cycles.

3.3.3 Monotonic and Cyclic Flexural Testing on PSB Beams

3.3.3.1 Methodology

The original hypothesis, before fabricating PSB beam specimens, was that ballast-RPF particle bonds and PSB flexural capabilities would be present after RPF injection. Furthermore, that injection of RPF into the ballast layer can be done to create a bound layer resembling a cement-stabilized soil or a pavement layer. Testing of PSB beams was chosen to determine the fatigue life of a polyurethane-stabilized ballast trackbed layer as discussed in Appendix A. Analyzing flexural strength and fatigue of bound material is common practice for use in the National Cooperative Highway Research Program's (NCHRP) Mechanical-Empirical Design and Rehabilitated Pavement Structures Guide (MEPDG). In pavement layer design, flexural strength of materials is an important factor for determining slab thickness. In the case of polyurethane-stabilized materials, the flexural strength may be an important factor if stabilization creates layers that begin to act as *in situ* continuous slabs, which would be below the subsurface where visual signs of degradation tend to go unnoticed.

The method for testing beam specimens is consistent with methods in the AUSTROADS procedure (Midgley and Yeo 2008), Federal Aviation Administration Report (Arellano and Thompson 1998), and from ASTM C78 and ASTM D1635. From these procedures and standards, a "third-point" loading setup was selected, which is different from a "Center-Point Loading" setup (e.g., ASTM C293), sometimes referred to as a "Three Point Bending Flexural

Test." A "third-point" loading setup is ideal for reducing the effects of shear stress during flexural testing and allows stronger analysis of flexural strength and fatigue properties.

Dimensions for typical cement-stabilized soil beams are provided in ASTM D1635 and Midgley and Yeo (2008). These dimensions were 76 mm x 76 mm x 290 mm; in this study, the dimensions of the beams were increased by a ratio of 2.63:1 to account for the large particle sizes in ballast. The dimensions used for the PSB beam molds were 200 mm x 200 mm x 763 mm. Though the ratio of maximum ballast particle diameter to specimen diameter was less than PSB cylinders; however, the ballast was still compacted to a maximum dry unit weight of 15.8 kN/m^3.

Load was applied to the "third-point" loading setup through a servo-hydraulic system (MTS®, loading capacity of ~22 kN). During cyclic and monotonic loading, vertical deflection of the specimens was measured using two (for redundancy) linear variable differential transducers, LVDTs, (Omega, 10±0.005-mm, Model AX/5/S) mounted to an LVDT stand that was setup to measure deflection internal to the beam loading setup and at the beam mid-span (i.e., load frame and beam platform strains were external to deflection measurements). For monotonic flexural beam testing, the strain rate recommended in ASTM D1635 was 0.02 mm/s mid-beam deflection. The nominal strain rate used in RPF cylinder testing was 0.02 mm/min. Methods used for analyzing RPF monotonic-triaxial compression results were taken from ASTM C78 and ASTM D1635.

3.3.3.2 Specimen Fabrication

Fabrication of beam specimens involved drilling an injection rod to the bottom of a pre-compacted ballast specimen contained within a beam mold (Figure 3.3.3). Typical RPF injections consisted of injecting a specified quantity of liquid RPF every 152 mm of height within the specimen. Each beam specimen, with dimensions 200 mm x 200 mm x 763 mm, would

have a specified injection quantity at the base, 152 mm from the base, 304 mm from the base, 457 mm from the base, and 611 mm from the base. Typical injection quantities for PSB beams are shown in Table 6.2.2. During injection, leakage of molten foam was detected in the seams of the specimen mold; however, this was advantageous as polyurethane expansion pressure was relieved. Despite molten foam leaking during injection, all of the beams formed as a continuous and uniform PSB beam.

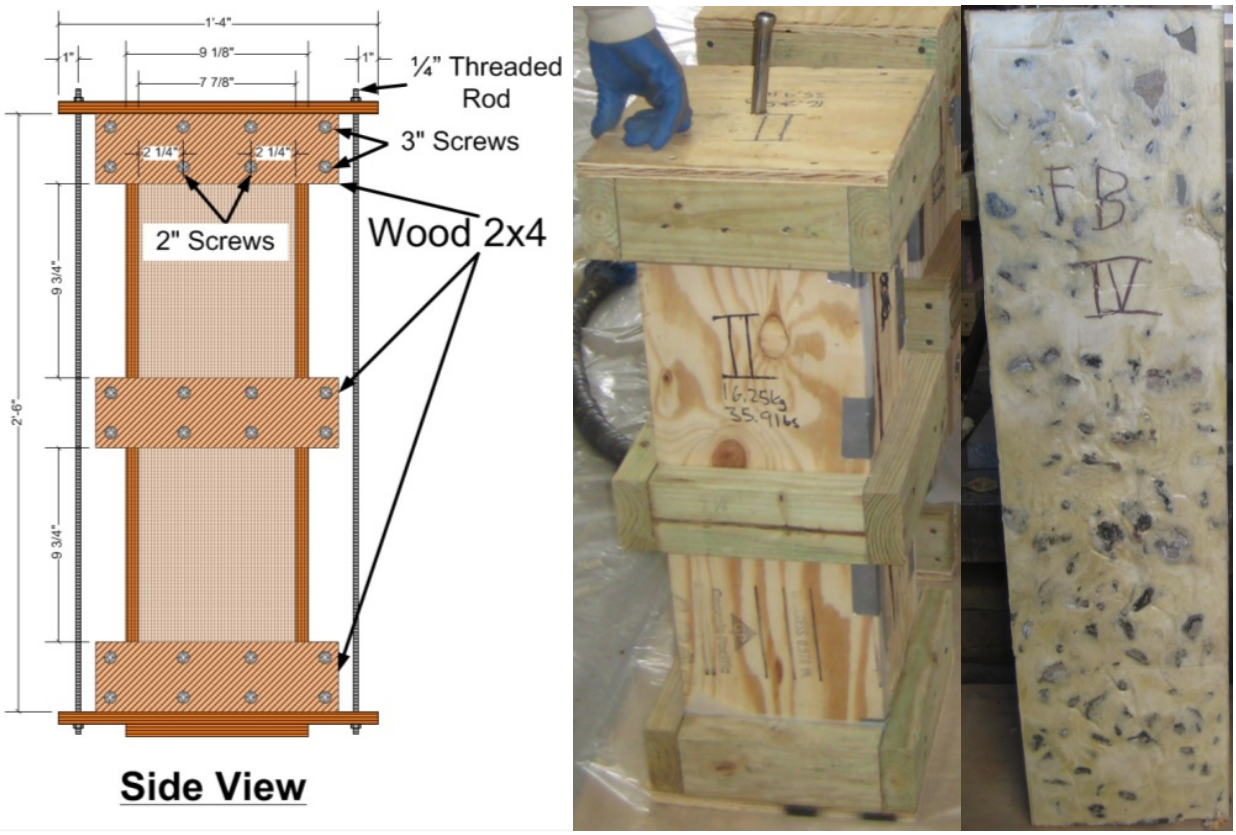

Figure 3.3.3: PSB beam mold schematic (left), fabricated wooden beam mold (middle), PSB beam (right).

3.3.3.3 Analysis of Monotonic and Cyclic Flexural Tests

The test frame setup used is the same for both flexural strength and flexural fatigue testing of beams. Since beam dimensions were increased by an appropriate factor (ASTM D1635 and from Midgley and Yeo 2008), the geometry of the test setup was also increased.

The flexural strength of the beams was determined using protocols from ASTM C78 and ASTM D1635. In the standards, constant rate loading is applied until the beam specimen ruptures. The load is applied to a fixture that distributes the load evenly through two loading rollers at the two center “third-points” of the beam and the beam is supported by rollers on the two outer “third-points” of the beam. The flexural strength, otherwise known as rupture modulus (R), is calculated as

$$R = \frac{P \cdot L}{w \cdot h^3} \qquad (3.3.5)$$

where P is the peak load (kN) during the test or load before rupture, L is the span length (m) between the bottom supports of the setup, w is the base width (m) of the beam, and h is the depth (m) or dimension of the beam between the top and bottom supports, all of which are shown in Figure 3.3.4.

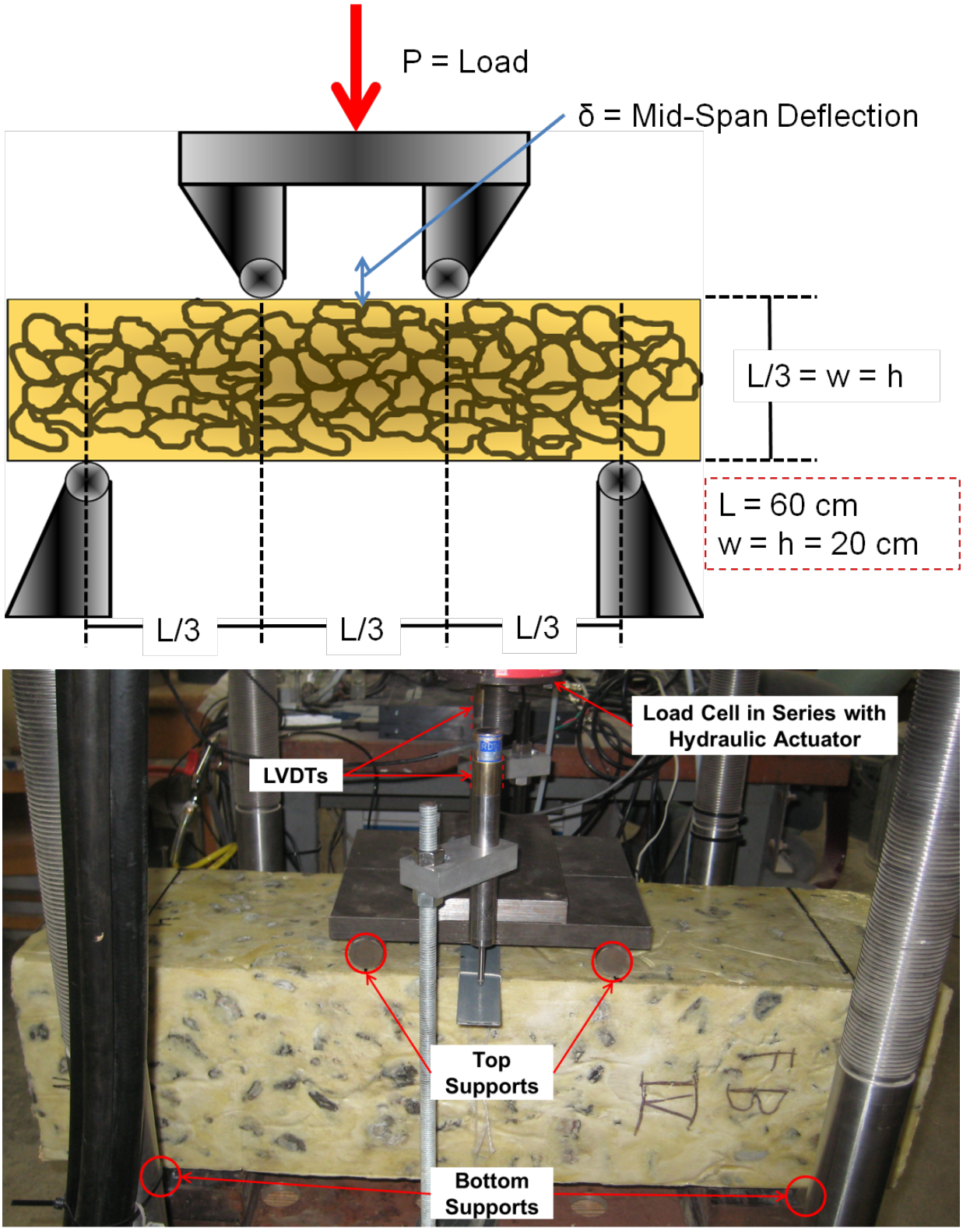

Figure 3.3.4: Typical “third-point” loading setup and chosen dimensions for PSB beams.

The cyclic load in flexural fatigue testing was applied as a 2-Hz haversine, bell-shaped loading pulse with peak and rest loads. A haversine wave with 2-Hz loading frequency was also used in the AUSTROADS procedure in Midgley and Yeo (2008) for beam fatigue testing. The flexural modulus is derived using beam theory where flexural stress and strain are inferred from applied loads and corresponding deflection of the beam at the mid-span. Otte (1987) indicated that in beam testing the material response in compression is supposed to be the same when in tension. Litwinowicz and Brandon (1994) conducted direct strain measurements between the bottom supports during beam tests and found that the direct strain measured was approximately the same as strain calculated using equations correlating mid-span deflection to peak tensile strain beneath the beams (i.e., elastic beam theory). In Midgley and Yeo (2008) and this study, the beam flexural modulus, flexural strain, and flexural stress were calculated using elastic beam theory as

$$S_{max} = \frac{\sigma_t}{\varepsilon_t} \times 10^3 = \frac{\frac{P \cdot L}{w \cdot h^2} \times 10^3}{\frac{108 \cdot \delta \cdot h}{23 \cdot L^2} \times 10^3} = \frac{23 \cdot P \cdot L^3}{108 \cdot w \cdot h^2 \cdot \delta} \quad (3.3.6)$$

where S_{max} is the flexural modulus (MPa), σ_t is the flexural stress (kPa), ε_t is the flexural strain (m/m), P is the peak load (kN), w is the width of the beam (m), h is the height of the beam (m), L is the span (m) between bottom two supports of the “third-point” loading setup, and δ_h is the deflection (m) at the mid-span occurring at peak load.

For each fatigue test, the load applied is typically chosen as a percentage of the average flexural strength, commonly referred to as the stress ratio, which is

$$Stress\ Ratio = \frac{Flexural\ Stress}{Flexural\ Strength} \quad (3.3.7)$$

For fatigue testing, a number of tests are conducted at varying stress ratios until fatigue failure. The number of cycles to fatigue can be correlated to stress ratio with the typical form given by

$$log\ N = \frac{k_1 - S}{k_2} \quad (3.3.8)$$

where N is the number of load cycles to failure, S is the stress ratio being applied, and k_1 and k_2 are fitting parameters for specific materials and behavior.

3.3.4 Unconfined Compressive Strength Testing on PSB Prisms

3.3.4.1 Methodology

For conservation of PSB material, after rupture of PSB beams, remaining segments of the beams cut with a concrete masonry saw to a 2:1 height-to-width ratio (PSB prisms) and subject to unconfined compressive strength (UCS) tests. A 2:1 height to width ratio was selected to reduce the effect of friction at the ends of the specimens (Bishop and Green 1965). This minimal height-to-width ratio is also recommended in applicable unconfined compressive strength test standards, which included ASTM D7012 for compressive strength and elastic moduli of intact rock core specimens and ASTM D1621 for compressive properties of rigid cellular plastics. Methodology from each of these standards was combined for testing on PSB prisms and subsequent analysis.

Load was applied to the prisms through a servo-hydraulic system (SATEC®, loading capacity of ~1,780 kN). Vertical deflection of the specimens was measured using extensometers as part of the SATEC NuVision Computer system during monotonic loading. The stress rate recommended in ASTM D7012 was 0.5 to 1.0 MPa/s for intact rock core specimens. The nominal stress rate used in PSB prism testing was 0.834 MPa/s. The test setup and corresponding diagram of the method is shown as Figure 3.3.5.

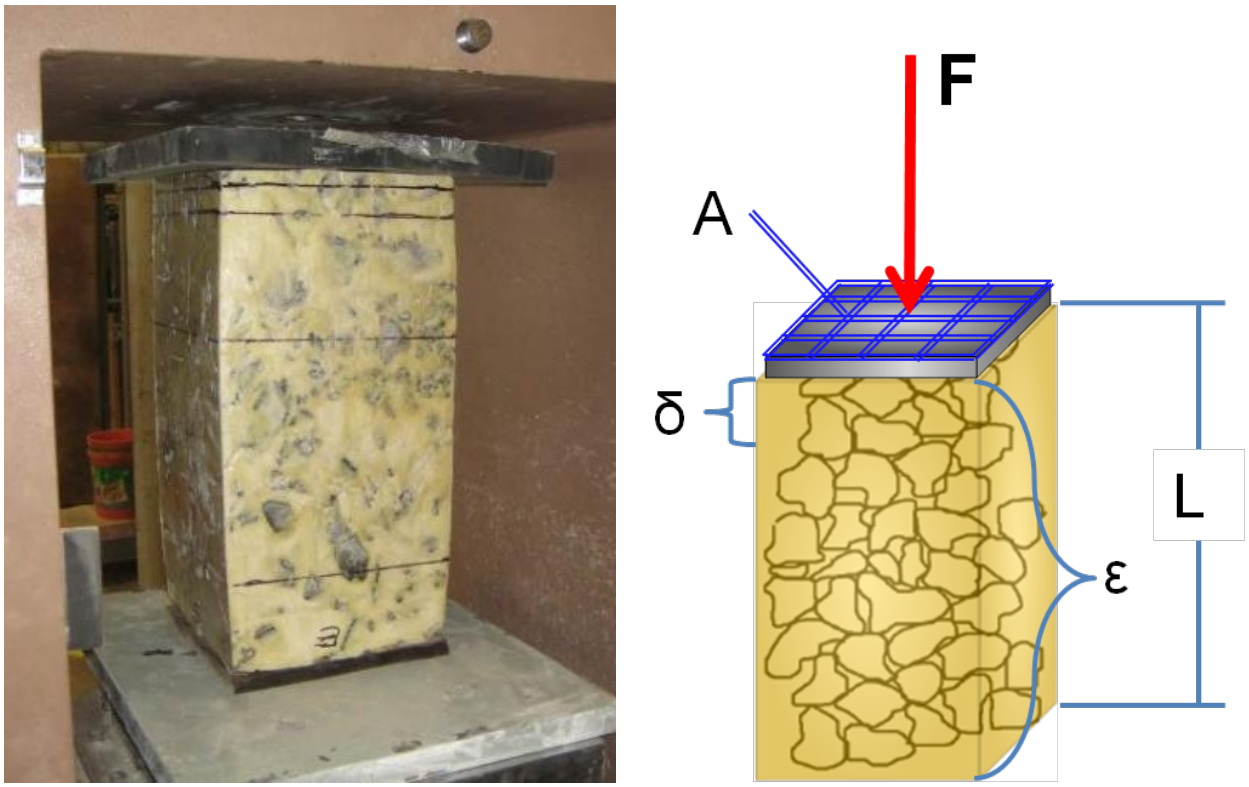

Figure 3.3.5: Picture of compression testing apparatus and diagram of compression testing parameters.

3.3.4.2 Specimen Fabrication

Failed beams were cut down to prismatic specimens with a 2:1 (height-to-width) ratio had nominal prism dimensions of 200 mm x 200 mm x 400 mm. These remaining beam segments were subjected to UCS tests, which involved placement in a loading machine that compressed the specimens while measuring load and displacement.

Since prism compression tests were not conducted on freshly fabricated specimens, there is some concern as to whether the compressive characteristics of PSB were adequately captured. In Section 4.7, the compressive and flexural properties from experimental testing of PSB are evaluated. PSB compressive strength (2,606 kPa) is much greater than flexural strength (938 kPa), but compressive modulus (95 MPa) is much less than flexural modulus (274 MPa). Therefore, the compressive strength was not exceeded during flexural testing. Average (AVG) compressive strain at failure was 2.34%, whereas AVG flexural strain at failure was 0.94%; thus, there is less strain tolerance in flexure than in compression. When forming the half-beam specimens, the areas of the beams where flexural rupture occurred were cut off, i.e., the segment where the highest stresses and strains occurred during flexural testing were not present in specimens subjected to compressive testing. Based on these results and fabrication methods, any damage in PSB beam specimens (i.e., occurring from failure) was unlikely to affect the properties measured during PSB compressive testing.

3.3.4.3 Analysis of Unconfined-Compression Tests

Unconfined compressive strength (σ_c) is

$$\sigma_c = \frac{F}{A} \tag{3.3.9}$$

where F is peak axial load applied and A is the area over which it is applied, both are diagramed in Figure 3.3.5. A typical phenomenon in elastic-plastic material is that initially elastic strain (ε_e)

increases linearly with axial stress until reaching the yield point, where plastic strain (ε_e) increases and the relationship to stress is no longer linear. Young's modulus, E, occurs within the linear region and is defined by

$$E = \frac{\sigma_a}{\varepsilon_e} \tag{3.3.10}$$

where σ_a is the axial stress being applied within the elastic range of the material.

At the beginning of compression tests, there is usually an accumulation of strain that occurs due to seating of the loading apparatus. In addition, for rigid cellular plastics, non-linear behavior may occur earlier in the test. For non-linear behavior and seating issues, methodology was adopted from ASTM D1621 for applying a compliance correction that allowed consistent data analysis techniques of PSB specimens evaluated using UCS tests. In typical UCS testing, significant accumulation of strain occurs at the beginning of the test under small loading, which should not be considered in modulus calculations. Per ASTM D1621, this accumulation of strain is removed by applying the compliance correction, where the linearly sloped line indicating the elastic range (i.e., Young's modulus) of the material is shifted to the origin.

3.4 RPF INJECTION PROCEDURES AND PSB MATERIAL COMPOSITION

3.4.1 PSB Phase Calculations

Calculations commonly used in soil mechanics for determination of index properties and phase quantities of soils were used in this study to define the density of ballast, RPF, and PSB of each fabricated specimen. For each PSB specimen, the ballast was compacted into a prefabricated mold prior to RPF injection utilizing the compaction procedure developed in Ebrahimi (2011). For each type of mold (e.g., cylinder, beam, etc.), a specified weight of ballast (W_b) was compacted into the initial mold volume. With the specified weight and initial volume of the compacted ballast, the void ratio and dry density were calculated using a specific gravity of ballast solids of 2.6 for the granitic ballast as determined in Ebrahimi (2011). Therefore, the void space was known for use in RPF injection quantity calculations.

After RPF injection, each PSB specimen was weighed (W_{PSB}) and measurements taken to determine the final volume (V_{PSB}). The PSD density (ρ_{PSB}) was determined by

$$\rho_{PSB} = \frac{W_{PSB}}{V_{PSB}} \tag{3.4.1}$$

A phase diagram (Figure 3.4.1) illustrates the phase relationships (i.e., densities of ballast and RPF) within the PSB composite. The RPF injection protocol and RPF density (ρ_{RPF}) calculations were experimentally determined during specimen fabrication. The remaining subsection demonstrates calculations for determining the quantity of each material phase (i.e., RPF and ballast) within the composite.

If mold expansion occurs, the new ballast density (ρ_b) is found using

$$\rho_b = \frac{W_b}{V_{PSB}} \tag{3.4.2}$$

After injection, RPF completely filled the void space of the ballast specimens; therefore, the RPF density could be found by

$$\rho_{RPF} = \frac{W_{RPF}}{(Final\ Void\ Space\ \%) * V_{PSB}} \quad (3.4.3)$$

During reaction, the effects of the blowing agent cause a release of CO_2 gas (Szycher 1999). For simplicity in these calculations, the mass loss of the gas is assumed negligible. Finally, the following equation is to calculate the percent of RPFby weight as

$$\%RPF = \frac{W_{RPF}}{W_{PSB}} \quad (3.4.4)$$

For the PSB specimens, on average, ballast was 95% by weight and 58% by volume, the PU (airless phase of RPF) was 5% by weight and 7% by volume, RPF was 42% by volume, and Air+CO_2 made up 35% by volume. Additional CO_2 is present due to the blowing agent and foaming process. Since the RPF phase (percent RPF by weight) was approximately 5% by PSB weight and ballast phase was approximately 95% by weight, the overall PSB density is controlled by the ballast phase density, as shown in Figure 3.4.1. There was no substantial correlation between RPF phase density with overall PSB or ballast phase densities.

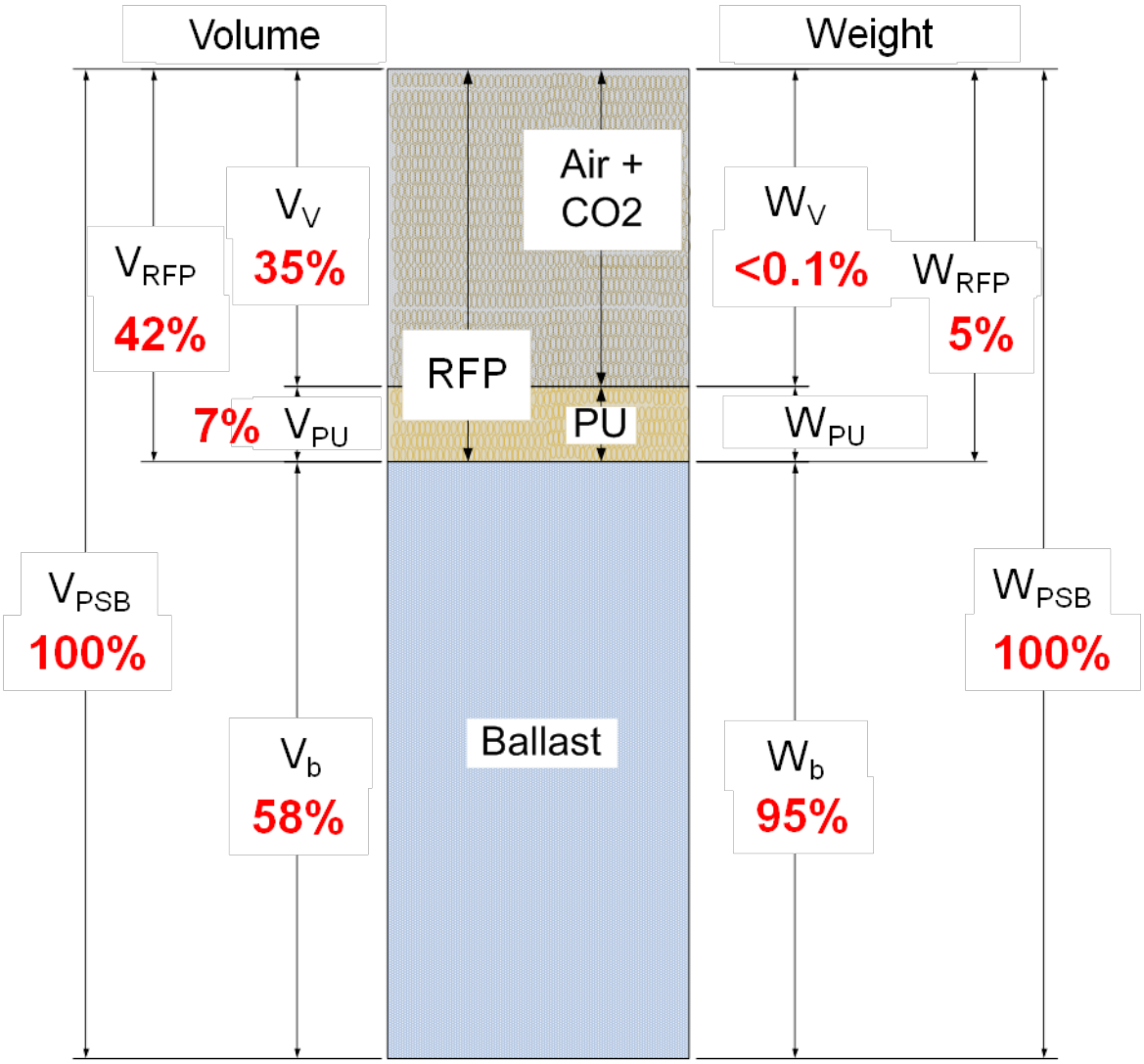

Figure 3.4.1: Phase diagram of a typical PSB specimen and average percentages for PSB compositions.

3.4.2 RPF Rheological Properties:

The rheological properties of RPF (486STAR-4 BD) during liquid, transition, and curing phases are important for administering ballast injections for stabilization purposes. The properties include the initial and final viscous characteristics of the expanding polyurethane and the force with which the polyurethane expands. Viscous forces, expansion rates, and achievable densities are dependent on injected volume, pressure of injection, rate of injection, resistive pressures, intrinsic permeability of pore space, and volume of pore space (Gupta et al. 2000; Martins et al. 2010). The final PSB specimen compositions are typically 5% RPF by weight.

In this study, the rheological behavior of the 486STAR-4 BD RPF was determined through index testing used by Uretek USA Inc. These index tests are temperature dependent as shown in Figure 3.4.2. The specifics regarding phase reactions and timing are critical for targeted injections and are given in Appendix A and shown in Figure 3.4.3.

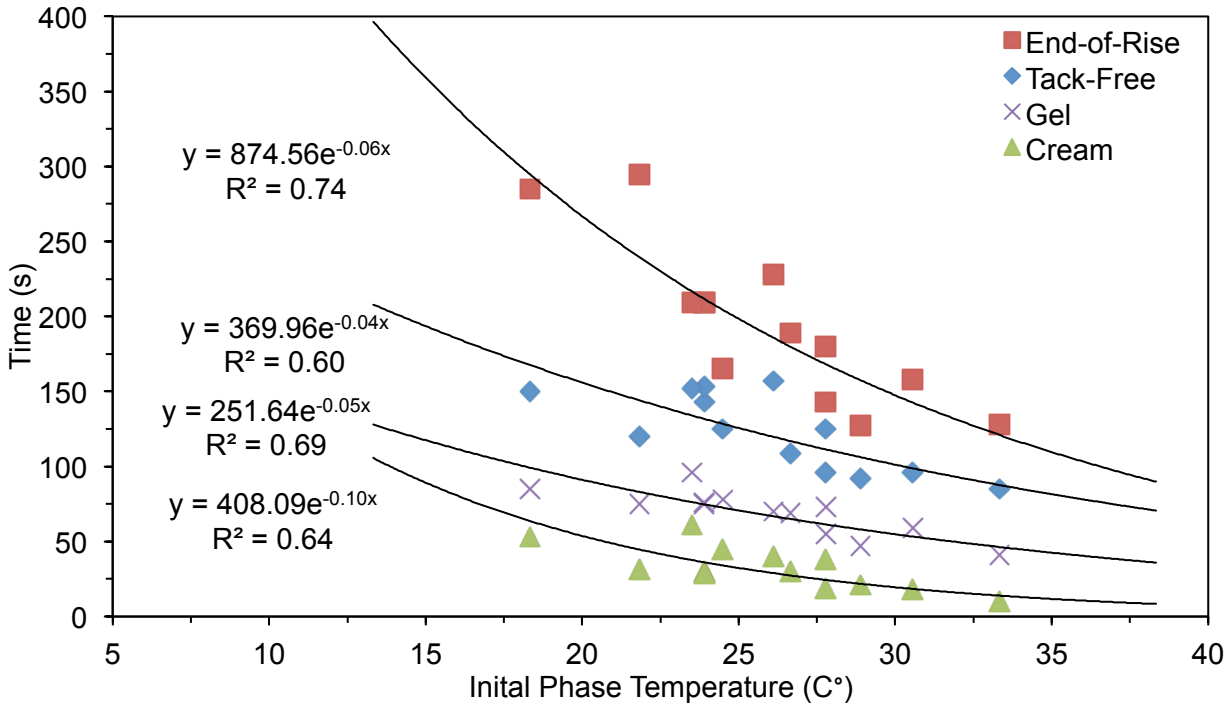

Figure 3.4.2: Trends were applied for the time of transition for each phase based on the measured initial temperature of the RPF liquid.

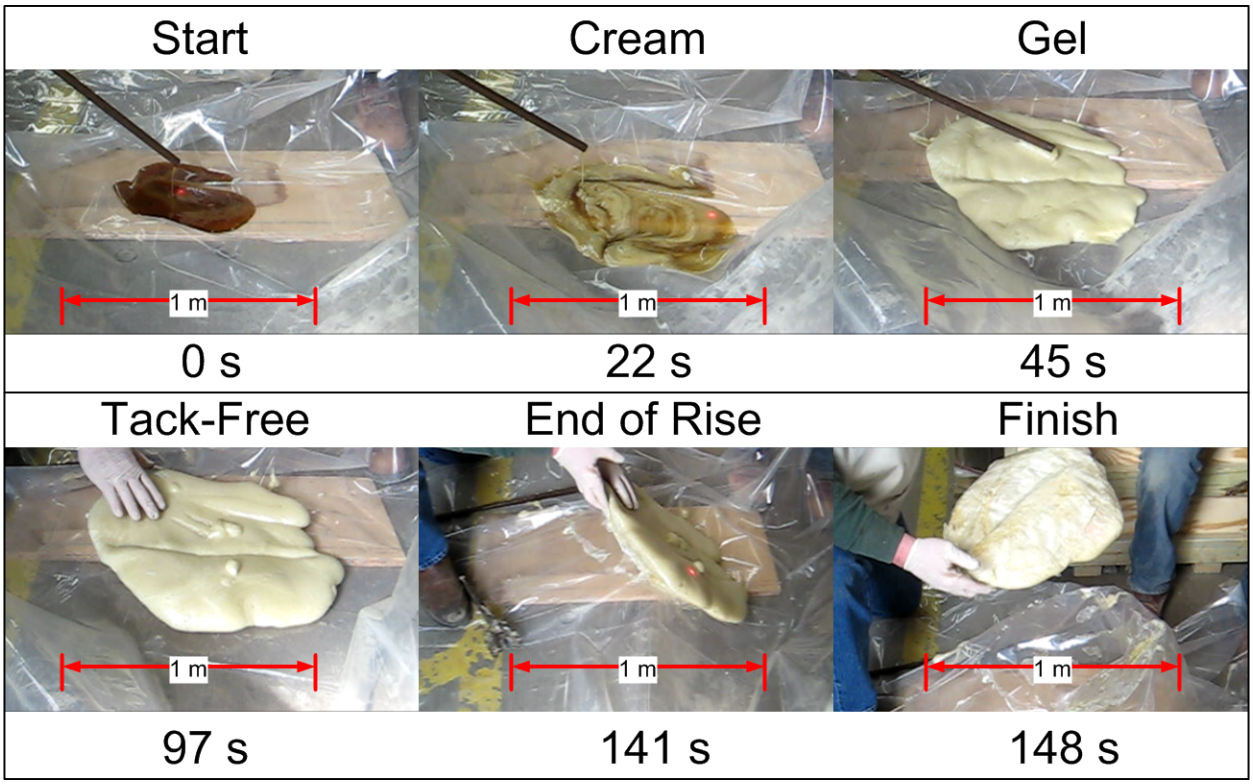

Figure 3.4.3: Pictures displaying each phase of the RPF reaction process with timings displayed for a 35°C starting temperature.

3.4.3 Polyurethane Expansion Pressure and Injection Development

To reach targeted RPF volume and density, during specimen fabrication, timed injections were used to prevent too much reacting RPF from being injected into the compacted ballast specimen. To control the amount of expansion force produced, injections were conducted at different heights within the specimens and timed at specified intervals. The time interval between injections was 45 ± 15 s. The 30 s minimum injection interval was established to ensure that there was not too much reacting polyurethane injected at the base of the specimens and so successive injections would occur while RPF was expanding (i.e., rising vertically). No more than 60 s was allowed between injections to prevent RPF from curing within the injection nozzle, thus compromising the procedure. This approach was developed and improved by assessing failed specimen fabrications that occurred early in the research. Further details regarding expansion pressure and injection development are covered in Appendix A.

3.4.4 Ballast Layer Injection Methods

Prototype ballast layers were constructed and used to simulate RPF injection into the ballast layer and to develop procedures for how the ballast layer can be injected to target particular outcomes in the field. The RPF injections selected were aimed at observing injection of RPF into an open ballast layer as opposed to a specimen in a mold and for determining the resulting geometry of the stabilized areas. In the ballast layer prototypes, two types of injection scenarios were developed. One scenario involved application of RPF along the surface (percolation-injection) to determine the depth the RPF would reach while in liquid phase and how much lateral expansion through the void space would occur. The other scenario involved injecting RPF at half the depth of the ballast layer (subsurface-injection) to determine how much lateral and vertical RPF expansion would take place and the resulting geometry of the subsurface injections.

With the RPF percolation-injection approach, the result was the formation of PSB extending from the ballast surface down to the base of the ballast layer, as depicted in Figure 3.4.4. Details of the RPF percolation-injection procedure are detailed in Appendix A, mechanistic properties of this type of PSB formation is detailed in Section 4.2 and 4.3, and a model evaluating the effect of these formations on track response is covered in Chapter 6. When the RPF subsurface-injection technique was employed, a layer of PSB was formed at the base of the ballast layer prototype as shown in Figure 3.4.4 and detailed in Appendix A. The mechanistic properties pertaining to this type of PSB formation (RPF subsurface-injection) are detailed in Section 4.4 and 4.5 and a model evaluating the effect of these formations on track mechanical response is covered in Chapter 5.

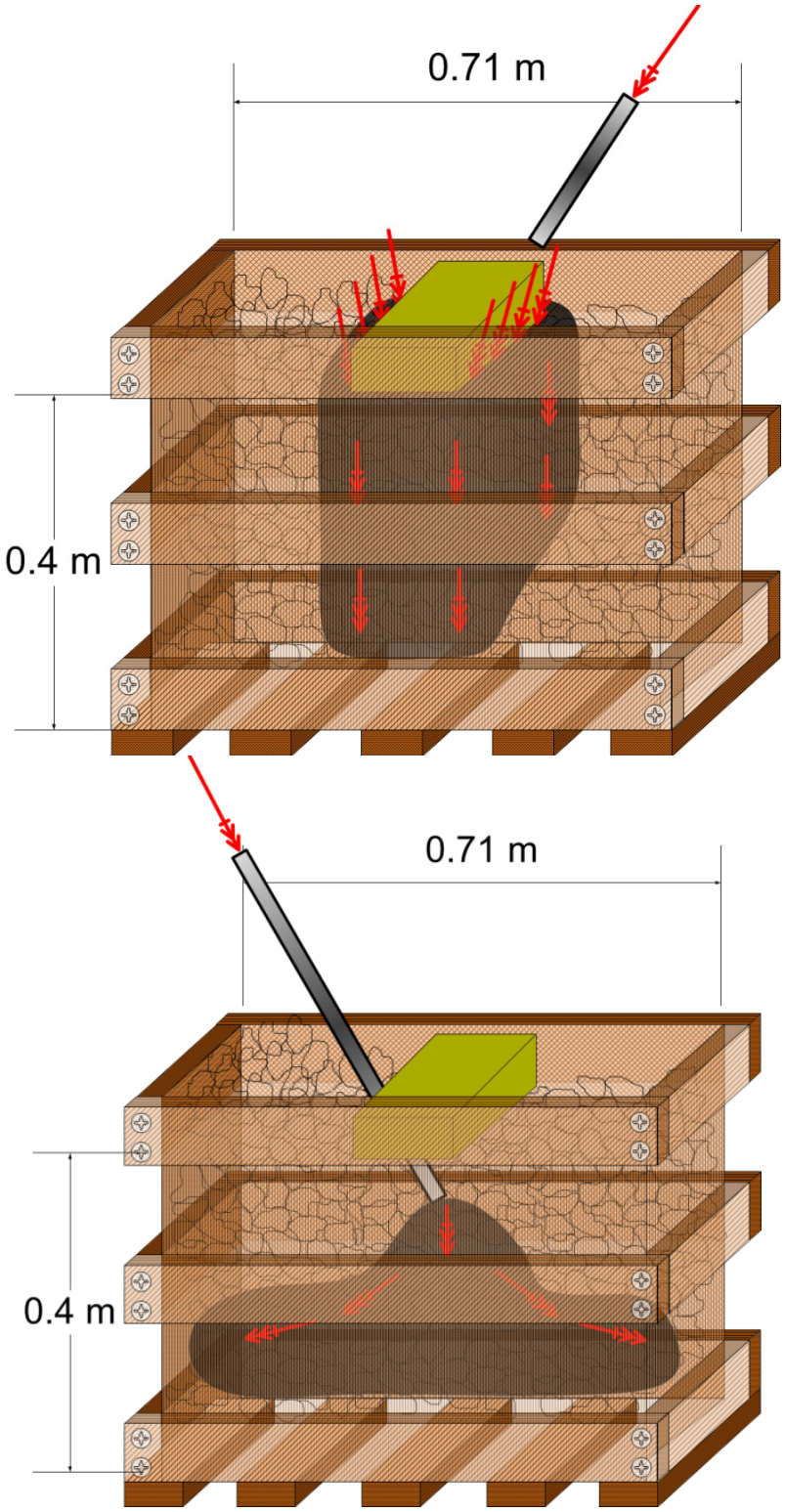

Figure 3.4.4: Illustration of methodology for ballast layer prototype with RPF percolation-injection (top) and RPF subsurface-injection (bottom).

4 EVALUATION OF MECHANICAL BEHAVIOR

4.1 INTRODUCTION

In the following sections, the mechanical behavior of PSB was compared to PSB composition Cyclic triaxial compression testing is used for determining plastic and elastic deformational behavior of infrastructure materials commonly exposed to repetitive compressive loading in the field. Plastic and elastic deformation of material in rail track substructure is an important aspect for determining required maintenance frequency and track life cycle (Ebrahimi 2011). This laboratory testing method was used to determine mechanical properties of PSB formation using the percolation-injection method introduced in Section 3.4.

Flexural fatigue testing is typically used for determining fatigue characteristics of bound materials that undergo repetitive bending in transportation infrastructure, such as concrete, asphalt, and cement-stabilized soils. Fatigue and resilient response of materials in the track are important aspects for determining required maintenance frequency and life cycle of bound layers Huang (2004). This laboratory testing method was used to determine mechanical properties of a PSB formation using the subsurface-injection method introduced in Section 3.4.

Unconfined compressive strength (UCS) testing is typically used for determining strength and Young's modulus of materials as a reference index to verify that other mechanical properties can be confirmed in the material (e.g., UCS tests on concrete for confirming tensile strength). The strength and modulus of the PSB prisms were found to correlate with the phase properties (i.e., PSB density, ballast density, percent RPF by weight, etc.) of the specimens, methodology and phase density calculations are detailed in Section A.1.2 of Appendix A. Constitutive relationships were established based on the empirical results and phase properties of the PSB prisms presented herein (Section 4.6).

In Section 4.7, the mechanical properties of RPF and PSB are compared with each other and to other materials such as cement-stabilized materials (CSM) and concrete. Effects from other features of PSB and RPF composition on the overall mechanical behavior and a more detailed discussion on the constituents of PSB mechanics are presented.

4.2 PLASTIC DEFORMATIONAL BEHAVIOR UNDER CYCLIC-COMPRESSION

Similar to cyclic triaxial compression testing on railway ballast, preliminary testing involved subjecting PSB cylindrical specimens to cyclic loading under a representative state of stress as defined in Ebrahimi (2011). Initial cyclic triaxial tests were conducted at a deviator stress, σ_d, of 300 kPa, PSB deformational behavior varied as RPF density varied (Figure 4.2.1). In Phase I, during specimen fabrication when no confinement was applied and where RPF was allowed to expand the ballast void space, (i.e., a "high volume increase"), the PSB specimen had cumulative plastic stain, ε_P, of 0.43% or 63% less than clean ballast over 200,000 loading cycles. In cases during specimen fabrication where full confinement was applied during RPF injection (i.e., a minimal or "low volume increase"), the PSB specimens had cumulative ε_P of 0.15% or 87% less than clean ballast. The high and low volume increases are described by using the percent RPF by weight (see A.1.1 of Appendix A). In both high and low volume cases, the deformational behavior of the PSB is far less than clean ballast (Figure 4.2.1).

In Phase II, injection quantities were targeted that would produce a minimal amount of RPF expansion/reaction pressure (i.e., optimum void filling behavior). As detailed in A.2 of Appendix A, the ideal practice for injection involves filling the ballast pore space while producing minimal expansion of the pore space, thereby retaining ballast layer geometry and minimizing quantity of RPF injected. In Figure 4.2.1, the plastic deformational behavior of a specimen with the optimum injection is compared to the two specimens with the high and low volume increase. The PSB specimen with optimum injection had cumulative ε_P of 0.22%, which is 74% less than clean ballast over 200,000 loading cycles. The deformational behavior of the PSB specimens under the representative state of stress (Ebrahimi 2011), measured by accumulation of plastic strain, ranged from 63% to 83% less than clean ballast within 250,000 loading repetitions (Figure 4.2.2); therefore, PSB can be expected to have a much higher resistance to plastic deformation under normal cyclic loading conditions.

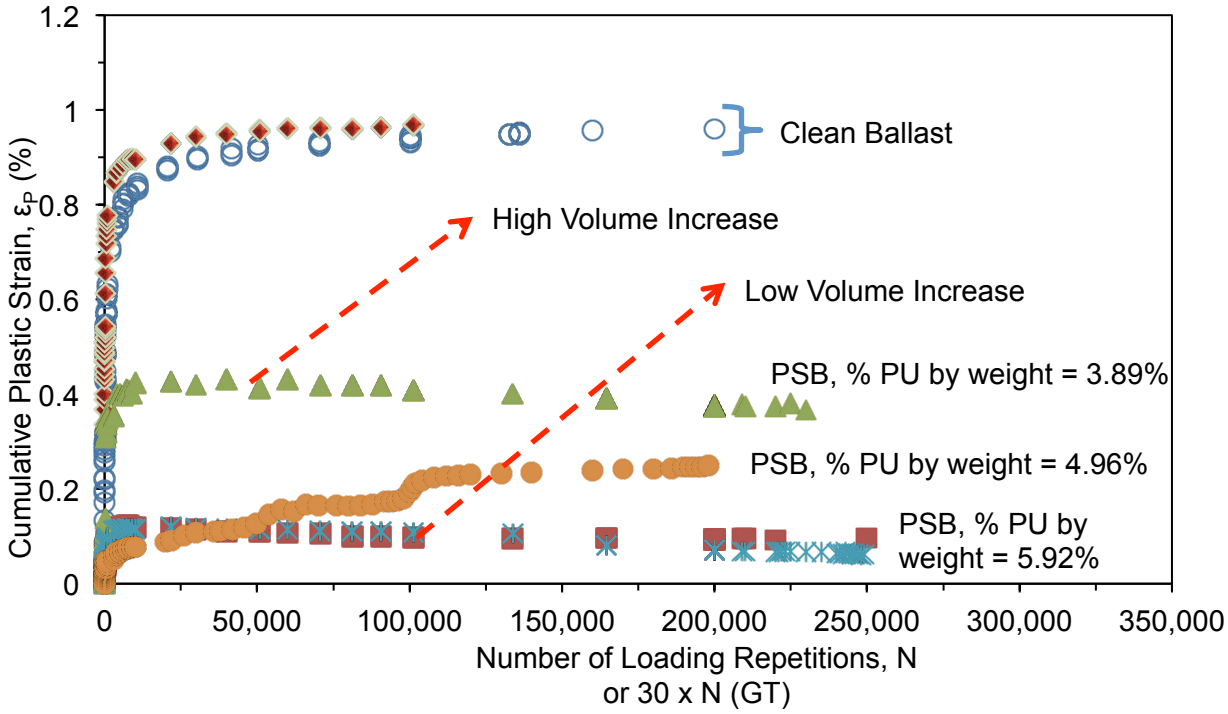

* PSB tests conducted at σ_d=300kPa, σ_c=100kPa

Figure 4.2.1: Cyclic triaxial compression testing on clean ballast and PSB specimens with confining stress, σ_c, of 100 kPa. Overlapping clean ballast data sets were taken from two different triaxial cells.

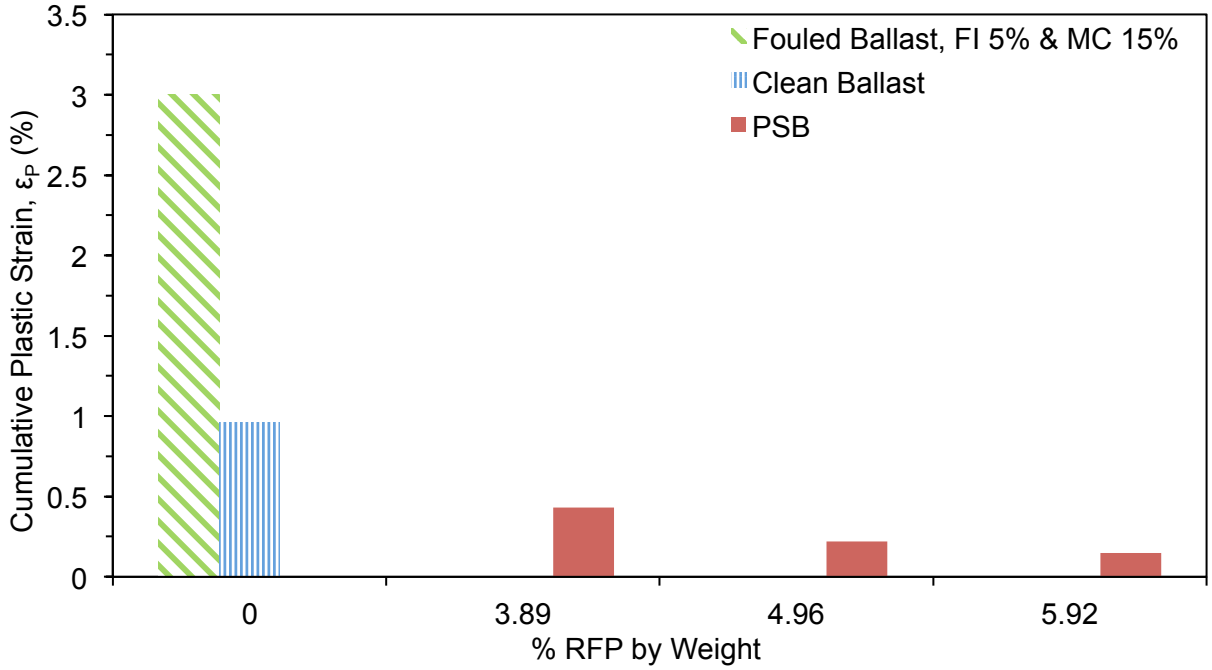

Figure 4.2.2: Cumulative plastic strain after 200,000 cycles in fouled ballast, clean ballast, and PSB at a deviator stress, σ_d = 300 kPa. *Note: FI=fouling index, MC=moisture content.

The representative state of stress (Ebrahimi 2011) applied as repetitive loading can be converted to a traffic quantity measurement that is commonly used in the rail industry, known as million gross tons (MGT), where representative axel load is 264 kN (30 standard tons). The conversion from number of loading repetitions (N) to million gross tons is given by

$$MGT = \frac{N \times 30}{10^6} \qquad (4.2.1)$$

Similar representative axel loads were used in other studies, such as Salim (2004), where a nominal axel load of 250 kN was assumed for cyclic triaxial testing. Under typical stresses, the deformational response of PSB is compared to clean and fouled ballast, where the cumulative plastic strain of PSB is far less than clean ballast and various fouled ballast compositions (i.e., FI = 5%, 10%, 20% & 25%, MC=15%) characterized in Ebrahimi (2011), as seen in Figure 4.2.3.

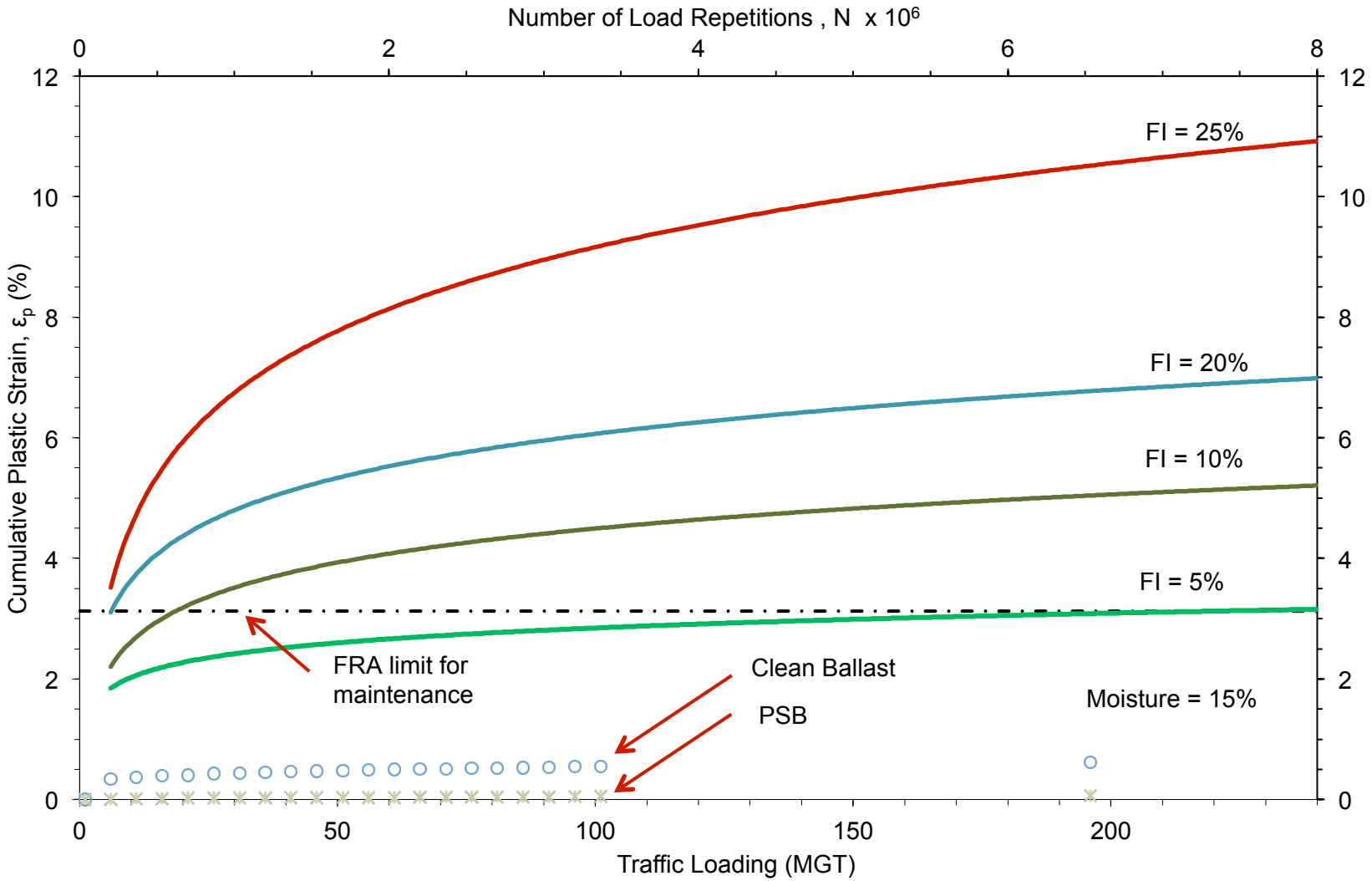

Figure 4.2.3: Comparison of different materials at the same states of stress in the cyclic triaxial compression tests. Fouled ballast data from Ebrahimi (2011). *Note: FI=fouling index, MC=moisture content.

Several studies (e.g., Indraratna et al. 2011) document that forces generated in the track can far exceed that of the static axel load from a train. Higher forces in the track are typically generated by dynamic loading of passing high-speed trains and freight trains loads that are amplified at lower speeds (i.e., when passing over defects in the track). In Banimahd & Woodward (2007), railway tracks near bridge abutments or tunnels required more frequent maintenance and commonly sustained damage from dynamic loading associated with passing freight trains. Banimahd & Woodward (2007) listed several other track and substructure defects that can lead to an amplification of the load on the track and inconsistencies in track stiffness. Some defects include penetration of the ballast layer into the subgrade, cracks in concrete sleepers or slab track, and permanent track deformation due to substructure degradation. Lichtberger (2005) listed rail superstructure and surface defects that can produce dynamic loads with high-speed trains, such as train wheel slip marks, track gauge defects and substructure settlement, and natural train oscillations. Since a large range of stresses are typically exhibited on the track substructure in areas that undergo high dynamic loading (i.e., bridge and tunnels approaches, bolted rail joints, rails with track gauge defects, etc.), PSB was tested under repetitive loading at higher stresses to observe the deformational behavior of the material.

Aursudkij et al. (2009) conducted tests on clean ballast up to a cyclic deviator stress of 360 kPa to determine deformational response; however, in their study, they determined that stresses up to 260 kPa were typical from rail loading. In Lichtberger (2005), the pressure at the top of the ballast layer was reported as high as 370 kPa. Since the objective behind application of RPF for stabilizing ballast is to increase track substructure strength and thereby enhance railway capacity, a range of stresses were selected that would exceed loading conditions in most situations, including the those previously mentioned. To understand the deformational behavior of PSB under higher loading conditions, PSB specimens were tested at deviator stresses ranging from 300-400 kPa.

To determine the deformational behavior of PSB, cylindrical specimens were tested at σ_d of 300, 350, 375, and 400 kPa. For comparison to clean ballast at the representative state of stress (Ebrahimi 2011) with σ_d = 300 kPa, the PSB specimen had cumulative plastic strain, ε_P, of 0.22%, or 74% less over 200,000 loading cycles (see Figure 4.2.4). As the range of σ_d from 300 to 400 kPa was applied, the ε_P of PSB over 200,000 cycles ranged from 0.22% to 1.3%, as seen in Figure 4.2.5. The increase in ε_P of PSB from 0.22% to 1.3%, when increasing the deviator stress from 300 to 400 kPa is a significant increase. However, the ε_P in PSB (1.2%) was only marginally higher than clean ballast (ε_P = 0.96%) tested at 300 kPa. ε_P of PSB tested at σ_d of 400 kPa was still 60-90% less than fouled ballast (σ_d = 300 kPa) with FI ranging from 5% to 25% and MC held constant at 15%. In addition, after 200,000 cycles up to 500,000 cycles, there was minor increase in ε_P of PSB tested at σ_d of 400 kPa whereas fouled ballast experiences a continual increase in ε_P under cyclic loading (Ebrahimi and Keene 2011). From the range of deviator stresses used in cyclic triaxial compression tests on PSB specimens, the material resisted permanent deformation far better than clean ballast and moderately fouled ballast (FI = 5%, MC = 15%), as seen in Figure 4.2.5.

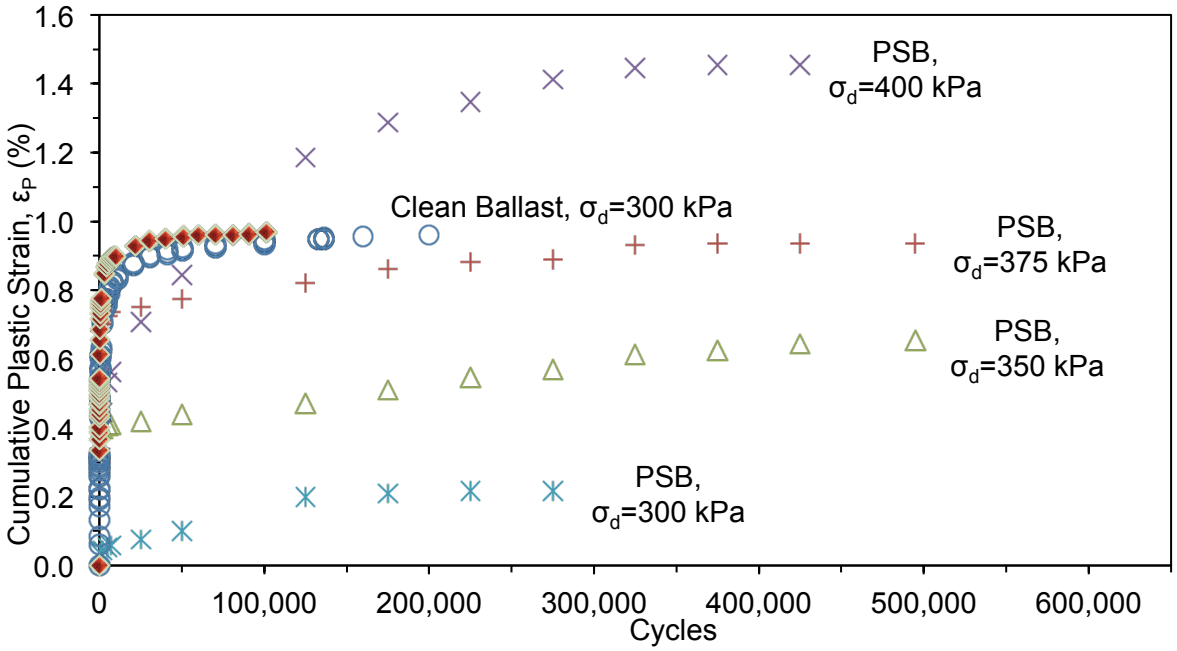

Figure 4.2.4: Results of cyclic triaxial compression tests; clean ballast density was 1,600 kg/m^3 and average PSB densities were 1,630 kg/m^3. Axis with loading repetitions was not labeled MGT because higher deviator stresses do not apply to load class.

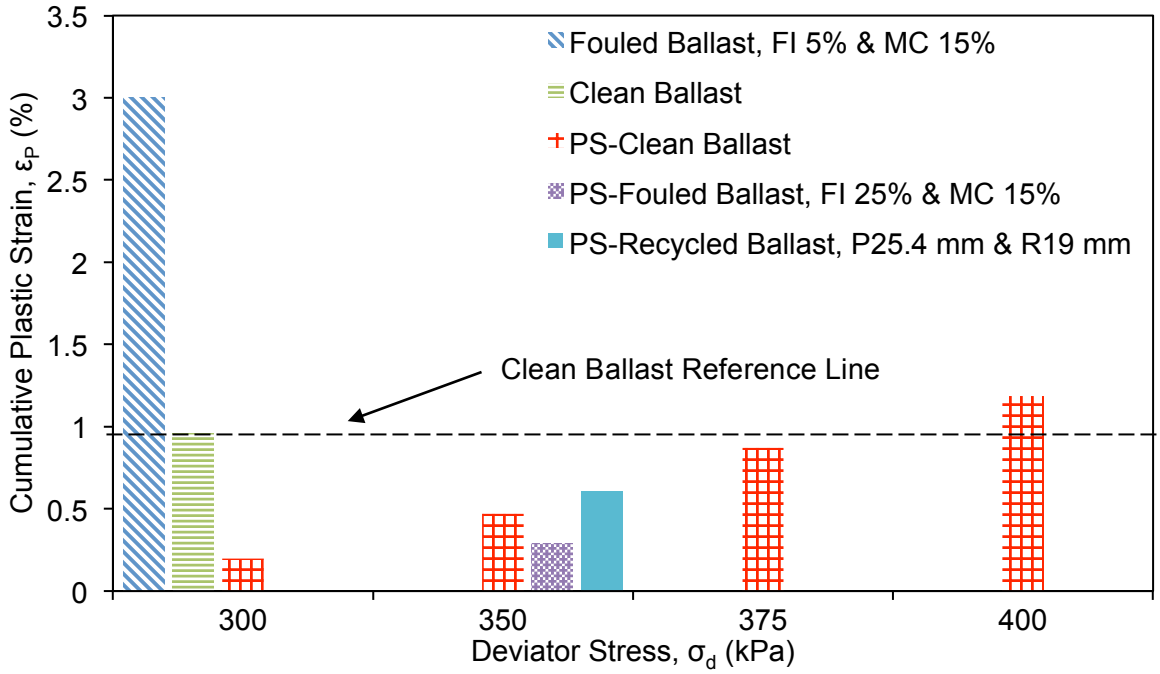

Figure 4.2.5: Comparison of cumulative plastic strain over 200,000 loading repetitions for untreated clean and fouled ballast with polyurethane-stabilized clean ballast, recycled ballast, and fouled ballast. *Note: FI = fouling index, MC = moisture content.

In other studies conducted on railway ballast using cyclic triaxial equipment, a large range of loading repetitions are used to characterize deformational behavior. In Anderson and Fair (2008), loading repetitions applied during cyclic triaxial testing ranged from 100 to 1.8 million cycles to measure long-term deformation, particle breakage, and volumetric strain. In Aursudkij et al. (2009), 100,000 cycles were typically used in cyclic triaxial testing under differing deviator and confining pressures, which were compared to a full-scale model where 1 million cycles were applied. In Ebrahimi (2011), typical cyclic triaxial compression tests were conducted up to 200,000 cycles, after which the test was concluded or conditions of the material being tested were changed to simulate maintenance or weather events (i.e., compaction for simulating tamping or addition of water for simulating a rainfall). In Salim (2004), cyclic loading tests on ballast were conducted in a laboratory model apparatus up to 500,000 loading repetitions, similar in extent of loading repetitions and use of full-scale prototype as in Aursudkij et al. (2009). In Salim (2004), wet and dry samples of clean ballast, recycled ballast, and ballast reinforced with a geocomposite material were tested. In all of the materials tested, the accumulation of plastic strain or "ballast settlement" was observed to stabilize after 100,000 loading repetitions with only marginal increase in settlement thereafter. PSB specimens that were fabricated in Phase I were tested up to 250,000 loading cycles to compare deformational behavior to clean ballast over a typical test increment for cyclic triaxial compression testing of ballast and railway materials.

Ebrahimi and Keene (2011) extrapolated the long-term deformational behavior of the railway by calculating the plastic strain rate (r_P) of clean and fouled ballast materials. For clean ballast and ballast with a fouling index (FI) below 5%, the r_P was constant up to 10,000 loading repetitions (which was designated the initial compaction phase, ICP) and then the r_P began to approach zero over the remaining 190,000 loading repetitions. Similar to Salim (2004), there was only a marginal increase in ε_P of clean ballast after 100,000 loading cycles were applied. In

Ebrahimi and Keene (2011) for the case of fouled ballast (e.g., FI=25%, MC=15%), the r_P was constant up to 10,000 loading repetitions (ICP) and then the rate of plastic strain began to increase linearly over the remaining 190,000 loading repetitions; this is termed the fouling impact phase, FIP. Where the rate of plastic strain increases linearly, the accumulation of plastic strain therefore increases logarithmically, at which point fouled ballast has typically exceeded deformation (i.e., ε_P) limitations set by the Federal Railway Administration. To determine the deformational behavior of PSB in cyclic triaxial tests, the PSB specimens fabricated in Phase II were subject to 500,000 loading repetitions, which was similar to typical full-scale tests and longer than the cyclic triaxial compression tests discussed in studies mentioned previously. Under the deviator stresses used in cyclic triaxial testing of PSB specimens, ε_P appeared to only marginally accumulate after 300,000 cycles at the highest stress level (σ_d = 400kPa). At lower deviator stresses minimal increases in ε_P was after 100,000 loading repetitions (Figure 4.2.4). Therefore, 500,000 loading repetitions were used for determining the long-term deformational behavior of PSB under cyclic loads.

A limited number of PSB specimens were fabricated successfully with different soil compositions (i.e., different levels of fouling and use of recycled ballast); thus, a higher deviator stress greater than 300 kPa used by Ebrahimi (2011) was selected. Cyclic triaxial compression tests were also conducted on polyurethane-stabilized (PS) fouled ballast and PS–recycled ballast to determine plastic and elastic deformational behavior. A cyclic deviator stress of 350 kPa was selected to confirm that stabilization of fouled and recycled ballast would increase resistance to cumulative of plastic strain under cyclic loading and thereby increasing rail freight capacity in accordance with the objectives of this study. When comparing to a PS-clean ballast (previously referred to as PSB) specimen, the PS–recycled ballast specimen had an accumulation of plastic strain, ε_P 0.62%, or 13% greater over 200,000 loading cycles. The PS–

fouled ballast had ε_P of 0.29%, or 54% less than the PS-clean ballast had over 200,000 loading cycles (Figure 4.2.6).

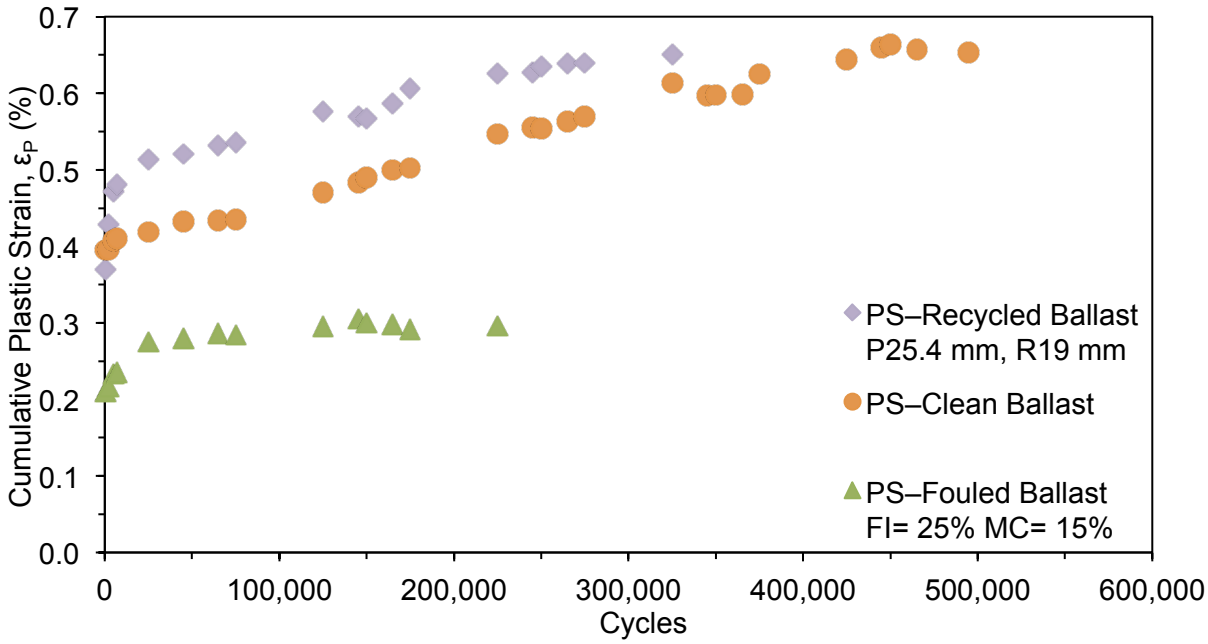

Figure 4.2.6: Soil compositions stabilized with polyurethane tested at the same deviator and confining stress in the cyclic triaxial test. PSB tests conducted at σ_d = 350 kPa, σ_c = 35 kPa.

Ebrahimi (2011) conducted cyclic triaxial compression tests on untreated recycled ballast and untreated clean ballast finding that recycled ballast has 50% higher ε_P than clean ballast over 200,000 cycles under the representative state of stress. Salim (2004) explained that ε_P of recycled ballast is higher than clean ballast because of the roundness of the recycled ballast aggregates and the lower friction angle relative to clean ballast. Poor recycled ballast plastic deformational behavior (compared to clean ballast) can be attributed to recycled ballast consisting of aggregates taken out of service that have likely undergone long-term weathering and track loading. Weakness in recycled ballast compared to clean ballast may contribute to the higher ε_P observed in PS-recycled ballast relative to PS-clean ballast.

Perry and Gillott (1997) found that behavior of concrete in compression is controlled by the dependence of mortar-aggregate bond strength on aggregate-surface texture. They showed that unconfined compressive strength of concrete is greater with aggregates that are angular and with surfaces that are rough. Similar binder-aggregate bonding and geometric interaction likely exist within PSB and explain why the PS-clean ballast resisted accumulation of plastic strain more than PS-recycled ballast, despite having a similar bulk density (i.e., PSB density) and RPF content (percent RPF by weight). However, in this chapter, the hypothesis presented supports that the mechanical behavior of PSB is related more to the percent RPF by weight and PSB density than angularity of the aggregates within.

The fouled ballast specimen that was stabilized had a fouling index (FI) of 25% and moisture content (MC) of 15%. When ballast with these fouling conditions was tested by Ebrahimi (2011) at a deviator stress of 300 kPa and confining stress of 100 kPa, ε_P reached 11% over 200,000 loading repetitions. In this study, the PS-fouled ballast (FI=25%, MC=15%) was tested at a greater deviator stress (350 kPa) than in Ebrahimi (2011) and a 97% decrease in ε_P (0.3%) was observed due to RPF stabilization. One characteristic that likely plays a role in the decrease in deformational behavior of fouled ballast is that the fouling materials become

integrated with and enclosed by the injected RPF, thus preventing an initial compaction phase and transformation to a fouling impact phase, as described in Ebrahimi (2011). Other aspects of PS–fouled ballast behavior may involve RPF bonding characteristics within PS-fouled ballast and the aggregate density of fouled ballast prior to injection. The important consideration is that fouled ballast stabilized with polyurethane outperformed PS–clean ballast and PS–recycled ballast.

When comparing quantity of stabilization in clean ballast to that of fouled ballast, the percent RPF by weight was 2.9% in fouled ballast, which fell below the average percent RPF by weight (5%) injected into the clean ballast specimens. The phase RPF density, ρ_{RPF}, calculated to be within fouled ballast was 185 kg/m^3, which is in the lower range of the clean ballast specimens fabricated (ρ_{RPF}=200 ± 36 kg/m^3), as seen in Table 6.2.1. Therefore, a similar RPF density can be achieved in a well-graded material (i.e., fouled ballast), as in a coarse-graded material (i.e., clean ballast). The density of the aggregates within the fouled ballast specimen (19.4 kN/m^3) was much greater than the clean ballast specimens (15.8 kN/m). The influence of density on the plastic and elastic deformational behavior of the material are consistent with other aspects of PSB mechanical behavior discussed later in this chapter. The stabilization of fouled ballast was more effective for resistance to ε_P that clean ballast under cyclic loading conditions. Even though the RPF density was similar in both materials, greater resistance to accumulation of plastic strain in PS-fouled ballast compared to PS-clean ballast can be attributed to the higher aggregate phase density in PS-fouled ballast. Similar behavior is observed in asphalt (Tia 2003), where denser aggregate continuum is ideal because performance, strength, and load bearing capacity are controlled by the aggregate skeleton (i.e., packing of particles and density).

Aggregates in asphalt typically comprise of 90-95% of the weight and 75-85% of the volume. From PSB investigated in this study, the clean ballast was 93-95% by weight and 56-

64% by volume. The PS-fouled ballast specimen consisted of aggregates with 97% by weight and 71% by volume. For asphalt, detailed tests and calculations must be conducted to determine percent air voids, percent voids in the mineral aggregates, and percent voids filled. These calculations are conducted to ensure that adequate amounts of asphalt binder are added so specified bonding and strength properties can be achieved. Asphalt binder content must be increased when aggregate surface area and void space is increased (Tia 2003), but in PSB, the RPF expands and fills the void space achieving what must be done through heating, mixing, and compaction with asphalt. These phase density characteristics that influence PSB mechanical behavior are conceptually the same as the properties (e.g., aggregate shape and texture, binder design, etc.) studied for understanding asphalt mechanical behavior. The constituent materials (i.e., RPF and ballast) of PSB likely control the plastic and elastic deformational behavior of PSB as is presented in the remaining sections.

Due to void space filling behavior of RPF when injected into ballast, the generation of fine particles from ballast breakage, infiltration of fouling into the ballast layer from external sources, and flow of water through ballast is prevented. Consequently, mechanisms that generate fouling and infiltration of water from precipitation events may not play a role in the permanent deformational behavior of PSB and thus become a secondary concern. For simulating ballast/substructure conditions between maintenance intervals, Ebrahimi (2011) tested a sample of moderately fouled ballast at 200,000 cycle increments, between which the ballast conditions were adjusted (i.e., tamping and rain events simulated), see Figure 4.2.7. The deformational behavior of fouled ballast under the loading, maintenance, and weather conditions simulated in Ebrahimi (2011) is used for comparison to the deformational behavior of PSB. The un-stabilized ballast is highly dependent on weather conditions and maintenance conducted, while the PSB specimen accumulates marginal levels of plastic strain within the simulated maintenance interval. Furthermore, the PSB specimen represented in Figure 4.2.7

was tested at a deviator stress 50 kPa higher than the un-stabilized ballast material. Therefore, PSB has resistance to permanent deformation at higher loads and has superior performance relative to that of clean or moderately fouled ballast, which are susceptible to changing weather conditions and timing of maintenance events. In the event that durability testing (e.g., freeze-thaw cycles, wet-dry, cycles, etc.) is conducted for PSB, an elastic-wave based (non-destructive seismic) testing method was developed in this study and use of the method for detecting damage in PSB materials was validated (see Appendix C).

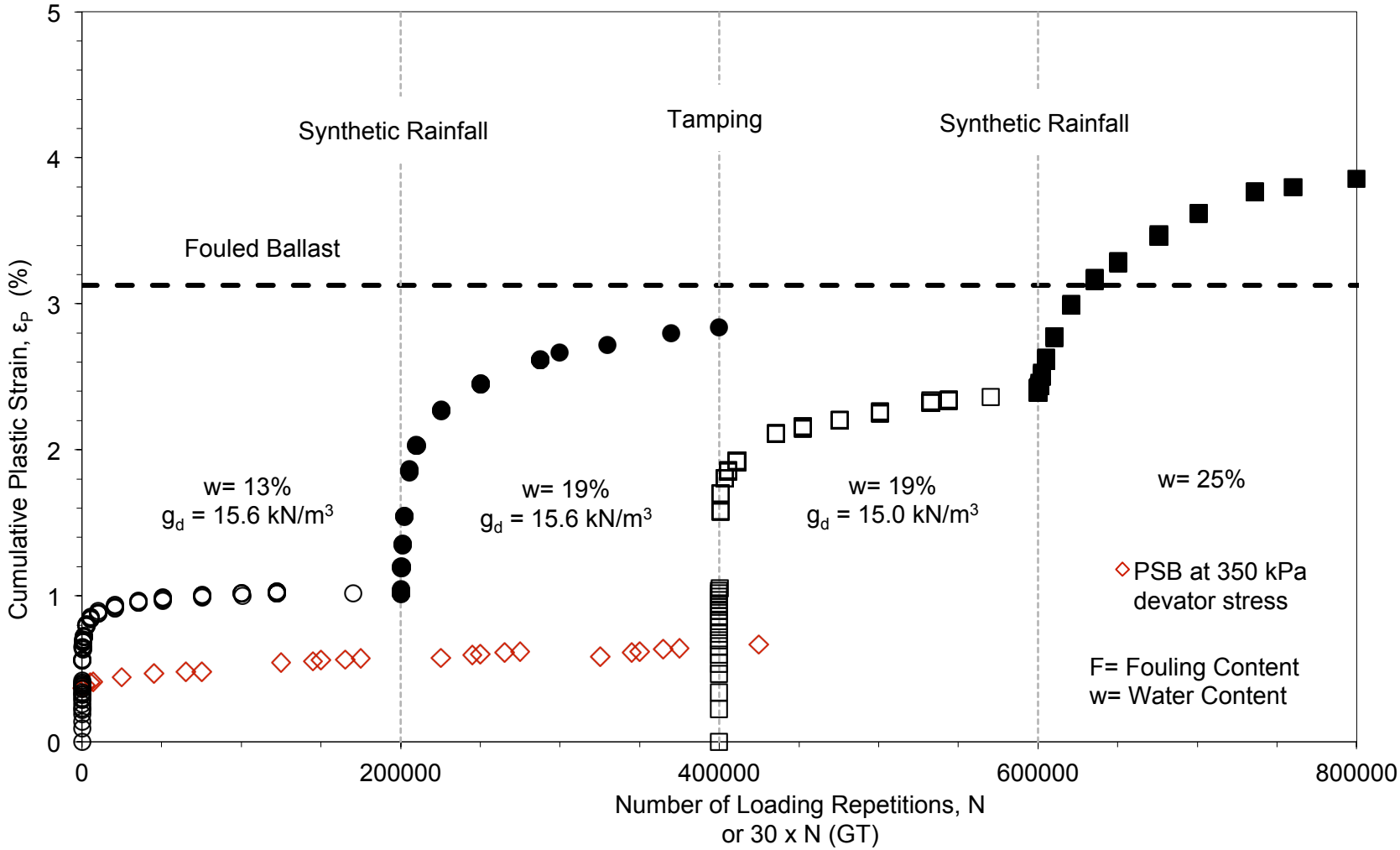

Figure 4.2.7: Simulated ballast/substructure conditions within a typical ballast layer maintenance interval (Ebrahimi 2011). Unstabilized ballast (i.e., fouled ballast) was tested at σ_d=300 kPa, σ_3=100 kPa. PSB was tested at 350 kPa deviator stress and 35 kPa confining stress.

4.3 ELASTIC DEFORMATIONAL BEHAVIOR AND RESILIENT MODULUS UNDER CYCLIC-COMPRESSION

An important aspect of track response to loading is the elastic deformational behavior of the superstructure and substructure. Maintenance and design based on elastic response of the track under loading is important for ensuring rider comfort, reducing dynamic loading effects on the track, and providing proper interaction with the rail car suspension system. In Aursudkij et al. (2009), data collected from cyclic triaxial compression testing on clean ballast, was also used to calculate the resilient modulus. From the cyclic triaxial compression tests conducted on PSB and clean ballast in this study, the elastic strain and resilient modulus was calculated from measurements taken throughout the test (see Section 3.3.2).

When comparing PSB and clean ballast at the representative state of stress defined in Ebrahimi (2011), the elastic strain of clean ballast decreased 26% over 200,000 cycles from the elastic strain of the first cycle, whereas the PRB specimens decreased only 5-9%. Therefore, Over the 200,000 loading cycles, PSB resisted change in elastic strain and resilient modulus. The resistance to change in elastic strain and resilient modulus is an indicator that the material retains its elastic properties despite numerous loading repetitions. However, as displayed in Figure 4.3.1 and Figure 4.3.2, the resilient modulus of PSB was less than that of the clean ballast tested in this study and from other studies (e.g., Aursudkij et al. (2009)).

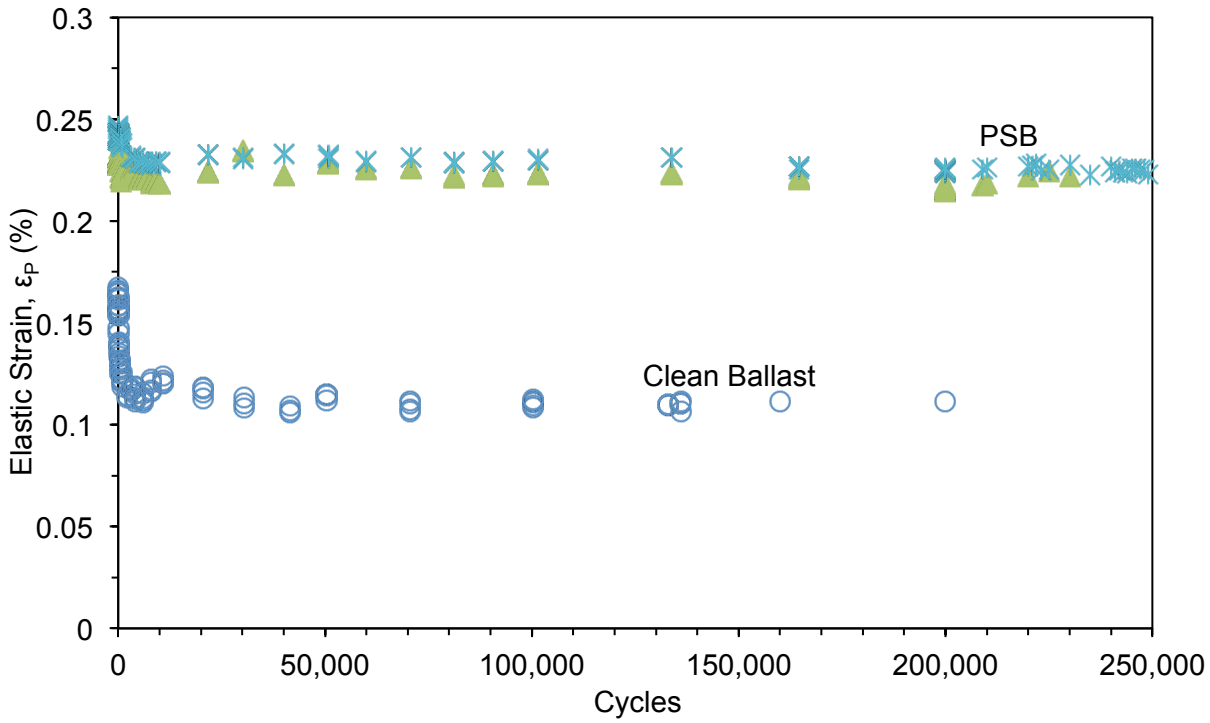

Figure 4.3.1: Comparison of elastic strain measured throughout cyclic triaxial test between typical clean ballast and PSB specimens. Tests were conducted at a deviator stress of 300 kPa and confining stress of 100 kPa.

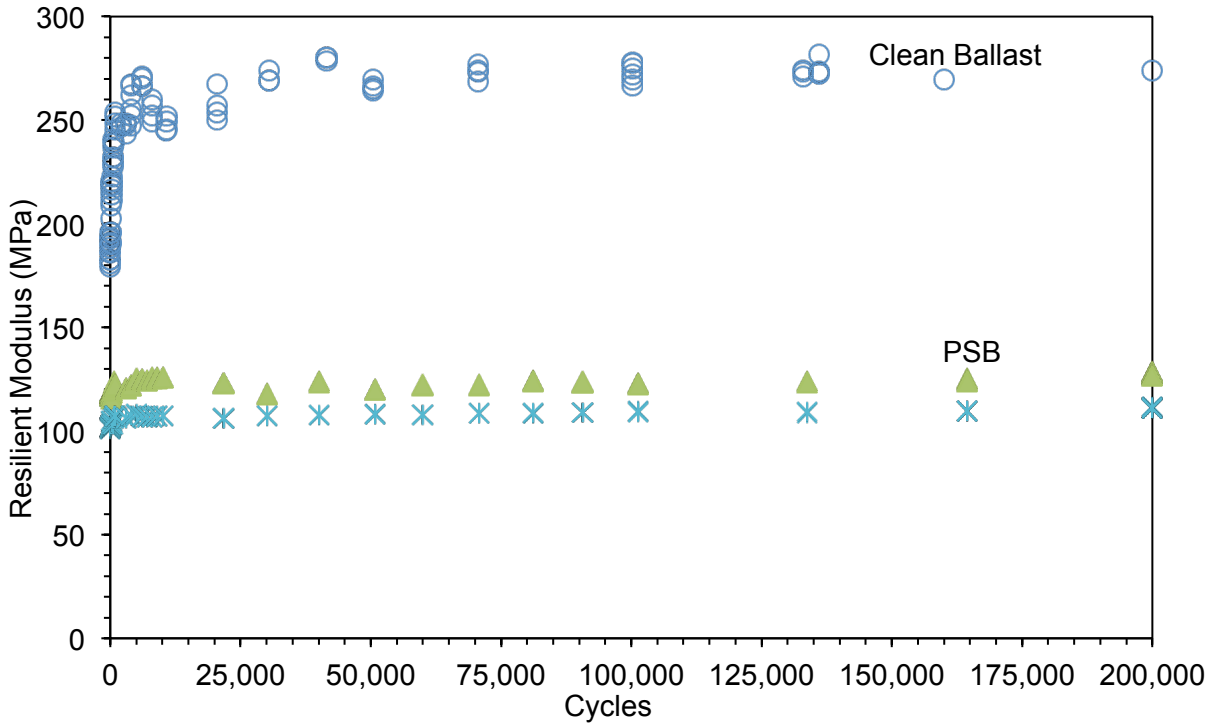

Figure 4.3.2: Comparison of resilient modulus measured throughout cyclic triaxial test between typical clean ballast and PSB specimens. Tests were conducted at a deviator stress of 300 kPa and confining stress of 100 kPa.

For clean ballast, the resilient modulus typically increases over the first 10,000 loading repetitions due to particle rearrangement and further compaction beyond initial compaction from specimen preparation. This phenomenon is typically known as plastic hardening, which can occur under lower stress ratios for clean ballast (Lim 2004). Further compaction initially causes an increase in the stiffness of the specimen with very little marginal increase after 10,000 cycles. This behavior within the first 10,000 cycles coincides with plastic strain rate behavior described in Ebrahimi (2011), where the first 10,000 cycles are classified as the initial compaction phase (ICP). For clean ballast, the rate of plastic strain diminishes after the ICP and, for fouled ballast, the rate of plastic strain increases linearly. The resistance to accumulation of plastic strain (Section 4.2) and change in resilient modulus can be attributed to quantity of RPF (percent RPF by weight) within the pore space of ballast preventing further ballast compaction, RPF-ballast bonds minimizing particle rearrangement within PSB, and superior dynamic loading performance of RPF (see Appendix B).

Once RPF is injected into ballast, the ballast particle configuration is essentially locked in place and, in some cases, particle proximity is decreased due to void space expansion, (see Appendix A). Since RPF is present within the ballast pore space and between ballast particles, the mechanical properties of RPF must contribute to the plastic and elastic deformation of PSB. In cyclic triaxial tests, the range of plastic strain accumulated in each of the PSB specimens is far less than the elastic strain range of the RPF material (see Appendix B). However, the resilient and Young's modulus of PSB (average of 110 MPa and 90 MPa, respectively) is less than the resilient modulus of ballast (250 MPa) and greater than the Young's modulus of RPF (average 16 MPa; Section 4.7). The composite properties of PSB thus incorporate the stiffness of the ballast particles and compliance of RPF within the ballast pore space. A visualization of these attributes of elastic strain absorption under cyclic loading is provided as Figure 4.3.3.

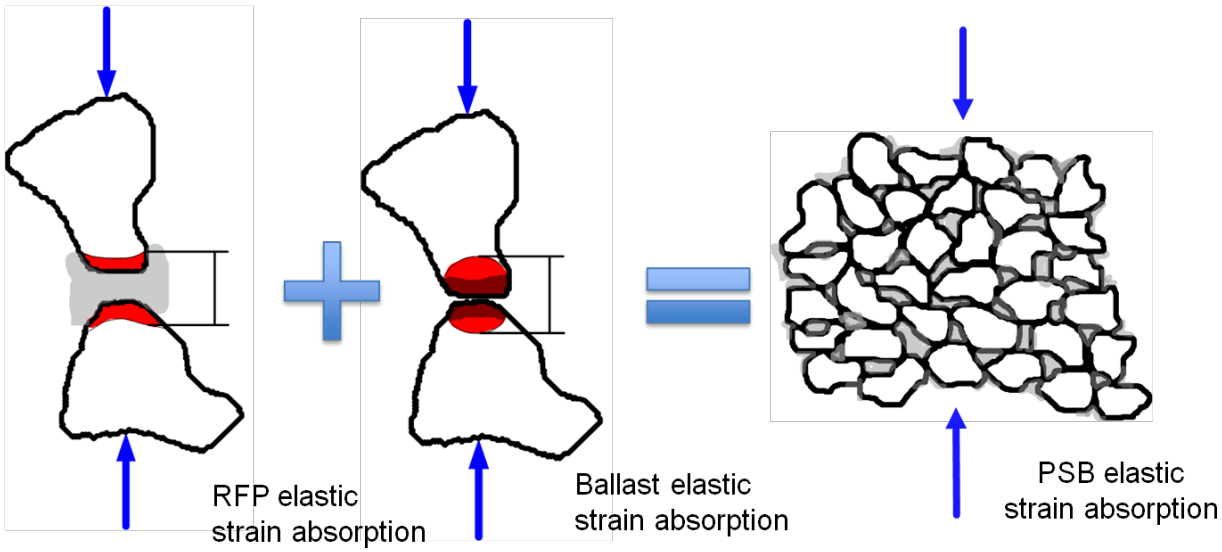

Figure 4.3.3: Visualization of attributes of PSB composite elastic strain absorption under cyclic loading.

In asphalt, the aggregates provide the load bearing capacity of the asphalt mixture, while the asphalt binder is used to maintain geometry, performance, and functionality of the pavement layer (Tia 2003). For PSB, the resistance to change in resilient modulus can be attributed to RPF controlling and preserving the resilient behavior of the PSB composite. Accumulation of plastic strain in PSB can be attributed to two possibilities: (1) ballast particle breakage and localized rearrangement of fractured ballast particles (i.e., movement of fractured particles within the RPF encasement) or (2) frictional wear and foam degradation due to the interaction of fragmented ballast and RPF.

The compressive modulus of RPF (see Section 4.7) is less than ballast and the yield strain, ε_Y, of RPF (ε_Y = 3%) is far greater; therefore, yielding or breakage of ballast particles (i.e., particle breakage and localized rearrangement) within PSB would occur while RPF is still being strained elastically. Consequently, while particles are fractured in PSB and no longer providing full mechanical support, elastic strain that may occur in RPF during cyclic loading can be misinterpreted as plastic strain. RPF is a much more elastic material than ballast and RPF has 'memory' (i.e., recovers with time once unloaded) after being strained elastically. Therefore, deformation can be potentially miscalculated as accumulation of plastic strain. Frictional wear and foam degradation due to the interaction of fragmented ballast and RPF is addressed with more detail in Section 4.7 regarding flexural strength and fatigue testing of PSB.

The applied state of stress may not be sufficient to cause accumulated damage to PSB or exceed the RPF elastic strain range during the cyclic triaxial tests conducted. Therefore, targeting PSB resilient response that coincides with the anticipated and designed track resilience maintained in the railway is important for implementation. PSB configurations and track elastic deformational behavior is investigated and is presented in Chapter 6.

The resilient modulus was determined from each test by averaging the resilient modulus of each cycle after 10,000 cycles, which is similar to what is represented in Aursudkij et al. (2009). As seen in Figure 4.3.2, there is little change in resilient modulus after the first 10,000 cycles. A trend was found between the resilient modulus averaged after 10,000 loading cycles and the PSB density, ρ_{PSB}, of the specimens. Materials with different composition (i.e., PS–recycled or PS–fouled ballast) lie outside of this trend (Figure 4.3.4). The correlation between the ρ_{PSB} and resilient modulus (R^2 = 0.82) was similar to the correlation of between the ballast phase density (density of aggregate matrix) within the PSB specimens and resilient modulus. In Figure 4.3.5, there is a strong correlation (R^2 = 0.93) between ballast phase density in the PSB specimens and resilient modulus. Therefore, the ballast phase density (i.e., particle matrix) likely controls the resilient modulus (i.e., elastic deformational behavior) of PSB. This type of relationship is similar for the behavior of asphalt, where the aggregate matrix controls the load bearing behavior (Tia 2003).

Since the modulus of ballast is greater than the modulus of RPF, the stiffness of the ballast aggregates and continuity of the ballast matrix controls the elastic deformational response of PSB. The resilient response incorporates the elastic strain contributed by the RPF, which is evidence by the resilient modulus of PSB being lower than unbound clean ballast. The resilient modulus will depend more on the ballast density within the PSB composite; however, RPF likely preserves the resilient modulus of PSB under cyclic loading since the ε_P of plastic strain in cyclic triaxial compression tests, RPF preserves the original shape of PSB (i.e., resists permanent deformation).

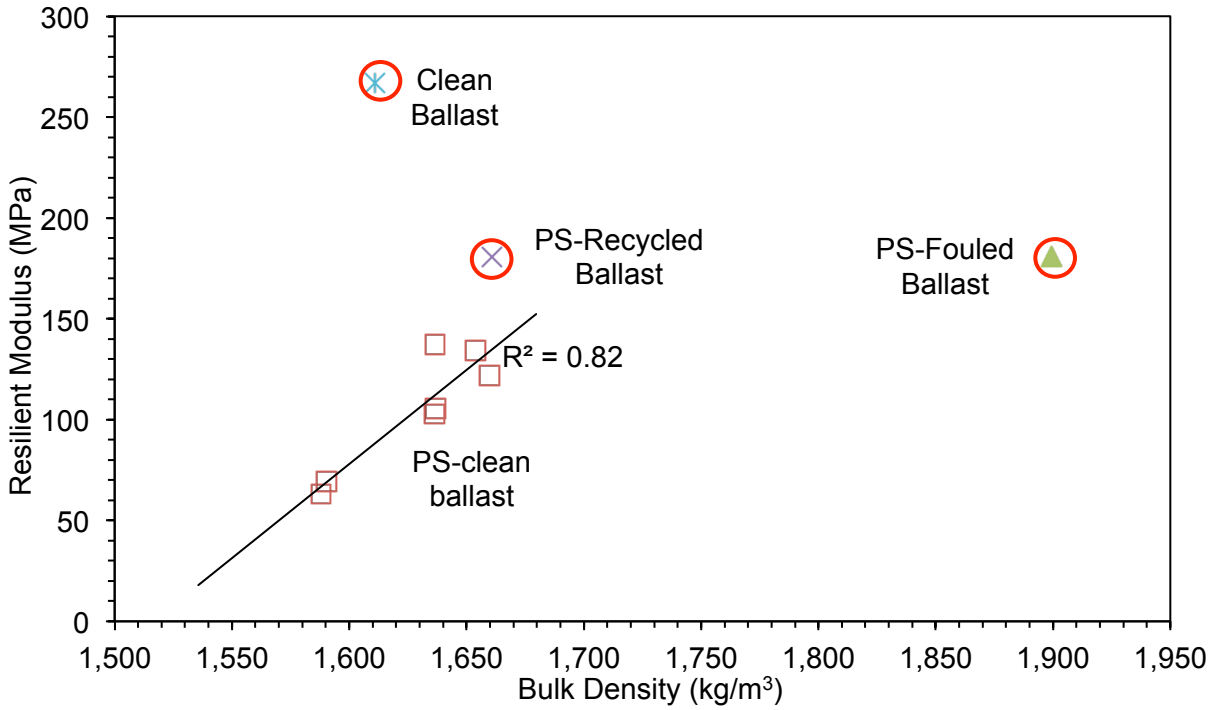

Figure 4.3.4: Resilient modulus of PSB cylinders averaged after 10,000 loading-repetitions in cyclic triaxial test versus PSB cylinder densities. Recycled and fouled ballast specimens separated due to indicated effects of differing material compositions.

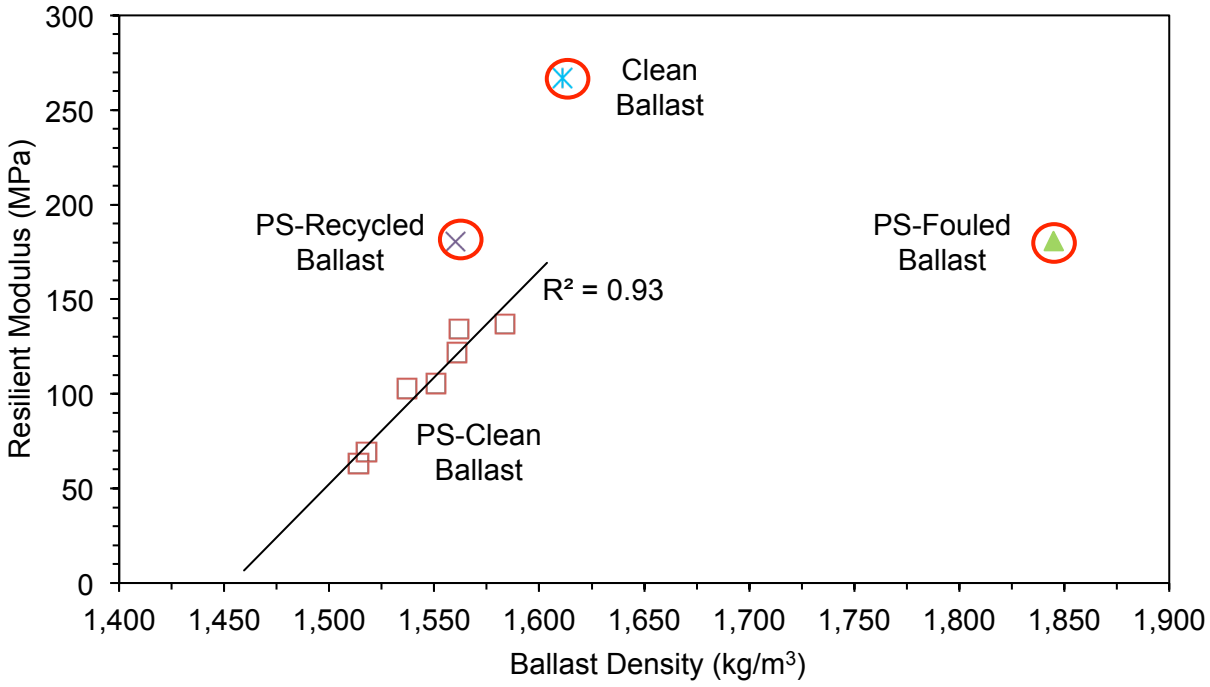

Figure 4.3.5: Resilient modulus of PSB cylinders averaged after 10,000 loading-repetitions in cyclic triaxial test versus ballast-phase density within PSB cylinders. One outlier removed because of PSB cylinder defect and recycled ballast specimen separated due to differing material composition.

4.4 MECHANICAL BEHAVIOR UNDER MONOTONIC-FLEXURAL LOADING

Following ASTM D1635, five PSB beams were prepared in the “third-point” configuration and loaded at a constant rate (monotonically) until rupture. Similar behavior was observed in the five beams, where deflection increased linearly and there was little warning before failure (i.e., brittle failure in monotonic flexural loading), as evidenced in Figure 4.4.1. For use in flexural fatigue testing, the average (AVG) rupture strength was 938 kPa with coefficient of variation (COV) at 23.7%. For comparison, in a study by Midgley and Yeo (2008), the flexural strength of Hornfels cement-stabilized material (CSM) with 3% cement and siltstone CSM with 4% cement had average rupture strengths of 1,260 kPa and 1,030 kPa, respectively. The variability among the rupture strengths for the Hornfels CSM and siltstone CSM were 20% and 15%, respectively. Therefore, PSB beams have similar flexural strength characteristics to cement-stabilized materials. Further comparisons between cement-stabilized soils and PSB are detailed in Section 4.7.

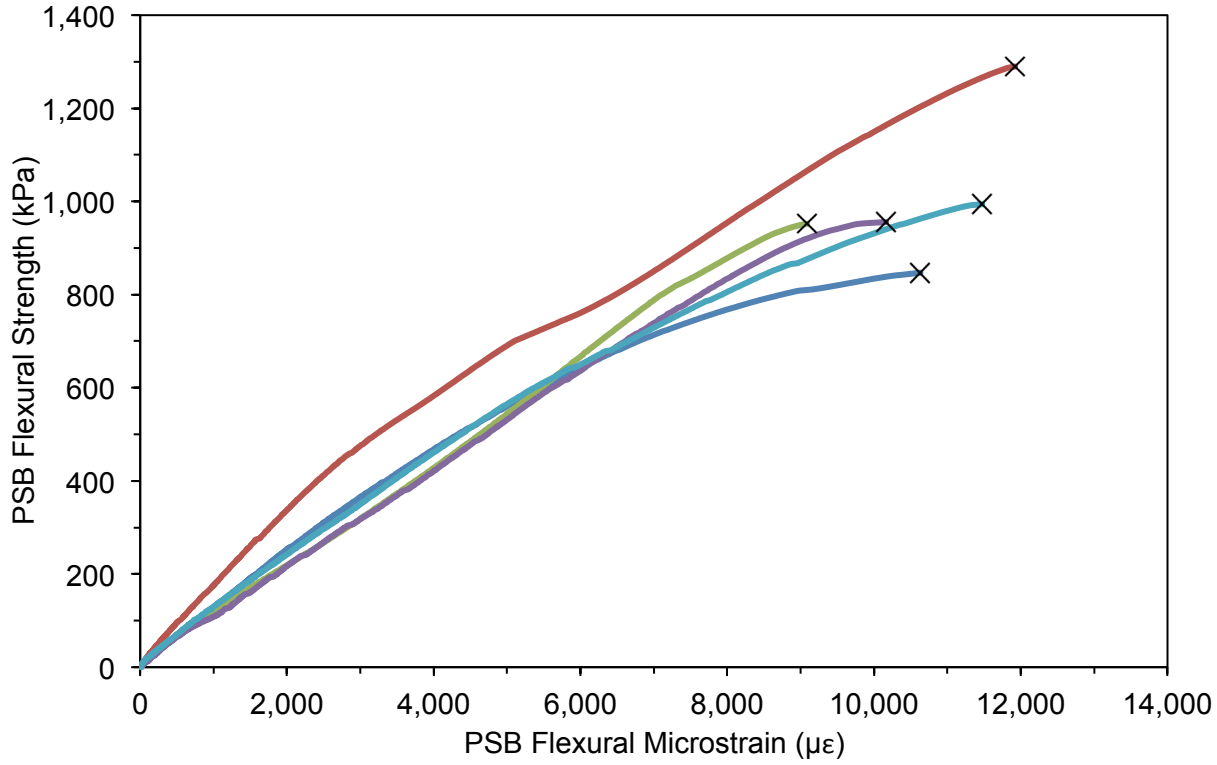

Figure 4.4.1: Flexural strength tests conducted on 5 PSB beams. Average rupture modulus, R = 938 kPa with coefficient of variation = 23.7%.

From the flexural tests conducted, the flexural strength increased as the percent RPF by weight of the specimen increased (Figure 4.4.2). Zhang and Wei (2011) studied the increase in flexural strength versus percent binder for cement-stabilized soils and reported that the flexural strength increased as the cement content of the specimen increased (comparison to PSB is shown in Section A.3). There was some correlation (R^2 = 0.79) between the flexural strength and percent RPF by weight (Figure 4.4.2); however, the average flexural strength was used for determine the stress ratios being applied in fatigue testing. In Section 5.1, constraints on phase quantities within PRB material were presented for analytical modeling purposes of PSB deformational behavior. The limits on phase quantities were based on percent RPF, ρ_{PSB}, and β_{ref}; a comparison between flexural strength and $[\beta_{ref}/((\rho_{PSB}*(\text{percent RPF})^2)]$ (see Section 5.1) is presented in Figure 4.4.2.

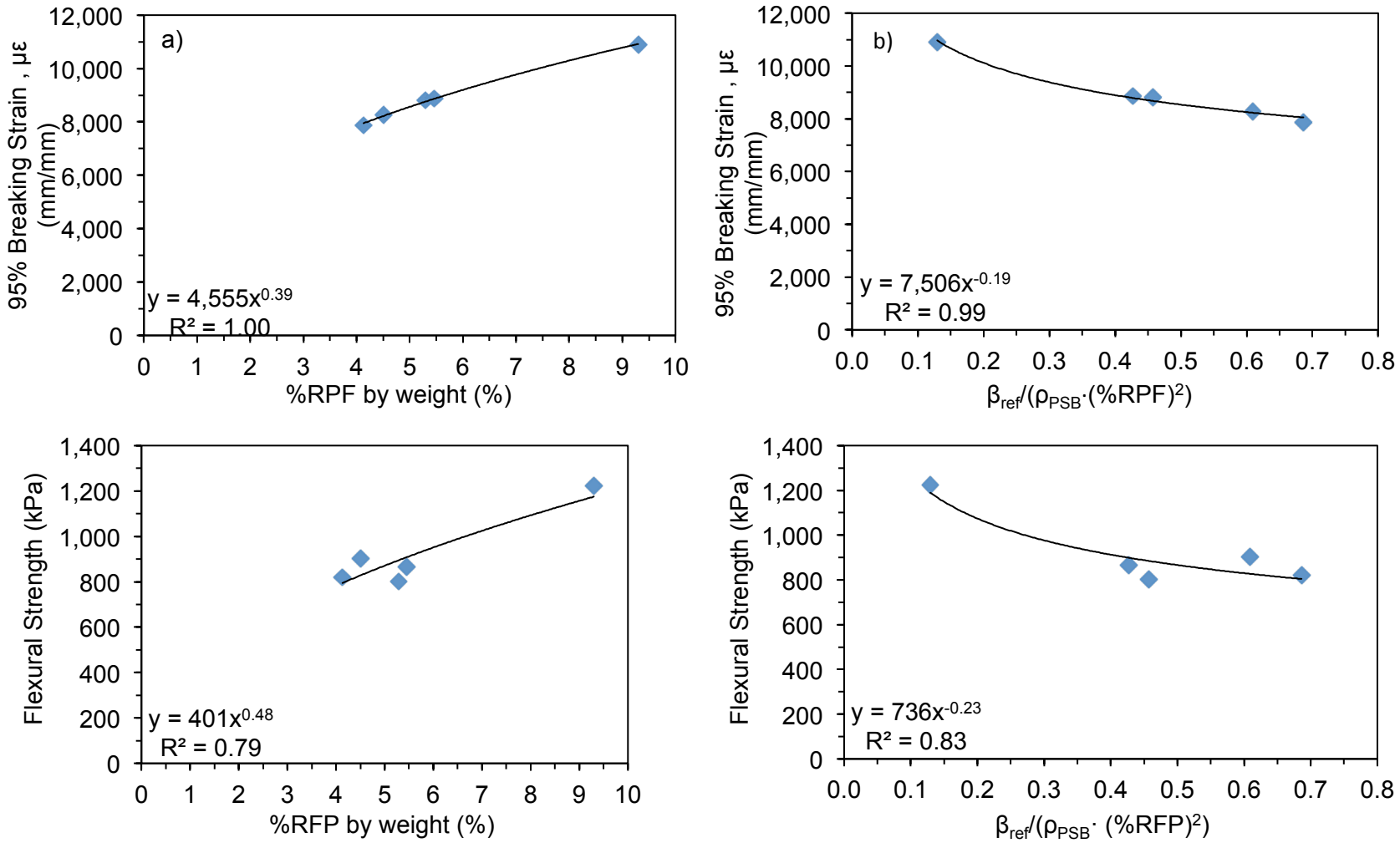

Figure 4.4.2: Comparison of PSB phase properties with PSB flexural strength and breaking strain plotted at 95% of the rupture load.

An additional use for monotonic flexural strength testing involves measuring the strain at or near rupture of the beams. Similar to methodology of using stress ratio in fatigue analysis, after determining the breaking strain, a strain ratio can be applied during cyclic loading. The breaking strain is commonly used for cement-stabilized soils and asphalt mixes to find average breaking strain for materials with similar composition and mix design. As recommended in Litwinowicz and Brandon (1994) for CSM, the breaking strain from monotonic testing was measured at 95% of the rupture load for the PSB beams. Since the strain increases abruptly when the beam ruptures, selecting a breaking strain at 95% of the rupture load is more representative of the breaking strain when establishing constitutive relationships from beam testing. From most studies involving flexural testing, the flexural strain during flexural strength and fatigue tests is the tensile strain at the base of the beam presented in microstrain (με) (Litwinowicz and Brandon (1994); Zhang and Wei (2009); Carteret and Jameson (2009)). Similar to the comparison of flexural strength and the phase properties in the PSB beams, a strong correlation (R^2 = 1.00) was also observed between the breaking strain (με) and the PSB phase properties (percent RPF), as displayed in Figure 4.4.2.

Commonly analytical fatigue models incorporate flexural modulus for predicting fatigue life from cyclic flexural fatigue testing instead of monotonic testing. However, in Arnold (2009) the flexural modulus was also measured from monotonic flexural tests. For initial observation, flexural modulus of the PSB beams is compared with PSB phase properties using monotonic flexural test results (Figure 4.4.3). The average flexural modulus was 126.2 MPa with a COV of 20.1%. Within the PSB beams, the average RPF phase density calculated was 200 kg/m^3 (Table 6.2.2). The flexural modulus of PSB (with 200 kg/m^3 RPF phase density) is much greater than the flexural modulus of only RPF (with a 200-kg/m^3 bulk density, see Appendix B). PSB flexural modulus is likely a combination of the RPF stiffness and the stiffness of ballast particles in tension (see Section 4.7).

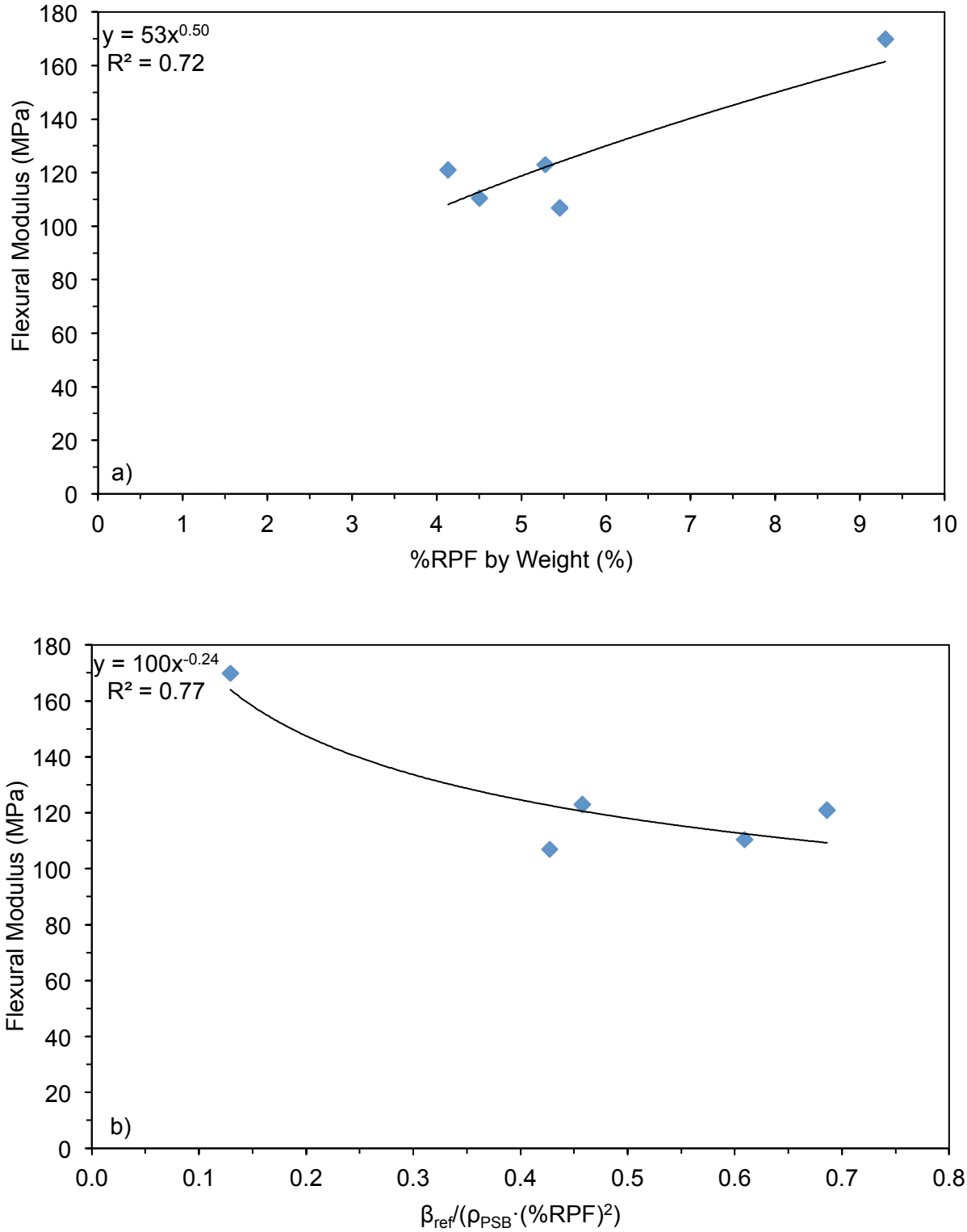

Figure 4.4.3: Comparison of PSB flexural modulus to PSB phase properties.

Even when a RPF phase density of 200 kg/m^3 is present (i.e., calculated) within PSB, the flexural strength of PSB (938 kPa) is much less than the flexural strength of pure RPF (3,752 kPa) at a density of 200 kg/m^3 (see B.2 of Appendix B). In Salim (2004), ballast particle crushing strength was used to determine characteristic tensile strength based on particle diameter. Salim (2004) cites Jaeger (1967) for explaining that fracture of rock grains occurs due to tensile failure and that fracture strength can be measured indirectly through "diametral compression between flat platens." When comparing trends established from literature with RPF tensile strength versus density (included in Appendix B), at an RPF density of 200 kg/m^3, the tensile strength of RPF (3,912 kPa) is less than the characteristic tensile strength (5,400–22,300 kPa) of the granite ballast used in this study and tested in Ebrahimi (2011). Since, the characteristic tensile strength of ballast is higher than the tensile strength of RPF; RPF may contribute to flexural failure in monotonic loading tests.

Even through the ballast particles themselves may possess higher tensile strength than RPF, since flexural characteristics of PSB are only present due to RPF-ballast bonding, the strength of the bonds likely control PSB flexural strength. As described in Section 4.2, the rounded nature of the recycled ballast was responsible for the higher accumulation of plastic strain in the PS–recycled ballast relative to rough aggregates in the PS–clean ballast. Hence, the surface characteristics of the aggregate played a key role in the bonding properties. Further details regarding RPF-aggregate interaction are detailed in Section 4.7 where it is shown that the flexural strength and tensile strength of RPF are greater than the flexural strength of PSB; consequently, the RPF-aggregate interaction in PSB likely controls flexural strength.

4.5 FATIGUE BEHAVIOR UNDER CYCLIC-FLEXURAL LOADING

Following procedures outlined in literature (such as the AUSTROADS procedure outlined in Midgley and Yeo (2008)) regarding flexural fatigue testing, nine PSB beams were prepared in the “third-point” configuration and cyclically loaded at different flexural stresses until rupture. Beam deflection under cyclic loading increased throughout the tests; crack propagation at the base of the beam was observed and foam ‘tearing’ sounds were heard as the specimen approached failure (picture of beam before fatigue failure is shown in Appendix F). Signs of specimen fatigue were noticeable between 100 to 1000 cycles before rupture, depending on the cyclic stress ratio applied. Approach to failure was signified by a rapid increase in the measured deflection and visual crack formation and crack propagation. The stress ratio versus cycles to failure for the PSB specimens is shown in Figure 4.5.1. For comparison, concrete fatigue observed by Arellano and Thompson (1998) is also shown; however, an important consideration is that concrete fatigue is relative to concrete flexural strength, which is much greater than PSB flexural strength. The purpose of the comparison is to display material fatigue behavior relative to material flexural strength.

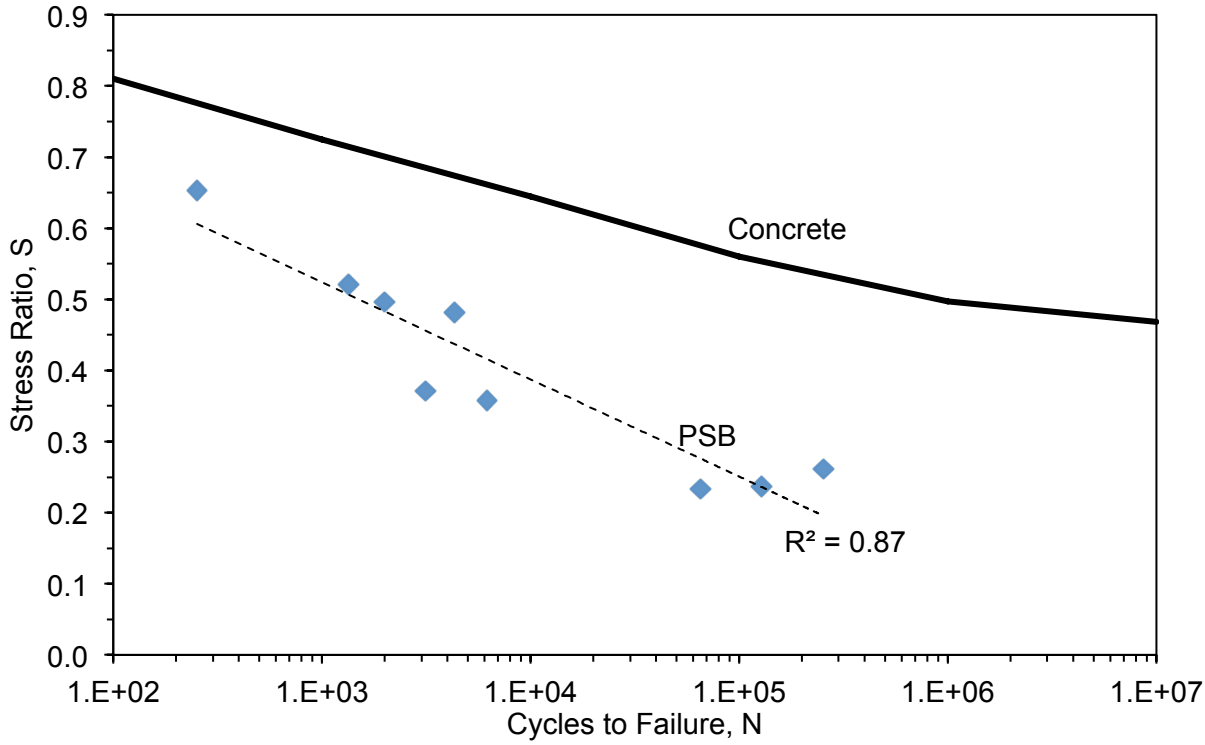

Figure 4.5.1: Data shown for PSB beam fatigue testing and trend shown for concrete beam fatigue taken from Federal Aviation Administration (Arellano and Thompson 1998).

From Adhikari and You (2010), an equation used to model fatigue was

$$log\ N = \frac{(k_1 - S)}{k_2} \quad (4.5.1)$$

where N is the cycles to failure, S is the stress ratio corresponding to the cyclic load applied, and k_1 and k_2 are material fitting parameters. From Arellano and Thompson (1998), concrete k_1 and k_2 are 0.9722 and 0.0825, respectively. Since k_1 is the intercept of the trend, the value should be close to 1 where failure should occur at a stress ratio of 1, which can depend on the strain-rate applied if time-dependent mechanical properties are present. k_2 signifies the fatigue resistance of the material being tested; as k_2 increases, the material's resistance to fatigue decreases. The trend for concrete is shown in Figure 4.5.1, the trend representing PSB flexural fatigue is also shown with the equation presented in Table 4.3.1.

During flexural beam testing, the variable that controlled the flexural modulus of the PSB specimens was percent RFP by weight of the PSB beams. The flexural modulus is compared to the RPF density within the PSB specimens, where the flexural modulus increases as the RPF density increases (Figure 4.5.2). Since flexural properties exist in PSB solely due to the presence of RPF, the quantity and density of RPF present is a logical factor for predicting PSB flexural modulus. In Kumar et al. (1994), foams at varying relative densities (i.e., ρ_{RPF} /ρ_{PU}) were subjected to tensile tests to reveal that the higher the relative density of the foam, the higher the tensile and flexural strength as well as tensile and flexural modulus. Therefore, the flexural response of the PSB composite beams can be attributed to the quantity and density of RPF within the ballast pore space. Details regarding contribution of RPF to PSB mechanical properties are discussed in Section 4.7.

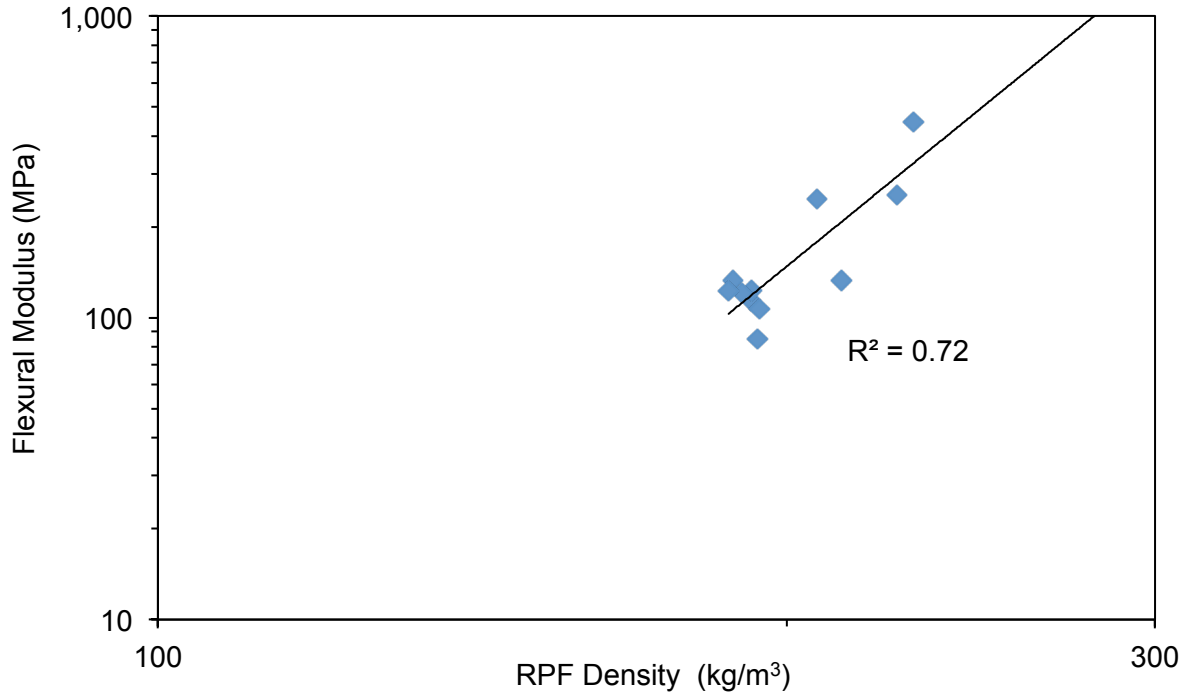

Figure 4.5.2: The flexural modulus of the PSB beams subjected to flexural fatigue testing is compared to the percent RPF by weight of PSB.

When determining fatigue of materials, Midgley and Yeo (2008) described another feature in beam fatigue testing; if a low enough stress ratio is applied, the material does not fail in flexural fatigue testing or cycles to failure are exceedingly large. More specifically, the stress ratio applied appears to fall below a fatigue threshold, which can also be inferred when there is limited modulus decrease early in the test and no change is observed over a large number of cycles. In Carteret and Jameson (2009), the fatigue threshold is called the endurance limit, which is maximum stress ratio applied where no fatigue occurs in the material or the trend (stress ratio versus cycles to failure) becomes asymptotic. For concrete (Figure 4.5.1), a stress ratio of 0.45 is the asymptotic limit or the endurance limit. In this study, due to the limited number of beams tested, the trend for PSB fatigue behavior did not appear to approach a fatigue threshold. Consequently, the endurance limit for PSB cannot be confirmed; however, as shown in Figure 4.5.1, the proximity of the three tests at low stress ratios may indicate that the endurance limit is near a stress ratio of 0.2. Depending on the application of PSB in infrastructure, the material fatigue behavior can be an important factor for determining life cycle of the treated layer or area.

The analysis of fatigue behavior is used in life cycle design of stabilized layers such as asphalt and CSM. The number of cycles to failure and magnitude of strain applied are evaluated. As introduced in Section 4.4, the breaking strain for PSB beams was measured during monotonic tests and can be used for determining strain ratio applied in PSB beam fatigue testing. This analysis process is used to normalize the fatigue data and show dependence of fatigue life on intrinsic materials properties (Litwinowicz and Brandon 1994). When using the ratio of the applied flexural strain to the average breaking strain at 95% of the rupture load, the following equation is applied

$$log\ N = \frac{(k_1 - \varepsilon_0/\varepsilon_b)}{k_2} \qquad (4.5.2)$$

where ε_0 is the initial strain during the fatigue test found by averaging the strain over the first 50 cycles (Midgley and Yeo 2008) and ε_b is the 95% breaking strain. When using the strain ratio versus cycles to failure in fatigue analysis, in the instance where the average 95% breaking strain was used, k_1 was significantly greater than 1, indicating that the trend fitting to the data may be unreasonable as possible fatigue loads should not exceed monotonic loads. From monotonic tests, trends were stabilized between 95% breaking strain and percent RPF and $[\beta_{ref}/((\gamma_{PSB}*(\text{ percent RPF})^2)]$, as defined in Section 4.4. In order develop a more realistic trend the breaking strain used was specific to the PSB beam phase properties of each specimen. The 95% breaking strain was selected from trends found in monotonic testing; these were used for the strain ratio applied in fatigue tests, which were thus based on the beam phase properties. The two constitutive relationships between breaking strain and phase properties were used for developing analytical models that possessed less variability and trends that are more realistic; analytical model development is discussed in Section 5.2.

Empirical equations were fit to the fatigue data so that constitutive relationships can be used to determine PSB beam fatigue life; the equations are shown in Table 4.3.1. Since different phase densities were present in each of the beams and constitutive equations were developed for selecting the breaking strain, using these equations for selecting breaking strain and strain ratio based on phase properties appears reasonable for a fatigue life prediction model. In Figure 4.5.3, the fatigue life results are presented using the average 95% breaking strain for determining strain ratio and 95% breaking strain based on percent RPF of the specimens. The fatigue life based on $[\beta_{ref}/((\gamma_{PSB}*(\text{percent RPF})^2)]$ is presented in the Chapter 5.

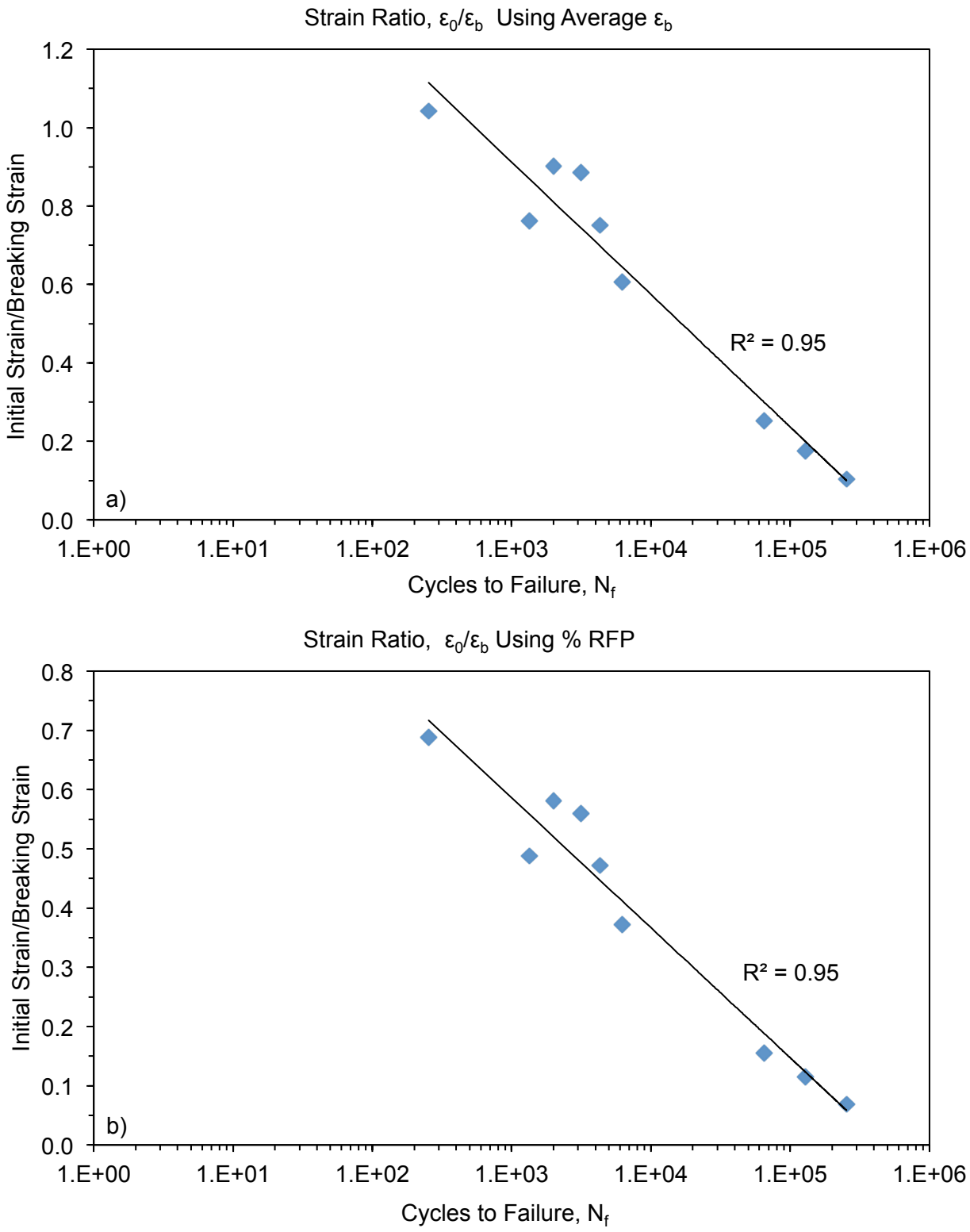

Figure 4.5.3: Empirical equations were fitted to the fatigue data using the average 95% breaking strain and 95% breaking strain based on percent RPF, for determining strain ratio.

After fatigue tests on the PSB beams, the plane of failure in the beam could be used to identify which of the PSB constituent materials (i.e., ballast or RPF) contributed to beam failure. The cross-sections of the failed specimens contained ballast particles that had split during testing (Figure 4.5.4). Splitting of the ballast particles (granitic composition) in fatigue testing underscores that significant bonds are present between the RPF and ballast particles, which play a role in the flexural fatigue of PSB. Tensile capacity in the geocomposite can only be attributed to the bonds between the ballast particles and RPF; therefore, the ITZ for PSB controls flexural strength (see Section 4.4). Most of the split ballast particles shown in Figure 4.5.4 were fractured near the interface of the aggregate with RPF; however, some fractures occurred through the ballast particle and left similar sized fragments on either side of the fracture. Since ballast particle fracture was only observed in flexural fatigue testing and not under monotonic loading, the fatigue of the ballast particles likely contributes to fatigue of PSB. The locations of fractured ballast particles in the fracture plane were near the base of the beams where the tensile stress in the beam would be the highest. Despite ballast particle fracture, the PSB beam fracture faces consisted of mostly ballast particles with very thin RPF film on the surfaces of the particles. Consequently, the ITZ of PSB was observed to contribute most to fracture of beams in flexural strength and fatigue testing. Details regarding the constituents of PSB mechanics and ITZ properties are covered in Appendix B. Further investigation may reveal how much more these fatigue characteristics can be associated with the RPF/ballast bond interface relative to the fatigue characteristics of the ballast particles.

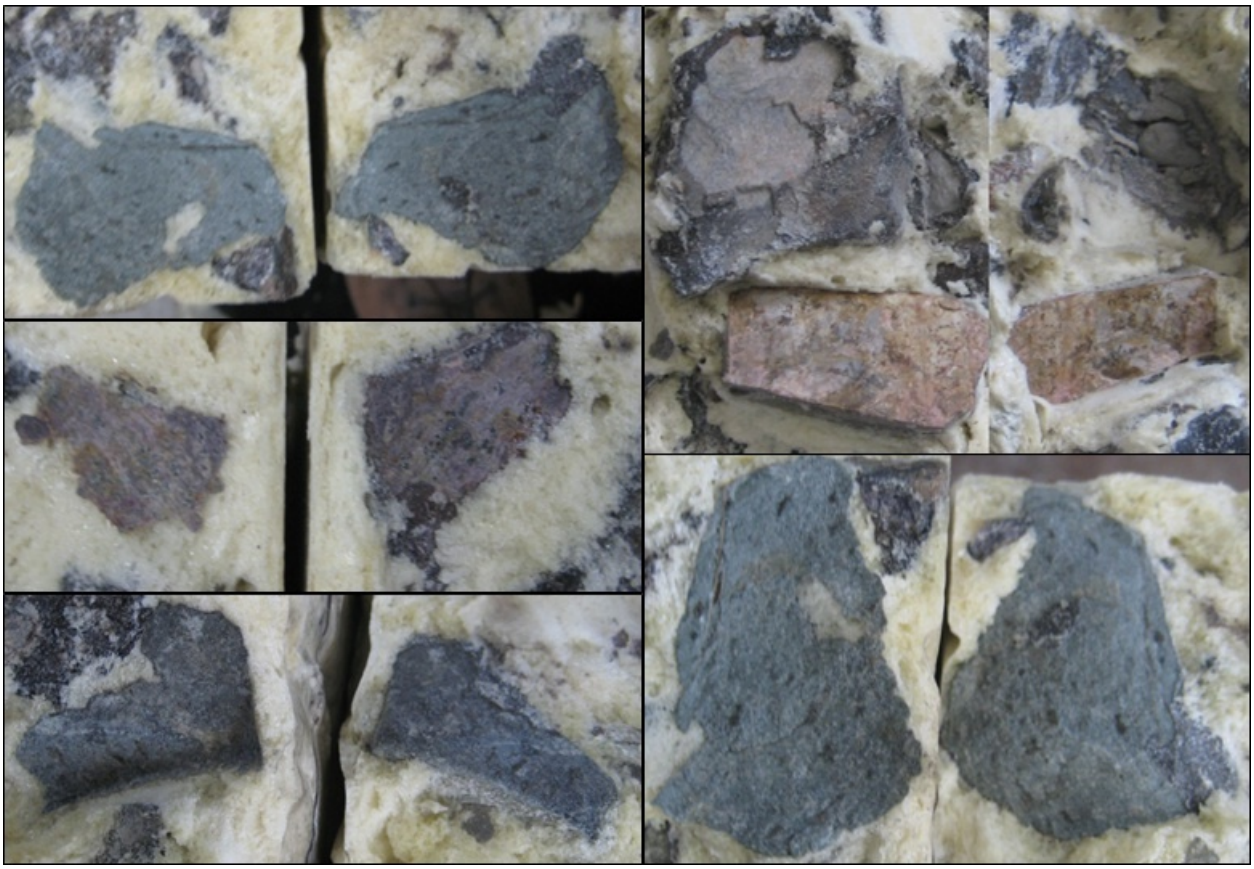

Figure 4.5.4: Photographs of PSB beams subject to flexural fatigue tests with ballast particle splitting. Pictures were taken at different scales, but each ballast particle is between 25–63 mm.

4.6 MECHANICAL BEHAVIOR UNDER UNCONFINED COMPRESSION

In cyclic triaxial compression tests PSB possessed much greater resistance to accumulation of plastic strain and change in elastic strain than clean ballast, the same influences on mechanical properties were observed for PSB tested in unconfined compression and ballast tested in monotonic triaxial compression. Figure 4.6.1 shows results from UCS testing without confinement compared to monotonic triaxial compression tests on clean ballast at different confining pressures from Ebrahimi (2011). PSB possessed much higher ultimate strength than clean ballast. When comparing the failure mode of PSB to concrete, concrete yields around 0.002 m/m, whereas PSB yields around 0.02 m/m (i.e., an order of magnitude greater); however, the minimal yield strength of concrete is designed around 21 MPa (3,000 psi) and the PSB yielded around 1.5 MPa (220 psi), 90% less. Based on these attributes, the compliance (i.e., yield strain) of PSB is much more than concrete. The failure mode observed during testing was a delaminating and ductile response, which is unlike that of materials with brittle attributes (i.e., high-carbon steel, glass, or acrylic).

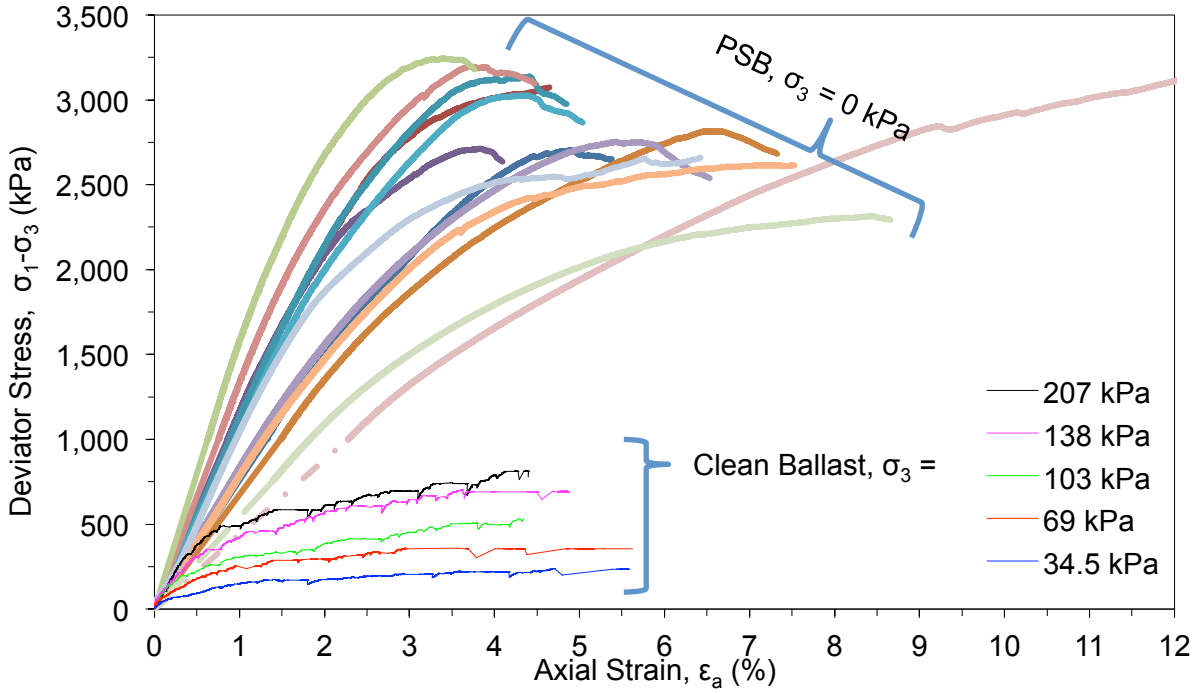

Figure 4.6.1: Unconfined compression tests conducted on PSB prisms and monotonic triaxial compression tests conducted on clean ballast from Ebrahimi (2011).

Similar to that of most soils and geomaterials, clean ballast has a non-linear stress-strain relationship as observed from monotonic triaxial compression tests on clean ballast from Ebrahimi (2011). The PSB specimens exhibit linear-elastic behavior after compliance correction (see Section 3.3.4). The average strength of the PSB prisms was 2.60 MPa with a coefficient of variation (COV) of 6.85% and average ρ_{PSB} was 1,674 kg/m^3 with COV of 4.32%; therefore, the strength had little correlation with PSB phase properties. For comparison to PSB, CSM (at 28 days cure age) from the study by Midgley and Yeo (2008) is used. The UCS of Hornfels stabilized with 3% cement and siltstone material stabilized with 4% cement, had average UCS of 7.1 MPa and 6.5 MPa, respectively. Therefore, PSB has a UCS approximately 60% less than CSM from Midgley and Yeo (2008).

Additional aspects of the data displayed in Figure 4.6.1 were evaluated to understand the variability during UCS tests on PSB (i.e., dissimilarity among the stress-stain curves). The average Young's modulus determined from the UCS tests was 89.7 MPa, with COV of 32.6%; therefore, another factor was sought to explain variation of the Young's modulus. Figure 4.6.2 shows a comparison of Young's Modulus to PSB prism density.

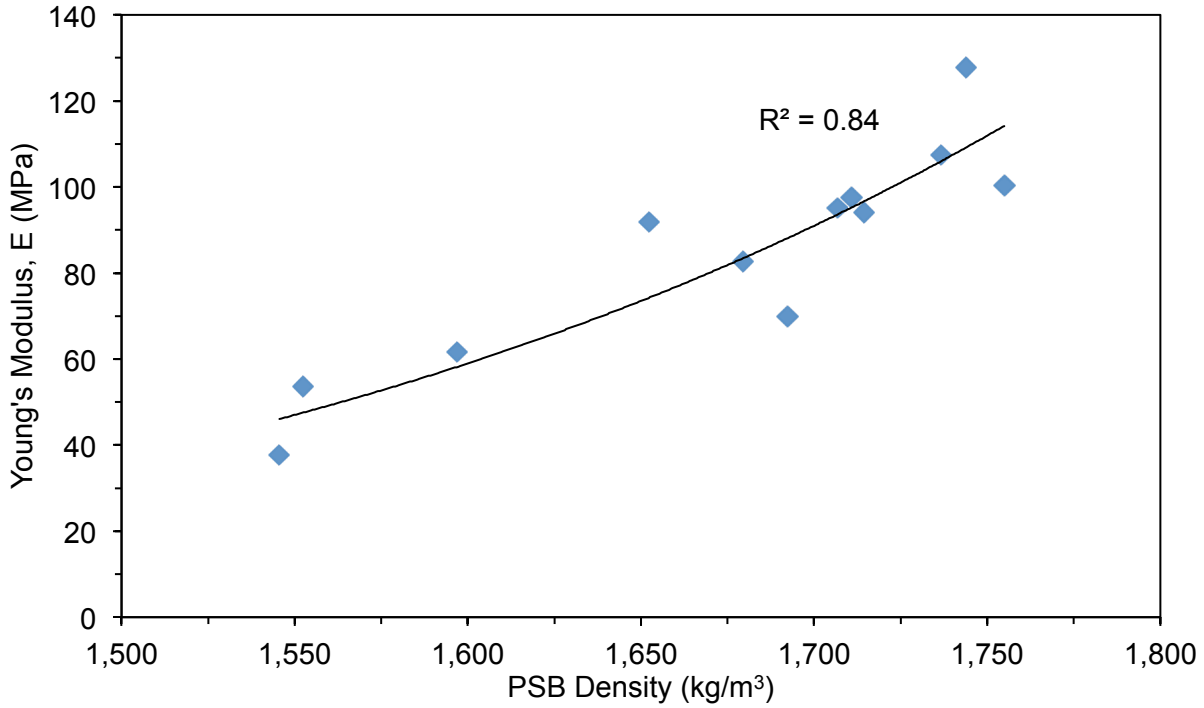

Figure 4.6.2: Young's Modulus obtained from PSB prism UCS tests compared with PSB prism density.

In Appendix A, the importance of phase densities of PSB on the composite mechanistic response was introduced. Since, the elastic response of railway substructure is an important attribute in modeling track response to loading (Ebrahimi 2011), the following equation is proposed to predict Young's Modulus from PSB density

$$E = 7.39 \cdot 10^{-22} \times \rho_{PSB}{}^{7.15} \qquad R^2 = 0.84 \qquad (4.6.1)$$

where E is the Young's modulus (MPa) and ρ_{PSB} is the PSB density (kg/m^3).

Using the average flexural strength results from Section 4.4 and the average compressive strength results the following relationship is presented

$$Flexural\ Strength = 0.51 * Compressive\ Strength \qquad (4.6.2)$$

The relationship presented serves as a preliminary comparison between PSB flexural and compressive strength. From Arellano and Thompson (1998) the flexural strength for concrete is compared to the compressive strength by

$$Flexural\ Strength = 0.5 * (Compressive\ Strength)^{0.88} \qquad (4.6.3)$$

Based on this relationship, the compressive strength of concrete relative to the flexural strength is much larger than the relationship of PSB compressive strength to flexural strength. This relationship is also used in Section 4.7 for comparing concrete compressive and flexural strength to PSB.

As shown in Figure 4.6.2, as the PSB density increased the Young's modulus increased. The same behavior exists in concrete modulus compared to concrete design strength (e.g., 3 ksi, 4 ksi, and 5 ksi), as the design strength and concrete density increase the Young's modulus increases (Grider et al. 1999). Correspondingly, as the Young's modulus increases the yield strain decreases. The yield strain of PSB versus PSB density is shown in Figure 4.6.3, where

PSB yield strain decreases as PSB density increases. PSB yield strain versus PSB Young's modulus is shown in Figure 4.6.4, where the Young's modulus increases the yield strength decreases. Therefore, these comparisons confirm that PSB mechanical properties are similar to that of other bound materials (i.e., concrete, asphalt, and cement-stabilized soil) used in transportation infrastructure.

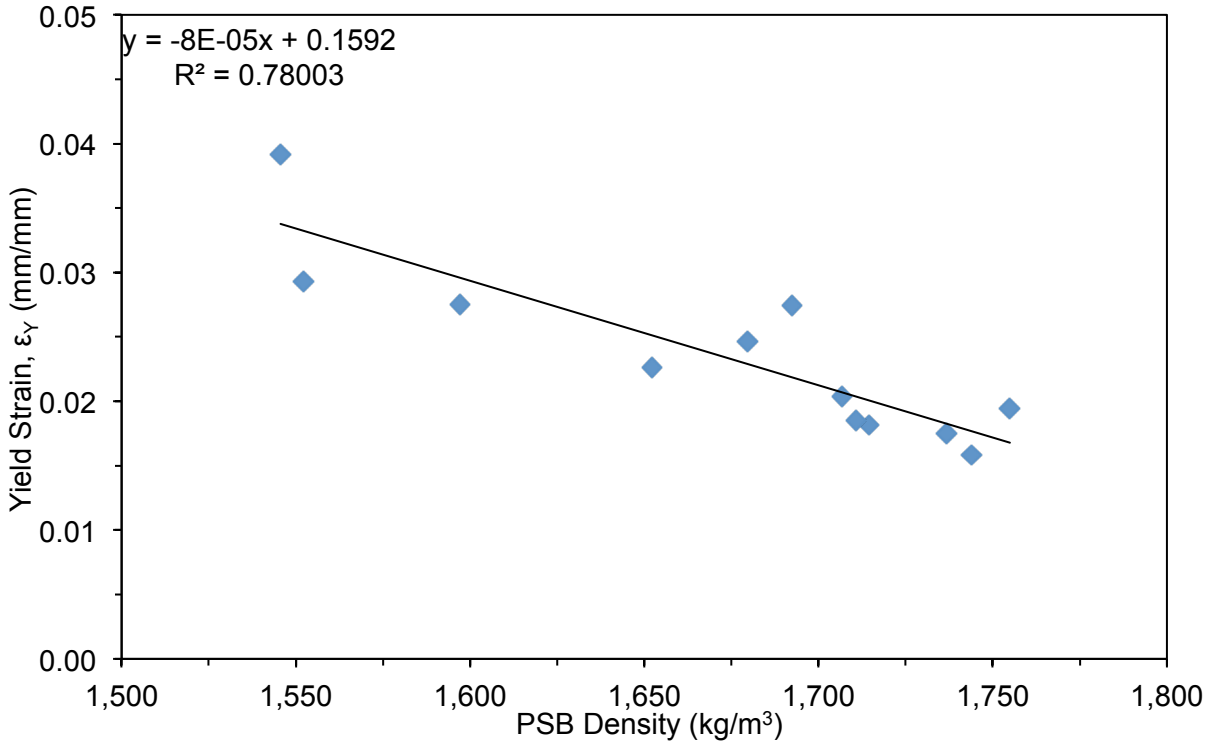

Figure 4.6.3: Yield strain obtained from PSB prism UCS tests compared with PSB prism density.

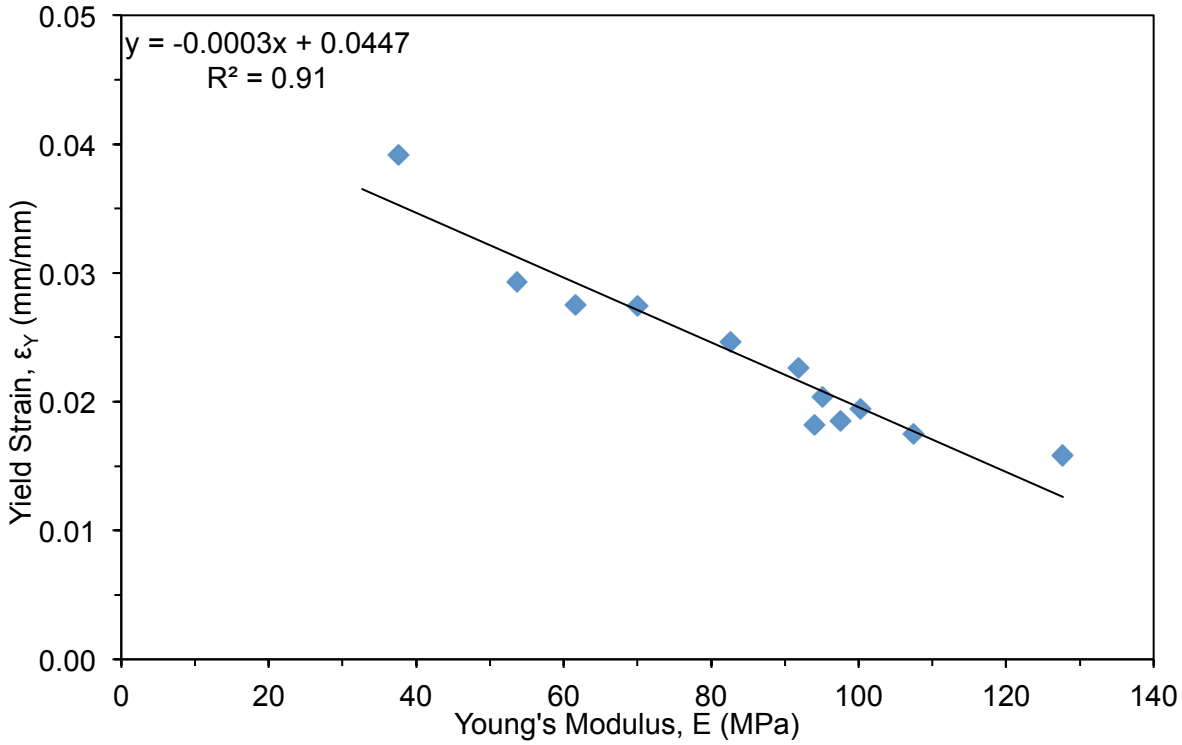

Figure 4.6.4: Yield strain versus Young's Modulus obtained from PSB prism UCS tests.

4.7 MECHANICAL PROPERTIES OF PSB AND INFRASTRUCTURE MATERIALS

4.7.1 PSB Constituent Mechanical Properties

In this subsection, moduli and strength of each of the materials within PSB (i.e., ballast and RPF) are compared to each other and to PSB composite properties. The constituents of the PSB mechanical properties can be used to infer the mechanical properties obtained from other modes of testing (i.e., compressive, flexural, and tensile).

RPF strengths are similar in each mode of testing, as seen in Figure 4.7.1. When comparing flexural test results, when the average (AVG) RPF density, ρ_{RPF}, is 200 kg/m^3, the AVG PSB flexural modulus (274 MPa) is greater than the AVG RPF flexural modulus (124 MPa); however, the AVG PSB flexural strength of 938 kPa is less than the AVG RPF flexural strength 3,652 kPa as shown in Figure 4.7.1. Greater flexural stiffness of PSB compared to RPF can be attributed to the stiffness of the ballast particles. The lower flexural strength of PSB relative to RPF can be attributed to weakness in the bonding interface between the ballast particles and RPF. As described in Akcaoglu et al. (2003), the surface texture and the bonding area between cement binder and aggregates are critical to concrete strength and stiffness. Akcaoglu et al. (2003) defined this bonding area as the interfacial transition zone (ITZ) and described this zone as the weakest component in concrete mechanical behavior. The ITZ is 10–50 μm thick, and the strength in this region is controlled by the constituents in concrete mixtures (i.e., coarse aggregate, cement, and admixtures); therefore, concrete strength in this instance was defined on the microscopic level. An average cement-particle diameter is 10 μm and cement crystallization involves a gel forming around the cement particles with interactions taking place on the nanoscale (Mamlouk and Zaniewski 2006). Therefore, reactions involved during cementation in an ITZ occur on a micro and nanoscale.

For RPF on the microscopic level, RPF cell wall thickness ranged from 3–4 μm and cell diameter from 10–100 μm. In RPF, the wall thickness is 3 to 4 times less than the diameter of a typical cement particle. RPF on the nanoscopic level (i.e., cell wall composition) contains crystalline structures or ‘hard’ segments, which are rigid due to hydrogen bonds making up these structures. The hard segments are cross-linked with flexible structures or ‘soft’ segments through covalent bonds (Oertel 1985). The elasticity and flexibility of RPF is attributed to the soft segments of the polyurethane and the hard segments prevent permanent deformation of the soft segments during loading (Randall and Lee 2002).

If establishing an ITZ for PSB, the scale of the structure would involve a molecular interaction on the nanoscale involving mineralogical and polymeric chemical interactions and a mechanical interaction involving cell structure and aggregate surface geometry on the microscale. At the nanoscale, the interaction would occur between the hard and soft segments and the mineral grains within ballast. At the microscale, the interaction would involve cell aperture, cell elongation, and cell wall thickness with the surrounding mineral aggregate structure and roughness. When focusing on an ITZ for PSB, the strength of the composite can be attributed to two likely factors: (1) RPF-ballast bond interface strength and (2) PSB composite/matrix strength based on cell orientation/geometry within the ballast pore space and around ballast particles. Further details regarding RPF-aggregate interaction are detailed in Appendix A and Appendix B, where the flexural strength and tensile strength of RPF are greater than the flexural strength of PSB; consequently, the ITZ for PSB likely controls flexural strength.

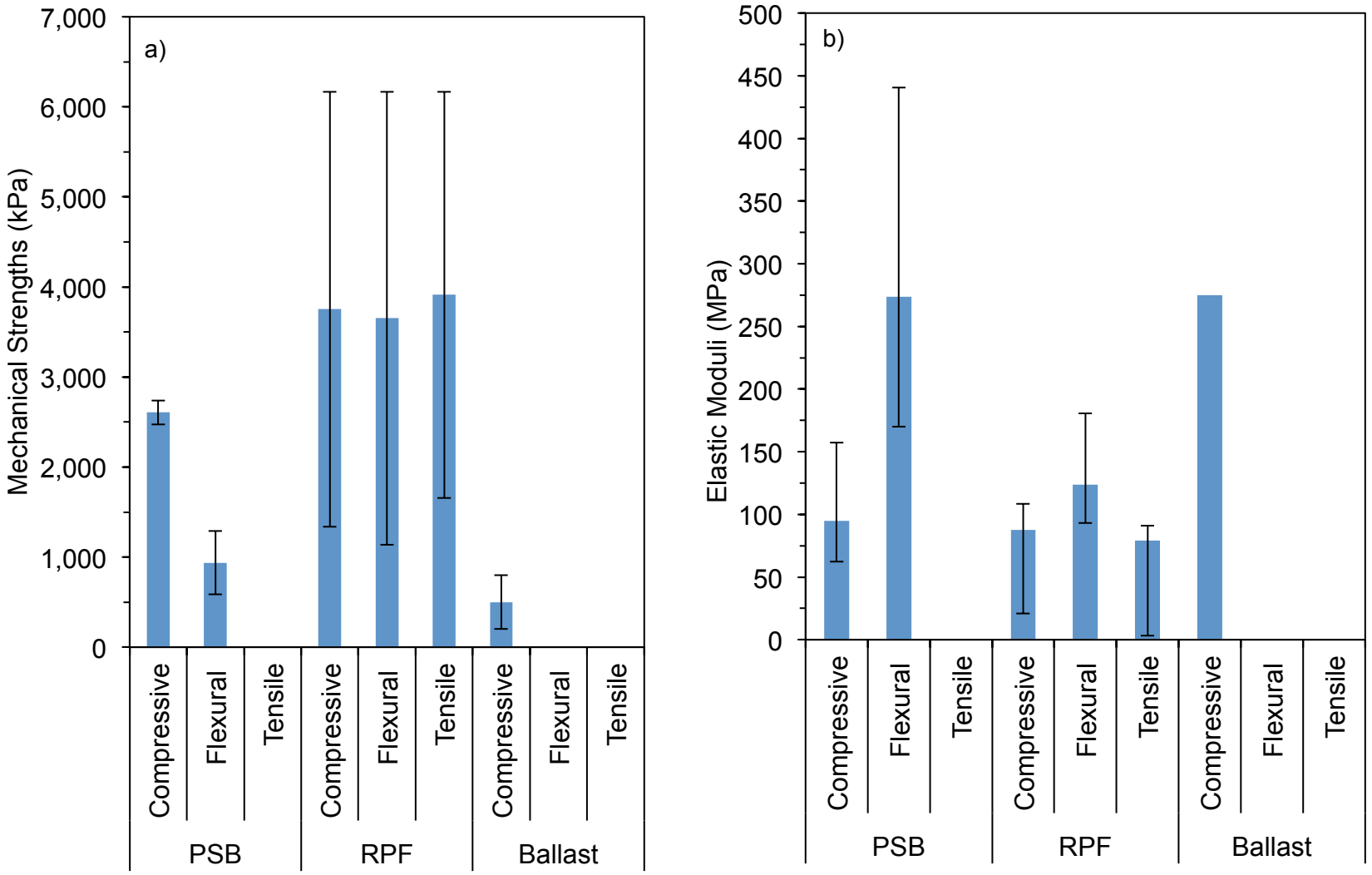

Figure 4.7.1: Shown are the mechanical parameters for materials making up the PSB composite and overall composite properties. The representative mechanical properties presented for RPF were taken where RPF density was 200 kg/m^3. Representative ballast compressive modulus and strength were taken where confining pressure, σ_3 was 100 kPa. Error bars indicate maximum and minimum values (i.e., range) of the mechanical properties measured in each material with varying confining stresses (ballast) or density (RPF and PSB).

In Salim (2004), ballast particle compressive strength was used for determining the characteristic tensile strength of ballast particles. As discussed in Section 4.4, with a characteristic RPF density of 200 kg/m^3 the tensile strength of RPF is 3,912 kPa, which is less than the characteristic ballast particle tensile strength of 5,400 to 22,300 kPa (Ebrahimi 2011). Since the characteristic tensile strength of ballast is higher than tensile strength of RPF, RPF may contribute to the rupture strength in monotonic flexural loading tests. However, failure likely occurs at the ITZ since the AVG PSB flexural microstrain (με) at rupture (8.94 με) is less than RPF (ρ_{RPF} = 200 kg/m^3) flexural microstrain at rupture (28.7 με).

Characteristic tensile strength of ballast particles is the only instance where ballast would contribute to the overall strength of PSB instead of RPF. Higher tensile strength of ballast particles (i.e., higher stiffness) must also play a role in the flexural stiffness of PSB being higher compressive stiffness of PSB. However, it is likely that in fatigue testing, fatigue of ballast particles contributed to fatigue failure since ballast particle fracture was observed after fatigue testing (Figure 4.5.4). Therefore, ballast particles may fatigue under flexural/tensile loading before RPF fatigue occurs.

Similar to the PSB constituent flexural strengths, the RPF (ρ_{RPF} = 200 kg/m^3) compressive strength (3,752 kPa) is higher than the AVG PSB compressive strength (2,607 kPa); ballast compressive strength, at 100 kPa confining pressure, is 594 kPa or 77% less than PSB. Limitations in PSB compression strength, relative to RPF compressive strength, is likely attributed to lack of bonding strength, as was identified for PSB flexural strength. However, Increase in PSB compressive strength, relative to ballast compressive strength, is likely attributed to both the predominant strength of RPF and high characteristic ballast tensile strength.

When making a comparison between two modes of testing, the AVG PSB compressive modulus (95 MPa) is less than the AVG PSB flexural modulus (274 MPa) similar to how RPF compressive modulus (88 MPa) is less than RPF flexural modulus (124 MPa). RPF compressive modulus is slightly less than PSB. Therefore, PSB stiffness (in compression) is likely limited by the stiffness of RPF and stiffness of the ITZ (similar to flexural test results). PSB constituent compressive properties are presented in Figure 4.7.1.

Marginal differences were observed between PSB compressive modulus (95 MPa) in static loading tests and resilient modulus (100 MPa) in cyclic triaxial tests; therefore, monotonic testing on PSB can be a useful alternative for predicting PSB resilient modulus (under cyclic compressive loading). In addition, PSB cylinders were tested using a cyclic triaxial method where minimal accumulation of plastic strain, ε_p, was observed over 200,000 loading repetitions at a representative state of stress (Ebrahimi 2011). Specimens tested up to 500,000 loading repetitions had a marginal increase in plastic strain. Over the first 200,000 loading repetitions, PSB plastic strain (ε_p=0.22%) was far less than clean ballast (ε_p=0.96%) or fouled ballast (ε_p=3%). Since the cumulative plastic strain under cyclic loading conditions in PSB specimens was significantly reduced, PSB elastic properties are more important for design of PSB in rail substructure. Since PSB and RPF strengths are far greater than the clean ballast compressive strength (at the representative confining stress), the functionality of PSB in rail infrastructure would likely be driven by PSB compressive modulus (formed using a percolation-injection method as described in Appendix A.3.3).

4.7.2 PSB Mechanical Properties Compared to Bound and Unbound Aggregates

In this section, Moduli and strength of each of the materials within PSB (i.e., ballast and RPF) are compared to each other and to the PSB composite material. The mechanical properties of PSB and PSB constituents (RFP and ballast) are compared to other materials such as cement-

stabilized materials (CSM), natural base-course aggregates, and concrete. Compressive and flexural strength of PSB and RPF are compared to CSM (at different cement-binder contents) to show the similarity in relative strengths of these materials. Resilient modulus of PSB, ballast, MN DOT Class 5 aggregate, and CSM are compared to show the elastic behavior of the materials under cyclic loading conditions. Flexural strength of CSM and PSB are compared to demonstrate increase in strength with increase in binder content (i.e., percent cement and percent RPF by weight). The strength-to-bulk-density ratio (σ/ρ) of PSB, RPF, ballast, CSM, and concrete are compared to show how each material possesses σ/ρ properties that can be favorable depending on the application. The this section is to understand the mechanical properties of PSB, how these properties compare to other materials commonly used in transportation infrastructure, and the suitability for use of PSB in track-infrastructure.

When comparing the compressive strength of PSB and RPF to CSM as shown in Figure 4.7.2, PSB has 2.5 times greater compressive strength. RPF with a 200-kg/m^3 density has a compressive strength of 3,752 kPa and ballast (tested at 100 kPa confining pressure) has a compressive strength of 594 kPa; therefore, both materials possess lower compressive strengths than CSM. From RPF test results compiled from literature, RPF with a density ranging from 26 to 417 kg/m^3, the range of compressive strength is 2,774–6,167 kPa (Figure 4.7.2); therefore, CSM still possesses higher strength than RPF formed at high densities.

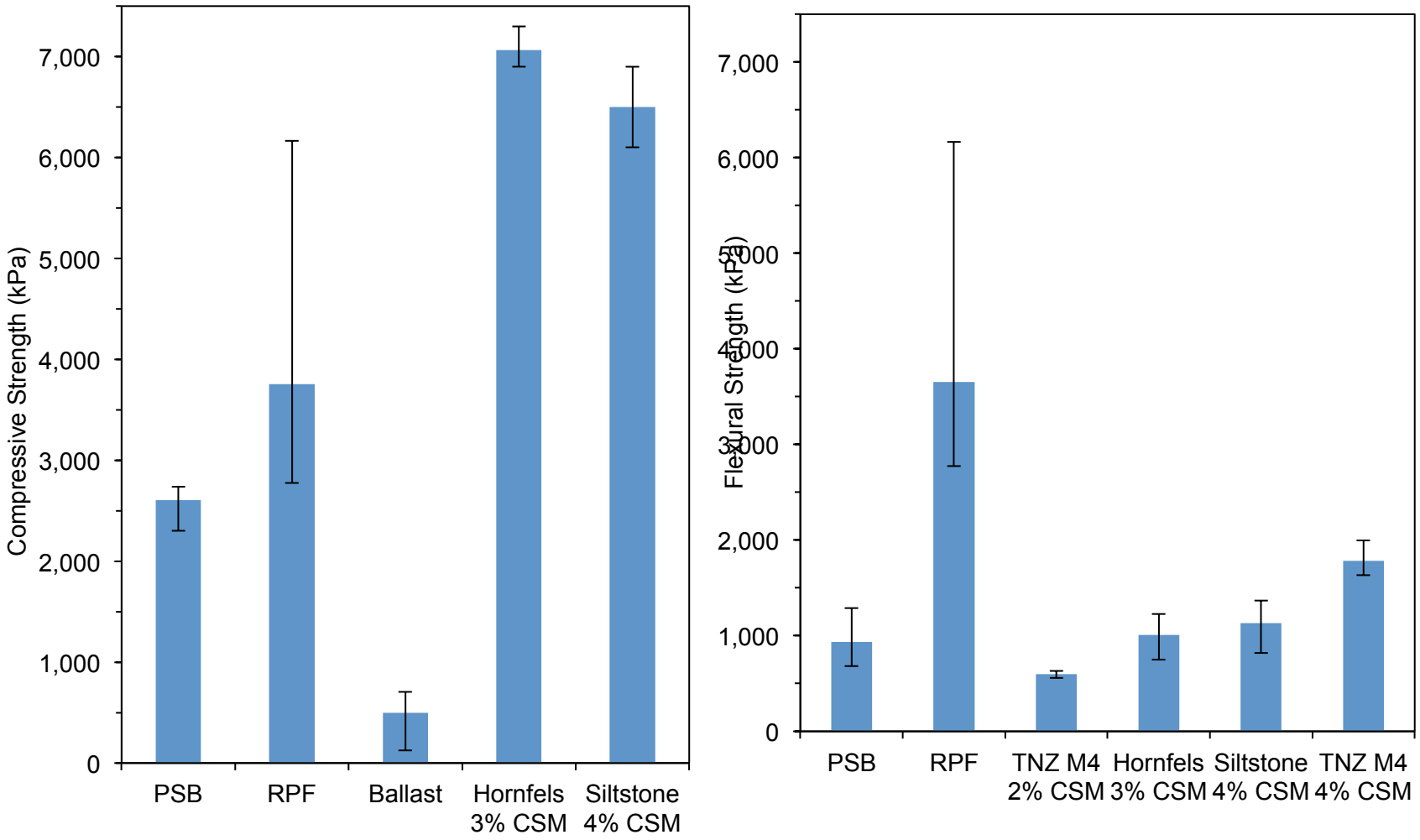

Figure 4.7.2: Comparison of RPF and CSM compressive strengths (left) and comparison of RPF and CSM flexural strengths (right). Hornfels and Siltstone data are from Midgley & Yeo (2008) and TNZ M4 are from Arnold (2009).

When comparing the flexural strength of PSB and RPF to CSM, as shown in Figure 4.7.2, PSB has a flexural strength similar to that CSM flexural strength at 28-day curing time in Midgley & Yeo (2008). RPF (ρ_{RPF} = 200 kg/m^3) possesses a much higher flexural strength (3,652 kPa) than PSB and CSM. With RPF densities ranging from 26 to 417 kg/m^3, the range of RPF flexural strength (2,774–6,167 kPa) is still greater than PSB and CSM (Figure 4.7.2). In Midgley and Yeo (2008), the flexural modulus increased as the relative density increased, similar to how modulus of PSB increases as PSB density increases. Unlike each material being compared, RPF has similar strengths in each mode of load application (i.e., compressive, flexural, and tensile) and as indicated later in this subsection RPF has superior σ/ρ.

Since PSB and CSM have similar AVG flexural strength properties, a comparison is also made between flexural strength and the percentage of binder content. A study from Zhang and Wei (2011) is used for comparison where the flexural strength of CSM (at 28-day curing time) was marginally higher than CSM in Midgley & Yeo (2008) used in earlier comparisons. With a range of binder content (% cement) from 4 to 7%, CSM flexural strength in Zhang and Wei (2011) ranged 1,150–1,895 kPa or a 39% increase in flexural strength with 3% increase in binder content. Over the same range of binder content in PSB (percent RPF by weight), PSB flexural strength ranged approximately 682–1,290 kPa or 28% increase, PSB and CSM flexural strength versus binder contents are shown in Figure 4.7.3. Consequently, increase in cement binder content has more influence on increase in CSM flexural strength than increase in RPF binder content has on the increase in PSB flexural strength. In addition, increase in volume of RPF in PSB is much higher than increase in volume of cement needed to obtain the same proportional increase in flexural strength.

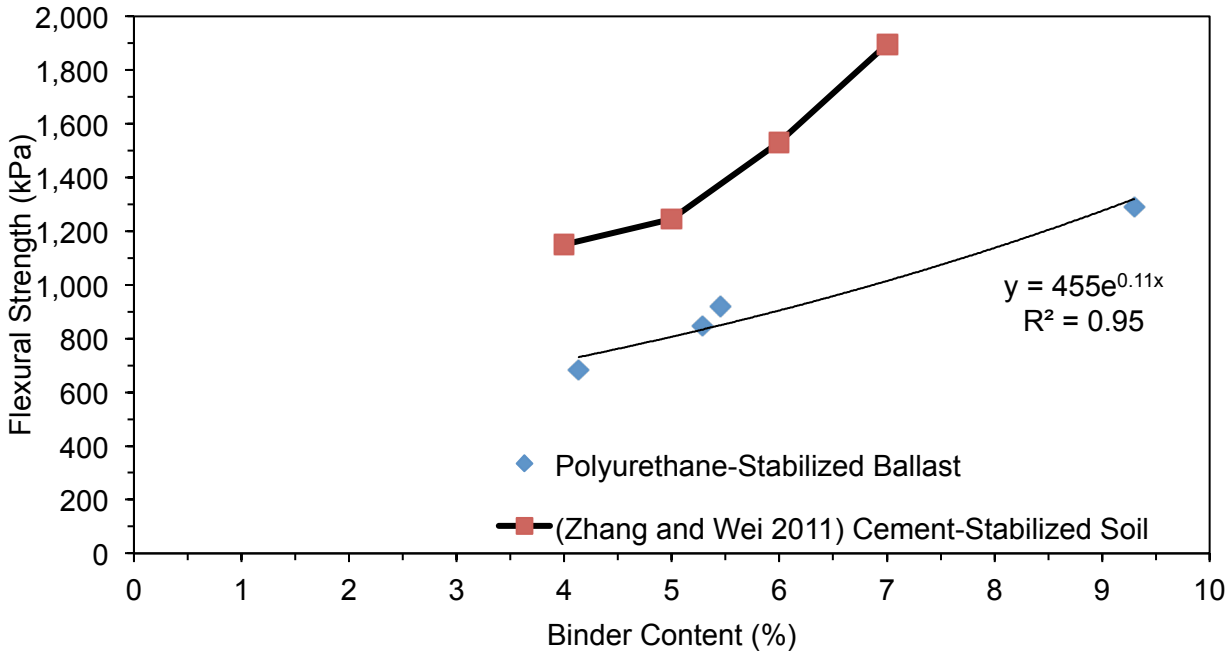

Figure 4.7.3: Comparison of PSB and CSM flexural strength versus binder content (percent RPF and percent cerement, respectively).

The flexural strength of RPF is superior compared with other materials (e.g., CSM and PSB); however, CSM has greater compressive strength than PSB or RPF at a density of 200 kg/m^3. In addition, CSM has far greater flexural modulus (AVG 13,800 MPa) than PSB and RPF (274 and 124 MPa, respectively). Consequently, CSM would perform more favorably in application where minimal compliance (i.e., elastic strain) is allowed under operational flexural loading conditions, hence the typical application of CSM in roadway construction. For rail infrastructure, compliance of PSB may be favorable due to the strains that can be tolerated under the loads distributed from the superstructure down through the substructure.

When evaluating the resilient modulus, M_R, of PSB, ballast, MN DOT Class 5 aggregate, and CSM (Figure 4.7.4); PSB (AVG 100 MPa) has the lowest M_R while CSM with 2% cement binder tested by Arnold (2009), has the highest modulus. MN DOT Class 5 tested at a bulk stress of 208 kPa, had a M_R 18% less than ballast and over 2 times greater than PSB. The M_R of ballast (275 MPa) was over 2.5 times greater than PSB. When PSB density ranged 1,536 to 1,683 kg/m^3 the M_R ranged 63–181 MPa, which was still less than the ballast M_R. As is the case for flexural properties of CSM, CSM would perform more favorably in applications where higher stiffness is required for design under compressive loading. However, for use of PSB in rail infrastructure, a finite element method was used in Chapter 5 to determine the effect on the overall track elastic response of having PSB with lower compressive modulus formed in the ballast layer, which was found to be inconsequential.

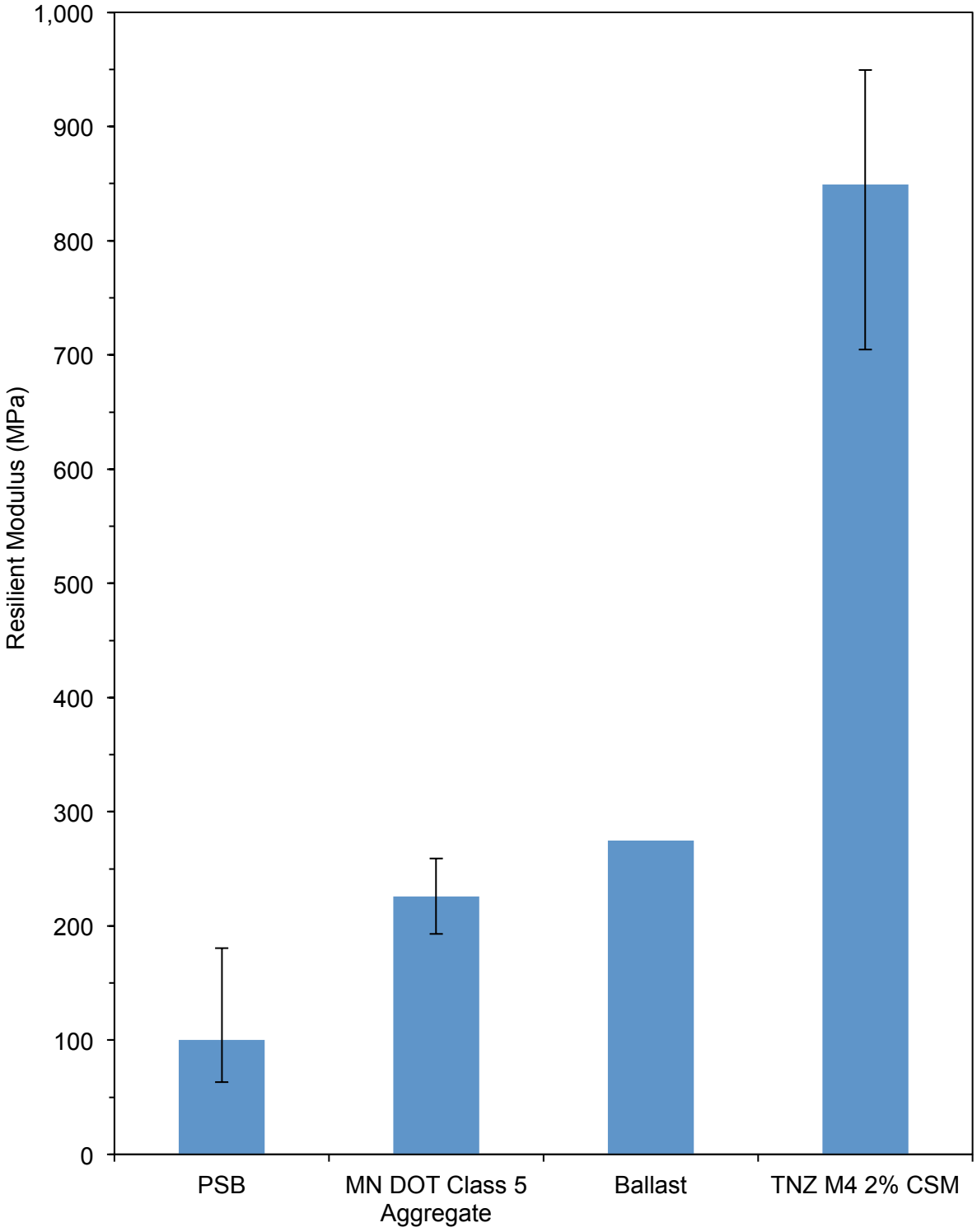

Figure 4.7.4: Comparison of resilient modulus of PSB, clean ballast at bulk stress of 600 kPa (Ebrahimi 2011), summary resilient modulus of MN DOT Class 5 tested at a bulk stress of 208 kPa, and CSM with 2% cement binder tested by Arnold (2009).

The compressive properties of PSB, RPF, and ballast are compared using average strength-to-bulk-density ratio (σ/ρ, kPa/kg/m^3) in compression to show how the strength compares to the density or weight of the materials (Figure 4.7.5). RPF (σ/ρ = 18.8) has a σ/ρ far greater than that of ballast (σ/ρ = 0.31) tested at 100 kPa confining stress. Since PSB has a compressive σ/ρ of 1.54, RPF increases ballast σ/ρ ratio by a factor of 5. CSM with 4% cement, from Midgley & Yeo (2008), with an AVG bulk density of 2,146 kg/m^3, had a σ/ρ of 3.03 and concrete with 20.7 GPa (3,000 psi) design compressive strength, with a typical bulk density of 2,403 kg/m^3 (150 pcf), has a compressive σ/ρ of 8.61.

The mechanical properties of PSB and RPF are also compared using average flexural σ/ρ to show how the strength compares to the weight of the materials under flexural loading conditions (Figure 4.7.5). As was seen for compressive σ/ρ, RPF (σ/ρ = 18.3) has the highest σ/ρ of the materials. For comparison, PSB has a flexural σ/ρ of 0.57, CSM with 4% cement, from Midgley & Yeo (*7*) (AVG bulk density of 2,146 kg/m^3), had a σ/ρ of 0.53, and concrete (2,403-kg/m^3 bulk density), designed for 20.7 GPa (3,000 psi) compressive strength, has a flexural σ/ρ of 1.31. When comparing flexural σ/ρ, RPF has the same ratio in compression as in flexure. As was seen with flexural strength properties of PSB and CSM, both materials have a very similar flexural σ/ρ, with CSM having a marginally lower σ/ρ than PSB.

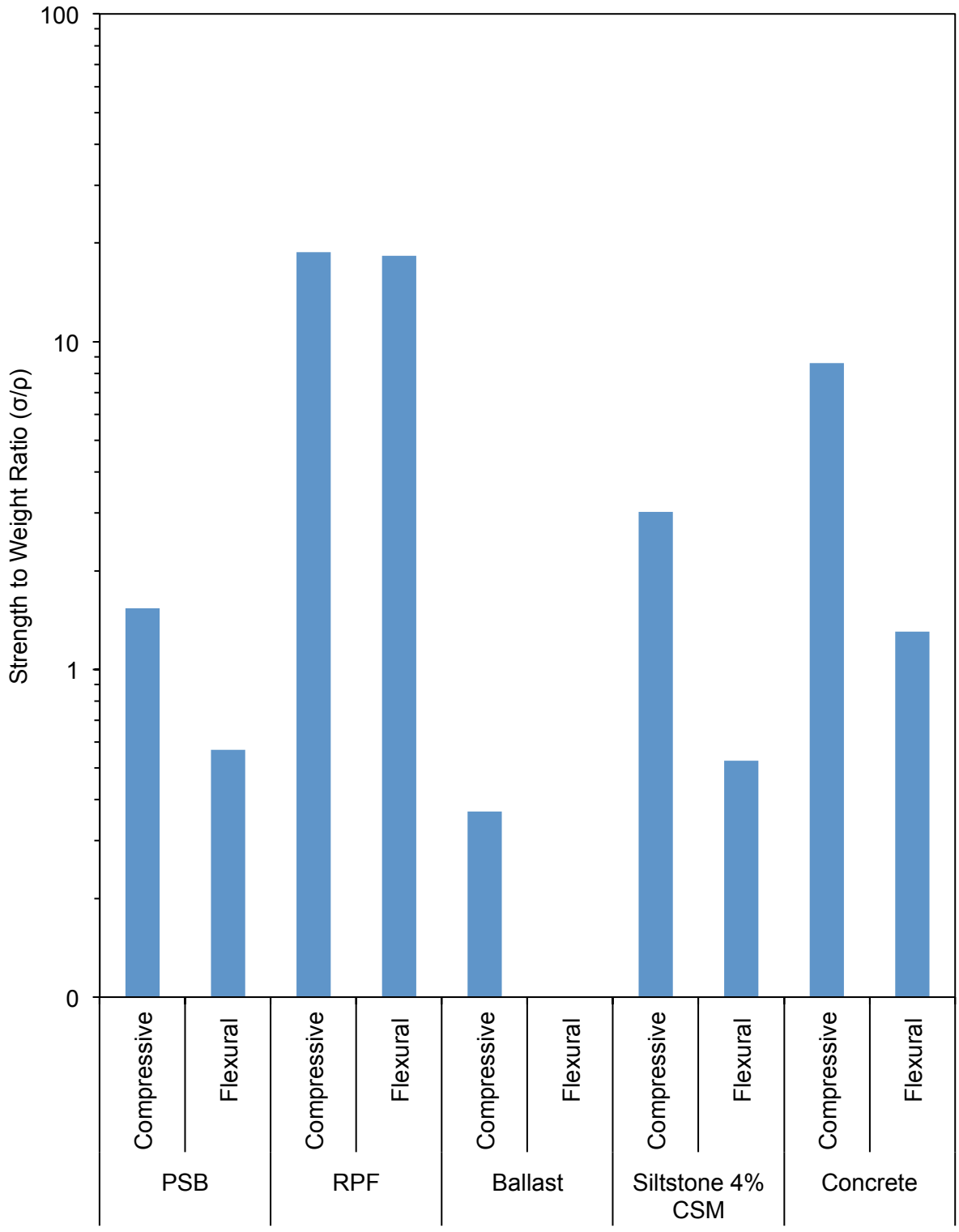

Figure 4.7.5: Comparison of the strength to weight ratio (log-scale) of PSB constituents, PSB, typical 20.7 GPa (3 ksi) concrete, and 4% cement siltstone from Midgley & Yeo (2008). Log-scale used so that each ratio can be visualized in the figure.

5 ANALYTICAL AND CONSTITUTIVE MODELS

5.1 EMPIRICAL MODEL DEVELOPMENT

Empirical equations were fit to the PSB data from cyclic triaxial compression tests. In Ebrahimi and Keene (2011), similar empirical equations were developed into constitutive relationships for predicting vertical rate of plastic strain (r_p) in cyclic triaxial compression tests from fouling index, water content, state of stress, and loading history. Since, introduction of RPF enhances the properties of ballast, in contrast to the effects of fouling index and water content as presented in Ebrahimi and Keene (2011), an alternative set of constitutive relationships were defined for PSB. The governing equations for rate of plastic strain are redefined to have a transition limit at 10^3 cycles which is different from the transition from initial compaction phase to fouling impact phase as defined in in Ebrahimi and Keene (2011). The reconfigured equations for rate of plastic strain are given by

$$r_p = \frac{d\varepsilon_p}{d\ ln N} = b \qquad N < 10^3 \qquad (5.1.1)$$

$$r_p = \frac{d\varepsilon_p}{d\ ln N} = b + a\ log(N - 10^4) \qquad N > 10^3 \qquad (5.1.2)$$

where N is the number of loading repetitions, r_p is the rate of plastic strain, and “a” and “b” are parameters that incorporate the effect of fouling index and moisture content on r_p, which are redefined for PSB mechanical behavior. The parameters “a” and “b” are normalized based on the applied state of stress experimentally determined for PSB as

$$\frac{a}{a_{ref}} = 0.0544\left(\frac{\sigma_1}{\sigma_3}\right) - 0.509 \qquad (5.1.3)$$

$$\frac{b}{b_{ref}} = 0.0194\left(\frac{\sigma_1}{\sigma_3}\right) - 0.179 \qquad (5.1.4)$$

where σ_3 is the confining stress applied, σ_1 is the vertical stress (i.e., $\sigma_1 = \sigma_d + \sigma_3$), and "$a_{ref}$" and "$b_{ref}$" have constitutive relationships with the density of PSB and percent RPF by weight. Due to the closed cell content of RPF within PSB, there is little effect from confining pressure (see B.2 in Appendix B regarding effects of confining pressure on RPF); therefore, a constant *in situ* reference confining stress is used at 35 kPa as was used during experimental testing. Different than the constitutive equations for fouled ballast in Ebrahimi and Keene (2011), for PSB "a_{ref}" and "b_{ref}" are found using

$$a_{ref} = S_a * \left(\frac{\beta_{ref}}{\rho_{PSB} * (\%RFP)^2}\right) \qquad R^2=0.91 \qquad (5.1.5)$$

$$b_{ref} = S_b * \left(\frac{\beta_{ref}}{\rho_{PSB} * (\%RFP)^2}\right) \qquad R^2=0.90 \qquad (5.1.6)$$

where S_a and S_b are determined based on the post-injection PSB density, ρ_{PSB}, percent RPF is the proportion by weight of injected RPF, and β_{ref} is a factor for the minimum amount of effective RPF to be injected. The rate of plastic strain is dependent on the state of stress applied and the overall PSB density and percent RPF by weight present. Limitation in the model (i.e., PSB density and percent RPF by weight) are based on β_{ref}. Below a certain ratio of ρ_{PSB} to percent RPF the deformation model reverts to the equations and parameters in Ebrahimi and Keene (2011) for clean and fouled ballast deformational behavior. The constitutive relationships between the prediction parameters and PSB phase properties are shown in Figure 5.1.1.

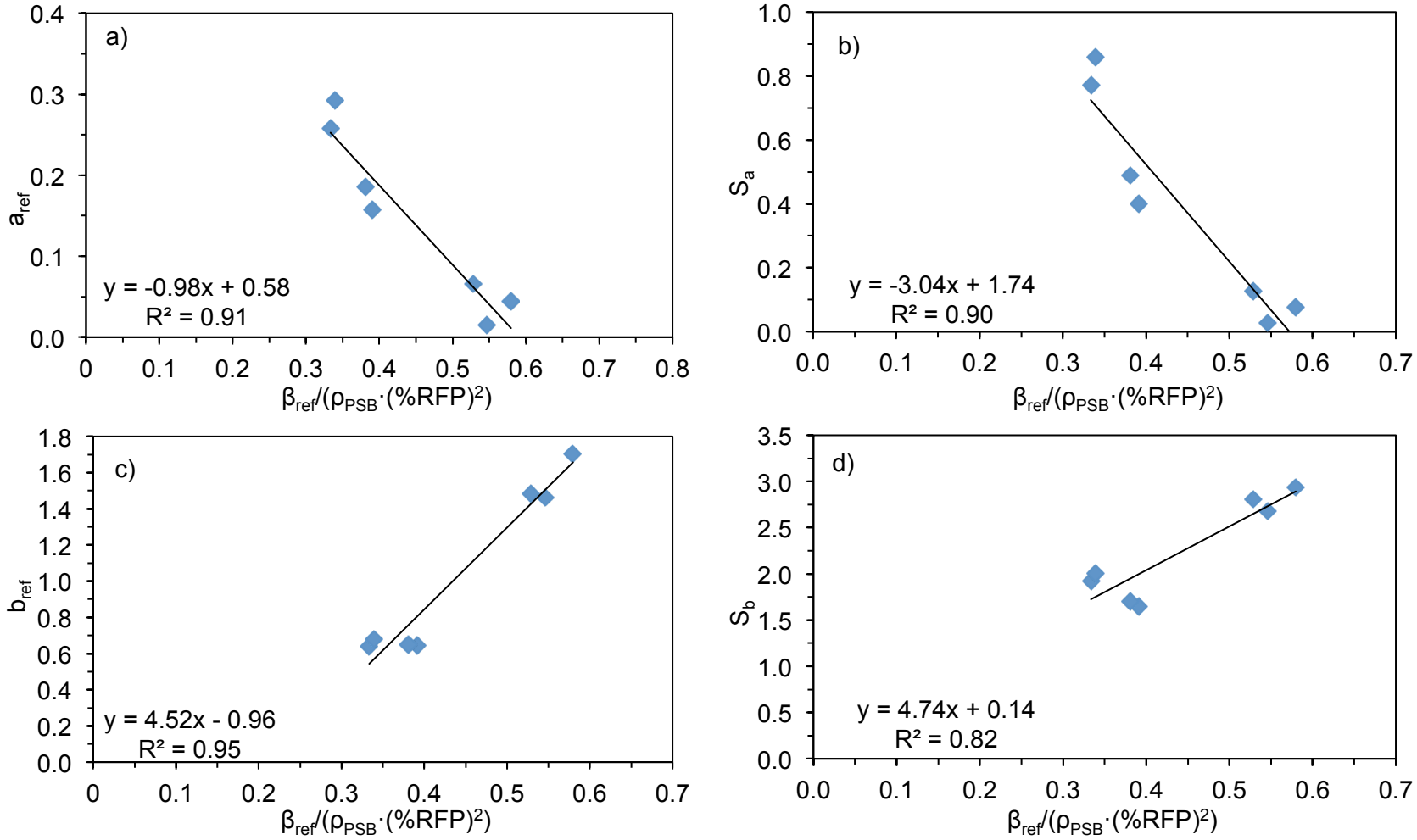

Figure 5.1.1: Parameters 'a' and 'b' in Deformation Model of Polyurethane Stabilized-Ballast (PSB) as a Function of $\beta_{ref}/(\rho_{PSB}$*(percent RPF)^2).

The parameter “b” as a function of ρ_{PSB}, percent RPF, and state of stress is a more conservative estimation of cumulative plastic strain before 1,000 cycles in the cyclic triaxial tests. The parameter “a” as a function of ρ_{PSB}, percent RPF, and state of stress is far more accurate and represents the deformational behavior after a large number of loading repetitions. Consequently, the model developed herein is more accurate for deformational behavior after 10,000 cycles. Measured versus Predicted model values are shown in Figure 5.1.2. The PSB specimens accumulated plastic strain more gradually during the initial 10,000 cycles, which is unlike the response of clean ballast. The inaccuracy of the model within the first 10,000 loading cycles can be attributed to the difference in PSB deformational behavior to that of clean ballast. In clean ballast, particle breakage, rearrangement, and initial compaction lead to a constant rate of strain that diminishes after 10,000 cycles. Since, there is no particle rearrangement or compaction in PSB, other material behavior must be responsible for the accumulation of plastic strain over numerous loading repetitions.

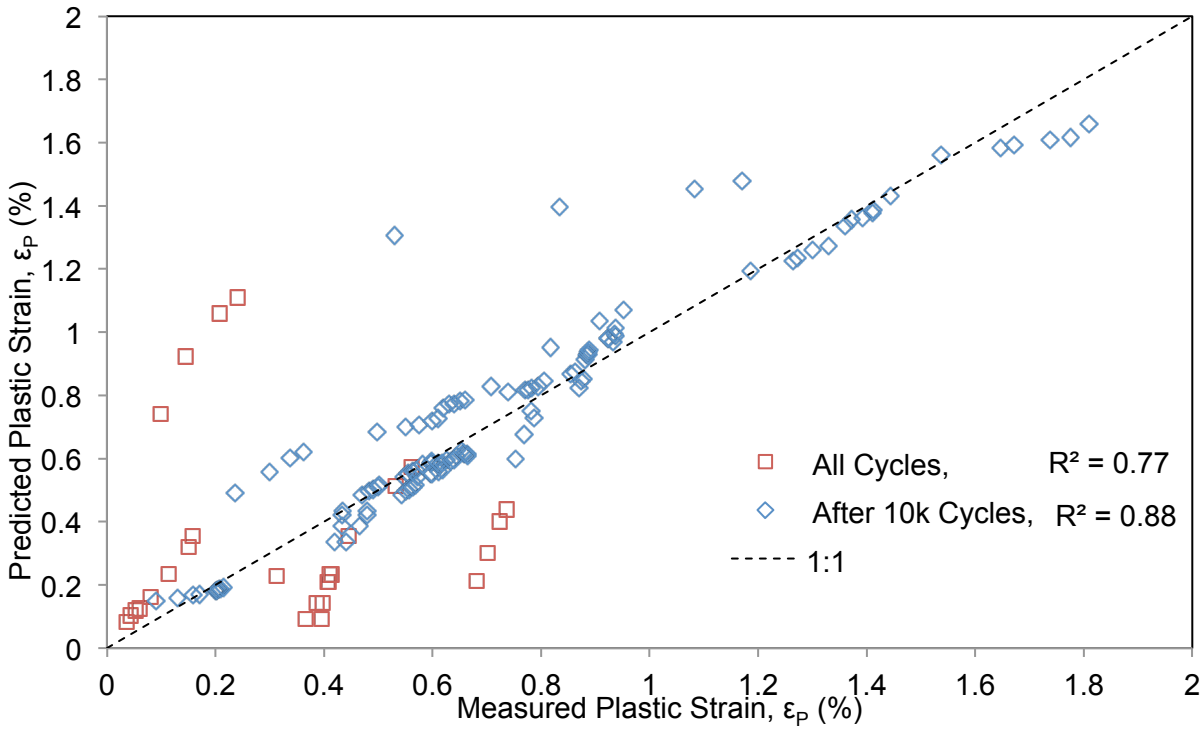

Figure 5.1.2: Strength of prediction model for all cycles and after 10,000 cycles.

The accuracy of the proposed model is most suitable for predicting deformational behavior after 10,000 loading cycles. As detailed in Section 4.3, the resilient modulus calculated for the PSB specimens from the cyclic triaxial data was an average of the resilient response after 10,000 cycles. Since the objective for stabilization of ballast and track substructure is to provide long-term track stability, the observed variable behavior and model inaccuracies pertaining to low cycle deformational and resilient response do not play a key role in modeling PSB behavior. In Aursudkij et al. (2009), the resilient modulus was measured at different stress ratios and was represented as resilient modulus, M_r (kPa), versus sum of principal stresses. The relationship established was a power relationship given as

$$M_r = k_1 \cdot \left(\frac{\theta}{P_{ref}}\right)^{k_2} \tag{5.1.7}$$

where empirical constants as k_1 (kPa) and k_2 are material constants in the power model based on the M_r of ballast, which is controlled by the sum of the principle stresses, θ (kPa), and P_{ref} is a reference stress (kPa) with a value of 1. A similar model was used by Selig and Waters (1994) for predicting subgrade and subbase elastic response for use in modeling track substructure response in the program GEOTRACK®. However, a linear model was used for modeling ballast behavior. This power model equation is commonly used for determining resilient modulus of base course materials used in U.S. highway pavement systems. This model was also introduced by Moosazedh and Witczak (1981), where a similar power model was proposed and θ is the bulk stress defined as

$$\theta = \sigma_1 + 2 \cdot \sigma_3 \tag{5.1.8}$$

where σ_1 is the sum deviator stress and the confining stress, σ_3.

The effect of stress ratio and use of a power model is appropriate for testing and predicting the resilient behavior of aggregates used in railway and highway infrastructure, as

was determined in Moosazedh and Witczak (1981), Selig and Waters (1994), and Bozyurt (2011). The deformational response of PSB was not found to depend on the confining pressure. This behavior is confirmed from observations made when conducting tests at varying confining pressures on RPF (see Section B.2). Results from cyclic triaxial and monotonic triaxial tests confirm that PSB and RPF deformational behavior have little correlation with confining stress applied during the test and are highly dependent on the phase densities within the PSB specimens. Similar how PSB density and percent RPF by weight influenced plastic deformational behavior of PSB, the influence of these material properties on resilient modulus of PSB is given by

$$M_r = 1.31 \cdot [\gamma_{PSB} \cdot (1 - \%RPF)] - 1{,}909 \qquad R^2{=}0.95 \qquad (5.1.9)$$

where M_r is given in MPa, γ_{PSB} is given in kg/m^3, and %RPF is given as the percent of RPF by weight.

The material phase properties are configured in the equation so that the value of the bulk or PSB density of the specimen contributes to the resilient modulus of the material, which also correlates well with the ballast phase density, as detailed in Section 4.3. However, contribution of RPF to the compliance of the PSB composite material was discussed in Section 4.3 and mechanical properties for RPF presented in B.2, where the compliance increases as RPF content increases. Consequently, in the equation for predicting resilient modulus of PSB, as the percent RPF increases the compliance of the material increases corresponding to a decrease in resilient modulus. Finally, when reconfiguring the phase relationships defined in Section A.1.2, the ballast phase density for a specimen should equal the PSB density multiplied by one minus the percent RPF, ($\rho_{ballast}=\rho_{PSB}$*(1- percent RPF)). The prediction of resilient modulus from cyclic triaxial tests based on PSB material phase properties are presented as Figure 5.1.3

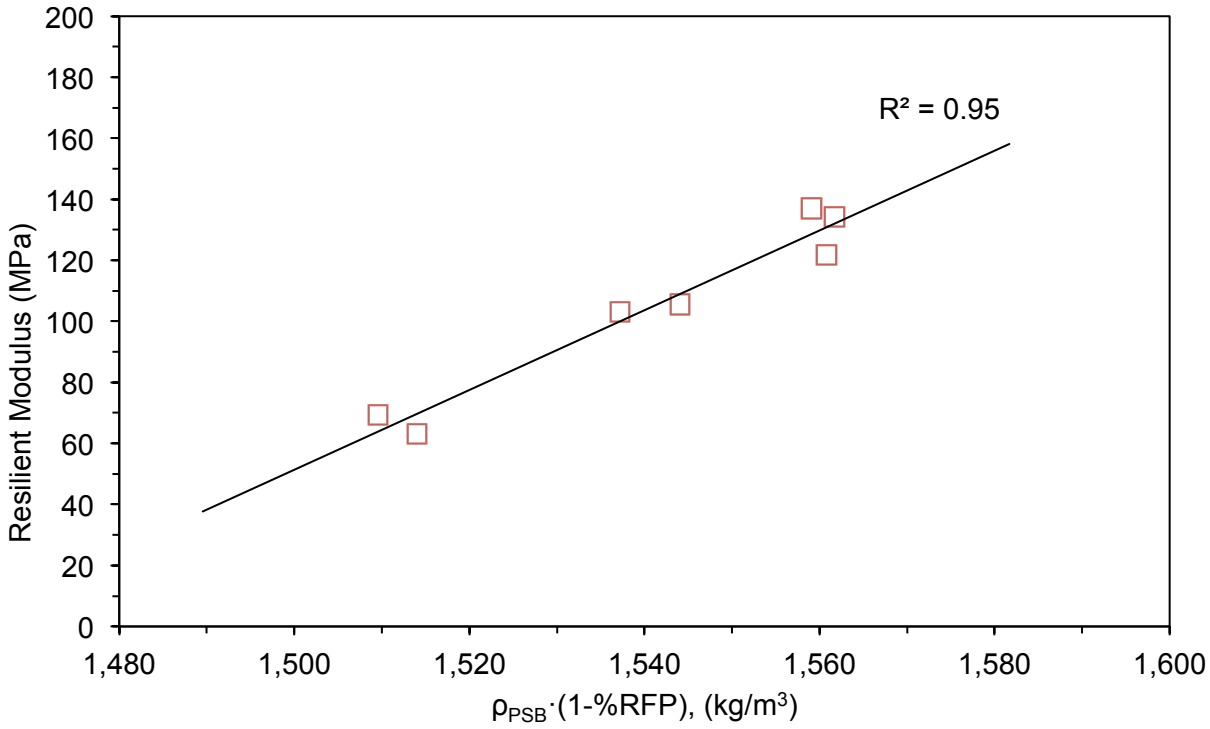

Figure 5.1.3: Prediction of resilient modulus from cyclic triaxial tests based on PSB material phase properties.

Based on the empirical relationships developed between accumulation of plastic strain and resilient modulus with number of loading cycles, material properties, and state of stress, a constitutive model is presented that allows application of the mechanistic properties of ballast, fouled ballast, and PSB for use in prediction of railway track mechanistic and long-term deformational behavior. Constitutive modeling of deformational behavior under cyclic loading is commonly presented as (Salim 2004):

$$\varepsilon_T = \varepsilon_P + \varepsilon_E \qquad (5.1.10)$$

where ε_T is the total strain, ε_P is the plastic strain, and ε_E is the elastic strain. From the constitutive equations developed, this expression can be used to incorporate the resilient and plastic deformational of PSB and ballast materials for use in a constitutive model. Similar methods are used for constitutive modeling for cyclic loading on sands (Niemunis 2005), where expressions are defined for elastic strain and plastic strain based on state of stress, number of loading cycles applied, and other constitutive relationships. The model developed in Niemunis (2005) provides a method for predicting total strain from each loading cycle, which can be determined mathematically or configured into numerical modeling software for numerical computation.

The model developed for PSB applies to clean ballast stabilized with RPF. The model at this point is limited to providing a prediction of the mechanistic properties of PSB with specific RPF injection protocols. In addition, model assumptions are based on full void space filling of RPF, negligible effects of confining pressure, and application of only one ballast type and particle size distribution. The objectives of the model presented herein are to establish a preliminary method for incorporating PSB material properties into engineering design and as a railway maintenance option. Findings of the model can serve for use in the WiscRail® software presented in Ebrahimi and Keene (2011) as an option for maintenance procedure selection. In

addition, preliminary analytical relationships developed from experimental testing can be used for input into finite element modeling software to investigate track plastic and elastic deformational behavior from having strategically placed PSB in the track. To this effect, modeling of elastic deformational behavior of a stabilized layer is presented in Chapter 6.

5.2 MODEL FOR PSB LAYERS

In the paving industry, rigid concrete pavements are more commonly used in areas where the traffic loading must be distributed over a large surface area beneath the concrete slab, due to weaker subgrade or low subgrade stiffness. Barnes (2008) explained that the fatigue life of the asphalt pavement layer increases as the tensile strain in the layer decreases; however, as the elastic modulus increases, the fatigue life decreases. Therefore, depending on the loading conditions, it may be more favorable to transfer the loads more directly to the subbase in compression rather than design a pavement layer with high stiffness where loads are carried by the layer primarily in flexure. Similar methodology applies to track-substructure where asphalt trackbeds are used and would also be applicable in the case of forming a PSB trackbed (i.e., layer). Details regarding methodology behind trackbed layers and applicability for PSB trackbed layers are given in Appendix D.

The concept of stabilized layers in rail infrastructure has been investigated in Rose et al. (2003), which involves construction of an asphalt layer above the subballast layer and beneath the ballast layer. Huang (2004) indicated that placing a complete HMA layer (HMA overlayment) without a ballast layer (i.e., beneath the superstructure) leads to a significant increase in the tensile strain at the base of the HMA layer. Adequate design thicknesses required for complete HMA trackbeds would require a large thickness for the HMA layer, which is not commonly feasible for track design (Huang et al. 1987). Therefore, similar concerns may apply when considering the creation of a PSB overlayment using the same approach as a HMA overlayment.

Placing an HMA layer beneath the ballast layer is known as an HMA underlayment. As indicated in Rose and Lees (2008), the purpose of the HMA underlayment is to reduce the stresses that are transmitted from the ballast layer to the subgrade layer and to serve as a

barrier between the layers. If the subgrade stiffness is poor, an underlayment may be uneconomical because a large ballast thickness would be required (Huang et al. 1987). Therefore, to set a thin HMA underlayment with a reasonable ballast layer thickness, good subgrade quality or the addition of a subballast layer above the subgrade is required. For the HMA layer, the tensile strain at the bottom of the layer controls the life cycle of the layer. For the subgrade/subballast, the accumulation of plastic strain controls the life cycle of the layer (Rose and Konduri 2006). If implementing a PSB underlayment similar conditions must be addressed, such as subballast/subgrade stiffness, PSB layer thickness, and remaining ballast layer thickness.

For asphalt pavement layers, the failure criterion is commonly represented by a model for fatigue cracking of the pavement layer based on layer strain and modulus. In Barnes (2008), a fatigue model, incorporating stain and modulus, using the Asphalt Institute method to represent asphalt fatigue life was presented as

$$N_f = f_1 \cdot (\varepsilon_t)^{-f_2} \cdot (E_1)^{-f_3} \qquad (5.2.1)$$

where N_f is the number of cycles to failure, ε_t is the tensile strain at the bottom of the layer, E_1 is the flexural modulus of the layer, and f_1,f_2, & f_3 are material and model fitting parameters. Rose et al. (2003) used a similar model for use of HMA in rail trackbed design, as did Harvey et al. (1996) for flexural beam tests conducted on asphalt. The model presented for PSB fatigue life is given in Table 4.3.1. Percent RPF by weight and PSB density have been included so that the phase properties of the material serve as direct input into the fatigue model. The model developed from PSB beam testing and the respective fitting parameters are shown in Table 4.3.1. A plot of the predicted number of cycles to failure from the fatigue model and the measured number of cycles to failure from PSB beam tests is shown in Figure 5.2.1. The strains generated in the track with varying PSB placements and moduli are detailed in Chapter 5.

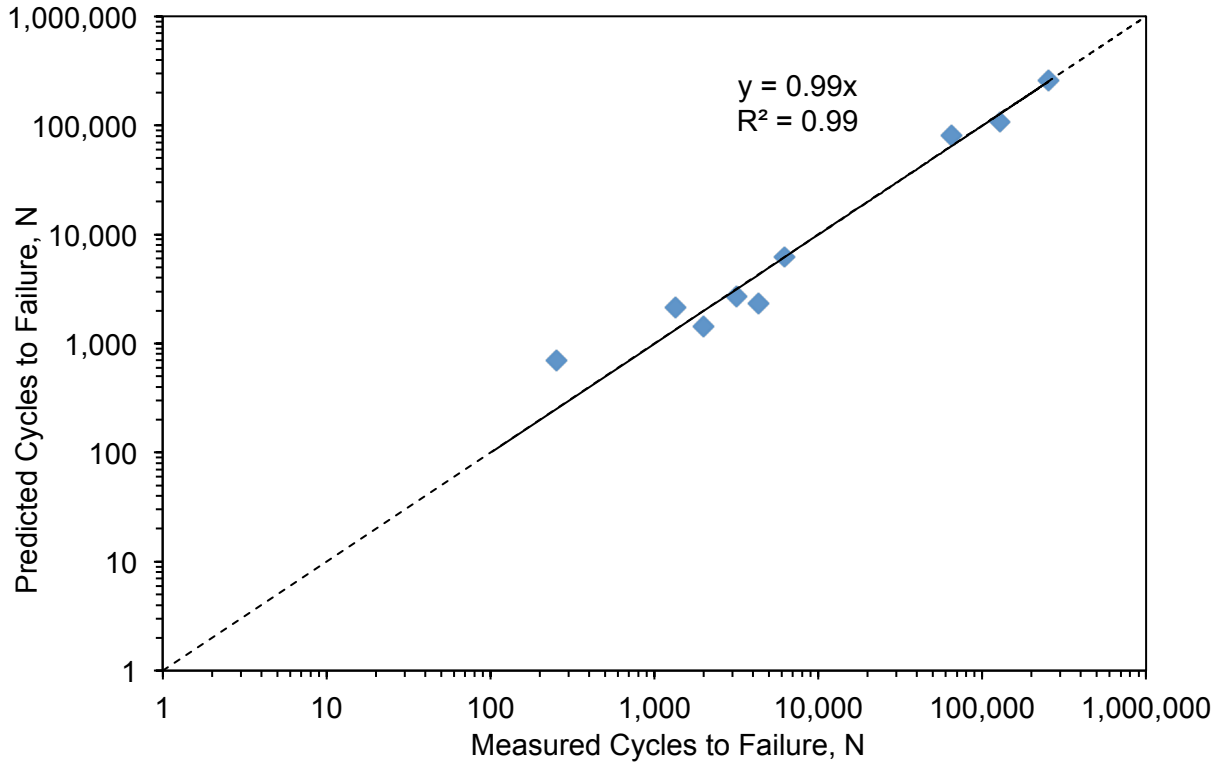

Figure 5.2.1: Predicted number of cycles to failure from the fatigue model versus the measured number of cycles to failure from PSB beam tests.

PSB is less stiff in flexural and compression than asphalt. The strain tolerance of the PSB material is also much greater than in asphalt. Therefore, PSB can transmit compression loads to good subgrade or tolerate flexural strain when loaded over weaker subgrade. The comparison of PSB flexural modulus, flexural strength, Young's modulus, and compressive strength are detailed in Section 4.7. Analysis of the loads transmitted from the superstructure through the ballast layer to a PSB trackbed were evaluated outside of this thesis, where a parametric study was conducted using a finite element model of a railway embankment with varying ballast, PSB underlayment, and subgrade/subballast thicknesses and moduli.

Regarding the effects of environmental conditions on stabilized layers in railway trackbeds, Rose and Lees (2008) noted that the HMA underlayment is protected from sunlight by the overlying ballast layer and is maintained at a relatively constant temperature and environment. When having a PSB underlayment, the RPF component will be protected by the overlying ballast layer. Since RPF is susceptible to ultraviolet radiation (Buzzi et al. 2008) and higher temperatures, subsurface injections are will preserve ambient temperature mechanical properties. Huang et al. (1987) noted that HMA underlayments were preferable to overlayments because required thickness of the HMA layer is minimal and conventional ballast layer maintenance can still be conducted. Similar methodology can be applied for PSB stabilized layers concerning conflict with ballast layer maintenance.

The model developed for PSB applies to clean ballast stabilized with RPF. The model is limited from providing a prediction of the mechanistic properties of PSB when specific RPF injection protocols discussed in Appendix A are not used. In addition, model assumptions are based on full void space filling of RPF, and application of only one ballast type and particle size distribution. The objectives of the model presented herein are to establish a preliminary method for incorporating PSB material properties into engineering design and as a railway maintenance option. Preliminary analytical relationships developed from experimental testing can be used for

input into finite element modeling software to investigate track resilient response and establish failure criterion for strategically placed PSB layers in the track.

Table 5.2.1: Empirical relationships and analytical models developed for PSB flexural strength, strain, modulus, and fatigue.

Model #	Model	R^2	Using	Eqn.	Ref.
Initial Flexural 95 % Breaking Strain					
1	$95\%\ \text{Breaking Strain}, \varepsilon_b = 7{,}506 * \left(\frac{\beta_{ref}}{\rho_{PSB} \cdot (\text{percent RPF})^2}\right)^{-0.19}$	0.99	PSB constitutive parameters	5.2.2	
2	$95\%\ \text{Breaking Strain}, \varepsilon_b = 4{,}555 \cdot (\text{percent RPF})^{0.39}$	1.00	Percent RPF by Weight	5.2.3	
Fatigue Life					
3	$\log N = \frac{(0.9340 - S)}{0.1366}$	0.88	Average Flexural Stress	5.2.4	Adhikari and You (2010)
3	$\log N = \frac{(1.926 - \varepsilon_0/\varepsilon_b)}{0.3379}$	0.95	Average 95% breaking strain	5.2.5	Litwinowicz & Brandon (1994)
4	$\log N = \frac{(1.2445 - \varepsilon_0/\varepsilon_b)}{0.2195}$	0.95	Percent RPF	5.2.6	
5	$\log N = \frac{(1.2458 - \varepsilon_0/\varepsilon_b)}{0.2194}$	0.95	$\left(\frac{\rho_{PSB} \cdot (\text{percent RPF})^2}{\beta_{ref}}\right)$	5.2.7	
Initial Flexural Stiffness					
6	$S_{max} = 1.57 \cdot 10^{-11} \cdot (\text{percent RPF})^{5.64}$	0.72	Percent RPF by Weight	5.2.8	
Prediction Model for Fatigue Life					
7	$N_f = 0.0167 \cdot \left(\frac{\rho_{PSB} \cdot (\text{percent RPF})^2}{\beta_{ref}}\right) \cdot (\varepsilon_t)^{-3.494} \cdot (S_{max})^{-1.661}$	0.98	Flexural modulus, flexural strain, and PSB constitutive parameters	5.2.9	Barnes (2008)

6 NUMERICAL ANALYSIS OF TRACK-SUBSTRUCTURE SYSTEMS

6.1 INTRODUCTION

To improve maintenance capabilities for problematic rail infrastructure elements (i.e., bolted rail joints, intersections, bridge approaches, etc.), a method involving polyurethane reinforcement of the ballast layer has thus far been proposed. The performance and behavior of polyurethane-stabilized ballast was investigated in the laboratory; however assessing how this material influences resilience of the track (to prevent severe wear in tie and rail) still needs to be evaluated. In an attempt to evaluate behavior of the polyurethane-stabilized railway substructure, a finite element model has been developed to simulate the rail, tie, ballast, subballast, and subgrade system. The numerical model can be used to determine the impacts that location, thickness, and properties of polyurethane reinforcement in the ballast layer have on track resilient behavior. Simulations were conducted for understanding the effect on individual substructure layers and overall track response due to localized areas of differing modulus (PSB formation) in the ballast layer. In Section 6.3.2, having stabilized areas beneath the rail tie extending through the ballast layer (PSB pile-layment) is investigated in correlation with the percolation-injection method (see Appendix A) and mechanical results are detailed in 4.2 and 4.3. Having stabilized areas at the base of the ballast layer (PSB underlayment) is investigated in correlation with the subsurface-injection method (see Appendix A) and mechanical results are detailed in 4.4 and 4.5. Simulations conducted herein may provide insight on how the use of polyurethane can influence the performance of railway structures and potentially reduce maintenance costs.

6.2 BACKGROUND

6.2.1 Railway Modeling

In Selig and Waters (1994), a computer track model was developed, called GEOTRACK, and validated using comparisons to the FAST facility in Pueblo, Colorado. At the FAST facility, strain gauge and extensometer instrumentation were installed to measure strains in each of the track components under railcar loading. In the model, the substructure material properties were varied to match the stresses and strains calculated in the model with the strain data that was generated in the field. Validation at very low and very high states of stresses was incomplete due to the limited loads generated in field tests. Beyond selecting a geometric configuration that matched that of the field track, the distribution of loads from the distance between axels was modeled to reflect the difference in proximity of the axels existing between locomotive and hopper cars. Selig and Waters (1994) found that a group of axels causes more track deformation than an individual axel passing over a point on the track. From the strains generated in the field and a parametric study conducted using computer modeling of the states of stresses versus strains, Selig and Waters (1994) proposed nominal values for the moduli of the substructure layers (Table 6.3.1).

The parametric comparisons in Selig and Waters (1994) were also disseminated in Stewart and Selig (1982) where the stresses and strains measured in the FAST test track were incorporated into a numerical model. In Stewart and Selig (1982), track modulus was calculated which is a parameter that describes the amount of deflection that will occur in the track corresponding to the magnitude of the load applied, similar to that of a spring constant. In Stewart and Selig (1982), the track modulus was described as a theoretical formulation with the assumption that the superstructure and substructure layers act like an elastic foundation and

that the rail acts like a continuously supported beam. Therefore, track modulus, u was presented as

$$u = \frac{1}{4} \cdot \sqrt[3]{\left(\frac{P}{\delta}\right)^4 * \frac{1}{E*I}} \tag{6.2.1}$$

where P is the wheel load, δ is the deflection of the rail beneath the wheel load, E is the Young's modulus of the rail, and I is the moment of inertia of the rail.

In many cases, the deformational response of the track under loading is described numerically by a more simplistic track modulus. The calculation for track modulus (k) is defined in Lichtberger (2005) as vertical track rigidity, which is given by

$$k = \frac{Q}{z} \tag{6.2.2}$$

where Q is the vertical track force (wheel load) and z is the track settlement under load. This method has been used in many other studies, including Selig and Waters (1994), where the track modulus was calculated to quantify the elastic deflection of the track under rail loads.

In other studies, the track modulus is broken down into spring constants for each of the individual track components to predict the vertical elastic response of the track under loading. In Kerr (2003), spring constants were defined from the railway pad down to the subgrade layer. Giannakos (2010) used a similar approach, which calculated the track modulus as the inverse of the coefficient of rail support modulus (ρ_{total})

$$\frac{1}{\rho_{total}} = \sum_{i=1}^{\nu} \frac{1}{\rho_i} \tag{6.2.3}$$

where ν is the number of layers and ρ_i is the spring constant for each of the layers. This approach is used by Kerr (2003) where the track modulus is defined from the rail pad and below, and the response of the rail is defined using an equation for a continuously supported

beam acting orthogonal to the axis with which the vertical spring constants are defined. In many approaches, separate methodology is used to model the behavior of the superstructure and substructure.

In Lichtberger (2005), a systematic approach is taken to correlate the wheel loads applied to the rail and the stresses and strains that are distributed throughout the substructure layers. In Lichtberger (2005) static and dynamic loading effects are taken into account. Several analytical relationships are presented that can be used to determine the stress distribution from the wheel load through the superstructure down through the substructure. As indicated in Indraratna et al. (2011), the AREMA engineering manual provides a few equations that define the stress applied to the subgrade from the stress applied to the ballast layer; however, these equations do not account for the stress distribution through compacted subgrade or subballast layers.

Constitutive relationships can be limiting when attempting to develop a model of a rail track, where each element must act independently through differing material property definition, but with specified interface behavior. Consequently, a more appropriate approach may include computer finite element software for understanding stress distribution through more complex problems and systems. Elastic models have been defined using constitutive relationships and similar material models have gained popularity for finite element modeling of rail infrastructure. Background and future work regarding constitutive and numerical modeling are addressed in Chapter 8.

6.2.2 Railway Finite Element Modeling

Finite element modeling (FEM) has commonly been used by mechanical engineers for modeling the mechanistic response of a complex system of various moving parts. In civil engineering, a common application of FEM has been for structural analysis under static and dynamic loading

conditions. The use of finite element analysis for modeling elements in transportation infrastructure and geotechnical engineering has been growing as FEM software, pre-constructed material models, and computational resources have increased. The use of FEM for geotechnical modeling applications allows modeling of complex problems such as *in situ* soil behavior. Some cases may involve modeling soil formations where access and installation of instrumentation is limited and expensive. Complex materials models can be defined by researchers for investigating the mechanistic integration of soil layers, *in situ* stabilization, and interaction and interface between materials of differing composition and mechanical properties.

A few studies have been conducted using FEM for rail infrastructure and the behavior of stabilization with the XiTrack^{TM} technology. Banimahd and Woodward (2007) used finite element modeling to investigate track resilience and substructure foundation elasticity for railway bridges and bridge approaches. In their study, they modeled a bridge approach, which involved the typical stiffness of ballasted railway track and track on a concrete rail bridge. In the model, constitutive soil models and models involving bridge behavior to loading where used. The purpose of their investigation was to model vertical deflection of the railway segment approaching the railway bridge and the rails on top of the bridge deck. Due to the elasticity of the bridge approach segment relative to the bridge deck, as expected, the deflection was greater in the rails on the ballast foundation and far less in the rails on the bridge deck. Banimahd and Woodward (2007) demonstrated that the magnitude of stress was greater during the bridge approach due to the effect of dynamic loading, which was generated by the transition of the carload from the stiff bridge deck to the more elastic ballast-track foundation. This increase in stress due to dynamic loading, from change in track elasticity and deflection of the railway, was found to contribute to further superstructure and substructure degradation.

Research technology available for FEM of railway segments or bridges has been conducted using Abaqus, a powerful finite element modeling software package. Similar to the

type of study conducted in Banimahd and Woodward (2007) for XiTrack™, Abaqus was used to model a railway bridge in Koskinen (2005) where the response of a railway embankment and bridge structure to loading was investigated. From the finite element analysis (FEA), the distributions of stresses and deflections were observed in the modeled railway bridge and the ballast-track foundation. The model was validated by comparing full-scale tests conducted in the field to the model results. Koskinen (2005) demonstrated that Abaqus and finite element modeling is an appropriate tool for modeling railway segments and features.

6.3 DEVELOPMENT OF TRACK MODEL FOR FINITE ELEMENT ANALYSIS

6.3.1 Finite Element Model Development (ABAQUS 6.9-2)

6.3.1.1 Model Development

The construction of a finite element model was conducted in ABAQUS 6.9-2 using several sources for the geometry of the track segment, mechanical and material properties of the superstructure and substructure, and typical representative railway loads. The geometry of the modeled substructure consisted of soil and aggregate layers that typically make up a railway embankment. The layers in the model consisted of the subgrade, subballast, and ballast layer. The superstructure consisted of the rails and the tie. The depth and geometry of the substructure layers was taken from Chapter 6 of the Army Corps of Engineers Railroad Design and Rehabilitation Technical Instructions. A typical cross-section for tangent track was used for basic model construction, shown as Figure 6.3.1 and Figure 6.3.2. In Indraratna (2011), the FEM package PLAXIS was used for modeling a railway embankment subjected to repetitive loading. In the developed model the subgrade dimensions used were 6 m width to the center line of the track and 3 m depth for the subgrade layer. The selected model geometry was based on construction plans used for building a railway track and based on other numerical modeling studies involving a track cross-section and foundation dimensions and constraints. Figure 6.3.3 displays the vertical displacement in the model under typical material property and loading conditions.

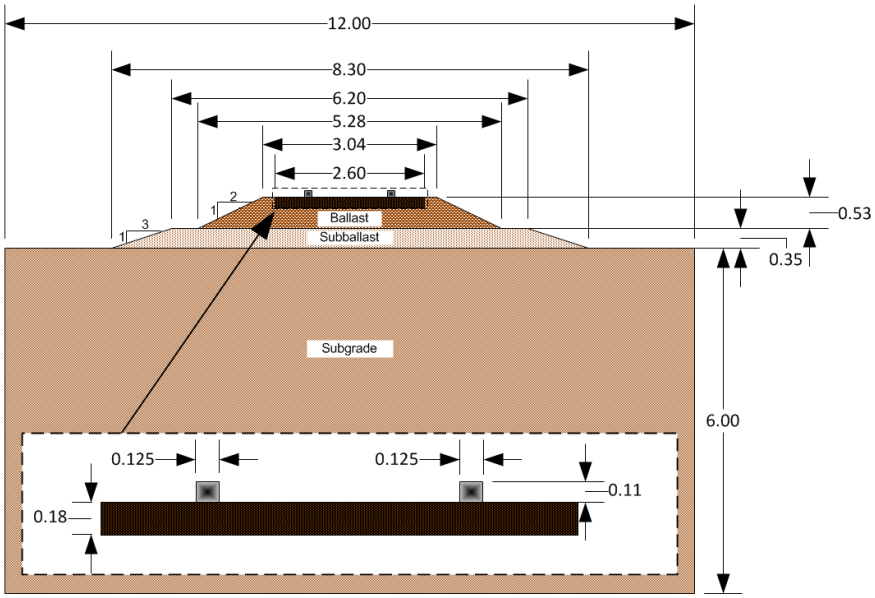

Figure 6.3.1: Typical railway segment cross-section dimensions (in meters) selected for finite element modeling analysis.

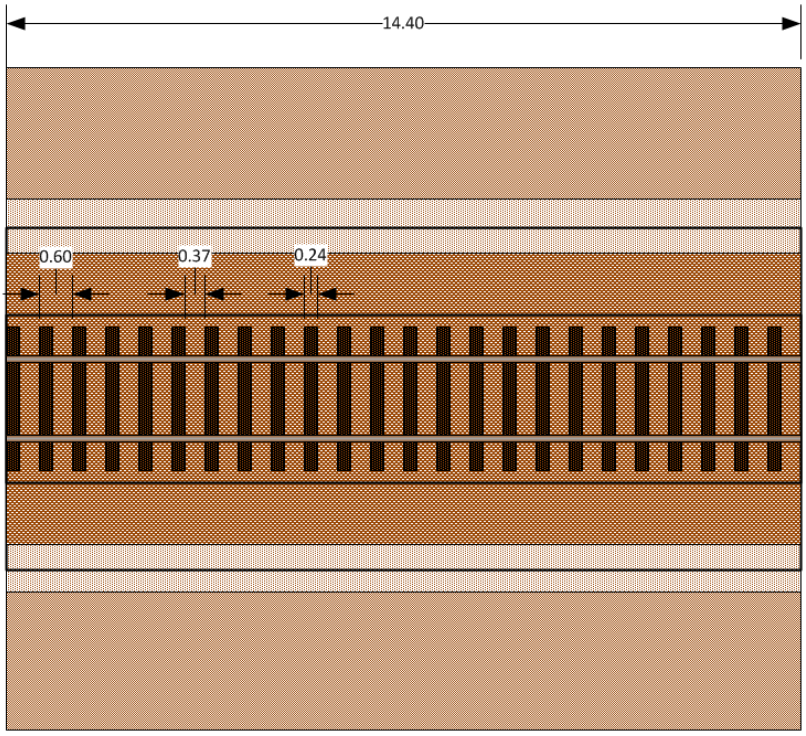

Figure 6.3.2: Railway segment length and element dimensions (plan-view) in meters selected for finite element modeling analysis.

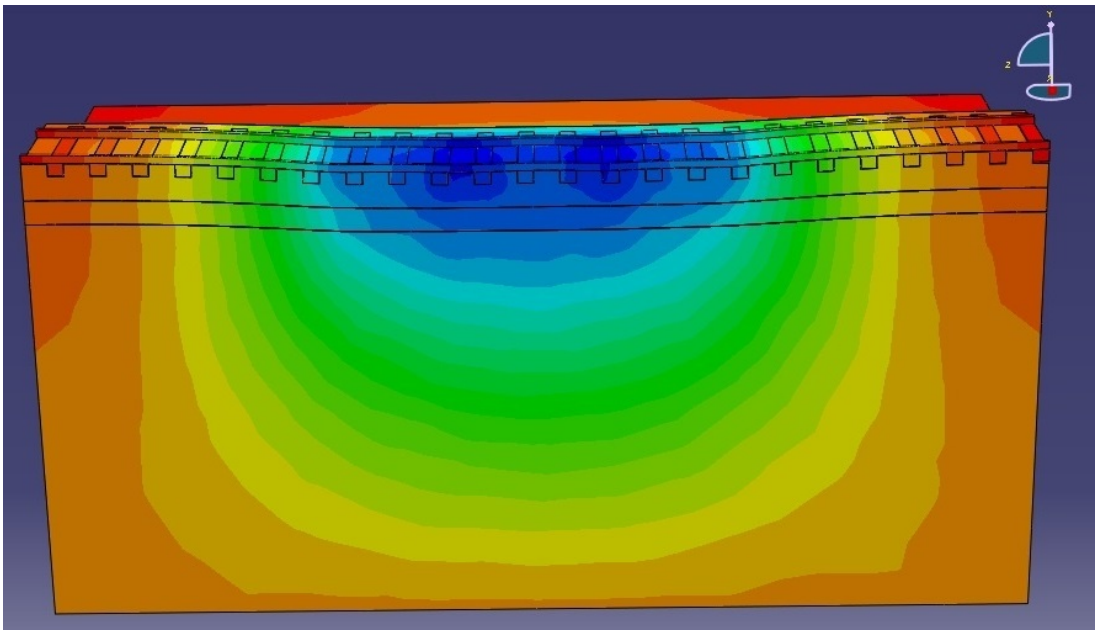

Figure 6.3.3: Model output (model width = 14.4 m) from general loading scenario and analysis with typical material properties and 4 axel loading. Scale of deformation exaggerated.

To generate the 3D behavior of the railway embankment, a linear-elastic model in ABAQUS was selected. The selection of this model allowed the validation of the results with studies by Stewart and Selig (1982) and permitted the modeling of variations in track elastic response. In order to perform 3D finite element analysis, the model was discretized into basic first-order (linear), 3D-stress tetrahedral-element mesh. The discretization chosen consisted of 121,194 4-node linear tetrahedron finite elements due to model geometry and complex meshing. The ABAQUS meshing verification tool was used to ensure that no elements were distorted. For model efficiency, mesh density was decreased with depth. Boundary conditions applied to the models included:

(i) Zero vertical displacement at the base of the subgrade layer, zero longitudinal displacement for the edges of the model orthogonal to the direction of the model-track geometry (i.e., subgrade, subballast, ballast, and rail tie and PSB when applicable), and zero lateral displacement of the edges parallel to the direction of the model-track geometry (i.e., subgrade).
(ii) Zero longitudinal and lateral displacements were applied to the rail model end, but vertical displacements and rotational degrees of freedom (DOF) were left unconstrained. Model-rails were rigidly connected to model-sleepers at single contact points to represent the fastening system. The rotational degrees of freedom are constrained between the two model parts to simulate the tied-constraint between rail and sleeper in the track superstructure.

Further details regarding boundary condition, finite element selection, finite element meshing, and material/layer interaction properties are covered in Appendix E.

6.3.1.2 Load Applications

The loads selected for application in the model were based on wheel loads and configurations identified in several studies. In the parametric study conducted by Selig and Waters (1994), the

GEOTRACK computer model was used for representing the conditions of the track segment tested at FAST track. In the model, four axels were used with wheel loads ranging from 22–146 kN and axel spacing from 1.49–1.98 m. In Kerr (2003), axel spacing within each bogie was 1.78 m. Spacing between bogies, for the inside axels, within a car was 10 m and 11 m in Selig and Waters (1994) and Kerr (2003), respectively. Spacing between bogies, for the outside axels, between two cars was 2.05 m in Kerr (2003). The distribution of loads chosen were modeled after the distance between axels in a bogy (1.778 m) and axel spacing based on distance between hopper cars (2.05 m).

In Selig and Waters (1994), the nominal case for representing a wood tie track involved no stress-dependent moduli for the substructure materials and a wheel load of 142 kN. The main responses studied were rail seat load, layer displacements, layer stresses at the surface of each layer, and the track modulus. In Indraratna et al. (2011), 142 kN wheel loads were assumed for the static loading case and 175 kN for dynamic loading based on a dynamic impact factor (DIF). Hardening soil and elasto-plastic material models were used in PLAXIS for modeling the permanent deformation over numerous loading repetitions. The developed model was two-dimensional and symmetric with one wheel load applied to the rail. The assumed geometric and material mechanical properties are included in Appendix G.

In Lichtberger (2005), the pressure distribution from the train wheel through the superstructure into the substructure was illustrated. The surface area over which the wheel load was distributed to the rail was shown as 3 cm^3. This surface area was used for applying the different wheel loads applied in the model developed in this study, the stress was recalculated based on the surface area in Lichtberger (2005) and the load to be applied. The purpose of this was for realistically modeling the load application to the rail into the superstructure; in addition, applying over a surface area prevents unrealistic strains in the rail that could adversely affect the model. In this study wheel loads were selected at 89, 142, and 175 kN.

6.3.1.3 Analytic Approach

From the strains generated in the field and a parametric study conducted using computer modeling of the states of stresses versus strains, Stewart and Selig (1982) proposed nominal values for the moduli of the substructure layers and typical wheel loads applied to the track (Table 6.3.1).

Table 6.3.1: Parameters Used in GEOTRACK Model and in This Study

Reference	(Stewart and Selig (1982)	(Stewart and Selig (1982)	This Study
Study	Parametric-Numerical	Representative-Numerical	Base Model-Finite Element
Program	GEOTRACK	GEOTRACK	ABAQUS
Rail E (MPa)	207,000	207,000	207,000
Rail I_z (m^4)	$0.395 \cdot 10^{-4}$	$0.395 \cdot 10^{-4}$	$0.132 \cdot 10^{-4}$
Sleeper E (MPa)	3,400–20,700	10,300 (wood)	10,300 (wood)
Sleeper Size (l, t, w) (m)	2.59 x - x 0.229	2.59 x - x 0.229	2.6 x 0.18 x 0.229
Sleeper I_z (m^4)	$1.07 \cdot 10^{-4}$	$1.07 \cdot 10^{-4}$	$1.11 \cdot 10^{-4}$
Sleeper s (m)	0.245–0.914	0.495	0.495
Ballast E (MPa)	173–689	310	290
Ballast v	0.1-0.49	0.3	0.3
Ballast t (m)	0.38-0.53	0.38	0.38
Subballast E (MPa)	31–126	N/A	100
Subballast v	0.4	0.4	0.4
Subballast t (m)	0.15 & 0	0.15	0.15
Subgrade E (MPa)	31–126	55	50
Subgrade v	0.4	0.4	0.4
Subgrade t (m)	> 0.91	> 0.91	6
Wheel Load (kN/#axels)	22–146 / 4-axel	142 / 4-axel	89-175 / 4-axel

Notes: v = Poisson's ratio, E = Young's Modulus, I_z = moment of inertia, s = spacing, t = thickness, w = width, l = length, * PSB Poisson's ratio (0.3) found experimentally, selected sleeper and rail Poisson's ratio (0.15) are from Indraratna (2011).

Material properties (e.g., rail modulus, ballast modulus, Poisson's Ratio, etc.) (Table 6.3.1) were held constant while the PSB modulus was varied (130, 290, and 400 MPa). Though PSB modulus in the lab was typically less than the modulus of the ballast, higher values were selected to understand the effects of having localized areas in the ballast layer that have lower

modulus as well as higher modulus than the surrounding ballast layer. In Stewart and Selig (1982) and this study, the strain in each layer was calculated as

$$\varepsilon_b = \frac{\delta_b}{d_b} \tag{6.3.1}$$

where ε_b is the strain in the ballast layer, δ_b is the maximum deflection in the model at the ballast/subballast layer interface (i.e., base of the ballast layer) subtracted from the maximum deflection at the tie/ballast interface (i.e., base of the tie), and d_b is the thickness of the ballast layer between the tie interface and subballast interface of the layer (0.38 m). Similar formulation for strain was used for the subballast and subgrade layers.

Stewart and Selig (1982) also calculated the track modulus, u, presented as

$$u = \frac{1}{4} \cdot \sqrt[3]{\left(\frac{P}{\delta}\right)^4 \cdot \frac{1}{E \cdot I}} \tag{6.3.2}$$

where P is the wheel load, δ is the deflection of the rail beneath the wheel load, and E·I are the Young's modulus and the moment of inertia of the rail.

6.3.1.4 Model Validation

The model developed and presented herein was validated using comparisons to the GEOTRACK model presented in Stewart and Selig (1982). The model geometry was adjusted to closely match the material properties, layer depths, and tie spacing used in Stewart and Selig (1982). In Selig and Waters (1994) the elastic response of the track model was relatively insensitive to variations in ballast type. Embankment slopes (i.e., ballast and subballast embankment slopes) were assumed and taken from Chapter 6 of the Army Corps of Engineers Railroad Design and Rehabilitation Technical Instructions. The rail cross-section dimensions were modified to simplify and economize model discretization and FEA computation while maintaining rail mechanical properties. The number of ties, width and depth of the subgrade

layer, and boundary conditions were found by experimentally adjusting the input parameters until yielding a track model that behaved well and showed minimal boundary condition effects.

The base model track was analyzed under various loads and strains measured in the ballast, subballast, and subgrade layer. In each comparison, the strains in each layer were slightly less than those measured and predicted in Stewart and Selig (1982). At lower loads the strain measured in the subballast and subgrade layers under predicted the strain measured and predicted in Stewart and Selig (1982); however, at higher loads the model track exhibited higher strains. Therefore, the model is more conservative at higher loads for the strain in the substructure layers (Figure 6.3.4).

In this study, the average track modulus, based on the formulation presented in Stewart and Selig (1982), was u = 35.3 MN/m/m. In Stewart and Selig (1982), the nominal track modulus was 33.8 MN/m/m and ranged from 15.5 to 39.5 MN/m/m. The range in track modulus was due to the variation in the parameters analyzed in their study, namely the fastener stiffness, ballast modulus, and tie spacing. In the developed track model there were marginal differences in track modulus. With wheel loads ranging from 22.3–175 kN, the track modulus ranged ± 0.32 kN/m/m. Variation in track modulus, as wheel loads varied, can be associated with the changing interaction of the entire track (i.e., interaction and behavior of the superstructure and substructure).

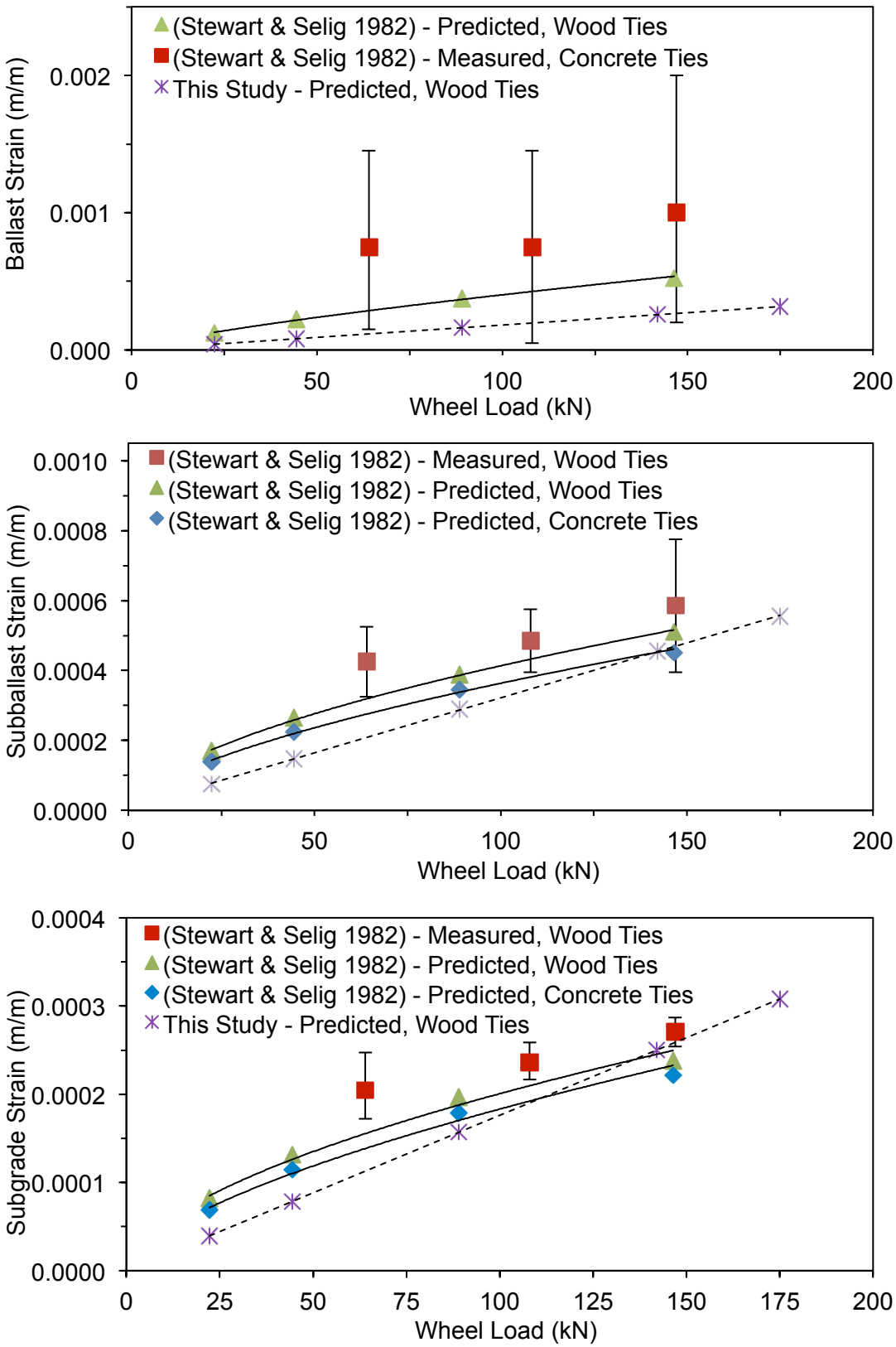

Figure 6.3.4: Modeled ballast (top), subballast (middle), and subgrade (bottom) strains

6.3.2 Parametric study for RPF percolation-injection (PSB Pile-layment)

The base model strains in the ballast, subballast, and subgrade layers were $2.48 \cdot 10^{-4}$, $4.39 \cdot 10^{-4}$, and $2.39 \cdot 10^{-4}$ (m/m), respectively (Figure 6.3.4). Based on PSB modulus values used in the model, strain in the ballast layer, ε_b, ranged from $1.58 \cdot 10^{-4}$–$3.34 \cdot 10^{-4}$ (m/m). The corresponding strain range in the subballast and subgrade layers was $2.80 \cdot 10^{-4}$–$5.98 \cdot 10^{-4}$ (m/m) and $1.56 \cdot 10^{-4}$–$3.13 \cdot 10^{-4}$ (m/m), respectively. Strain in the subballast layer was twice that of the strain in ballast and subgrade layers with almost twice the range of strain values. Consequently, the subballast layer is more susceptible to change in strain due to PSB formation in the ballast layer.

Since strains modeled in each layer had only minimal change due to PSB formation in the ballast layer, track modulus was calculated to understand elastic response of the entire track. Track surface deflection, δ calculated from the numerical model was used as input into Eq. 2 for determining track modulus. As PSB modulus ranged from 130 to 400 MPa, u ranged from 34.4 to 36.0 MN/m/m (± 2.3%) (Figure 6.3.5). The effect of track modulus due to PSB presence is compared to the effects of the parameters varied in Stewart and Selig (1982) from the nominal case (u = 33.8 MN/m/m), namely the fastener stiffness, ballast depth, and tie spacing are evaluated. The fastener stiffness contributed to the largest change in track modulus followed by ballast depth and tie spacing (Figure 6.3.6). Therefore, the PSB integration modeled was found to have an inconsequential effect on track elastic response compared to other key elements in the track.

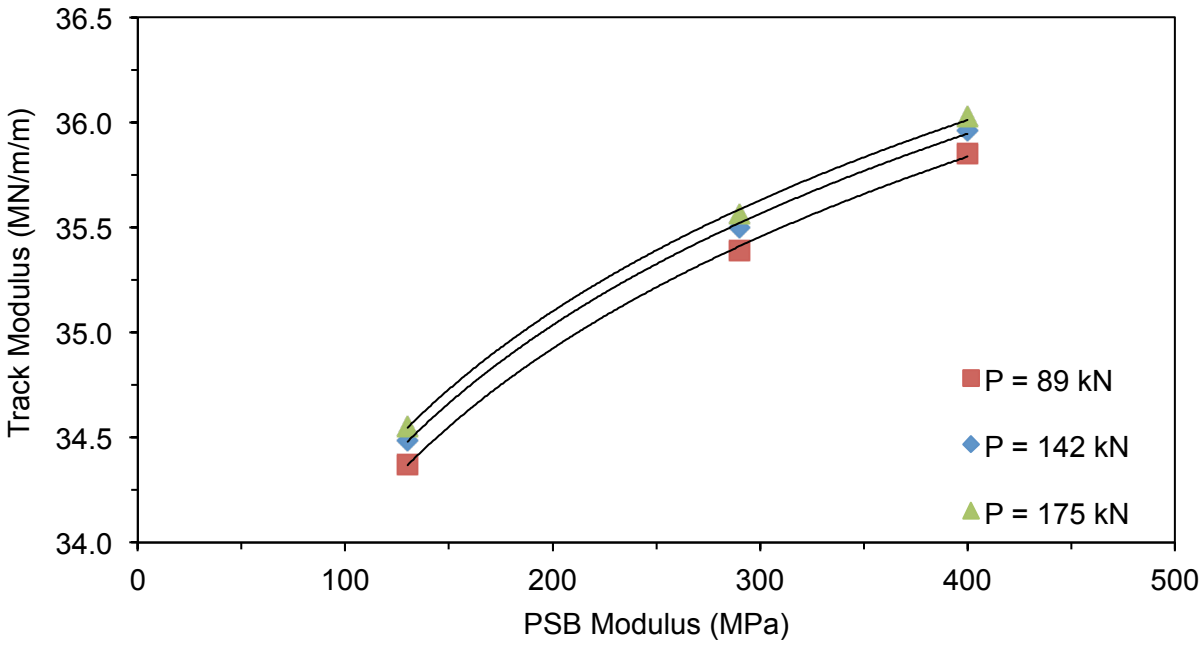

Figure 6.3.5: Measured track modulus vs. integrated PSB modulus, P = wheel load.

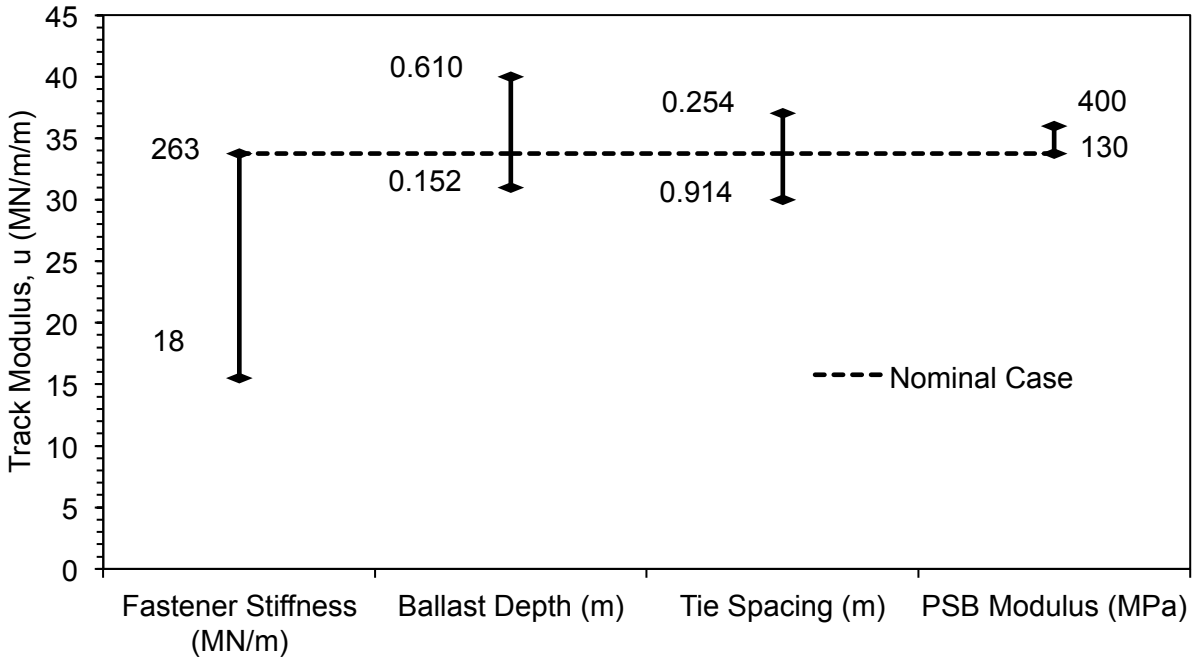

Figure 6.3.6: Calculated track modulus for the range of PSB modulus and track components modeled and field validated in Stewart and Selig (1982).

Given that a small change in track modulus occurs with the PSB integration, application of PSB into the ballast layer for enhancing track properties is considered a reliable approach. Other components that influence the track elastic response, such as substructure layer depths, superstructure and substructure material properties, and superstructure geometry (e.g., fastener stiffness), have a more significant effect. A larger range of PSB modulus, than observed in the laboratory, was also incorporated into the numerical model, which revealed that implementation of RPF stabilization would still have a negligible impact on the track modulus commonly used in track structural design.

The modeling conducted herein confirms that there would be very little difference in elastic strains in each of the substructure layers due to having localized areas of lesser modulus (PSB formation) in the ballast layer. In PSB experimental testing, PSB samples were found to have a lower elastic modulus than the host ballast that the RPF was injected into. However, PSB cylinders were tested using a cyclic triaxial method where minimal accumulation of plastic strain, ε_p, was observed over 200,000 loading repetitions at a representative state of stress (Ebrahimi 2011). Specimens tested up to 500,000 loading repetitions had a marginal increase in plastic strain. Over the first 200,000 loading repetitions, PSB plastic strain (ε_P=0.22%) was far less than clean ballast (ε_P=0.96%) or fouled ballast (ε_P=3%). In PSB specimens, the cumulative plastic strain under cyclic loading conditions was significantly reduced. Since PSB and RPF strengths are far greater than clean ballast compressive strength (at the representative confining stress), functionality of PSB in rail infrastructure would be driven by PSB compressive modulus where stabilized areas are formed using a percolation-injection method as described in Appendix A. This study shows that, for typical PSB moduli, the impact of PSB stabilization on track elastic response could be minimal.

7 CONCLUSIONS AND RECOMMENDATIONS

7.1 PSB MECHANICAL PROPERTIES, BEHAVIOR, AND APPROACH

After strategic injection of polyurethane into the ballast layer, areas that primarily absorb railway loads in the substructure (i.e., ballast beneath the bearing surface of the tie) are fortified and become monolithic; drainage of these areas becomes a secondary issue and particle rearrangement and settlement are averted. The pore space in compacted ballast conveniently allows injection of a rigid-polyurethane foam (RPF), allowing space for RPF expansion and for target RPF volumes and densities to be met. Large differences in mechanical behavior of clean ballast before and after polyurethane stabilization indicate that the introduction of RPF to ballast creates a geocomposite, referred to herein as polyurethane-stabilized ballast, with different and generally superior mechanical properties to that of clean ballast, recycled ballast, and fouled ballast.

Regarding deformational behavior of PSB in compression, PSB cylinders were tested using a cyclic triaxial method where minimal accumulation of plastic strain, ε_P, was observed over 200,000 loading repetitions at a representative state of stress (Ebrahimi 2011). Specimens tested up to 500,000 loading repetitions had a marginal increase in plastic strain. Over the first 200,000 loading repetitions, PSB plastic strain (ε_P=0.22%) was far less than clean ballast (ε_P=0.96%) or fouled ballast (ε_P=3%) with a fouling index of 5% and moisture content of 15%. When comparing to a PS-clean ballast (previously referred to as PSB) specimen, the PS–recycled ballast specimen had an accumulation of plastic strain, ε_P 0.62%, or 13% greater over 200,000 loading cycles. The PS–fouled ballast had ε_P of 0.29%, or 54% less than the PS-clean ballast had over 200,000 loading cycles. Track substructure materials (e.g., clean ballast, fouled ballast, recycled ballast, etc.) when stabilized with RPF have superior resistance to accumulation of plastic strain compared to untreated substructure materials and is thus an

applicable tool for maintaining track geometry and preventing ballast layer settlement. From evaluation of the elastic deformational behavior of PSB, the resilient modulus depended more on the ballast density within the PSB composite and resilient modulus of PSB was typically less than PSB. Since PSB samples had lower elastic modulus than the clean ballast, PSB elastic deformational behavior becomes a primary focus for PSB.

Results of flexural strength and fatigue tests clearly reveal that appreciable bonding and tensile capacity are present in PSB. Flexural strength of PSB (AVG 938 kPa) is similar to that of Cement-stabilized soils (AVG 1,030 kPa); however, flexural modulus of PSB (274 MPa) is much lower than cement-stabilized soils (AVG 13,800 MPa). This pattern between the two materials is similar when comparing PSB to other materials (i.e., clean ballast, concrete, asphalt, etc.); therefore, use care must be taken when designing use of PSB in applications where stiffness (i.e., functionality) controls design rather than overall strength (i.e., capacity).

Analytical and constitutive models were developed based on results of cyclic triaxial compression testing and flexural beam testing. From results obtained herein and models developed, PSB has a much longer life cycle compared to traditional track-substructure materials (i.e., ballast, subballast, and subgrade); therefore, use of PSB in track areas that undergo higher than anticipated loading can greatly increase track lifecycle and reduce maintenance requirements.

Because PSB has lower compressive modulus than clean ballast, numerical modeling was conducted and confirmed that there would be minimal difference in elastic strains of the substructure from PSB formation in the ballast layer. The functionality of PSB that is used in rail infrastructure would be driven by PSB compressive modulus. However, this study shows that, for typical PSB moduli, the impact could be minimal.

PSB is found to have suitable mechanical properties for use as a material in track-substructure. The ease of injections and negligible curing period for implementation of PSB makes it an attractive alternative for railway maintenance. In conclusion, PSB may find appropriate application for areas that cannot afford track shutdown or where traditional maintenance capabilities are impeded or unachievable.

7.2 PSB METHOD AND TRACK MAINTENANCE ALTERNATIVES

Having a stabilized layer of asphalt in the track substructure layer was investigated in Rose et al. (2003). As indicated in Rose and Lees (2008), the purpose of the asphalt underlayment is to reduce the stresses that are transmitted from the ballast layer to the subgrade layer and to serve as a barrier between the layers. For the asphalt layer, the strain at the bottom of the layer controls the life cycle of the layer (Rose and Konduri 2006). Using PSB for creating a stabilized trackbed layer would follow very similar principals as asphalt trackbed discussed in Section 5.2. PSB has much more elastic compliance (i.e., tolerance for elastic strain) than asphalt, which can be useful for application of a stabilized layer and designing corresponding layer thicknesses. In the case of asphalt trackbeds, the asphalt layer must be placed prior to ballast layer placement and superstructure construction. PSB application for trackbed stabilization is an *in situ* method that can be conducted on existing tracks. Therefore, PSB can serve as an economical alternative to create a stabilized layer for problematic areas where timely maintenance with limited interruption is critical.

Slab tracks made from concrete are commonly used in urban areas and in areas where there has been economic favorability for building a slab track while enduring capital and train delay costs. For areas where track replacement from a ballast track to a concrete slab track is not economically favorable, but certain areas see a high requirement for maintenance activities; stabilization with RPF may be a favorable alternative, as was determined using a non-expanding polyurethane in Thomson and Woodward (2004).

When considering the placement of a cement grout into ballast for stabilization, several adverse effects may occur; as discussed in Section 5.2, having a bound layer beneath the track above the subballast/subgrade layer can lead to high flexural stress and strain of that bound layer. Furthermore, the flexural stresses and strains of a grout-stabilized ballast layer have not

been well studied. A method that has involved use of cement grout in track stabilization was discussed in O'Kelly et al. (2008), where *in situ* cement piles were cast/formed on the side of the railway embankment for prevention of embankment slip. In Kouby et al. (2010), cement piles were also cast as *in* situ beneath the center of the track and ballast layer for prevention of ballast layer settlement. In each case, cement-grout for track stabilization was used as piles for supporting the track and cement-grout was not integrated with the ballast layer as has been done for the PSB method presented in this study. In the case of PSB, the magnitude of flexural strain that PSB is capable of encountering is far greater than the capability of asphalt used in a railroad trackbed, which is likely the case when comparing PSB to a cement-grout-stabilized ballast layer. PSB material, unlike cementitious grouts, cures immediately (reaching 90% of full compressive and tensile strength in 15 minutes) avoiding extended line closure; as it cures it does not shrink and continues to bond the ballast particles; and once cured has significant strength and durability for long-term effectiveness

When considering the difference in using rigid-polyurethane foam (expanding polymer) and non-expanding polymer, rigid-polyurethane foam has the capability of completely filling the void space thus preventing any effects of particle breakage and rearrangement. Furthermore, injection of polyurethane into the ballast layer in areas that primarily absorb railway loads in the substructure ensures the mechanical quality of these areas and allows drainage of these areas to become a secondary issue. The XiTrack™ (Thompson and Woodward 2004) method can take up to an hour for ideal mechanical properties and Elastotrack® (Boler 2012) was found to take up to 6 hours for ideal mechanical properties and required premixing for implementation. Though use of an non-expanding polyurethane has been found to greatly improve track-substructure mechanical properties, an option involving RPF has been thoroughly investigated in this study and may be preferred in emergency maintenance operations and where well studied mechanical properties can be targeted.

A concrete slab track, asphalt underlayment, grout stabilized layer, or non-expanding polyurethane treated ballast may only be favorable if traffic delay and the maintenance activity is economically feasible. Unlike the case of a concrete slab track, which is typically accompanied with larger capital and delay costs, and with cement-stabilization of soils; application of PSB formation is an *in situ* stabilization method that does not require premixing with aggregates or soil (with water), would not require track shutdown, and reaches 90% full strength in 15 minutes after application.

8 FUTURE WORK

8.1 CONFIRM POLYURETHANE SELECTION FOR STRATEGIC STABILIZATION

Based on the methods developed in this thesis, further research involving use of different varieties of polyurethane is recommended. A scenario includes using a low expansion RPF (i.e., less blowing agent) for percolation-injection method where increased compliance should be limited and stiffness preserved, plastic deformation arrested, and strength enhanced. Another scenario would include using a high expansion RPF (i.e., more blowing agent) for subsurface-injection method where increased compliance is preferred depending on layer depth, barrier between ballast and subballast applied, plastic deformation arrested, and wider distribution of load to the subballast employed.

8.2 FURTHER POLYURETHANE-STABILIZED BALLAST RESEARCH

In this study, a thorough investigation was conducted identifying the mechanical properties of RPF injections with clean ballast. The average (AVG) PSB compressive strength (2,607 kPa) was 77% greater than ballast compressive strength (594 kPa), at 100 kPa confining pressure. After RPF injections into ballast, resulting flexural properties, which do not exist in regular ballast, were significant for fostering PSB design capabilities. When comparing the flexural strength of PSB to cement-stabilized materials (CSM), PSB has a flexural strength (AVG 938 kPa) similar to that of 3% and 4% CSM flexural strength (AVG 1,010 and 1,130 kPa, respectively) tested at 28-day curing time in Midgley & Yeo (2008). However, unlike cement-stabilization of soil, PSB is an *in situ* method that does not require premixing with aggregates or soil (with water), would not require track shutdown, and reaches 90% full strength in 15 minutes after application

Fouled ballast and recycled ballast were also injected, finding that RPF injections were still applicable for those materials. The fouled ballast that was injected had a fouling index and moisture content that is considered to be highly fouled; therefore, fouled ballast with lower fouling index will also be an applicable material for RPF injection. The mechanical properties of polyurethane-stabilized (PS) fouled and recycled ballast were far greater than untreated clean, recycled, and fouled ballast and similar to that of polyurethane-stabilized clean ballast (Figure 8.2.1). In terms of elastic modulus, interestingly enough PS-fouled ballast had a higher modulus than PS-clean ballast.

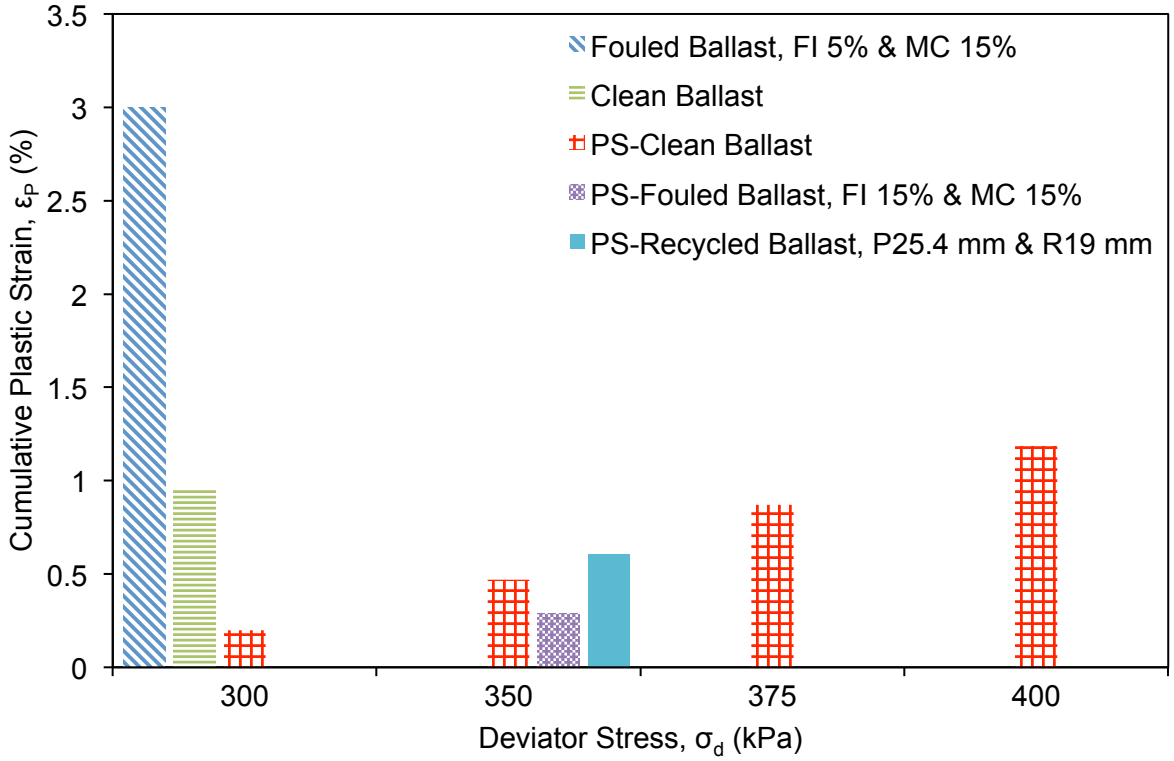

Figure 8.2.1: Comparison of cumulative plastic strain over 200,000 loading repetitions for untreated clean and fouled ballast with polyurethane-stabilized clean ballast, recycled ballast, and fouled ballast.

The focus of future research would be to explore the performance of already fouled ballast with various types of fouling materials (e.g., coal, clay, mineral), quantity, and moisture condition when injected with polyurethane. Recommended specimen fabrications can include injection of RPF into fouled ballast with varying fouling indices (FI) and moisture contents (MC) (i.e., FI=5,10,20,25; MC=0,5,15 per fouled ballast testing in Ebrahimi (2011)). Injection of fouled ballast is the more likely scenario in remediation of ballast/track degradation.

The recommended research involves laboratory specimen tests to determine the relevant mechanical of the materials involved, i.e., unbound ballast and polyurethane-stabilized ballast with varying fouling and water contents. The mechanical property tests are aimed at determining modulus and strength of these materials. The recommended testing program has multiple objectives: (i) understand the rheological properties of polyurethane injected into ballast with varying compositions for distinguishing the mechanism that governs: what subsurface conditions are treatable, the extent treatment will accomplish, and the type of PSB that will be materialized; (ii) to develop modulus and strength parameters for numerical analyses as a function of varying material compositions (i.e., specific fouling levels and moisture contents); and (iii) to determine service life for a typical ballast with or without polyurethane stabilization. Flexural beam fabrication and testing can be considered based on observations of the rheological properties of polyurethane injected into ballast with varying compositions.

8.3 CONSTITUTIVE AND NUMERICAL ANALYSIS FOR RAIL INFRASTRUCTURE

8.3.1 Constitutive and Finite Element Modeling Background

Several studies included the development of constitutive models for the deformational behavior of ballast under typical railway loading conditions. In Indraratna et al. (2011), case studies were developed involving field data and FEM with PLAXIS. They developed an elasto-plastic constitutive model that incorporates the typical components of a railway segment; i.e., rail, sleeper, ballast layer, subballast layer, and subgrade layer. In the FEM, material model parameters adopted from experimental data were selected for each of the substructure and superstructure components. In their FEA, the superstructure components (i.e., rail and concrete sleeper) were modeled as linear elastic. For the substructure components, determined from static loading data, a hardening soil model was used for the ballast layer and a Mohr-Coulomb model was chosen for the subballast and subgrade layers. The outcome of the FEM was compared to a field trial near the city of Wollongong in Australia. They determined that the constitutive model in PLAXIS revealed some deviation from the field data, which was attributed to not incorporating the real cyclic nature of loading on the track. Furthermore, the effects of dynamic loading were represented by using a dynamic impact factor, which only approximately represents the effects of cyclic loading.

Salim (2004) conducted an investigation to determine the physical mechanisms that contribute to the deformational behavior of ballast. A constitutive model was developed in Salim (2004) for modeling the deformational behavior of railway ballast and for representing the effects of cyclic loading. Another constitutive model was developed using Abaqus to model the deformational behavior of ballast. Each of the models was compared to laboratory tests (i.e., triaxial compression) conducted on ballast specimens. In the laboratory tests, monotonic triaxial compression tests were conducted at varying confining stresses. During the triaxial tests, the

volumetric strain in the specimen, the change in friction angle with varying confining stress, and the amount of particle breakage was measured. The model takes into account effects of volumetric strain, changes in friction angle due to particle breakage, and states of stress so that ballast deformation due to static loading can be reasonably predicted. From the empirical data, an incremental constitutive model was created., which successfully predicted the deformational behavior of ballast, ballast breakage, and volumetric strain that occurred in the monotonic triaxial compression tests. The model used in Abaqus was the Drucker-Prager model, which modeled similar results to the ballast behavior in the triaxial compression tests, but was not similar for the volumetric stain. In Salim (2004), the model was a better predictor of the deformational behavior of the ballast in the triaxial compression tests compared with the Drucker-Prager model in Abaqus.

Salim (2004) further developed the incremental constitutive model from the empirical data of laboratory cyclic triaxial tests. This model was also found to have a strong prediction of the deformational behavior of the ballast under cyclic loading. The model in Salim (2004) was based on similar methodology that was used in Niumenus (2005) where constitutive models were developed for predicting the deformational behavior of materials (i.e., sand) in response to cyclic loading. In Niumenus (2005), a constitutive model was developed for modeling the accumulation of plastic strain in sand due to cyclic loading. In the study, similar constitutive equations and relationships were developed as in Salim (2004), such as deformational response to states of stress and corresponding volumetric strain; however, in Niumenus (2005), a factor that related to the history of loading (i.e., number of loading repetitions) was incorporated. Based on conditions that were predicted by the aforementioned variables, a model developed in future work could predict the rate of plastic strain and the amount of incremental plastic strain during each loading cycle as was done in Ebrahimi (2011), but to be applied using a 3-dimensional finite element analysis.

Finite element modeling of the deformational behavior in response to cyclic loading was done by incorporating a user subroutine into Abaqus called “UMAT.” The “UMAT” subroutine is similar to other material models in Abaqus, except that it can be redefined by a user to define the behavior of particular materials. Niumenus (2005) developed constitutive equations for predicting material response to cyclic loading and configured a “UMAT” in the model to predict accumulation of permanent deformation in sand under cyclic loading. The developed model was compared to and found to correlate well with experimental data, validating the use of Abaqus and the “UMAT” subroutine for modeling material behavior to cyclic loading is thus a viable approach.

In Abaqus documentation, typical material models and corresponding constitutive equations for “UMAT” are provided. The fundamental construction of “UMAT” and the constitutive equations have similar framework to models developed in Salim (2004). Therefore, use of a “UMAT” in Abaqus are likely to have a more accurate numerical prediction of ballast deformational behavior than other predefined Abaqus material models.

In Ebrahimi and Keene (2011), a mechanistic-based maintenance model was developed from large-scale cyclic triaxial (LSCT) test data on clean and fouled ballast specimens. Similar to Niumenus (2005) and Salim (2004), this model involved empirical equations of deformational behavior in response to states of stress and loading history. However, in Ebrahimi and Keene (2011), additional constitutive parameters were defined based on ballast fouling conditions and moisture content. The model developed in the study predicts track deformational response based on input conditions entered into the model. Equations from previous studies were adopted from Chrismer and Selig (1994) and Li and Selig (1994) to determine subgrade deformational response and track surface deviation. The mechanistic-based maintenance model in Ebrahimi and Keene (2011) was validated by full-scale model tests in Ebrahimi (2011).

Further development of constitutive and finite element models (FEM) of polyurethane stabilization can be used to determine long-term deformation of the track with focus on the ballast layer, hence creation of a deformation model for a stabilized track substructure. The elastic and plastic deformational properties and analytical models presented herein can be incorporated into the model and the deformation of each material and track-substructure layer can be evaluated. The purpose of the deformation model would be to compliment laboratory tests and validate field methods for injecting RPF into the ballast layer.

8.3.2 Full-Scale Modeling Background

A common approach for validation of laboratory experimental testing and computer modeling involves validating information in a scaled prototype or full-scale laboratory modeled experiment. Aursudkij et al. (2009) simulated railway traffic loading at a railway test facility (RTF) where a full-scale model was developed and consisted of three ties with ballast and subballast layers. The experiment was setup to model full-scale track response and compare ballast deformational behavior in the RTF to large-scale cyclic triaxial (LSCT) testing. In the LSCT test, different states of stress were applied and permanent strain under cyclic loading measured. From the LSCT tests, a representative state of stress was determined where the vertical permanent strains in both tests were similar. The LSCT also involved determining the change in resilient modulus, change in Poisson's ratio, and volumetric strain. This method proved a reasonable approach for calibrating LSCT tests with full-scale model experiments for determining representative states of stress and material behavior under repetitive loading.

Kennedy et al. (2009) led a study where a full-scale model test was assembled and tested to determine the deformational characteristics of the ballast layer with and without polyurethane (non-expanding) reinforcement. The full-scale model consisted of a superstructure system of several rails and ties and substructure layer with a subgrade and a ballast layer. The

polyurethane supplied was XiTrack^{TM}. In their investigation, the accumulation of plastic strain in the full-scale model over 500,000 loading repetitions was measured. The tests were conducted in the GRAFT facility, where loading repetitions applied to the full-scale model simulate railway traffic loading conditions on the substructure. Kennedy et al. (2009) found that settlement of the ballast layer in the model was 95-98% less for the treated substructure than untreated substructure modeled at their facility as well as other tests on untreated substructure at other test facilities.

In Ebrahimi (2011), a full-size track model experiment (FSTME) was used to validate the representative state of stress conditions used in LSCT testing of ballast. The FSTME used in the study was a full-size prototype for rail substructure with a cross-sectional dimension that represented half of the track width due to symmetry. The width was equal to typical tie spacing in a railway track of 0.6 m. The model consisted of subgrade, subballast, and ballast substructure layers with a rail tie through which cyclic loading was applied.

Use of a full-scale model may be a beneficial approach for confirming the mechanical properties and numerical modeling conducted in this thesis. A full-scale model would involve injection of RPF using one of the methods developed herein and cyclic loading used in the model can confirm long-term elastic and plastic deformational behavior of a ballast layer stabilized with RPF.

8.4 FIELD IMPLEMENTATION AND EVALUATION

Recommended field implementation and evaluation would involve use of PSB in test track or real track equipped with pressure plates and strain gauges to measure stresses and strains in substructure layers, depending on injection method used (e.g., percolation-injection or subsurface-injection). Use in the field would involve calibrating the injection procedures developed herein and confirming the enhanced mechanical response and life cycle of the track resulting from the RPF-stabilized ballast layer. PSB can be used in a real track while changes in maintenance inspection outcomes and scheduled maintenance intervals, depending on injection method used (e.g., percolation-injection or subsurface-injection) are evaluated.

8.5 FIELD EVALUATION AND MONITORING

Further methods are being developed at the University of Wisconsin-Madison using Time-Domain Reflectrometry (TDR), Ground-Penetrating Radar (GPR), and fiber optics. These methods can be used for identifying ballast fouling characteristics and contents (i.e., extent of fouling and moisture) and for corroboration of substructure properties with strain occurring in the rail (i.e., track deformational behavior). These methods can also be used for determining ballast layer composition for targeting RPF injection quantities and outcomes using the phase relationships and injection methods developed herein.

REFERENCES

Adhikari, S. & You, Z. (2010). "Fatigue Evaluation of Asphalt Pavement Using Beam Fatigue Apparatus." *Electronic Journal for Engineering Technology*: *Technology Interface Journal*, 10(3).

Aggregain. (2003). “Use of recycled ballast as fill to embankment on a railway.” *Aggregates Case Study*.

Ahlf, R.E. (2007). Railway Track Systems: Engineering and Design, Unpublished.

Akçaoğlu, T., Mustafa, T., & Çelik, T. (2003). "Effect of Course Aggregate Size and Matrix Quality on ITZ and Failure Behaviour of Concrete Under Uniaxial Compression." *Cement & Concrete Composites*, 26, 633–638. Elsevier Ltd.

Anderson, P., Cunningham C. J., & Barry, D. A. (2002). “Efficiency and potential environmental impacts of different cleaning agents used on contaminated railway ballast.” *Land Contamination & Reclamation* (10), 71–77.

Anderson, W.F. & Fair, P. (2008). “Behavior of Railroad Ballast under Monotonic and Cyclic Loading.” *Journal of Geotechnical and Geoenvironmental Engineering*, ASCE, 134(3), 316–328.

Arellano, D. & Thompson, M.R. (1998). *Stabilized Base Properties (Strength, Modus, Fatigue) for Mechanistic-Based Airport Pavement Design*. University of Illinois at Urbana-Champaign, Department of Civil Engineering. Urbana: Federal Aviation Administration Report, DOT 95-C-001.

Arnold, G. (2009). "Reducing the risk of pavement failure and utilisation of local materials in New Zealand through Repeated Load Triaxial and Beam Fatigue Tests." *AAPA Thirteenth International Flexible Pavements Conference*, Gold Coast, Queensland, Australia, October 11-13, 2009.

Aursudkij, A. (2007). "A Laboratoryh Study of Railway Ballast Behaviour under Traffic Loading and Temmping Maintenance." *PhD Thesis*, University of Nottingham.

Aursudkij, A., McDowell, G.R., Collop, A.C. (2009). “Cyclic Loading of Railway Ballast Under Triaxial Conditions and In A Railway Test Facility.” *Granular Matter*, (11), 391–401.

Avellaneda, D.C. (2010) “Inverted Base Pavement Structures.” *PhD thesis*, Department of Civil, and Environmental Engineering, Geogia Institute of Technology, 2010.

Banimahd, M. & Woodward, P.K. (2007). "3-Dimensional Finite Element Modelling of Railway Transitions." *Proceedings of 9th International Conference on Railway Engineering*, June 2007, London.

Barnes, C. (2008). *Structural Evaluation of the Point Michaud Road Pavement Rehabilitation Using Full-Depth Reclamation with Portland Cement*. Dalhousie University, Halifax, Nova Scotia. Intelligent Structures and Innovative Materials Group.

Bayer Material Science (2010). *486STAR Polyurethane Foam Grout*. Technical Data Sheet, Spring, Texas.

Becker, R. and Patrick, V. (2005). “Integral Ballast Recycling to Sustainable Development.” *Railway Gazette International*, 161(1), 44–46.

Bishop, A.W. & Green, G.E. (1965). “The Influence of End Restraint on the Compression Strength of a Cohesionless Soil.” *Geotechnique*, (15), 243–266.

Boler, H. (2012). "On the Shear Strength of Polyurethane Coated Railroad Ballast." *MS Thesis*, Department of Civil and Environmental Engineering, University of Illinois at Urbana-Champagne.

Bozyurt, O. (2011). "Behavior of Asphalt Pavement and Recycled Concrete Aggregate as Unbound Road Base." *MS thesis*, Department of Civil and Environmental Engineering, University of Wisconsin-Madison.

Brinson, H. & Brinson, C. (2008). *Polymer Engineering Science and Viscoelasticity: An Introduction*. Springer Science+Business Media, LLC., New York, NY.

Buzzi, O., Fityus, S., & Sloan, S. (2010). "Use of Expanding Polyurethane Resin to Remediate Expansive Soil Formations." *Canadian Geotechnical Journal*, 47, 623–634.

Buzzi, O., Fityus, S., Sasaki, Y., & Sloan, S. (2008). "Structure and Properties of Expanding Polyurethane Foam in The Context of Foundation Remediation In Expansive Soil." *Mechanics of Materials*, 40, 1012–1021.

Carteret, R., Jameson, G., & Jones, A. (2009). *Asphalt Fatigue Endurance Limit*. Austroads Publication No. AP-T131/09. Austroads Ltd. Sydney, Australia

Chrismer, S. & Davis, D. (2000). "Cost Comparisons of Remedial Methods to Correct Track Substructure Instability." *Transportation Research Record*, 1713 (00-019), 10-15.

Chrismer, S.M. & Selig, E.T. (1994). *Mechanics-Based Model to Predict Ballast-Related Maintenance Timing and Costs*, Association of American Railroads, Report No. R-863, AAR-Technical Center, Chicago, Illinois, USA

Claypool, A. (2004). “Covering the Spread.” *Progressive Railroading: The Information Leader For The Railroad Industry*, (47), 46–49.

Connel Hatch. (2008). “Coal loss literature review coal loss management report Queensland Rail.” *Connel Hatch Infrastructure for Industry*.

Dersch, M.S., Tutumluer, E., Peeler, C.T., & Bower, D.K. (2010). "Polyurethane Coating of Railroad Ballast Aggregate for Improved Performance." *Proceedings of the Joint Rail Conference*, April 27-29, 2010, Urbana, IL, USA.

Ebrahimi, A. (2011). “Deformational Behavior of Fouled Railway Ballast.” *PhD thesis*, Department of Civil and Environmental Engineering, University of Wisconsin, Madison.

Ebrahimi, A. & Keene, A.K. (2011). "Maintenance Planning of Railway Ballast." *AREMA 2011 Annual Conference*, Minneapolis, Minnesota, September 18-22.

Erdemgil, M., Sağlam, S., & Bakır, B.S. (2007). “Utilization of highly expansive polymer injection to mitigate seismic foundation for existing structures.” *8th Pacific Conference on Earthquake Eng.*, December 5-7, 2007, Singapore.

Freitas, S.T., Kolstein, H., & Bijlaard, F. (2010). "Parametric Study of the Interface Layer Renovation for Orthotropic Steel Bridge Decks." *Computer-Aided Civil and Infrastructure Engineering*, 27, 143–153.

Giannakos, K. (2010). "Loads on Track, Ballast Fouling, and Life Cycle under Dynamic Loading in Railways." *Journal of Transportation Engineering, ASCE*, 136(12), 1075–1084.

Gibson, L.J. (1989). "Modelling the Mechanical Behavior of Cellular Materials." *Material Science and Engineering*, A110, 1–36.

Grider, A., Ramirez, J.A., and Yun, Y.M. (1999). *Structural Concrete Design – Structural Engineering Handbook*, Ed. Chen Wai-Fah, Ch. 4., CRC Press LLC, Boca Raton, FL.

Gupta, R.K. (2000). *Ploymer and Composite Rheology: Second Edition, Revised and Expanded*. Marcel Dekker, Inc., New York, NY.

Harvey, J.T., Deacon, J.A., Tsai, B.W., & Monismith, M.L. (1996). *Fatigue Performance of Asphalt Concrete Mixes and Its Relationship to Asphalt Pavement Performance In California*. Asphalt Research Program: CAL/APT Program, Institute of Transportation Studies, University of California at Berkeley, Berkeley, California, Report No. RTA-65W485-2.

Huang, H., Shen, S., & Tutumluer, E. (2009). "Sandwich Model to Evaluate Railroad Asphalt Trackbed Performance Under Moving Loads." *Transportation Research Record*, No. 2117, 57–65.

Huang, Y.H. (2004). *Pavement Analysis and Design – Second Addition*. Pearson Prentice Hall, Upper Saddle River, New Jersey.

Huang, Y.H., Rose, J.G., & Khoury, C.J. (1987) “Thickness Design for Hot-Mix Asphalt Railroad Trackbeds.” *Association of Asphalt Paving Technologists*, 54, 427–453.

Indraratna, B., Salim, W., & Rujikiatkamjorn, C. (2011). *Advanced Rail Geotechnology – Ballasted Track*, CRC Press, Taylor & Francis Group, London, UK.

Jaeger, J.C. (1967). "Failure of Rocks Under Tensile Conditions." *International Journal of Rock Mineral Science*, 4, 219–227.

Kalinski, M.E. & Thummaluru, M.S.R. (2011). “A New Free-Free Resonant Column Device for Measurement of Gmax and Dmin at Higher Confining Stresses” *ASTM Geotechnical Testing Journal*, Vol. 28, No. 2.

Kennedy, J.H., Woodward, P.K., Medero, G., & McKinney, J. (2009). “Full-Scale Cyclic Geopavement & Railway Accelerated Fatigue Testing.” *International Conference on Railway Engineering*, London, 2009.

Kerr, A.D. (2003). *Fundamentals of Railway Track Engineering*. Simmons-Boardman Books, Inc., Omaha, Nebraska.

Koskinen, M. (2005). " Modeling of Soil-Structure Interaction Between Railway Bridge and Soil." 2005 *Abaqus Users' Conference*, VR_Track Ltd., Finland.

Kouby, A.L., Bourgeois, E., & Lacoste, F.R. (2010). “Subgrade Improvement Method for Existing Railway Lines – an Experimental and Numerical Study.” *The Electronic Journal of Geotechnical Engineering*, 15(E), 461–494.

Krumbein, W.C. (1941). “Measurement and Geological Significance of Shape and Roundness of Sedimentary Particles.” *Journal of Sedimentary Petrology*, 11(2), 64–72.

Kumar, V., VanderWel, M., Weller, J., & Seeler, K.A. (1994). “Experimental Characterization of the Tensile Behavior of Microcellular Polycarbonate Foams.” *Journal of Engineering Materials and Technology*. 116, 439–445.

Kuncir, E.J., Roy, W.W., & Golbranson, F.L. (1990). "Load-Bearing Characteristics of Polyurethane Foam: An Examination of Structural and Compression Properties." *Journal of Rehabilitation Research and Development*, 27(3), 229–238.

Li, D. & Selig, E.T. (1994). "Cumulative Plastic Deformation for Fine-Grained Subgrade Soils." *Journal of Geotechnical Engineering*, *ASCE*, 122(12), 1006-1014.

Li, D., Rose, J., & LoPresti, J. (2001). *Test of Hot-Mix Asphalt Trackbed Over Soft Subgrade Under Heavy Axel Loads*. University of Kentucky at Lexington., TTCI, Technology Digest, Timely Technology Transfer 01–009.

Li, D., Yoshino, D., & Tunna, J. (2004). "RTML for track asset management." *Railway Track and Structures*, RT & S, 100, 15–17.

Lichtberger, B. (2005). *Track Compendium – Formation, Permanent Way, Maintenance, Economics*. Eurail Press, Hamburg, Germany.

Lim, W.L. (2004). "Mechanics of Railway Ballast Behavior." *PhD Thesis*, University of Nottingham, UK.

Litwinowicz, A. & Brandon, A.N. (1994). "Dynamic Flexural Testing for Prediction of Cement-Treated Pavement Life." *17th ARRB Conference, Gold Coast, Queensland*, August 15-19, 1994, 17(2), 229–247.

Mamlouk, M.S. and Zaniewski, J.P. (2006). *Materials for Civil and Construction Engineers*. Pearson Prentice Hall, Upper Saddle River, New Jersey.

Marsavina, L., Sadowski, T., Constantinescu, D.M., & Negru, R. (2008). "Failure of Polyurethane Foams Under Different Loading Conditions." *Advances in Fracture and Damage Mechanics VII*, 385, 205–208.

Martins, A., Waldmann, & Massarani, G. (2010). "Resistive Forces Quantification In Polymeric Solutions In Porous Media." *Journal of Porous Media*. 13(5), 409–422.

Midgley, L. & Yeo, R. (2008). *The Development and Evaluation of Protocols for the Laboratory Characterisation of Cemented Materials.* Austroads Publication No. AP–T101/08. Austroads Ltd. Sydney, Australia.

Mitiani, T. & Hamada, H. (2003). "Prediction of Flow Patterns in the Polyurethane Foaming Process by Numerical Simulation Considering Foam Expansion." *Polymer Engineering and Science*, 43(9), 1603–1612.

Monaghan, W. D. & Trevitis, M.A. (2004). *Application of Ground Penetrating Radar to Evaluate the Extent of Plolyurethane Grout Infiltration For Mine Roof Control: A Case Study*. National Institute for Occupational Safety and Health, Pittsburg, PA.

Moosazedh, J., & Witczak, M.W. (1981) "Prediction of subgrade moduli for soil that exhibits nonlinear behavior." *Transportation Research Record*, No. 810, 9–17.

Natioanl Asphlt Pavement Association, NAPA. (2012). < http://www.asphaltpavement.org> (Dec. 22, 2011).

Neilsen, M.K., Krieg, R.D., & Schreyer, H.L. (1995). "Constitutive Theory for Rigid Polyurethane Foam." *Polymer Engineering and Science*, 35(5), 387–394.

Niemunis, A., Wichtmann, T., & Triantafyllidis, T. (2005). "A High-Cycle Accumulation Model for Sand." *Computers and Geotechnics*, 32(4), 245–263.

O'Kelly, B.C., Ward, P.N., & Raybould, M.J. (2008). "Stabilization of a Progressive Railway Embankment Slip." *Geomechanics and Geoengineering: An International Journal*, 3(4), 231–244.

Oertel, G. (1985). *Polyurethane Handbook*. Hanser Publishers, Munich, Germany.

Otero, J., Martinez, J., Santos, M.A., & Cardona. S. (2011). "A Mathematical Model to Study Track Dynamics for the Prediction of Vibration Levels Generated by Rail Vehicles." *Journal of Railand Rapid Transit*, 255(F), 1–10.

Otte, E. (1979). "Structural Design Procedure for Cement-Treated Layers in Pavements." *PhD thesis*, Faculty of Engineering, University of Pretoria, Pretoria, South Africa.

Palley, J. (2012). *Freight Railroads Background*. Office of Rail Policy and Development, Federal Railway Administration.

Perry, C. & Gilliott, J.E. (1977). "The Influence of Mortar-Aggregate Bond Strength on The Behaviour of Concrete in Uniaxial Compression." *Cement and Concrete Research: Pergamon Press, Inc.* Elmsford, NY, 7, 553–564.

Phillips, P.J. & Waterman, N.R. (1974). "The Mechanical Properties of High-Density Rigid Polyurethane Foams in Compression: I. Modulus." *Polymer Engineering and Science*, 14(1), 67–71.

Pucci, M.J. (2010). “Development of a Multi-Measurement Confined Free-Free Resonant Column Device and Initial Studies.” *MS thesis*, Department of Civil, Arcitectural and Environmental Engineering, University of Texas, Austin.

Randall, D. & Lee, S. (2002). *The Polyurethanes Book*. John Wiley and Sons LTD., West Sussex, England.

Romanoschi, S.A., Nicoleta, N.I., & Octavian, D. (2006). *Resilient Modulus and the Fatigue Properties of Kansas Hot Mix Asphalt Mixes*. Kansas DOT, Kansas State University, The University of Kansas, Report No. K-TRAN: KSU-02-6.

Rose, J.G. & Konduri, K.G. (2006). "KENTRACK–A Railway Trackbed Structural Design Program." *AREMA 2006 Annual Conference*, Louisville, Kentucky, September 17-20.

Rose, J.G. Telxeira, P.F. & Ridgway, N.E. (2010). "Utilization of Asphlat/Bituminous Layers and Coatings in Railway Trackbeds – A Compendium of International Applications." *Proceedings of the 2010 Joint Rail Conference*, April 27-29, Urbana, Illinois, 1, 239–255.

Rose, R.G. & Lees, H.M. (2008). "Long-Term Assessment of Asphalt Trackbed Component Materials' Properties and Performance." *AREMA 2008 Annual Conference*, Salt Lake City, Utah, September.

Rose, R.G., Su, B., & Long, W.B. (2006). "KENTRACK: A Railway Trackbed Structural Design and Analysis Program." *AREMA 2006 Annual Conference*, Louisville, Kentucky, September 17-20.

Rudolf, B. & Vierlinger, P. (2005). “Integral ballast recycling contributes to sustainable development.” *Railway Gazette International*, 161, 44–46.

Salim, W.M. (2004). "Deformation and Degradation Aspects of Ballast and Constitutive Modelling Under Cyclic Loading." *PhD thesis*, School of Civil, Mining, and Environmental Engineering, University of Wollongong.

Schuettpelz, C.C., Fratta, D., & Edil,T.B. (2010). “Mechanistic method for determining the resilient modulus of base course materials based on elastic wave measurements.” *Journal of Geotechnical and Geoenvironmental Engineering*. 136(8), 1086–1094.

Selig, E.T. & Waters, J.M. (1994). *Track Geotechnology and Substructure Management*. Thomas Telford, New York, NY.

Shukla, S. K. (2002). *Geosythetics and their applications*. Reston, VA: Thomas Telford

Sivertsen, K. (2007). "Polymer Foams – Polymer Physics." *Massachusetts Institute of Technology*.

Skoglund, K.A. (2002). “A study of some factors in mechanistic railway track design.” *PhD thesis*, Norwegian University of Science and Technology.

Stagl, J. (2009). “The rock to railroads' roll.” *Progressive Railroading: The Information Leader For The Railroad Industry*, 52, 38-45.

Stefani, A. M. (2003). *Report of review of slow orders and track reclassification Federal Railroad Administration*. US Department of Transportation Office of the Secretary of Transportation, MH-2004-007, Washington DC.

Stewart, H.E. & Selig, E.T. (1982). “Predicted and Measured Resilient Response of Track.” *Journal of the Geotechnical Engineering Division, ASCE*, 108(GT11), 1423–1442.

Szycher, M. (1999). *Szycher’s Handbook of Polyurethanes*. CRC Press, Boca Raton, FL.

Talbot, A.N. (1980). *Stresses in Railroad Track - The Talbot Reports*, American Railway Engineering Association.

Thomson, D.,R. and Woodward, P.,K. (2004). “Track Stiffness Management Using the XiTrack Geocomposite.” *Journal of the Permanent Way Institution*, 122(3), 1–12.

Tia, M. (2003). *Bituminous Materials and Mixtures Civil Engineering Handbook, Second Edition.* CRC Press, Inc., Boca Raton, Florida, 45.1-45.36.

Toros, U. & Hiltunen., D.R. (2008). “Effects of Moisture and Time on Stiffness of Unbound Aggregate Base Course Materials.” *Transportation Research Record*, No. 2059, Washington, D.C., 41–51.

Traeger, R.K. (1967). "Physical Properties of Rigid Polyurethane Foams." *Journal of Cellular Plastics*, 3(9), 405–418.

Triantafillou, T.C., Zhang, J., Shercliff, T.L., Gibson, L.J., & Ashby, M.F. (1989). "Failure Surfaces for Cellular Materials Under Multiaxial Loads–II. Comparison of Models with Experiment." *International Journal of Mechanical Sciences*, 31(9), 665–678.

Tu, Z.H., Shim, V.P.W., & Lim, C.T. (2001). "Plastic Deformation Modes in Rigid Polyurethane Foam Under Static Loading." International Journal of Solids and Structures, 38, 9267–9279.

Wisconsin & Southern Railroad. (2002). Satisfying customers needs through continuous improvements. Wisconsin & Southern Railroad.

Woodward, P.K., Thomson, D., & Bahimahd, M. (2007). "Geocompostie Technology: Reducing Railway Maintenance." *Proceedings of the Institute of Civil Engineers*, (TR3), 109–115.

Zhang, P. & Wei, X. (2011). "Study on Flexural Strength and Flexural Modulus of Elasticity of Cement." *Advanced Materials Research*, 287-290, 990–993.

APPENDIX A – RPF INJECTION PROCEDURES AND PSB COMPOSITION

A.1 MATERIAL PHASE RELATIONSHIPS FOR PSB

A.1.1 PSB Terminology and Ballast Response to RPF Injection

Calculations commonly used in soil mechanics for determination of index properties and phase quantities of soils were used in this study to define the density of ballast, RPF, and PSB of each fabricated specimen. These properties were important for correlating the density of the different phases within the material to the mechanical properties outlined in Chapter 4. For many of the PSB specimens, RPF injections caused expansion in the initial mold volumes, which caused a decrease in density of the ballast within the PSB composite. Mold volume expansion and decreasing ballast density resulted in varying volumetric makeup of each specimen. When an overabundance of reacting RPF was present within the ballast continuum, the expanding foam increased the volume of the ballast pore space.

A.1.2 PSB Phase Calculations

For each PSB specimen, the ballast was compacted into a prefabricated mold prior to RPF injection utilizing the compaction procedure developed in Ebrahimi (2011). For each type of mold (e.g., cylinder, beam, etc.), a specified weight of ballast (W_b) was compacted into the initial mold volume. With the specified weight and initial volume of the compacted ballast, the void ratio and dry density were calculated using the specific gravity of ballast solids. Therefore, the void space was known for use in RPF injection quantity calculations. Upon injection, the foaming process began and resulted in RPF filling the ballast void space as shown in a cross-section of a specimen in Appendix Figure 1.

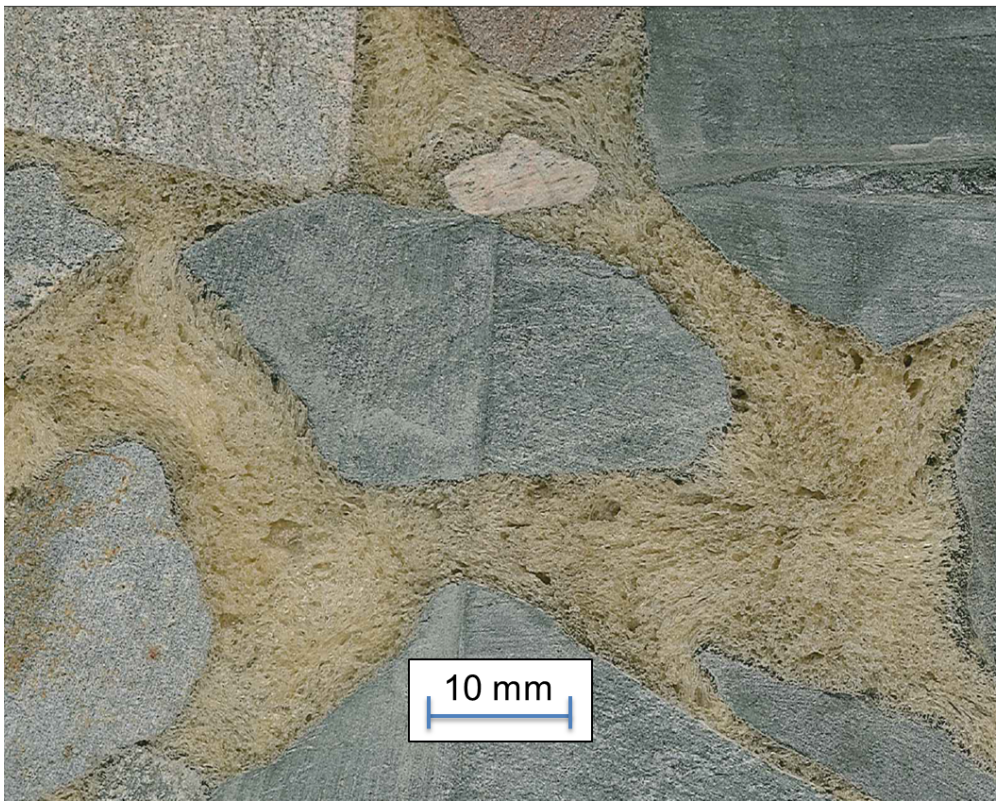

Appendix Figure 1: Picture of a beam specimen cross-section after being sawed in half by a concrete masonry saw.

After RPF injection, each PSB specimen was weighed (W_{PSB}) and measurements taken to determine the final volume (V_{PSB}). The PSD density (ρ_{PSB}) was determined by

$$\rho_{PSB} = \frac{W_{PSB}}{V_{PSB}} \quad (1)$$

The RPF injection protocol and RPF density (ρ_{RPF}) calculations were experimentally determined during specimen fabrication. The remaining subsection demonstrates calculations for determining the quantity of each material phase within the composite.

If mold expansion occurs, the new ballast density (ρ_b) is found using

$$\rho_b = \frac{W_b}{V_{PSB}} \quad (2)$$

The final void space percentage is found using the following simplified equation

$$Final\ Void\ Space\ \% = 1 - \left(\frac{W_b}{\gamma_S * V_{PSB}}\right) \quad (3)$$

where W_b is the ballast weight and γ_S is the solid unit weight of ballast determined from the specific gravity (G_S) of ballast found in Ebrahimi (2011), which was the same material used in this study; i.e., G_s=2.56. After injection, the RPF weight (W_{RPF}) is calculated from the following

$$W_{RPF} = W_{PSB} - W_b \quad (4)$$

After injection, RPF completely filled the void space of the ballast specimens; therefore, the RPF density could be found by

$$\rho_{RPF} = \frac{W_{RPF}}{(Final\ Void\ Space\ \%) * V_{PSB}} \quad (5)$$

The RPF solid volume is calculated from the known initial density of the polyurethane liquid components and the final weight of the RPF in the specimen. Depending on the polyurethane recipe, the liquid density, ρ_{PU}, of the mixture is determined by

$$\rho_{PU} = \frac{\%A*\rho_A+\%B*\rho_B+\cdots+\%N*\rho_N}{1+2+\cdots+N} \quad (6)$$

where %A is the ratio of component "A" used in the mixture, %B is the ratio of "B" used in the mixture, ρ_A is the liquid density of "A", ρ_B is the liquid density of "B", and %N and ρ_N account for any further added components. Therefore, solid volume of the RPF V_{PU} is

$$V_{PU} = \frac{W_{RPF}}{\rho_{PU}} \quad (7)$$

During reaction, the effects of the blowing agent cause a release of CO_2 gas (Szycher 1999). For simplicity in these calculations, the mass loss of the gas is assumed negligible. Finally, the following equations are used to calculate PU (airless phase of RPF) by weight and by volume

$$\%RPF\ by\ weight = \frac{W_{RPF}}{W_{PSB}} \quad (8)$$

$$\%RPF\ by\ Volume = \frac{V_{PU}}{V_{PSB}} \quad (9)$$

where V_{PU} is the solid volume of the RPF, not including air within the cellular matrix of the foam.

For the PSB specimens, on average, ballast was 95% by weight and 58% by volume, the PU (airless phase of RPF) was 5% by weight and 7% by volume, RPF was 42% by volume, and Air+CO_2 made up 35% by volume. Additional CO_2 is present due to the blowing agent and foaming process. Since the RPF phase was approximately 5% by PSB weight and ballast phase was approximately 95% by weight, the overall PSB density is controlled by the ballast phase density, as shown in Appendix Figure 2. A phase diagram is shown in Appendix Figure 3 to

illustrate the phase relationship of the PSB density compared with the ballast phase density. There was no substantial correlation between RPF phase density with overall PSB or ballast phase densities.

Further analysis needs to be conducted and considerations made for RPF reactions within specimens that possess substantial water content. The quantity of the RPF used in specimen fabrication (5% by weight) is approximately the same as the typical amount of asphalt cement used in most Hot Mix Asphalt (HMA) mixes (NAPA 2012). Therefore, influence by weight of RPF is comparable to that of binding properties of asphalt. Finally, no premixing is required for use of RPF, which distinguishes it from that of other aggregate stabilization materials, such as cement and asphalt.

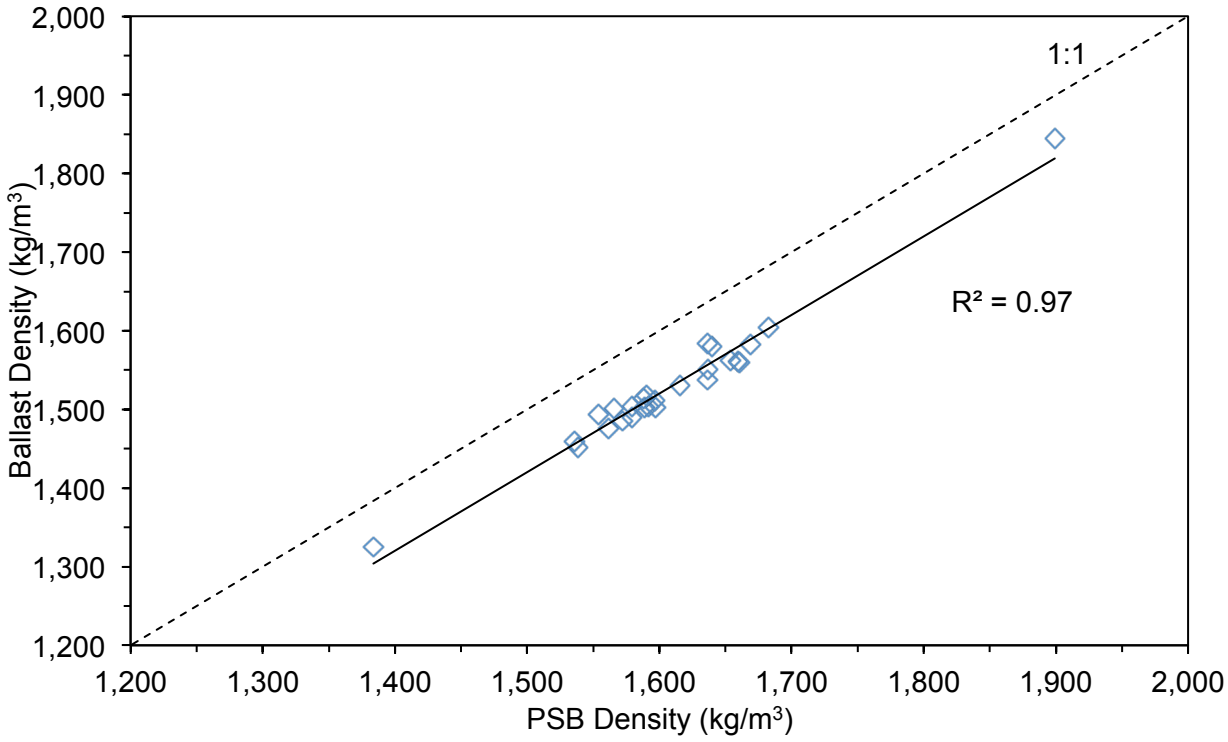

Appendix Figure 2: Relationship between ballast density and overall PSB density for fabricated PSB beams and PSB cylinders. Highpoint along trend is the specimen of polyurethane-stabilized fouled ballast.

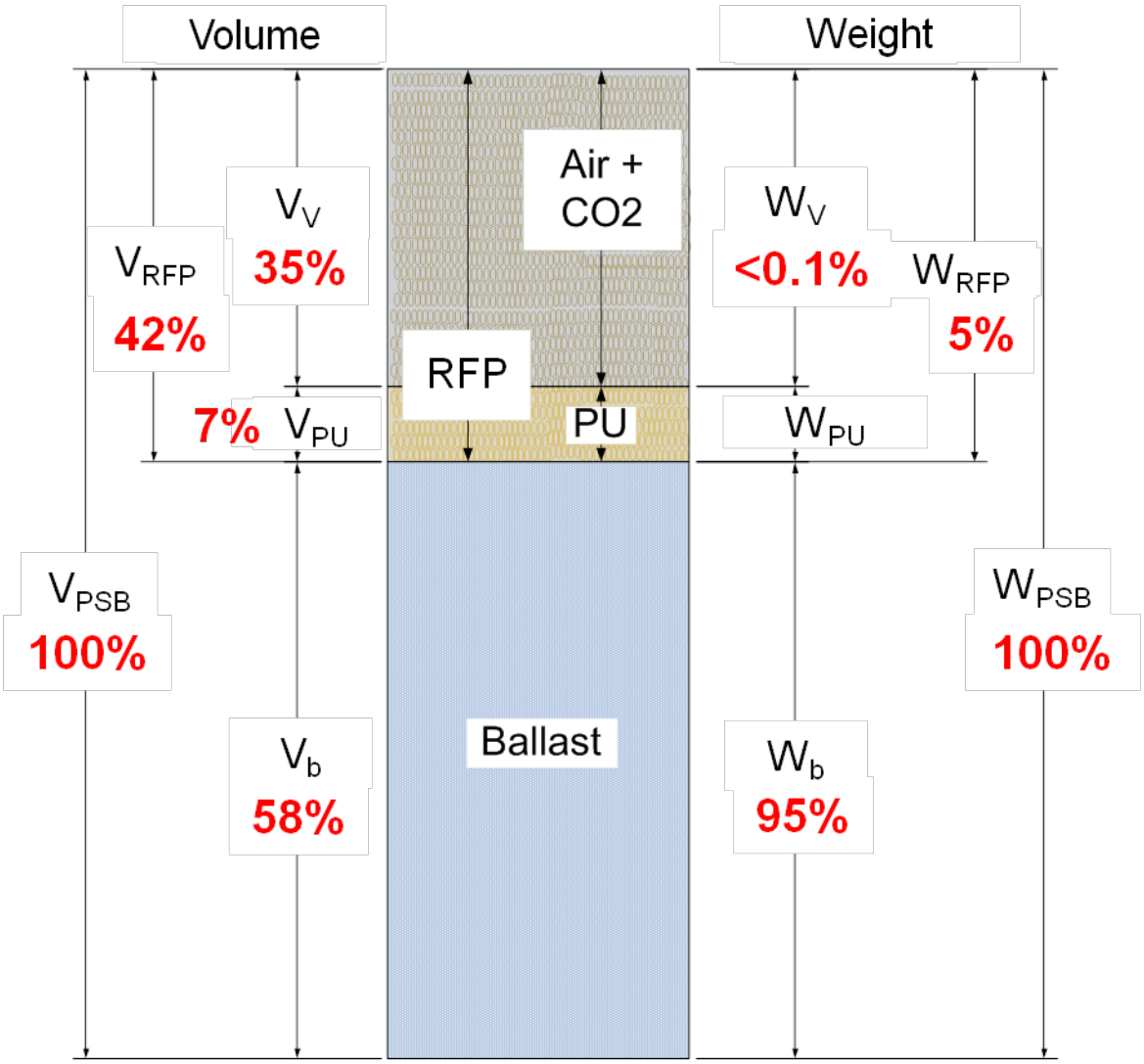

Appendix Figure 3: Phase diagram of a typical PSB specimen and average percentages for PSB compositions.

A.2 FLOW PROPERTIES AND BEHAVIOR

A.2.1 Ballast Rheological Properties:

For this research, the compaction method adopted from Ebrahimi (2011) achieves a ballast dry unit weight, $\gamma_{d\text{-field}}$ = 15.8 ± 0.5 kN/m^3 with a corresponding void ratio, e_b = 0.62 ± 0.02. Therefore, when compacted to $\gamma_{d\text{-field}}$, the resulting percentage of open space within a given sample of ballast (i.e., porosity) is 37.5 ± 0.1% of that given volume.

The ballast has a maximum particle size of 63 mm and a minimum particle size of 25 mm. Most of the particles of ballast have irregular shapes with particle aspect ratio (ratio of the largest and the smallest dimensions of a particle) between 1.5 and 3.5 as determined using the method developed by Krumbein (1941). Due to the large angularity and diameter and irregular shape, the packing of ballast particles typically yields a hydraulic conductivity of 0.025–0.050 m/s and an intrinsic permeability of $2.56 \cdot 10^{-5}$–$5.1 \cdot 10^{-5}$ m^2 (Selig and Waters 1994). The intrinsic permeability of a soil continuum is calculated from the hydraulic conductivity of the soil. Given the viscosity of a fluid, a basic computation using Darcy's Law can reflect the rheological properties of a fluid flowing within a porous media such as ballast. The properties of fluid flow in ballast vary because of the different ballast particle characteristics and ballast densities. Hydraulic conductivity of ballast significantly reduces with increasing fouling index (Selig and Waters 1994).

A.2.2 RPF Rheological Properties:

The rheological properties of RPF (486STAR-4 BD) during liquid, transition, and set phases are important for administering ballast injections for stabilization purposes. The properties include the initial and final viscous characteristics of the expanding polyurethane and the force with which the polyurethane expands. Viscous forces, expansion rates, and achievable densities are

dependent on injected volume, pressure of injection, rate of injection, resistive pressures, intrinsic permeability of pore space, and volume of pore space (Gupta et al. 2000; Martins et al. 2010). The final PSB specimen compositions are typically 5% RPF by weight.

In this study, the rheological behavior of the 486STAR-4 BD RPF was determined through index testing developed by Uretek USA Inc. The reaction of the RPF during an index test consists of 4 phases: cream, gel, tack-free, and end-of-rise. From observations during the index testing, the cream phase is identified when the RPF begins bubbling (blowing) and transitioning from a transparent caramel color to a translucent light-beige color; the phase typically lasts 10–40 s. The early stages of the cream phase consist of bubbling and color transformation; in later stages leading up to the gel phase, the RPF is no longer liquid, has a gelatin consistency, and begins to stick to objects. Considerable material expansion occurs during the cream phase, which typically lasts 30–50 s. Transition into the gel phase is identified when the RPF begins sticking to objects. The appearance of the transition from gel to tack-free can be characterized as a molten resin or foam flow (Mitani and Hamada 2003). The gel phase is the period in which polyurethane bonds are established with any material in contact, typically lasting 35–75 s. Material expansion continues into the tack-free phase, which begins when bonding is complete and the polyurethane is no longer sticking to objects. From initialization of the tack-free phase, the rate of expansion decays until expansion is no longer noticeable, at which point the material is considered in the end-of-rise phase. End-of-rise occurred 130–290 s after injection. A visualization of the RPF reaction phases and corresponding reaction times is illustrated as Appendix Figure 4.

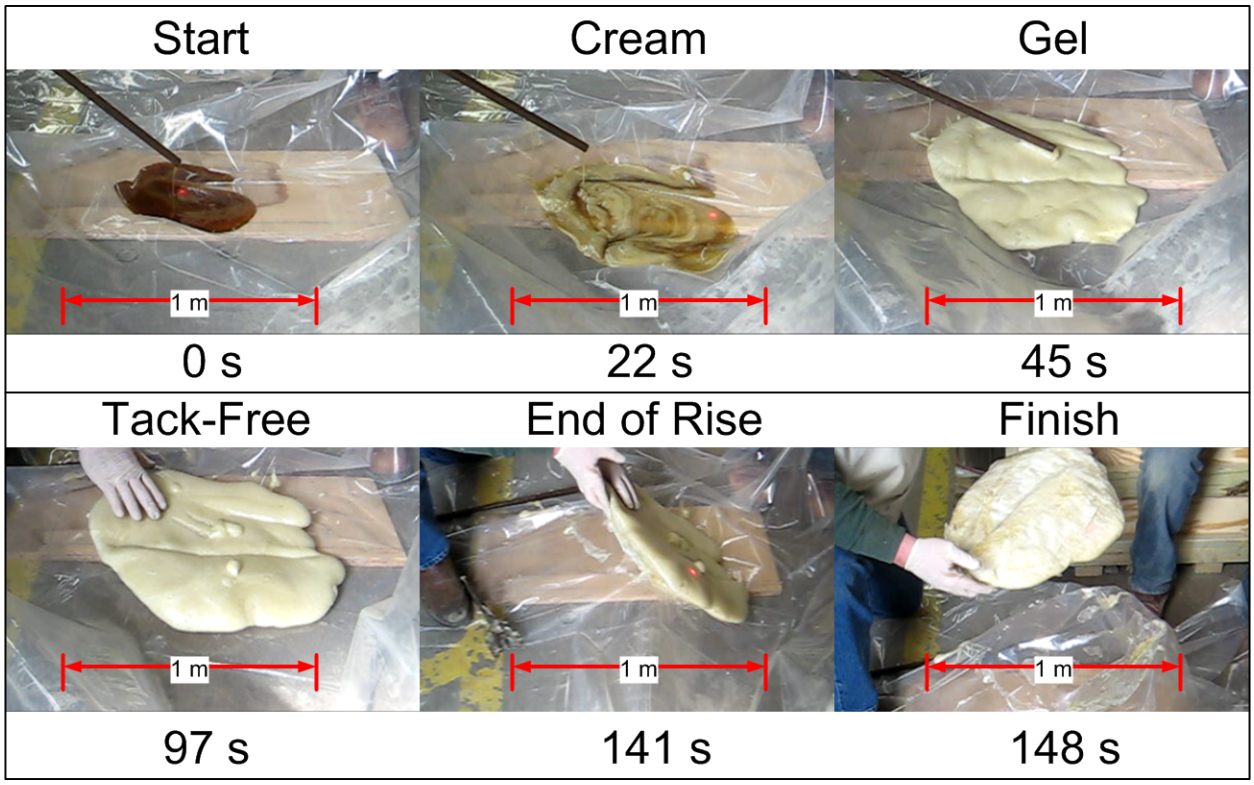

Appendix Figure 4: Pictures displaying each phase of the RPF reaction process with timings displayed for a 35°C starting temperature.

The dynamics of the polyurethane foaming reaction included some variability because the formation took place in a laboratory not equipped for highly controlled polymer processing. Consequently, the polyurethane reaction deviated (i.e., phase timing) from those described in literature. However, this setting is more appropriate since the application of RPF would typically occur in a wide variety of environmental settings. The initiation and transition time of each phase is dependent on initial RPF temperature and temperature of the phase testing surface. A set of equations defined from phase tests conducted before specimen fabrication is shown in Appendix Figure 5. The phase transition times were determined empirically over numerous trials and more mechanisms may be involved in overall RPF phase response timing and expansion rate (i.e., type and quantity of blowing agent used).

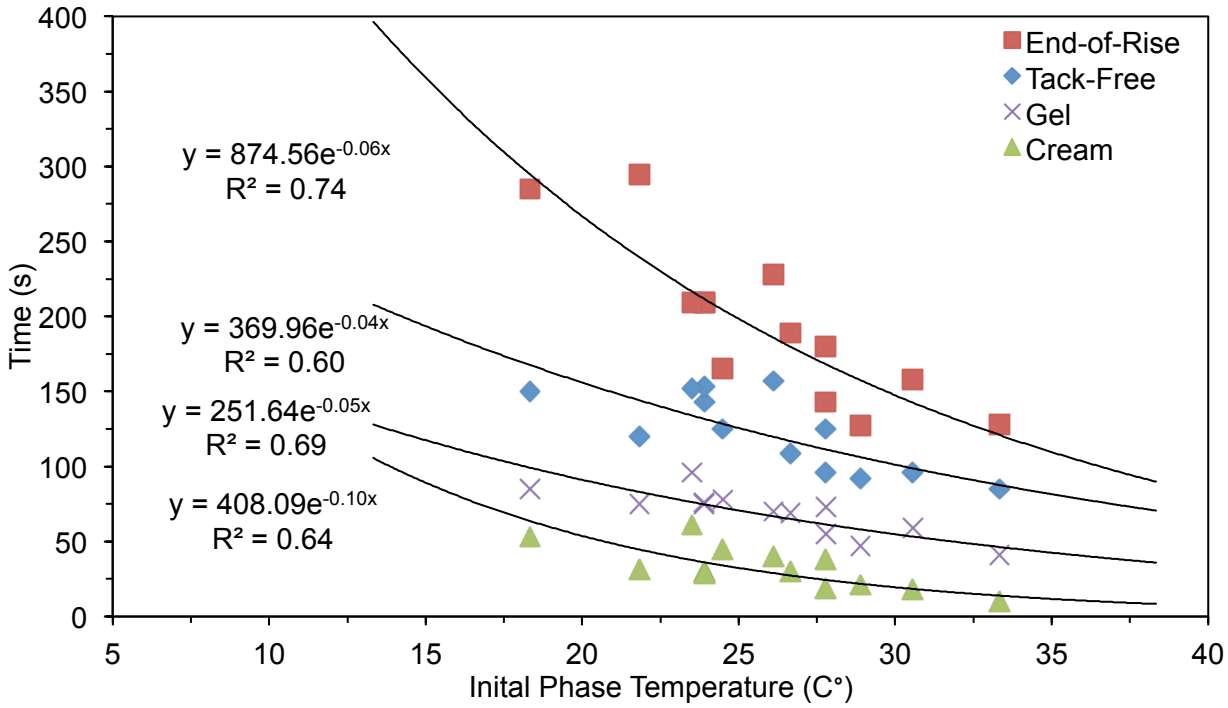

Appendix Figure 5: Trends were applied for the time of transition for each phase based on the measured initial temperature of the RPF liquid.

A study conducted by Mitani and Hamada (2003) defined several equations for predicting flow patterns during the polyurethane-foaming process. During the foaming process, the change in volume with respect to time is defined

$$V = V_0 \cdot 1 + \alpha t \qquad (10)$$

where V [L^3] is the volume at gel phase, V_0 is the initial injected volume, α [T^{-1}] is the rate of expansion, and t [T] is the time to gel. Because particle bonding occurs only during gel, while RPF expansion occurs from gel to end-of-rise, assigning two values of α seems appropriate to signify expansion from initial injection through gel (α_g) and from tack-free through end-or-rise (α_e). This approach, improved upon from Mitani and Hamada (2003), allows differentiation of the RPF expansion calculation for during and after the particle bonding process.

Knowing the time to end-of-rise and that the final viscosity is that of a semi-rigid object, the expansion rate (α_e) from tack-free to end-or-rise can be determined and validated. Understanding and applying phase timing and rate of expansion is useful for targeting final PSB densities, which have a constitutive relationship with PSB mechanical properties. As covered in Chapter 4, PSB mechanical properties have a strong relationship to the final phase densities (Section A.1.2) of the materials within the composite.

A.3 RPF FLOW AND PSB OBSERVATIONS

A.3.1 Flow of Polyurethane in Ballast and Other Subsurface Conditions

During the fabrication of PSB, RPF flows in the path of least resistance, which is the pore space of the ballast. Since the ballast matrix is intricate and essentially a packing of randomly placed aggregates, it can be assumed that the rise direction of the foam expanding through the pore space is essentially random. Several PSB specimens were cut in half to observe the void-space filling of RPF and the direction of the RPF cellular structure within PSB. The cells in RPF were observed to have large variability in the various rise directions within the pore space of the injected ballast specimen (Appendix Figure 6). This variability in rise direction was also observed in Buzzi et al. (2008) where RPF was injected into a soil formation and then exhumed for observation of the RPF integration with the soil formation and RPF rise directions within.

Buzzi et al. (2010) injected RPF into expansive clay (LL=75, PI=50) and found that the injection created hydrofractures while forming into dendritic paths of foam. In Buzzi et al. (2008), RFP was injected into a similar soil foundation and exhumed to measure the resulting RPF densities measured within the soil formation, which were 85–145 kg/m^3. In this study, the measured densities of the RPF injected into clean ballast were 152–250 kg/m^3. The RPF rheological behavior (i.e., during injection, expansion, and curing) in Buzzi et al. (2010) is evaluated for comparison with the RPF rheological behavior observed in this study. In finer grained aggregates, RPF hydrofractures the soil formation and forms dendrites (Buzzi et al. 2010) and in coarse-grained aggregates (i.e., ballast) RPF permeates through the void space, during injection and expansion, forming a uniform geocomposite material observed in this study.

In Buzzi et al. (2010), the response of the soil formation to RPF injection and flow of RPF (propagation of the resin) was found to be unpredictable. The soil mass in laboratory and *in situ* samples were observed to maintain the initial void space prior to injection. Based on

observations in this study, void space in clean ballast specimens was completely filled. Because of the hydraulic conductivity of clay (10^{-10} m/s) tested in Buzzi et al. (2010), RPF expansion rate and flow is far greater than the permeability of the clay would allow, which is evidenced by required RPF injection pressures of up to 200 kPa to initiate flow of RPF into the clay formation. No injection pressure was used for injection of RPF into clean ballast; the hydraulic conductivity of ballast (0.025–0.050 m/s) in this study enables minimal ballast particle displacement during RPF injection and RPF flow and expansion. Therefore, clean ballast is preferable to finer grained soils for having controlled injection quantities and targeted composite properties.

Similar as in Buzzi et al. (2008), the RPF cell size of RPF in this study, when injected into ballast, was found to be largely non-uniform within the PSB composite. Based on the cell elongation observed within PSB, the cells tend to form in an elongated fashion in proximity to the ballast particles (within 2 mm) and near ballast contact points (i.e., where RPF flow would be most restricted). The elongated orientation of the cells in RPF within PSB were observed to be mainly parallel to the ballast particle surfaces and orthogonal to the particle contact points (Appendix Figure 6). As described in Appendix B, the mechanical properties of PSB are dependent on the aggregate matrix within the PSB composite and the interface transition zone where bonding on a micro scale occurs. Consequently, the axis of cell elongation of RPF in PSB forms in directions that are known to have weaker mechanical properties for anisotropic (elongated cellular structure) RPF. Therefore, the formation of RPF within PSB may not utilize the potential mechanical properties of RPF formed with a homogeneous cellular structure. Since heterogeneity exists in the RPF within PSB, predicting PSB properties based on laboratory tested (free-rise) RPF specimens is limited.

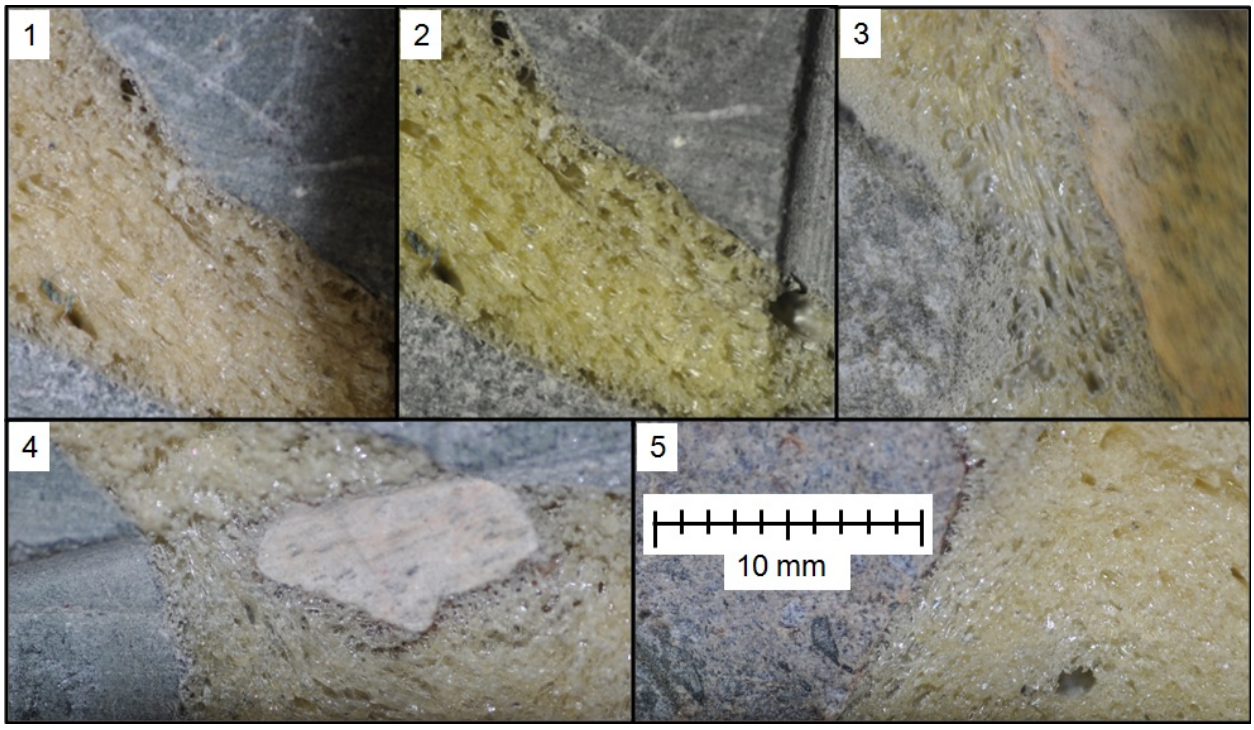

Appendix Figure 6: Pictures of PSB specimens cut in half revealing RPF cellular structure within the void space of ballast.

A.3.2 Polyurethane Expansion Pressure and Injection Development

The specimen fabrication process was designed to resemble the fabrication process for concrete (i.e., formwork). Certain modifications were made to the formwork to account for the expansive behavior of reacting RPF, which differs from forms designed for casting concrete. When concrete is placed in the field, a great deal of consideration must be made for the strength of formwork due to the hydrostatic pressure generated by liquid concrete. With PSB fabrication, the molds were designed to withstand compaction of ballast within the molds and expansive pressure of RPF injections. In some cases, tops were put on the molds to prevent vertical expansion of the ballast material due to RPF expansion within the void space.

Initial tests were conducted to determine how much force could be generated based on the amount of RPF injected into the ballast samples within the molds. Four trials were conducted to determine vertical force generated from injecting different liquid quantities of RPF into the ballast samples; the methodology for measuring vertical force is illustrated in Appendix Figure 7. The lateral expansion force was constrained by a bolted steel mold, while vertical expansion was confined by a steel plate equipped with a load cell above the plate. In one of the trials, the quantity of injected RPF did not generate any vertical expansion force; therefore, the quantity of 5% RPF by weight was determined to be an optimum amount for injection of ballast specimens. In another trial, a 20.2-kg ballast specimen, compacted at a dry unit weight of 15.8 kN/m^3 was injected with 1.2 kg of liquid RPF. The resulting percent RPF by weight (introduced in Section A.1.2) was 5.52%. The pressure generated was 75 kPa (12.7 psi) measured vertically above the top plate of the bolted steel mold. The vertical pressure generated by expanding RPF within the ballast pore space is shown in Appendix Figure 8.

The expansion pressure produced when a 5.52% by weight injection is conducted is compared to the hydrostatic pressure from liquid concrete. Concrete has a unit weight of

approximately 23.6 kN/m^3 (150 psf). Therefore, an equivalent amount of hydrostatic pressure would require a concrete depth of 3.2 m (i.e., a one story column or wall in a building) to produced pressure similar (75 kPa) to the amount from RPF reacting within the ballast pore space during fabrication of the 5.52% RPF by weight PSB specimen. Since large differences in expansion pressure with relatively small change in injection quantity was observed, precise regulation of RPF quantity by injection equipment is important for laboratory specimen fabrication. As large variability can exist for the intrinsic permeability of the void space within a compacted ballast specimen, irregular flow and expansion of RPF is likely to occur. This was evidenced when a fabricated mold was breached during RPF injection in a contained ballast sample (see Appendix F). Regulation of RPF quantity, on a laboratory scale, is of less importance than in field injection scenarios where more *in situ* overburden pressure exists. The lateral boundaries of the molds during laboratory fabrication of PSB do not represent conditions in the field (i.e., continuity of the ballast layer in the field). However, care should still be taken so that target areas are not over or under injected.

To reach targeted RPF volume and density, during specimen fabrication, timed injections were used to prevent too much reacting RPF from being injected into the compacted ballast specimen. To control the amount of expansion force produced, injections were conducted at different heights within the specimens and timed at specified intervals. The time intervals between injections was 45 ± 15 s. The 30 s minimum injection interval was established to ensure that there was not too much reacting polyurethane injected at the base of the specimens and so successive injections would occur while RPF was expanding (i.e., rising vertically). No more than 60 s was allowed between injections to prevent RPF from curing within the injection nozzle, thus compromising the procedure. This approach was developed and improved by assessing failed specimen fabrications that occurred early in the research.

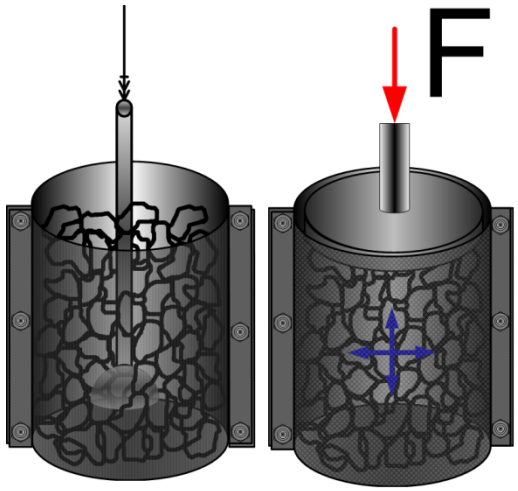

Appendix Figure 7: Illustration of injection nozzle within ballast sample (left) and illustration of expansion force within steel mold and method of measuring vertical force (right)

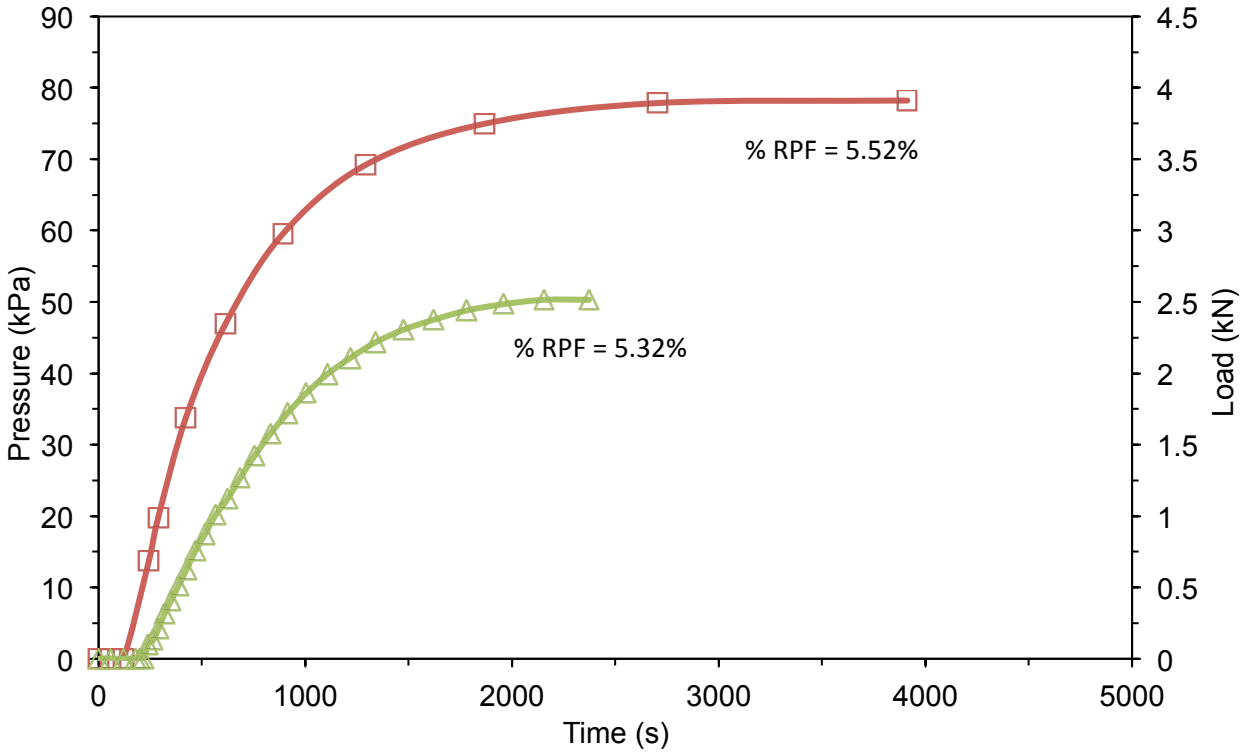

Appendix Figure 8: Vertical expansive pressure vs. time. Expansive pressure generated because of reacting RPF within the cylindrical ballast specimen.

A.3.3 Ballast Layer Injection Methods

A.3.3.1 Methodology

In Sections A.2.1 and A.2.2, an introduction into the rheological characteristics of ballast and RPF was presented. In Section A.3, this methodology was used for experimentally determining procedures for PSB specimen fabrication and general guidelines for *in situ* ballast injections. Discussed in this section is the use of prototype ballast layers that were constructed to simulate RPF injection into the ballast layer and to develop procedures for how the ballast layer can be injected to target particular outcomes. The dimensions of the ballast layer within the ballast layer prototypes were 0.40 m x 0.32 m x 0.71 m (Appendix Figure 9). The ballast layer height was 0.40 m, but with a 0.18 m-tall tie placed on top of the layer. The ballast layer prototypes developed were similar in size to the small-scale box developed in Selig and Waters (1994), which was developed for conducting cyclic loading tests on a representative ballast layer and measuring the amount of fines generated over 500,000 loading repetitions. The dimensions of the "ballast box" in Selig and Waters (1994) were 0.46 m x 0.30 m x 0.61 m; the height of the ballast layer included a rail tie placed in the center.

A.3.3.2 Prototype Ballast Layer Fabrication

Maximum dry density was achieved using the procedure developed in Ebrahimi (2011), resulting in a clean ballast void ratio (e_b)=0.62. Corresponding clean ballast dry unit weight (γ_d) and density (ρ_d) were 15.8 kN/m^3 and 1611 kg/m^3, respectively. These compaction characteristics were targeted for fabrication of each ballast layer prototype in this study. The depth of the ballast within the prototype was 0.4 m, which is within the range of typical ballast layers within railway track substructure; the ballast layer depths within the test track (FAST track) investigated in Selig and Waters (1994) ranged between 0.38 m and 0.53 m. The length of the prototype was 0.71 m, which is a little longer, but represents the distance between ties in

a track of 0.6 m centered on the tie. The width of the prototype was selected based on the dimensions of the load frame that would be used for mechanistic testing of the ballast layer prototypes, but was not limiting for the type of tests conducted.

The RPF injections selected, described in more detail in the next subsection, were aimed at observing injection of RPF into an open ballast layer as opposed to a specimen in a mold and for determining the resulting geometry of the stabilized areas. In the ballast layer prototypes, two types of injection scenarios were selected. One scenario involved application of RPF along the surface (percolation-injection) to determine the depth the RPF would reach while in liquid phase and how much lateral expansion through the void space would occur. The other scenario involved injecting RPF at half the depth of the ballast layer (subsurface-injection) to determine how much lateral and vertical RPF expansion would take place and the resulting geometry of the subsurface injections. The methodology behind the two scenarios is illustrated in Appendix Figure 10.

A.3.3.3 Analysis of Prototype Ballast Layer Injection

With the RPF percolation-injection approach, the result was the formation of PSB extending from the ballast surface down to the base of the ballast layer, as depicted in Appendix Figure 10. No vertical expansion of the ballast layer was observed. RPF expanded through the pore space of the ballast while percolating towards the base of the ballast layer. The outcome of the injection procedure is shown in Appendix Figure 11. This stabilization procedure creates a monolithic or bounded formation that is better described as a pile beneath the rail tie, similar to a pile or footing for a structural foundation. However, the mechanistic properties of PSB and interaction with the surrounding substructure materials and layers are far different from the mechanical interaction between a typical concrete pile and surrounding soil formations as discussed in later chapters. Laboratory methods developed to determine mechanical properties

relevant to RPF percolation-injection procedure are detailed in Appendix A, mechanistic properties of this type of PSB formation is detailed in Sections 4.2 and 4.3, and a model evaluating the effect of these formations on track response is covered in Chapter 5.

When the RPF subsurface-injection technique was employed, a layer of PSB was formed at the base of the ballast layer prototype (Appendix Figure 10). No vertical expansion of the ballast layer was observed. The RPF expanded through the pore space of the ballast layer along the base of the prototype and minimal vertical expansion through the pore space occurred. The outcome of the injection procedure is shown in Appendix Figure 12, where the RPF injection caused the formation of a longitudinally oriented PSB layer along the base of the ballast layer with the remaining overburden of ballast free of RPF.

Injection of RPF at the base of the ballast layer thereby forming a stabilized layer is similar to having an underlayment of asphalt beneath the ballast layer. Thus, unbound ballast is sandwiched between two bound layers (i.e., the asphalt underlayment and the railway superstructure), which has been investigated in several studies (Huang et. al 2009, Rose and Lees 2008, Rose and Konduri 2006). During track construction, placement of an asphalt layer above the subballast layer before forming the ballast layer is described in (Rose et al. 2010) as an asphalt/bituminous trackbed.

This type of stabilization resembles cement-stabilized subbase/subgrade layers in a pavement system, where an unbound layer is placed between two bound layers (i.e., between a stabilized and pavement layer). In a typical pavement system, the bound layer is the surface course for asphaltic pavement or a slab for concrete pavement, which is supported by an aggregate base, subbase, and natural subgrade (Huang 2004). The railway superstructure (i.e., ties, rails, and fastening system) is conceptually similar to a slab used for concrete pavement

where the loads are absorbed by a stiff system (i.e., the concrete slab or railway superstructure) and distributed over a large surface area (bearing area beneath a concrete slab or railway ties).

The injection procedure developed for PSB would in effect create a bound layer with the unbound ballast layer remaining between the PSB layer and the superstructure, conceptually similar to asphalt trackbed design with the exception that it can be installed in an existing track bed unlike the asphalt track bed. As is the case with design of an asphalt trackbed, PSB formation can be strategically implemented to form stabilized layers of specified thickness based on intended design. Discussed in Section 3.3.3 are the methods that were developed for flexural beam testing of PSB and for evaluation of flexural strength and fatigue properties, which are typically used to determine design thicknesses for constructing stabilized layers effectively. The mechanistic properties pertaining to this type of PSB formation (RPF subsurface-injection) are detailed in Appendix A and a model evaluating the effect of these formations on track response is covered in Chapter 5.

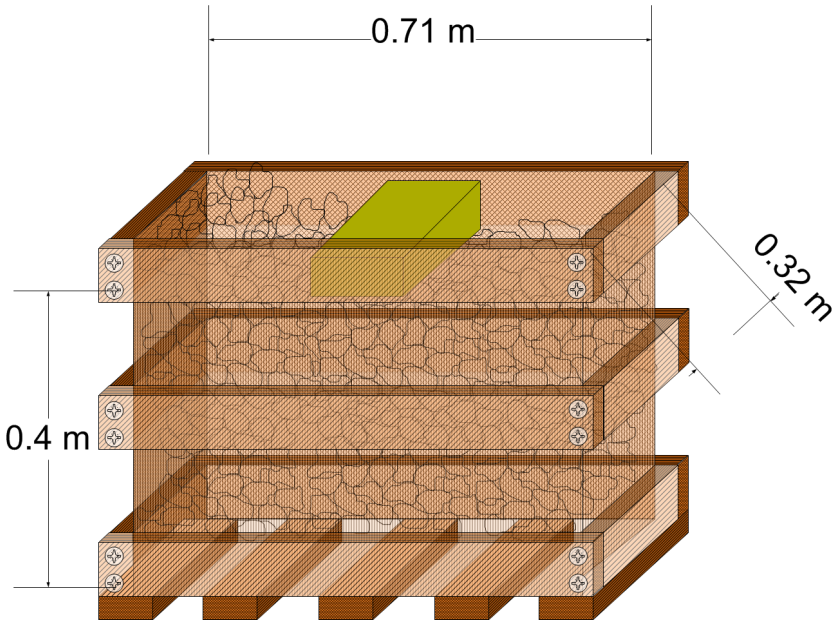

Appendix Figure 9: Schematic of the ballast layer prototype, with dimensions of the ballast layer shown.

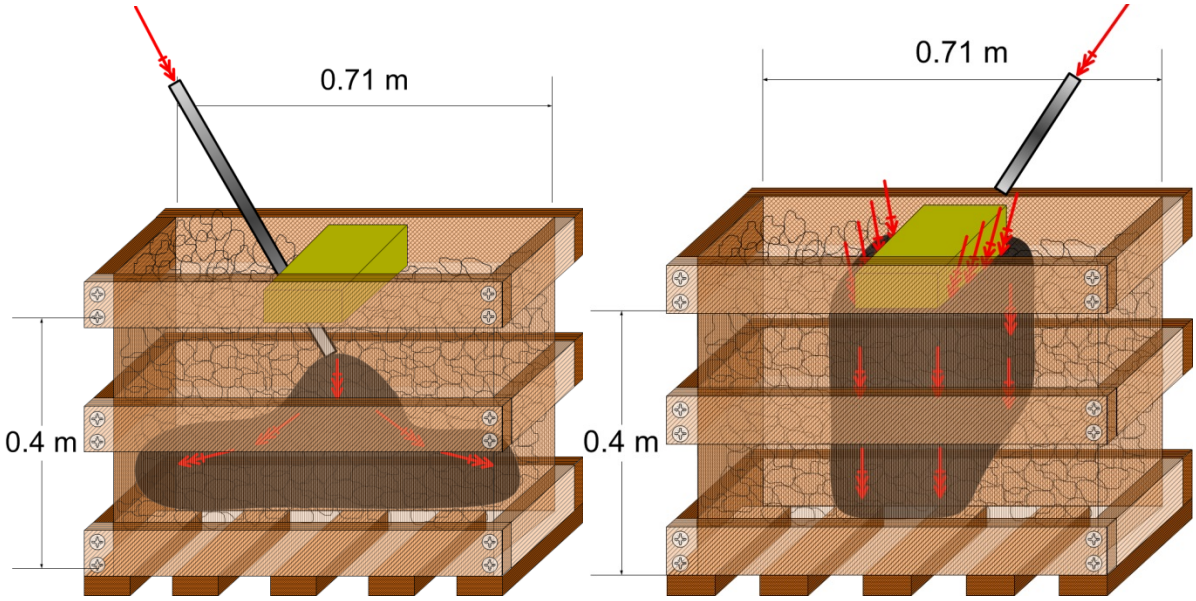

Appendix Figure 10: Illustration of methodology for ballast layer prototype with RPF subsurface-injection (left) and RPF percolation-injection (right).

Appendix Figure 11: Picture of ballast layer prototype with RPF percolation-injection along the surface (left) and resulting stabilized areas after removing loose ballast (right).

Appendix Figure 12: Photo of side-view of prototype with RPF subsurface-injection into ballast layer prototype (top) and base of injected ballast layer prototype (bottom). Effective height (top) = 20 cm and base dimensions (bottom) = 0.3 m x 0.66 m.

APPENDIX B – RPF TESTING AND MECHANICS

B.1 MECHANICAL PROPERTY TESTING METHODS FOR RPF

B.1.1 Methodology

Compression tests were also conducted on numerous RPF cylinder specimens that were fabricated in this study. The methodology of the tests conducted and specimen fabrication (described in APPENDIX B), were taken from ASTM D1621 for compressive properties of rigid cellular plastics and ASTM D7181 for consolidated-drained triaxial-compression tests of soils. Typical monotonic compression was applied under varying confining stresses. From the tests conducted, RPF mechanical properties remained relatively constant despite confining pressures applied; however, the mechanical properties strongly depended on RPF density. RPF in this study was compared to RPF tested in several other studies at varying RPF densities and with different testing modes such as tensile and flexural (Bayer Material Science (2010); Marsavina (2008); Tu et al. (2001); Neilsen et al. (1995); Traeger et al. (1967)). The mechanical properties in each mode of testing (compressive, tensile, and flexural) possessed a strong correlation with density; in addition, the mechanical property determined via one mode of testing can be used to infer other mechanical properties of the material (Section B.2).

RPF cylinders (2:1 height-to-width ratio) were fabricated for confirming mechanical properties of the RPF used in this study and then subjected to mechanical testing. Applicable compression test standards include ASTM D1621 (Compressive Properties of Rigid Cellular Plastics) and ASTM D2850 (Unconsolidated-Undrained Triaxial Compression Test for Cohesive Soils). However, specimens were tested in with drained conditions (i.e., air flow, via the effluent values, was allowed between RPF specimens and the external air). Methodology from each standard was combined for monotonic-triaxial compression testing on RPF cylinders (Appendix Figure 13).

Load was applied to the RPF cylinders through a screw-driven system (GEOTAC®, loading capacity of ~8.9 kN). Vertical deflection of the specimens during monotonic loading was measured using internal linear variable differential transducers, LVDTs, as part of the GeoJac™ step-motor system and data acquisition interface. The strain rate recommended in ASTM D2850 was 1%/min for plastic materials and 0.3%/min for brittle materials. The nominal strain rate used in RPF cylinder testing was 1%/min (0.69 mm/min). Methods used for analyzing RPF monotonic-triaxial compression results were taken from ASTM D1621 and ASTM D2850.

B.1.2 Specimen Fabrication

RPF cylinders were trimmed from larger RPF cylinders that were confined during injection to cause a limit to RPF expansion and an increase in RPF density. Cylinders were cut to a minimum 2:1 height-to-width ratio to reduce the effect of friction at ends of the specimens (Bishop and Green 1965). Nominal RPF cylinder dimensions were 200 m x 200 m x 400 m.

B.1.3 Analysis of Monotonic-Triaxial Compression Tests

Analysis of RPF cylinder testing involved calculations the same as unconfined-compression tests and are defined in Section 3.3.4.

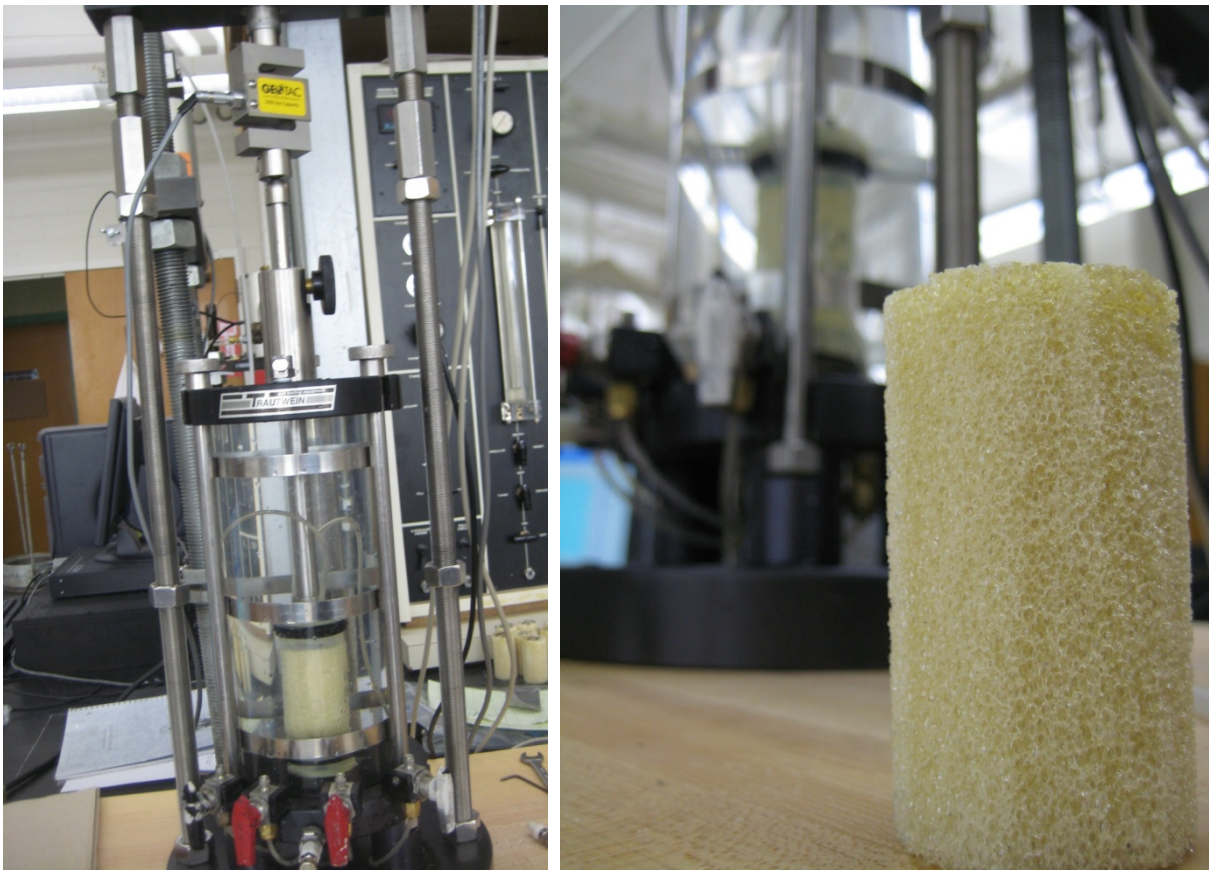

Appendix Figure 13: Picture of compression testing apparatus.

B.2 RPF RESULTS AND DISCUSSION OF EXPERIMENTAL TESTING

B.2.1 Laboratory Controlled Homogeneous and Isotropic Behavior

Compression tests were conducted on numerous RPF cylinder specimens that were fabricated, in the same laboratory conditions, while PSB specimens were being made. The RPF cylinders were cut from larger RPF samples that were created under confined conditions so that the RPF density would be higher and more uniform than the density of RPF created under free-rise conditions (free-rise conditions discussed later in this section). Typical monotonic compression was applied under varying confining stresses. 35 RPF cylinders were tested with RPF densities, ρ_{RPF}, ranging from 71–115 kg/m^3 at confining stresses, σ_3, ranging from 0–150 kPa. From the tests conducted, RPF compressive strength and modulus were found to remain relatively constant despite confining pressures applied as displayed in Appendix Figure 18; however, the mechanical properties depended on RPF density as displayed in Appendix Figure 14. From the triaxial compression tests conducted on RPF cylinders, the average compressive strength was 562 kPa with COV of 30% and average compressive modulus was 15.5 MPa with COV of 21%.

The RPF cylinders tested in this study were compared to RPF tested in other studies at varying RPF densities tested in compression (Appendix Figure 14). The trends for strength and modulus versus RPF density were very similar for RPF tested in this study and for RPF test results compiled from literature. RPF tested in other studies at varying RPF densities were also subject to tensile and flexural testing (Appendix Figure 17). The mechanical properties in each mode of testing (compression, tension, and flexural) possessed a strong correlation with the RPF densities of the specimens tested. Furthermore, only marginal differences were observed among the strength and modulus irrespective of the different modes of testing used. Therefore, RPF possesses consistent mechanical properties whether undergoing compressive, tensile, or flexural loading, as described in the next section (Section 4.7). Analysis conducted and

presented herein shows that a mechanical property determined via one mode of testing can be used to infer other mechanical properties of RPF.

The RPF results collected from literature were fitted with a model that can be used to determine the stiffness of RPF depending on RPF density. Traeger (1967) conducted tests on two types of RPF and established that a power relationship exists between the density of the RPF and any mechanical property being measured (e.g., Young's modulus, flexural modulus, tensile strength, etc.) with the exception of shear strength and shear modulus. In Traeger (1967), RPF with densities ranging from 32–480 kg/m^3 had shear strengths 60–80% to that of their compressive strengths; consequently, RPF is weaker when shear force is applied. For RPF mechanical properties, the relationship between the mechanical properties is a power relationship given by

$$Property = A * (Density)^B \tag{11}$$

where A and B are constants, 'property' pertains to the mechanical property being measured, and density is the RPF density (Traeger 1967; Phillips and Waterman 1974).

The following equations are developed for RPF foam mechanical properties from a collection of studies and from compression tests in this study, where RPF is fabricated and loaded at ambient room temperature and has an isotropic cellular structure and homogeneous density. The stiffness and strength of RPF can be found by

$$E = 13.72 \cdot \left(\frac{\rho_{RPF}}{m_{ref}}\right)^{1.690} \qquad R^2=0.92 \tag{12}$$

$$\sigma = 0.8412 \cdot \left(\frac{\rho_{RPF}}{s_{ref}}\right)^{1.612} \qquad R^2=0.94 \tag{13}$$

where under either compressive, tensile, or flexural loading, E is the stiffness (kPa), σ is the strength (kPa), and m_{ref} and s_{ref} are reference densities and are equal to 1. The results collected from literature for each mode of loading are compiled and displayed as Appendix Figure 15 with stiffness and strength versus RPF density. The predicted versus measured stiffness and strength values from the model are presented as Appendix Figure 16. For predicting modulus and strength of RPF, several assumptions and consideration must be made regarding the RPF heterogeneity, isotropy, fabrication and loading temperature, and closed-cell content. The effects of these attributes on RPF behavior are discussed in the following subsection.

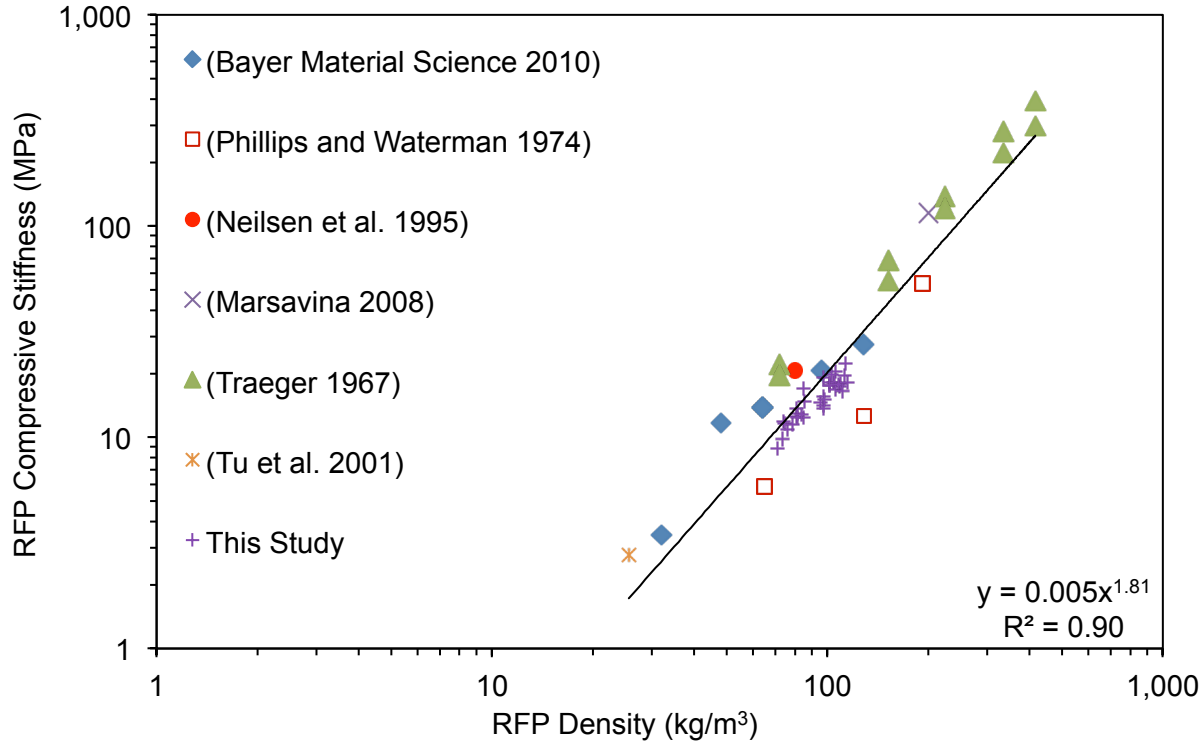

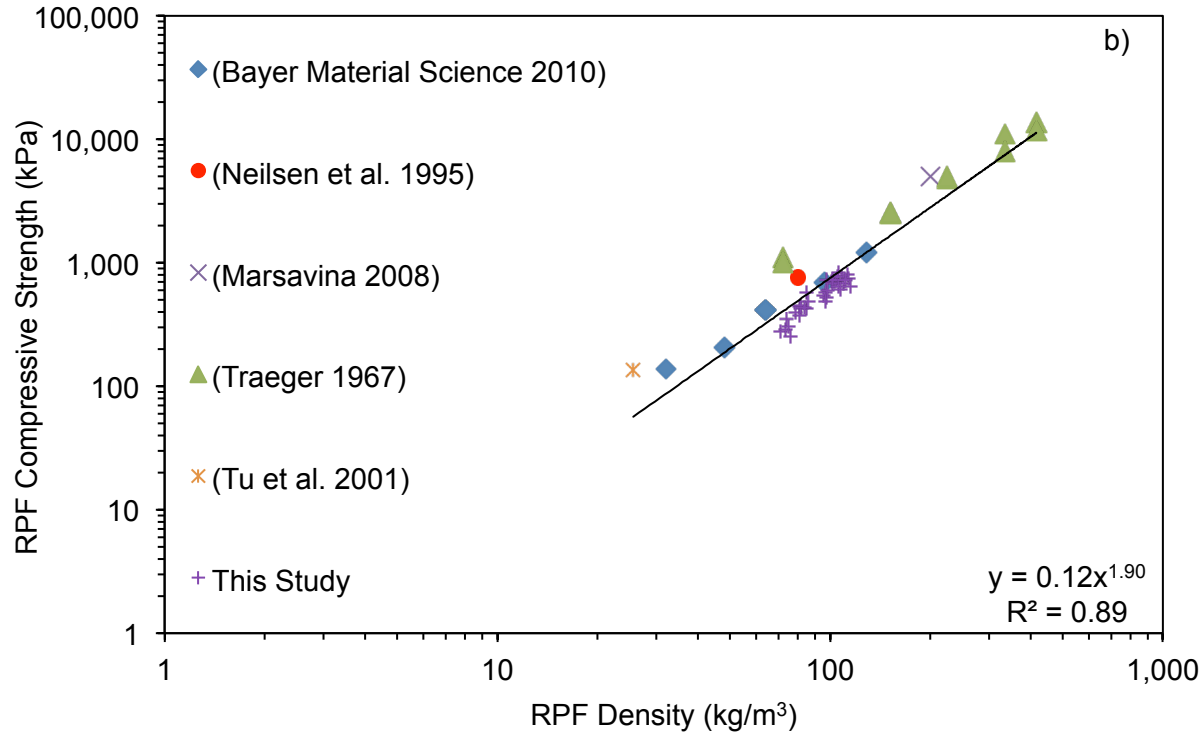

Appendix Figure 14: RPF compressive strength and moduli from literature and tests conducted in this study.

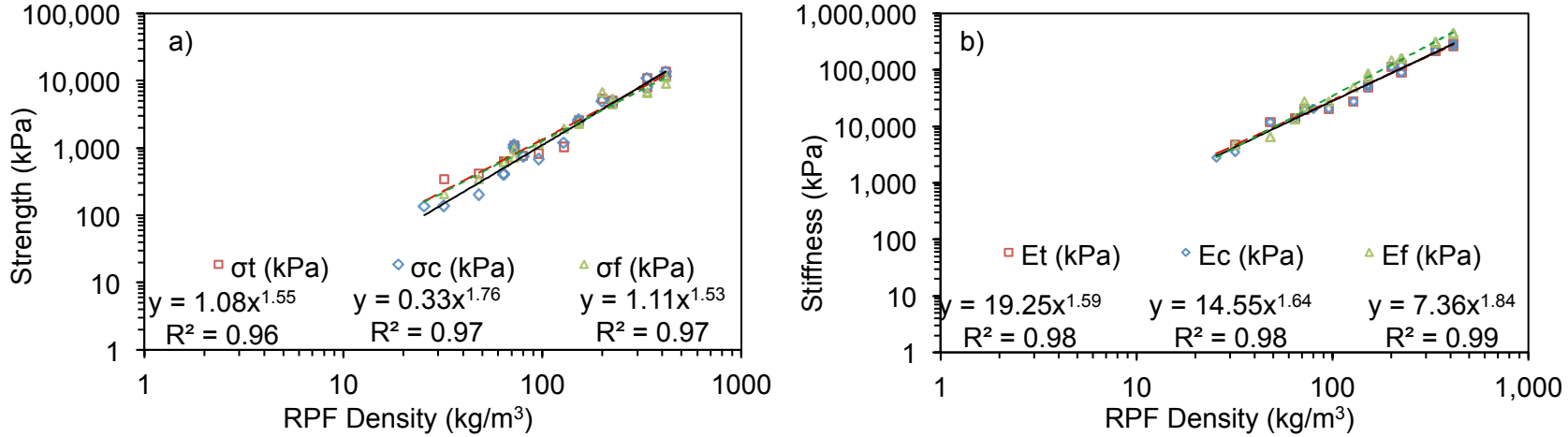

Appendix Figure 15: Relationship of RPF strength (left) and modulus (right) with RPF density. Data compiled from Bayer Material Science (2010), Neilsen et al. (1995), Tu et al. (2001), Traeger et al. (1967), Marsavina (2008), and tests in this study

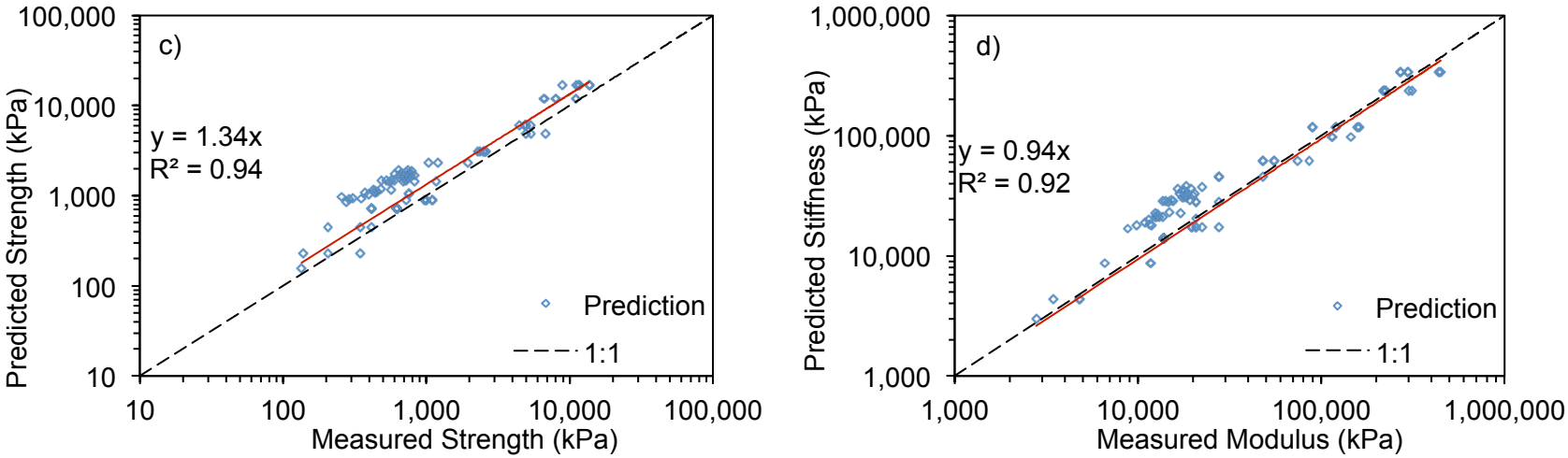

Appendix Figure 16: Predicted versus measured values for models predicting strength (left) and modulus (right). Data compiled from Bayer Material Science (2010), Neilsen et al. (1995), Tu et al. (2001), Traeger et al. (1967), Marsavina (2008), and tests in this study.

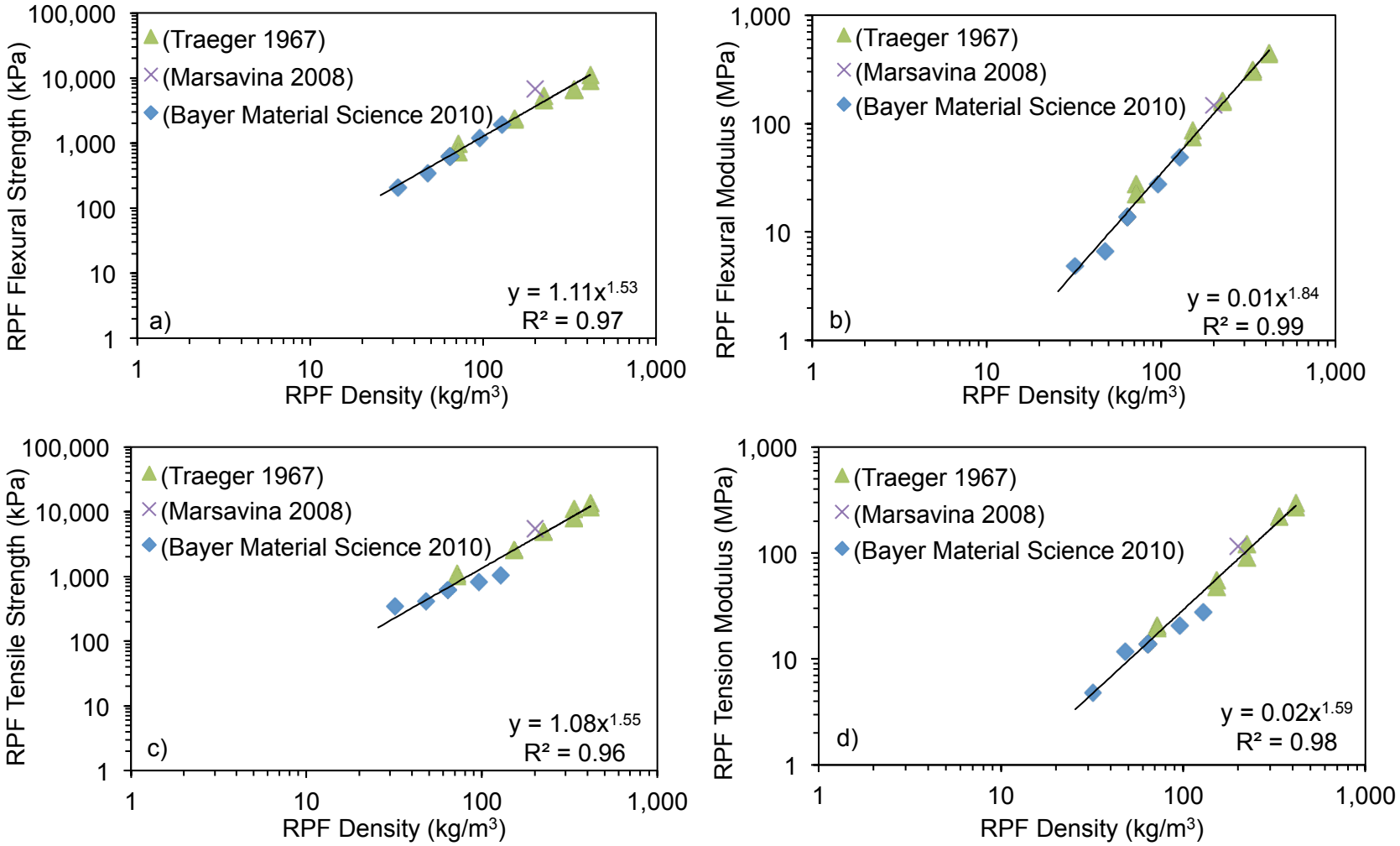

Appendix Figure 17: RPF flexural and tensile strengths and moduli compiled from literature.

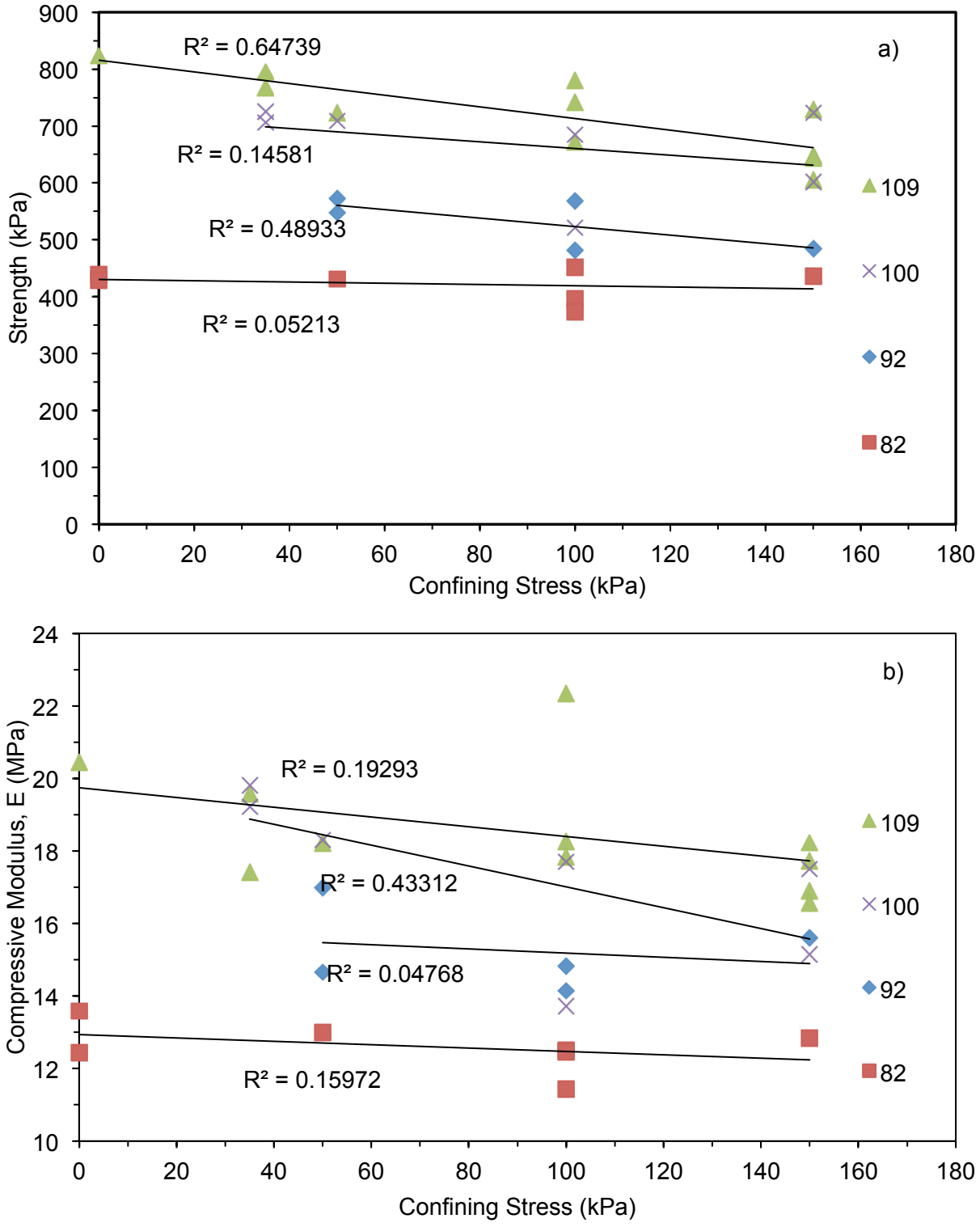

Appendix Figure 18: RPF compressive strength and moduli versus confining stress applied during testing.

B.2.2 Constituents of RPF Mechanical Properties

B.2.2.1 Closed-Cell Content

One of the critical properties for RPF strength and stiffness is the closed-cell content of RPF. Flexible-polyurethane foams typically have much higher open-cell content while rigid-polyurethane foams (RPF) have considerably low open-cell content (Sivertsen 2007), (closed or open-cell content for pure foams is found using ASTM D6226). Furthermore, the flexible foams have much lower density than the rigid foams. Kuncir et al. (1990) confirmed that as the compressive strength increases considerably as the closed-cell content increases. Sivertsen (2007), presented an equation that predicts RPF modulus based on close-cell content, RPF density, an initial PU density given by

$$\frac{M_f}{M_p} = (1-x) * \varphi^2 * \left(\frac{\rho_f}{\rho_p}\right) + x * (1-\varphi)\left(\frac{\rho_f}{\rho_p}\right) \quad (14)$$

$$\varphi = \left(\rho_p - \rho_f\right)/\rho_p \quad (15)$$

where M_f is the modulus of the RPF and M_p is the modulus of PU, φ is the volume fraction, x is the closed-cell content, and ρ_f and ρ_p is the density of the RPF and PU, respectively. In Triantafillou et al. (1989), the cell wall properties were identified by testing solid polyurethane (PU) where the density was 1,200 kg/m^3 with a Young's modulus of 1.6 GPa. From Bayer Material Science (2010), the PU density was 1,114 kg/m^3 and the closed-cell content was 90%.

In Bayer Material Science (2010), all of the RPF properties were available and when inputting the RPF properties into Equations 14 and 15 and a reasonable correlation was observed for the predicted RPF modulus with the measured RPF modulus compiled from the tests (Appendix Figure 19). These properties were not available from the RPF test conducted in this study or in the data compiled from literature. Consequently, without considerable testing of

foams with varying closed-cell contents and PU densities, Equations 14 and 15 only serve as a supplemental method of prediction and is not recommended for use in predicting RPF mechanical properties in stabilized aggregates or geomaterials until further testing has been conducted.

B.2.2.2 Temperature Effects

In Traeger (1967), RPF tested lost strength rapidly with increase in temperature. As was the case for most mechanical properties, the decrease in strength and stiffness occurred above 38 °C (100 °F). As temperature during testing decreased, RPF strength and modulus generally increased. In addition, the effects of temperature on RPF mechanical properties were more pronounced as the density of RPF increased. Of the two foams in Traeger (1967), one was designed to have more residual strength with increasing temperature; methodology which is commonly used in design of asphalt binder.

From the results in Traeger (1967), the following equations were derived to characterize RPF behavior under possible field (i.e., outdoor) operating temperature. For a temperature range from -18 to 54 °C (0–130 °F) the equations for compressive strength and modulus are respectively

$$\sigma_C = -k_1 * T * \left(\rho_{RPF}/\rho_{ref}\right)^{k_2} + k_3 * \left(\rho_{RPF}/\rho_{ref}\right)^{k_2} \qquad R^2 = 1.00 \qquad (16)$$

$$E_C = -k_4 * T * \left(\rho_{RPF}/\rho_{ref}\right)^{k_5} + k_6 * \left(\rho_{RPF}/\rho_{ref}\right)^{k_5} \qquad R^2 = 0.99 \qquad (17)$$

where σ_C is the compressive strength (kPa), E_C is the compressive modulus (MPa), T is the temperature (°C), ρ_{RPF} is the RPF density (kg/m^3), ρ_{ref} is the reference density equal to 1 kg/m^3, fitting parameters k_1, k_2, and k_3 are for compressive strength and are shown in Appendix Table

1, and fitting parameters k_4, k_5, and k_6 are for compressive modulus and are shown in Appendix Table 1.

For a temperature range from -18 to 54 °C (0–130 °F) the equations for flexural strength and modulus are respectively

$$\sigma_F = -k_1 \cdot T \cdot \left(\rho_{RPF}/\rho_{ref}\right)^{k_2} + k_3 \cdot \left(\rho_{RPF}/\rho_{ref}\right)^{k_2} \qquad R^2 = 0.99 \qquad (18)$$

$$E_F = -k_4 \cdot T \cdot \left(\rho_{RPF}/\rho_{ref}\right)^{k_5} + k_6 \cdot \left(\rho_{RPF}/\rho_{ref}\right)^{k_5} \qquad R^2 = 0.99 \qquad (19)$$

where σ_F is the flexural strength (kPa), E_F is the flexural modulus (MPa), T is the temperature (°C), ρ_{RPF} is the RPF density (kg/m^3), ρ_{ref} is the reference density equal to 1 kg/m^3, fitting parameters k_1, k_2, and k_3 are for flexural strength and are shown in Appendix Table 1, and fitting parameters k_4, k_5, and k_6 are for flexural modulus and are shown in Appendix Table 1.

Based on the equations derived and presented and the average RPF density found in PSB specimens of 200 kg/m^3, the compressive strength and modulus over a temperature range from -18 to 54 °C (0–130 °F) would range from 5,213 down to 3,551 kPa and 125 down to 97 MPa, respectively. With the same average RPF density and temperature range, the compressive strength and modulus would range from 3,963 down to 3,077 kPa and 148 down to 115 MPa, respectively. Therefore, temperature would affect the mechanical response of RPF at a density that was calculated to be within PSB specimens.

In Traeger (1967) the effects of temperature were more profound as the density of the foam increased; similar behavior was observed when testing RPF at differing confining stresses in this study. Neilsen et al. (2004) indicated that the internal cellular pressure contributes in the RPF mechanical response to loading. An increase in either temperature or pressure would result in an increase in internal cellular pressure (i.e., lowers mechanical strength and modulus).

Consequently, change in internal cellular air pressure due to external pressure and temperature may play a role in the response of RPF under loading.

The purpose of RPF stabilization is for *in situ* injection, RPF is more likely to remain at temperatures of the subsurface, which is less than the surface temperatures and less influenced by change in surface temperatures. Furthermore, due to the insulating properties typical of RPF, RPF is more likely to resist change in temperature and remain near subsurface ambient temperature, which was the typical temperature in which RPF mechanical properties were evaluated in this study. Since confining stress (pressure) during testing does not resemble increases in air pressure surrounding the composite material, further investigation is required to determine how fluctuating temperatures and confining stress effect the fatigue properties of PSB under compressive and in flexural loading.

Regarding the effects of temperature conditions on stabilized layers in railway trackbeds, Rose and Lees (2008) noted that the HMA underlayment is protected from sunlight by the overlying ballast layer and is maintained at a relatively constant temperature and environment. When having a PSB underlayment, the RPF component, which is sensitive to ultraviolet radiation, will be protected by the overlying ballast layer. Since RPF is sensitive to ultraviolet rays and higher temperatures, subsurface injections are preferable for preserving ambient temperature mechanical properties. Huang et al. (1987) noted that HMA underlayments were preferable to overlayments (i.e., asphalt layer replacing the ballast layer) because the required thickness of the HMA layer is minimal and conventional ballast layer maintenance can still be conducted. Similar methodology can be applied for PSB layers concerning conflict with ballast layer maintenance.

B.2.2.3 Cell Elongation and Size

When fabricating pure RPF, the foam starts at the base of a mold in liquid form. While the reaction is taking place, the foam expands in the path of least resistance. If a mold is oriented upward then the RPF will expand upward. The direction in which RPF is expanding during fabrication is known as the rise direction. In Tu et al. (2001) a strength ratio was developed based on the RPF rise direction and orthogonal to the rise direction. In the study it was found that the RPF strength ratio of the rise and direction orthogonal to rise was 2.14. Therefore RPF can be significantly weaker orthogonal to the rise direction and is stronger in the rise direction. A study by Triantafillou (1989) confirmed that RPF cells within the cellular structure are typically elongated in the rise direction. Observations and discussion regarding cell elongation in PSB is discussed in Section A.3.

Regarding cell size and wall thickness of the RPF cellular structure, in Marsavina et al. (2008) a sample of RPF with a 200-kg/m^3 density had a wall thickness of 3–4 μm. In Gibson (1989), a sample of RPF with a 32-kg/m^3 density RPF had a wall thickness of 3 μm and cell apertures ranging from 0.44 to 0.53 mm. In Triantafillou (1989), with RPF density ranging 64–192 kg/m^3 had cell apertures ranging 0.11–0.23 mm, with higher densities having smaller cell aperture. In Kuncir et al. (1990), the foam cell diameters were shown to slightly change the stress-strain behavior of RPF during compression; at high compression strains, the compressive behavior differs more. In this study, 80-kg/m^3 RPF cylinders with cell apertures ranging 0.25–1 mm were tested, as the cell apertures within the RPF cylinders varied, no noticeable difference was observed in RPF compressive strengths and moduli. Similar to other constituents of RPF mechanical properties, cell aperture may play a larger role with RPF at higher densities (e.g., 200 kg/m^3). RPF cell apertures within PSB were observed to have much greater variability than the RPF cylinders fabricated for testing.

Since PSB fails at lower strain than RPF in flexural and compressive loading, with RPF used for stabilizing ballast, the cell aperture would be less likely to contribute to PSB mechanical properties under typical operational loading conditions (i.e., stresses in the substructure layer of the track). Traeger (1967), indicated that for RPF used in structural applications, the elastic region of the curve is of more importance and in dynamic loading applications (i.e., crash impact loading) the peak or yield strength is more of a concern. Since cell size is more critical at higher strains where RPF behavior is inelastic (Kuncir et al. 1990), cell size may have less importance for use of PSB in rail infrastructure. Discussion of the effect cell aperture and elongation may have on PSB is discussed in Section A.3.

B.2.2.4 Impact Loading

As indicated previously, when RPF is used in dynamic loading applications (i.e., crash impact loading) the peak or yield strength is more of a concern. Tests were conducted on RPF with densities from 80 to 200 kg/m^3 in Traeger (1967) with strain rates (s^{-1}) applied ranged from 0 to 110 s^{-1}. For a 200-kg/m^3 foam, the compressive stress at yield increased from 4,205 to 5,100 kPa. With the strain rate increased from 0 to 64 s^{-1} the compressive modulus increased from 82 to 103 MPa, after which a further increase in strain rate from 64 to 103 s^{-1} resulted in a compressive modulus increase from 103 to 551 MPa, which was a drastic increase in modulus to strain rate. From the results in Traeger (1967), the compressive mechanical properties of RPF increase as the rate of strain applied increases.

As indicated in Aursudki et al. (2009) typical loading frequencies in the rail range from 8 to 10 Hz, but that the frequency can jump as high as 30 Hz for passing of high-speed trains. Vibrations are produced by a passing train and can cause problems to track structural integrity (Otero et al. 2011). These vibrations are typically caused by dynamic impact loading due to deviations in the wheel-rail contact. The dynamic forces generated in the track due to high

frequency loading can far exceed that of the static axel load from a train (Indraratna et al. (2011); Aursudki et al. (2009)). Higher forces in the track can be generated from dynamic loading of passing high-speed trains and freight train loads that are amplified at lower speeds (i.e., when passing over defects in the track). Lichtberger (2005) listed rail superstructure and surface defects that can produce dynamic loads with high-speed trains, such as train wheel slip marks, track gauge defects and substructure settlement, and natural train oscillations. Aursudki (2007) indicated that a sudden increase in loading frequency can results in a decrease in resilient modulus of the substructure materials when they are near saturation (i.e., fouled ballast and poor subgrade with high moisture content). Consequently, high loading frequency can have a detrimental effect in the case of substructure with high moisture contents as a result of pore pressure increases and corresponding decrease in substructure effective stress.

In the case of PSB, the high loads applied in cyclic triaxial testing (400 kPa deviator stress) resulted in an accumulation of plastic strain (ε_P = 1.2%) that was marginally higher that clean ballast (ε_P = 0.96%) tested at 300 kPa. The average elastic strain of PSB at a 400 kPa cyclic stress was 0.0038 m/m. The AVG PSB yield strain in unconfined compressive strength testing was 0.0223 m/m. RPF compressive stress at yield corresponds to a yield strain of 0.04 m/m. Therefore, the yield strain in RPF and PSB are a order of magnitude greater than elastic strain in PSB tested under cyclic loading at 400 kPa deviator stress and hence can withstand dynamic loads applied to the stabilized layer in excess of 400 kPa.

As determined from Traeger (1967), RPF mechanical properties are enhanced by increasing loading frequency. RPF was found to have no limit in performance even as strain rate was increased to 110 s^{-1}, which corresponds to a loading frequency of 110 Hz. PSB would have superior performance relative to clean and fouled ballast at higher stresses and larger loading frequencies. Therefore, RPF stabilization of the ballast layer may have significant outcomes in tracks that experience large cyclic stresses and high loading frequencies.

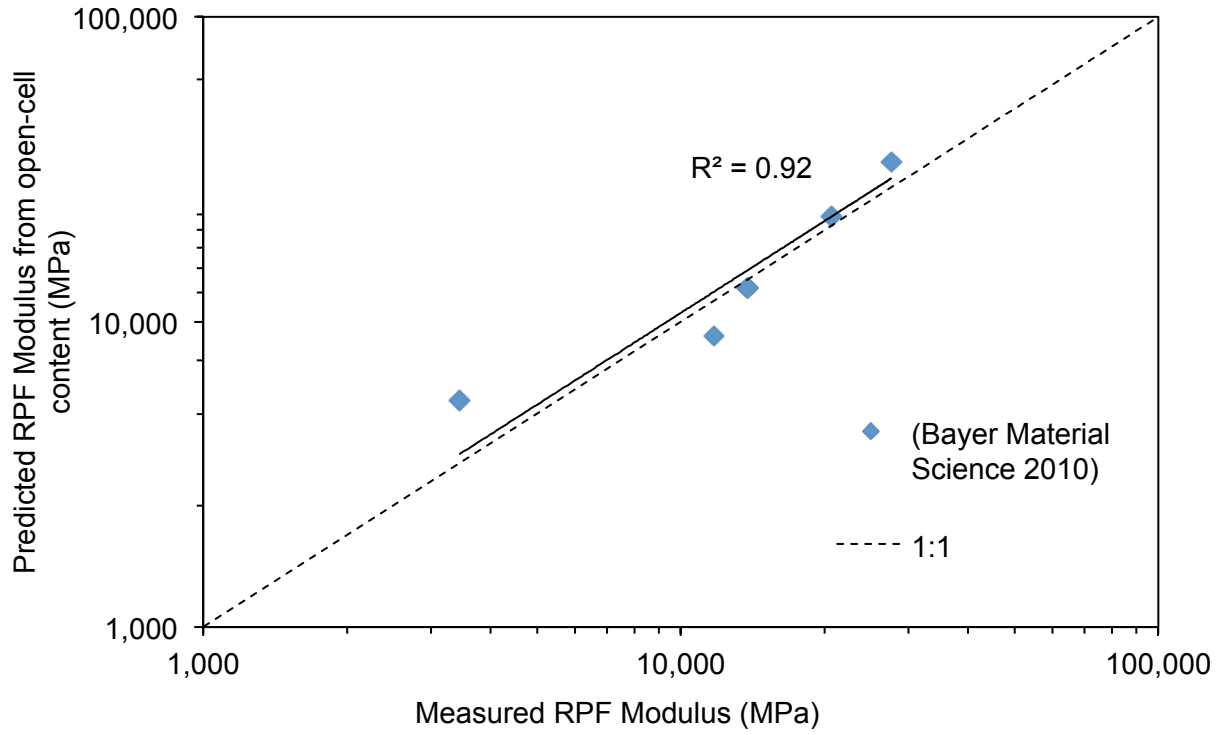

Appendix Figure 19: Predicted RPF modulus based on closed-cell content versus the measured RPF modulus from Bayer Material Science (2010).

Appendix Table 1: Fitting parameters for RPF temperature model.

FP	σ_C (kPa)	σ_F (kPa)	FP	E_C (MPa)	E_F (MPa)
k_1	5.23E-03	1.31E-02	k_4	5.59E-05	8.01E-05
k_2	1.584	1.292	k_5	1.669	1.633
k_3	1.087	3.990	k_6	0.017	0.024

Note: σ_C = compressive strength, E_C = compressive modulus, σ_F = flexural strength, E_F = flexural modulus, fitting parameters (FP). k_1, k_2, and k_3 are for compressive and flexural strength, and FP k_4, k_5, and k_6 are for compressive and flexural modulus.

APPENDIX C – ELASTIC-WAVE BASED TESTING

C.1 ELASTIC WAVE (NON-DESTRUCTIVE SEISMIC) – PSB

Small-strain, elastic wave testing methods are commonly used for field and laboratory investigations as non-destructive determination of the stiffness of materials. Traditional laboratory seismic modulus testing methods (ASTM C 215 and ASTM C 1198) determine the dynamic Young's modulus, shear modulus, and Poisson's ratio of specimens with high stiffness, such as Portland cement concrete and ceramics. Methods more appropriate for this type of laboratory investigation were adopted from previous studies (Pucci (2007); Toros and Hiltunen (2008)). The elastic-wave based (seismic) testing methods developed herein were used to correlate seismic results with damage occurring within PSB between intervals of loading repetitions applied during cyclic-triaxial compression tests (see Sections 3.3.2 and 4.2). The seismic testing methods can also be used in durability testing (e.g., freeze-thaw cycles, wet-dry, cycles, etc.) of PSB materials.

C.1.1 Methodology

Small-strain, elastic-wave testing was conducted on the PSB specimens prior to destructive testing. This method applies an impulse to a specimen (i.e., physically tapping) with an impact hammer, which sends a signal (compression wave) to be detected and recorded on the opposite side of the specimen using a sensor such as an accelerometer (Appendix Figure 20 and Appendix Figure 21). Knowing the travel time of the signal through the material and bulk density, a seismic modulus can be calculated.

Initial implementation of this method was experimental in Phase I. The PSB cylinders that were subjected to cyclic triaxial testing showed very little signs of physical deterioration and underwent little or no change in elastic strain. However, elastic wave testing was conducted

before and after the cyclic triaxial tests and revealed that there was a significant change in the seismic modulus (see Appendix Figure 21). Therefore, method development and implementation was carried forward to Phase II for further testing and characterization of the PSB cylinders. Using elastic-wave based testing, the stiffness of the PSB and ballast specimens was evaluated versus confining pressures similar to what was done in Pucci (2007) where sand and other soil types were studied using elastic-wave based testing. Cyclic triaxial compression tests were conducted at 100,000 cycle increments, between which elastic-wave based tests were conducted to track the change in small-strain (constrained) modulus or damage in the PSB specimens. The purpose for using this method was to evaluated changes in constrained modulus with deterioration (or destruction), which was also conducted by Toros and Hiltunen (2008), where the constrained modulus was measured in highway base-course materials between successive wet-dry cycles. Further adaptation and correlation of elastic-wave testing with destructive methods may allow development of non-destructive field methods for damage detection of subsurface materials, such as PSB.

Testing was conducted using a PCB-086C01 impact-hammer used for wave excitation and the signal was measured using a PCB-353B16 ICP Accelerometer. Signal acquisition was done through a Tektronix 2041 oscilloscope and data recorded using Tektronix OpenChoice Desktop software.

C.1.2 Specimen Fabrication

The PSB specimens used for small-strain elastic-wave (non-destructive testing) testing were the same specimens that were fabricated and used in the destructive testing applications. The purpose of this was to correlate the results of the non-destructive tests with those from the destructive tests. Non-destructive testing was conducted with no air pressure confinement for Phase I specimens and with caps and air confinement for Phase II specimens.

C.1.3 Analysis of Seismic Test

There are several procedures for determining elastic moduli of soil specimens in the laboratory using seismic testing methods. General methods involve excitation of the specimen in a manner that generates a p-wave traveling from one side of a specimen to the other (Appendix Figure 20). From a measurement of the p-wave travel time, the p-wave velocity (V_P) is calculated by

$$V_P = \frac{t_2 - t_1}{L} \tag{20}$$

where t_1 is the time of p-wave excitation, t_2 is the p-wave arrival time, and L is the length of the specimen.

The seismic testing setup involved PVC caps on either end of the specimen which act as a signal propagation mechanism and are used to apply a confining pressure to the specimen (Appendix Figure 21). The PVC caps possess a p-wave travel time, t_{CAP}, that must be added back to the travel time calculation to find true p-wave velocity. The equations for p-wave velocity is thus adjusted to

$$V_P = \frac{t_2 - t_1 + 2 \cdot t_{CAP}}{L} \tag{21}$$

where the cap travel time is multiplied by 2 to account for the two caps. With V_P and specimen bulk density (ρ_B) known, the constrained modulus (M) is calculated by

$$M = V_P^2 \cdot \rho_B \tag{22}$$

A method commonly used in other studies consists of assigning fitting parameters to the results of elastic wave-based testing on soils under differing states of stress, (Avellaneda 2010; Kalinski and Thummaluru 2011; Schuettpelz et al. 2010). The equation adopted from these investigations is used in this study in the form

$$V_P = \alpha \cdot \left(\frac{\sigma_3}{P_{ref}}\right)^{\beta} \quad (23)$$

where V_P is the P-wave velocity (m/s), α is the power model coefficient (m/s), σ_3 is the confining stress (kPa), P_{ref} is the reference stress (kPa) of 1, and β is the power model exponent. This equation represents the power model that was used to define material response to differing confining stresses applied. In this study only confining stress was used for determining the fitting parameters for P-wave velocity.

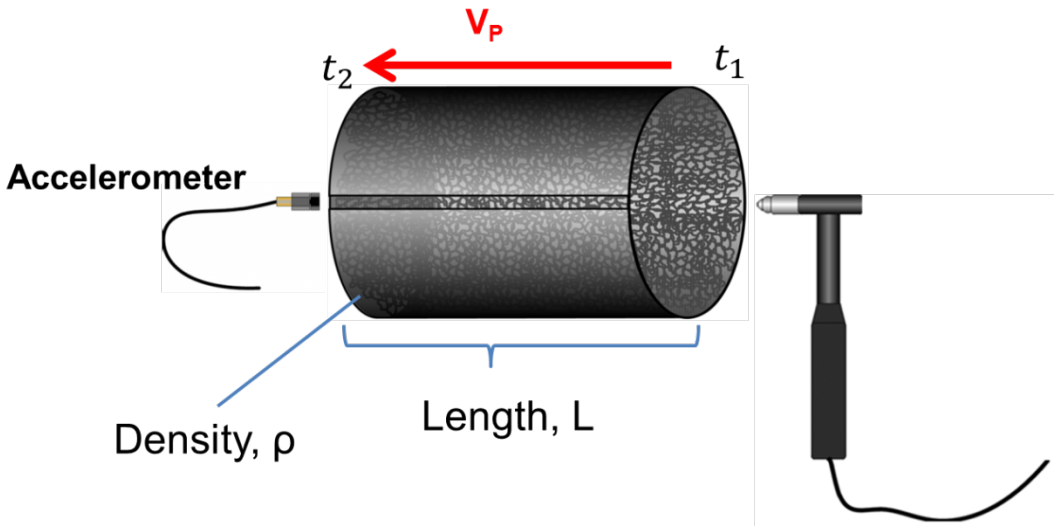

Appendix Figure 20: Small-strain elastic wave testing approach (compression wave excitation)

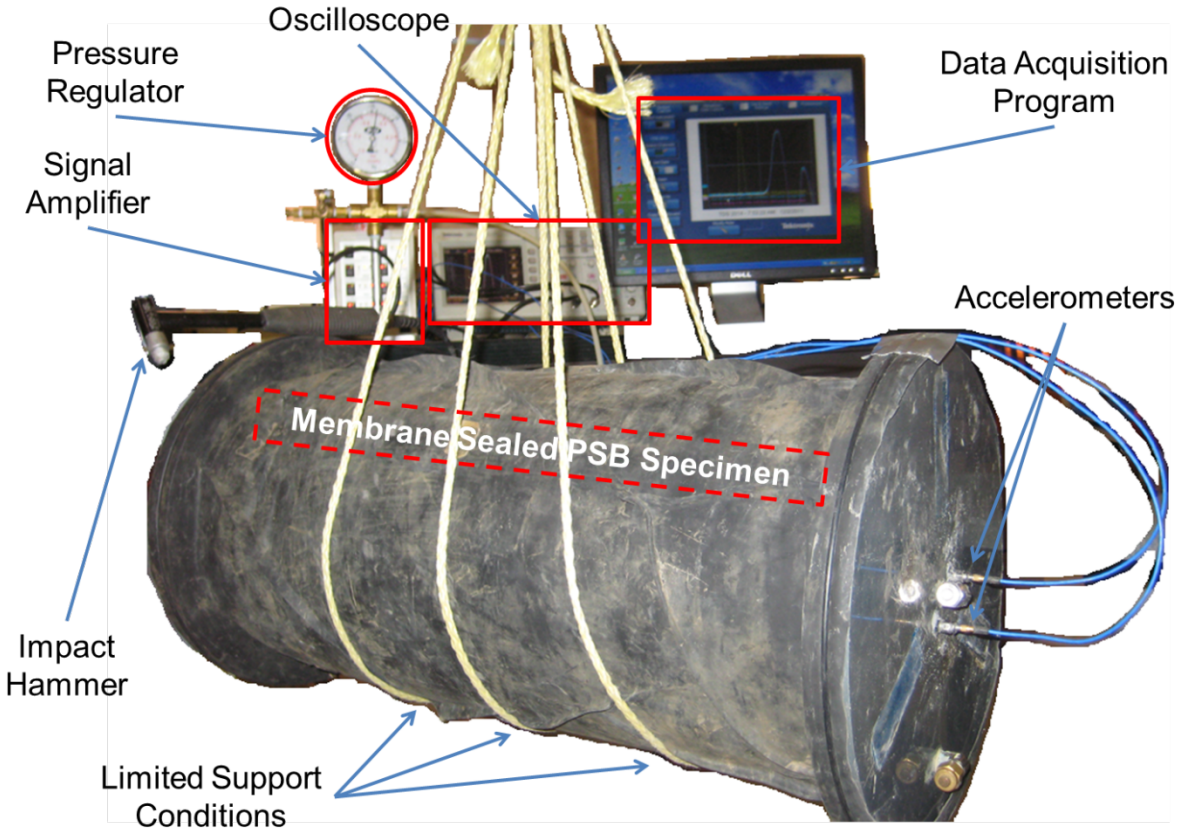

Appendix Figure 21: Picture of membrane-sealed PSB specimen subjected to small-stain elastic-wave based testing.

C.2 ELASTIC-WAVE BASED (NON-DESTRUCTIVE SEISMIC) TESTING RESULTS

Small-strain, elastic wave (seismic) tests were conducted on clean ballast and compared to results obtained from cyclic-triaxial compression testing on PSB specimens to verify use of seismic tests for detecting damage in PSB. Clean ballast possessed a density that was among the final densities of the PSB specimens; however, the constrained modulus of clean ballast (236 MPa) at a confining stress, σ_3, of 35 kPa was lower (Appendix Figure 22). The lower density PSB specimens reveal that the initial ballast void space is filled and then expanded by RPF, which occupies a greater volume than the initial void space. A strong correlation (R^2 = 0.96) was found between constrained modulus and PSB density. The results of the small-strain elastic wave tests conducted in Phase I indicate that the constrained modulus was a function of composite specimen density and underwent a significant decrease in constrained modulus after cyclic-triaxial loading of the specimen (Appendix Figure 22).

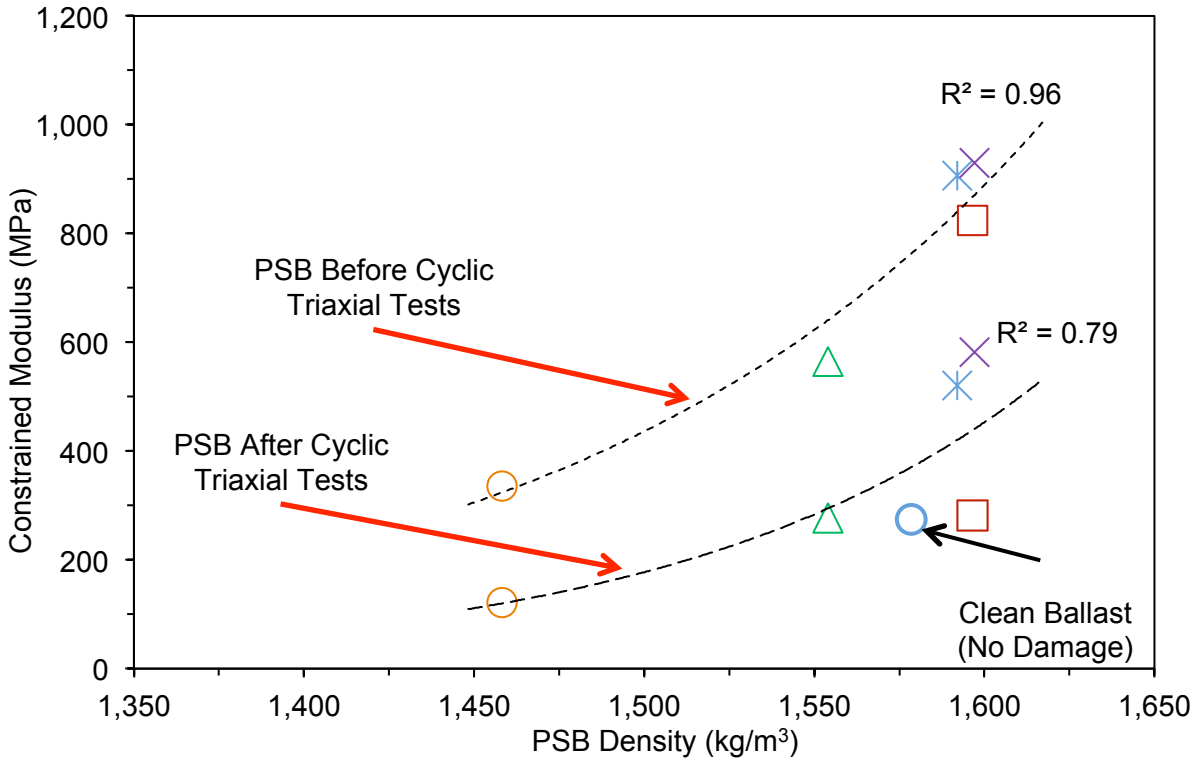

Appendix Figure 22: PSB tests run with σ_d = 300kPa to 250,000 triaxial loading cycles. Each symbol represents the same specimen before and after triaxial compression testing.

In Phase II, the PSB cylinders underwent seismic testing before triaxial compression loading cycles and after increments of 100,000 loading cycles. Three PSB specimens with different densities were selected for comparison and tested at the same cyclic stress, which was the highest deviator stress (σ_d = 400 kPa) applied for PSB cylinder testing. The cylinder with the highest density (1,636 kg/m^3) saw a decrease in constrained modulus of 37% after 100,000 loading cycles and a further 17% reduction after an additional 100,000 loading cycles. The cylinder that had lower density (1,588 kg/m^3) saw a decrease in constrained modulus of 56% after 100,000 loading cycles and a further 35% reduction after an additional 100,000 loading cycles. Furthermore, as confirmed in Appendix Figure 23, small-strain elastic wave testing for specimen damage detection reveals that the higher density PSB specimen has a greater resistance to accumulation of plastic strain from cyclic-triaxial compression tests than the lower density PSB specimen. Finally, percent RPF by weight was higher in the more dense specimen and correspondingly lower in the less dense specimen.

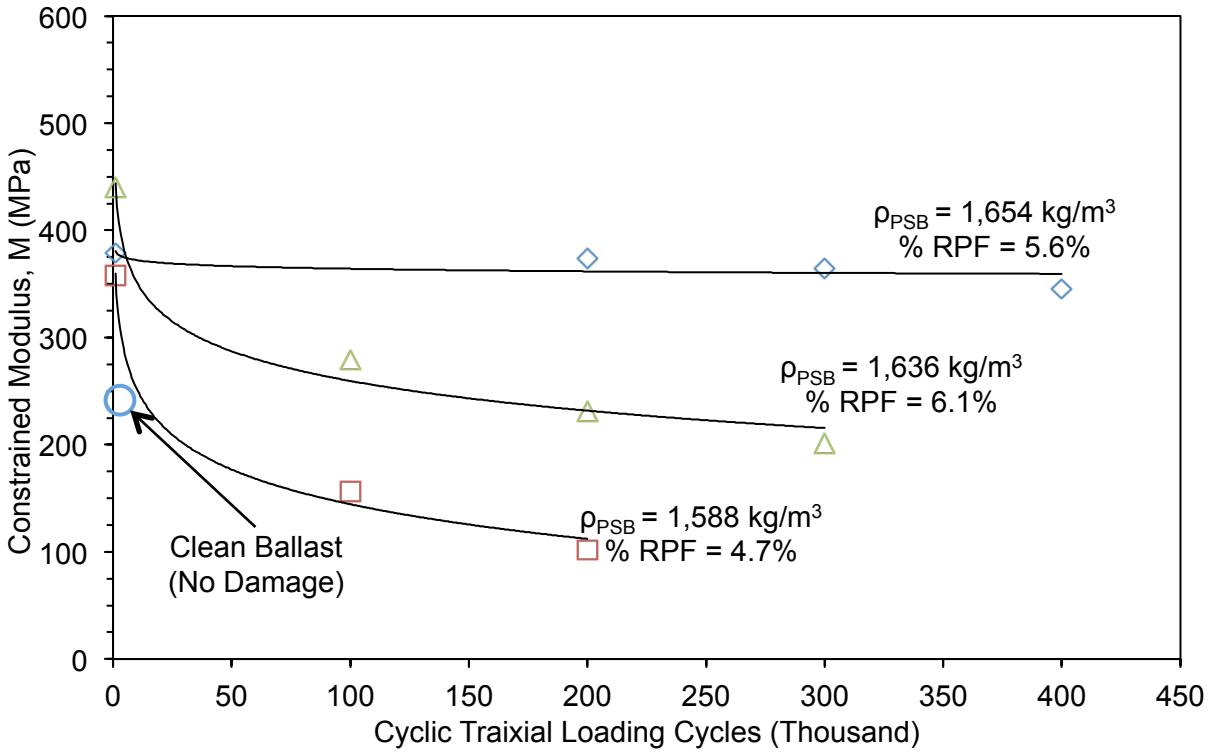

Appendix Figure 23: Constraint modulus of PSB specimens measured before cyclic triaxial compression tests, in increments of 100,000 loading cycles. Cyclic triaxial compression tests conducted with σ_d=400kPa, σ_c=35kPa.

Clean ballast was tested at σ_3 ranging from 10 to 40 kPa, more developed methods for applying confining pressure are needed for conducting seismic tests on clean ballast at a σ_3 (100 kPa) that is used in the representative state of stress defined in Ebrahimi (2011). However, based on the power equation (Equation 23) a strong relationship (R^2 = 0.96) was established between clean ballast P-wave velocity and confining stress. When extrapolating this relationship and using a σ_3 of 100 kPa, the clean ballast P-wave velocity is estimated at 598 (m/s). Using this p-wave velocity, the bulk density 1,581 kg/m^3 of the ballast specimen, and Equation 23, the corresponding ballast constrained modulus is estimated at 565 MPa. This is constrained modulus is among the constrained modulus of the PSB specimens presented in Appendix Figure 22; however, is higher than the constrained modulus of the PSB specimens presented in Appendix Figure 23. Since the PSB specimens in Appendix Figure 22 were formed under full confinement (i.e., no expansion allowed) and higher RPF contents were injected, a higher constrained modulus in some PSB specimens relative to clean ballast is realistic. Since the average resilient modulus (see Section 4.7) of PSB (100 MPa) is less than clean ballast (275 MPa), in Appendix Figure 23 the use of the seismic test presented herein adequately captured the difference in elastic deformational behavior of PSB relative to clean ballast (σ_3 = 100 kPa).

APPENDIX D – BACKGROUND OF TRACKBED LAYERS

D.1 BACKGROUND

This type of system is referred to as a railway track designed with a hot-mix asphalt (HMA) or bituminous trackbed. Several studies have been conducted where different HMA thicknesses and moduli have been investigated for determining design and construction methods for HMA trackbeds (Huang et al. 2009; Rose and Lees 2008). Use of HMA trackbeds was also studied at the Transportation Technology Center Inc. (TTCI^{TM}) as presented in Li et al. (2001). In their study, a significant increase in the overall track modulus was expected and the stresses in the subgrade measured beneath the HMA trackbed were lower than beneath a typical ballast layer (without a bound trackbed). In Rose and Konduri (2006), an elastic finite element computer program (KENTRACK) was developed to investigate the track elastic response to loading through each of the typical substructure layers (i.e., ballast, subballast, and subgrade). The computer program was used to investigate track elastic response for a HMA trackbed.

In Huang (2004), the fundamentals of having an HMA trackbed were explained by comparing the functions of the layered systems in pavement and railroads. When flexible surface layers are used in highway pavement systems, the wheel loads are concentrated with loads more easily transmitted in compression to the subbase/subgrade layer. On railroad trackbeds, the loads are transmitted through the superstructure to the substructure over a large surface area by the ties and the ballast layer (similar to a rigid pavement). Transmission and dissipation of the wheel loads through the layered systems in railways depends on stiffness of the layered system (Huang 2004). Transmission of forces over a larger surface area requires materials with higher stiffness that can withstand high flexural loads to distribute loads over larger areas. Therefore, when increasing the thickness of the HMA layer and decreasing the

thickness of the ballast layer, more load is carried by the HMA layer, leading to higher tensile stress at the base of the layer.

In Rose and Konduri (2006), a life cycle equation for subgrade/subballast is given as

$$N_d = 4.838\times10^{-5} \cdot (\sigma_c)^{-3.734} \cdot (E_s)^{+3.583} \quad (24)$$

where σ_c is the vertical compressive stress on the top of subgrade (psi) and E_s is the subgrade modulus (psi). In Rose and Konduri (2006), E_S was represented by resilient modulus based on the bulk stress, which is defined and can be found using the equations in Section 5.1.

For highway pavement systems, an equation presented by Huang (2004) represents the failure criterion of the subgrade/base based on the compressive strain on the top of the layer. In Rose et. al (2003) this failure criterion is determined based on the compressive stress transmitted to the layer and stiffness of the layer. In Rose, Su, and Long (2003), failure criterion for HMA trackbeds and supporting subgrade were combined into a design life equation given as

$$L = \frac{1}{\sum_{i=1}^{n} \frac{N_P}{N_a or N_d}} \quad (25)$$

where L is the design life given as number of years, N_P is the loading repetitions representing the amount of traffic during each period, N_a (given as N_f for PSB) and N_d provide the number of loading repetitions before failure of either the stabilized layer from fatigue cracking or the subgrade/subballast layer from permanent deformation, respectively.

In Rose and Konduri (2006), Talbot's equation is used for determining pressure applied to the subgrade due to pressure applied beneath the rail tie to the surface of the ballast layer. In Ebrahimi and Keene (2011) Talbot's equation (1985) was used to find the cyclic stress on subgrade (σ_{sd}). For a given thickness of ballast equal to h, stress on the subgrade is was reconfigured and found using

$$\sigma_{sd} = 957 \cdot \frac{\sigma_t}{h^{1.25}} \quad (26)$$

where the stress beneath the centerline of the tie at depth h (mm) below the tie, σ_{sd}, (kPa) is a function of stress over the bearing area of the tie (σ_t, kPa). These formulations can be used with the analytical models developed for PSB trackbed layers and for using an analytical approach for layer thickness of PSB trackbeds, stress distributed on the layer, and resulting stabilized layer life cycle.

APPENDIX E – ABAQUS FINITE ELEMENT MODELING DETAILS

E.1 ELEMENT TYPES AND MESHING

The model railway embankment was modeled in three-dimensional space using ABAQUS 6.9-2. The software has vast capabilities including modeling of complex geometries with several interacting parts possessing differing mechanical properties and material models. The choice of the linear-elastic modeling of the railway embankment was for validation with Selig and Waters (1994) and for modeling variations in track resilient response. Since the scope of the study was to understand the effects of having zones of differing mechanical properties in the ballast layer and the resulting effect on track resilient response, linear elastic material models were selected for the different layers and for the modeled stabilized zones.

In order to perform 3D finite element analysis the model was discretized into a basic first-order (linear), 3D constant stress tetrahedral element mesh (4-node linear tetrahedron, C3D4). The discretization consisted of 121,194 4-node linear tetrahedron finite elements due to model geometry and complex meshing. ABAQUS meshing verification tool was used to ensure no elements were distorted based on meshing of each part. For computational efficiency, mesh density was decreased with depth of the rail embankment in the model. Diagram of the finite elements is shown in Appendix Figure 24.

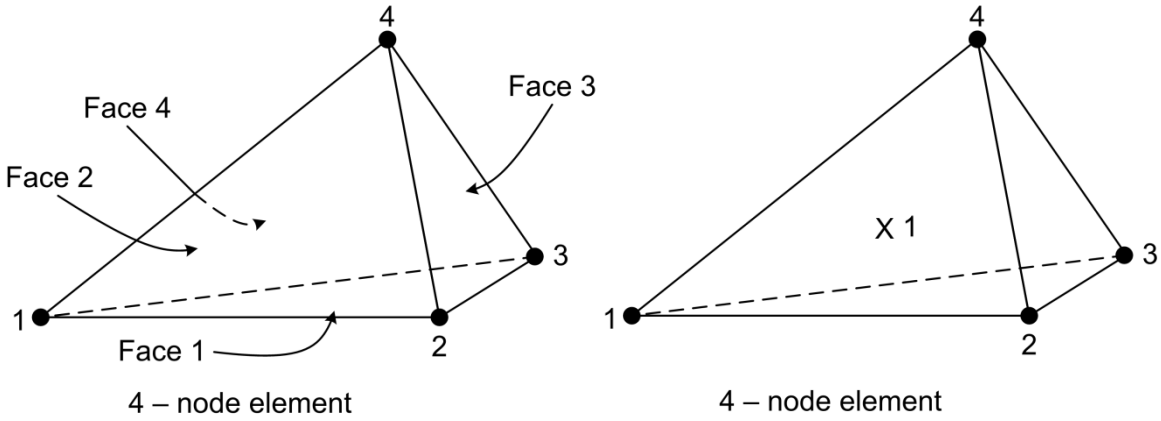

Appendix Figure 24: Typical 4-note tetrahedral elements.

E.2 BOUNDARY CONDITIONS AND MODEL CONSTRAINTS

Boundary conditions applied to the models included: (i) zero vertical displacement at the base of the subgrade layer, zero longitudinal displacement for the edges of the model orthogonal to the direction of the model-track geometry (i.e., subgrade, subballast, ballast, and rail tie and PSB when applicable), and zero lateral displacement of the edges parallel to the direction of the model-track geometry (i.e., subgrade). (ii) Zero longitudinal and lateral displacements were applied to the rail model edges, but vertical displacements and rotational degrees of freedom (DOF) were left unconstrained. When surfaces of separate parts (i.e., ballast layer and subballast layer interface) are in contact in ABAQUS, their interactions must be defined (e.g., tangential and normal behavior).

Model-rails were rigidly connected to model-sleepers at single contact point to represent connection of the fastening system. The rotational degrees of freedom are constrained between the two model parts to simulate the constraint between rail and sleeper in the track superstructure. The rail-ballast tangential behavior was assigned and the interaction was defined by isotropic friction with coefficient of 0.35.

In ABAQUS a penalty contact method can be assigned so that the contact force is proportional to the extent of penetration of one element or part into an adjoining element or part depending on master and slave surface assignment. This setting is selected so that rail penetration into the ballast layer is allowed to occur during model computation. Penalty contact method also prevents over constraints, alleviating stress concentration buildup from model inaccuracy. Linear normal behavior with “hard” contact is assigned with separation allowed after contact. Penalty contact method was also used for defining normal behavior between the rail and the ballast layer. Remaining specifications were default properties.

Tangential behavior was assigned when sleepers contact the ballast layer, defined by isotropic friction with coefficient of 0.5. This was done to simulate the level of interface friction that occurs between ballast particles and, specifically, wood ties used as part of the superstructure. Penalty contact method is used to define tangential behavior. Default normal behavior with “hard” contact is assigned for simplicity in model calculations with separation allowed after contact. Remaining specifications were default properties.

Tangential behavior was assigned for any two geomaterials (e.g., ballast, subballast, and subgrade) in contact, defined by isotropic friction with coefficient of 0.5. Default normal behavior with “hard” contact is assigned for simplicity in model calculations with no separation allowed after contact between geomaterials to prevent any tension generated in the model from separating the layers, which should not occur because geomaterials do not support tension forces. A shear stress limit of 400 kPa was assigned to prevent overstress concentrations at the interface between layers and optimize model calculations if stresses build up at layer interfaces. Remaining specifications were default properties. For all layer interfaces, finite sliding was selected to allow movement layers relative to the next in order to prevent unintended stress concentrations during model calculations and optimize model calculations involving interface behavior.

APPENDIX F – SUPPLEMENTARY PICTURES

F.1 PICTURES

Appendix Figure 25: Fabrication error in PSB Cylinder # 6, considered outlier in analysis.

Appendix Figure 26: Pictures of fabrication of PSB fouled ballast specimen. Pressure relief holes were drilled into fabrication mold where small amounts of soil mixed with RFB expelled from the specimen during RPF expansion/reaction.

Appendix Figure 27: PSB from percolation injection into ballast layer prototype.

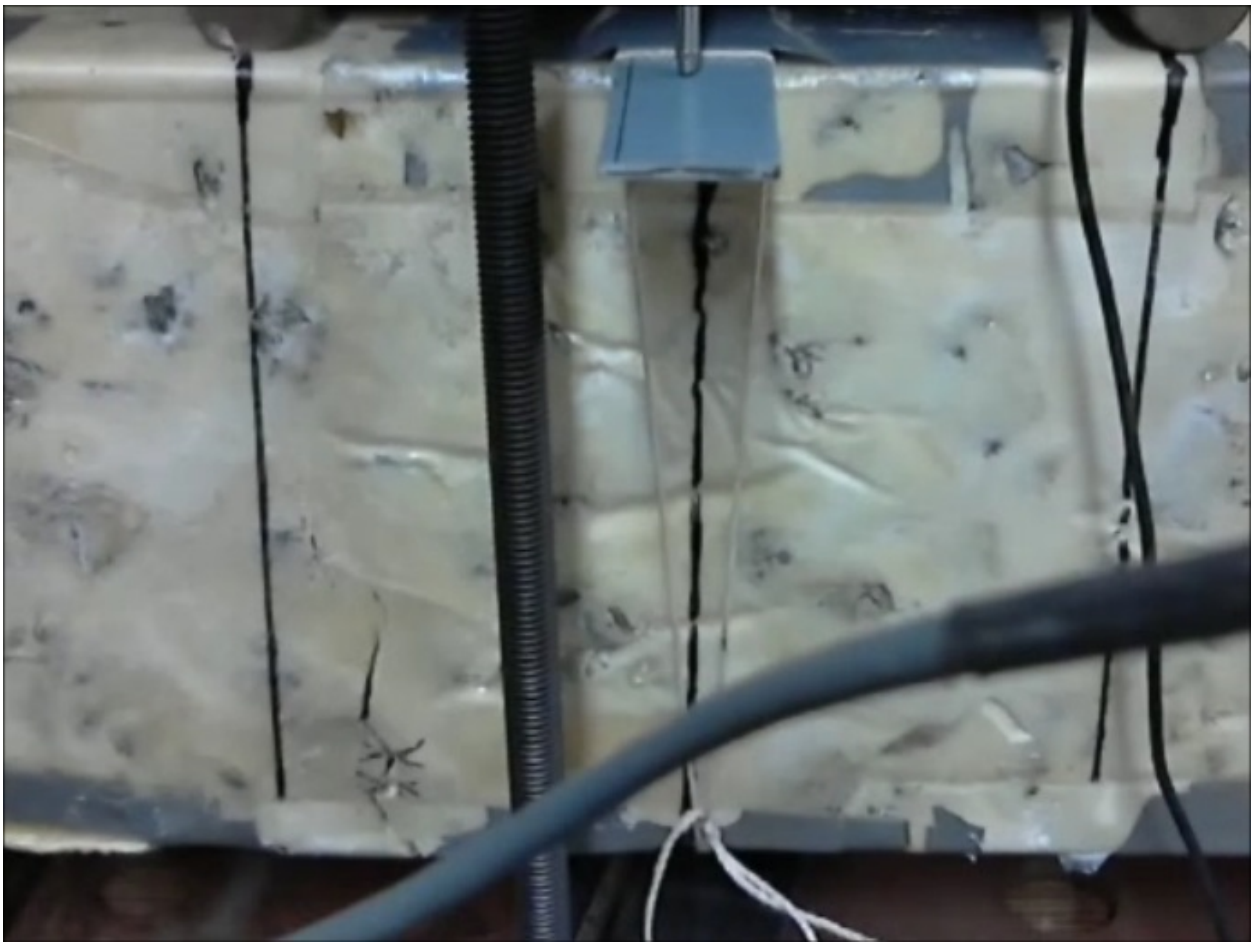

Appendix Figure 28: Picture of crack in beam at peak load within a loading cycle, the loading cycle when the picture was taken was the last cycle before beam rupture.

Appendix Figure 29: PSB prism specimens after failure in unconfined compression testing.

APPENDIX G – TABLES

Appendix Table 2: Table of PSB cylinder phase properties from Phase I (Roman Numeral) & Phase II (Numbered).

	Ballast Unit Weight	PSB Unit Weight	Final Void space	RPF Density	Ballast Density	PSB Density	RPF by weight	RPF by volume	PU by Volume	Air by Volume (m^3)
(Units)	**(kN/m^3)**	**(kN/m^3)**	**%**	**(kg/m^3)**	**(kg/m^3)**	**(kg/m^3)**	**%**	**%**	**%**	**%**
SM I (1)	14.6	15.2	42.8	141	1494	1554	3.89	42.8	5.42	37.4
SM I (2)	14.8	15.6	42.4	207	1504	1592	5.52	42.4	7.89	34.5
SM II (1)	14.8	15.7	42.1	202	1512	1597	5.32	42.1	7.62	34.5
SM II (2)	14.7	15.7	42.4	223	1503	1597	5.92	42.4	8.48	34.0
SM III (1)	13.0	13.6	49.2	119	1325	1384	4.23	49.2	5.25	44.0
SM IV (1)	15.4	16.2	39.8	191	1571	1647	4.63	39.8	39.8	33.0
SM IV (1)	15.0	15.8	41.3	186	1532	1609	4.79	41.3	41.3	34.4
CL1	15.5	16.0	40.3	192	1584	1636	4.73	40.3	6.95	33.3
CL2	14.8	15.6	42.0	176	1514	1588	4.66	42.0	6.64	35.4
CL3	14.9	15.6	42.2	192	1518	1590	5.09	42.2	7.26	34.9
CL4	15.2	16.1	40.9	227	1551	1637	5.66	40.9	8.32	32.5
CL5	15.3	16.2	40.2	229	1562	1654	5.56	40.2	8.25	31.9
CL6	14.3	15.1	44.1	173	1459	1536	4.96	44.1	6.84	37.3
CL7	15.3	16.3	40.2	246	1561	1660	5.96	40.2	8.87	31.3
CL8	15.1	16.0	41.1	241	1537	1636	6.05	41.1	8.89	32.2
CL9 (FB)	18.1	18.6	29.3	185	1845	1899	2.85	29.3	4.86	24.5
CL10 (RB)	15.3	16.3	40.2	250	1560	1661	6.05	40.2	9.02	31.2
Average	15.1	15.8	41.2	199	1537	1616	5.05	41.2	11.28	33.9
COV	6.4%	6.1%	9.2%	17.9%	6.4%	6.1%	17.1%	9.2%	98.5%	11.5%

Appendix Table 3: Table of PSB beam phase properties from Phase I (Roman Numeral) & Phase II (Numbered).

	Ballast Unit Weight	PSB Unit Weight	Final Void space	RPF Density	Ballast Density	PSB Density	RPF by weight	RPF by volume	PU by Volume	Air by Volume (m^3)
(Units)	(kN/m^3)	(kN/m^3)	%	(kg/m^3)	(kg/m^3)	(kg/m^3)	%	%	%	%
FB III	15.7	16.5	38.5	203	1604	1682	4.64	38.5	7.01	31.5
FB IV	15.5	16.1	39.5	152	1580	1640	3.67	39.5	5.39	34.1
FB VII	14.7	15.5	42.4	179	1504	1579	4.80	42.4	6.81	35.6
FBVIII	14.6	15.5	42.9	209	1490	1579	5.68	42.9	8.04	34.9
FB1	15.0	15.8	41.4	197	1616	1531	5.05	41.4	7.32	34.0
FB2	15.5	16.4	39.4	218	1669	1583	5.14	39.4	7.69	31.7
FB3	14.7	15.6	42.4	199	1589	1503	5.31	42.4	7.56	34.9
FB4	14.5	15.3	43.5	193	1561	1475	5.39	43.5	7.55	35.9
FB5	14.7	15.4	42.5	232	1566	1502	5.28	42.5	8.83	33.6
FB6	14.2	15.1	44.4	197	1539	1452	5.69	44.4	7.86	36.5
FB7	15.1	16.7	41.0	195	1707	1540	4.13	41.0	7.19	33.8
FB8	14.6	15.4	43.1	199	1572	1485	5.46	43.1	7.70	35.4
Average	15.2	15.5	41.7	198	1608	1521	5.02	41.7	7.41	34.3
COV	4.5%	3.9%	4.4%	9.8%	3.4%	3.1%	12.3%	4.4%	11.1%	4.5%

Note: PSB=Polyurethane-stabilized ballast, RPF=rigid-polyurethane foam, PU=solid phase of polyurethane, CL and SM are PSB cylinders, FB are PSB beams.

Appendix Table 4: Track properties used in modeling from other studies.

Reference	(Selig and Waters 1994)	(Selig and Waters 1994)	(Indraratna 2011)	(Indraratna 2011)	(Rose and Konduri 2006)
Study	Parametric-Numerical	Representative-Numerical	Representative-Analytical	Representative-Finite Element	Parametric-Numerical
Material Model	Elastic	Elastic	Elastic	Elasto-plastic	Elasto-plastic
Program	GEOTRACK	GEOTRACK	Analytic	PLAXIS	KENTRACK
Rail E, I_z (MPa, m^4)	207,000	207,000, $0.395*10^{-4}$		210,000	
Rail ν				0.15	
Rail Dim (t, w) (m)			- x 0.26		
Sleeper E, I_z (MPa, m^4)	3,400–20,700	10,300 (W), Iz = 1.07*10^-4		10,000 (C)	W
Sleeper ν					
Sleeper Dim (l, t, w) (m)	2.59 x - x 0.229		2.5 x - x 0.26 (C)	2.5 x - x 0.26 (C)	2.6 x 0.18 x 0.229 (W)
Sleeper s (m)	0.245–0.914	0.495		0.495	0.51 & 0.61
Ballast E (MPa)	173–689	310	310	64 / H-soil model	87-324
Ballast ν	0.1-0.49	0.3	0.3	0.15	0.25 & 0.35
Ballast Layer t (m)	0.38-0.53	0.305	0.38		0.15-0.3
Subballast, E (MPa / model)	31–126		125	80 / MC	138
Subballast ν	0.4		0.35	0.35	0.35
Subballast Layer t (m)	0.15		0.15		0.102
Subgrade, (MPa / model)	31–126	55	55	34.2 / MC	20-207
Subgrade ν	0.4	0.4	0.45	0.33	0.4
Subgrade Layer, t (m)	> 0.91	> 0.91			5.08
Wheel L (kN / #axels)	22–146 / 4-axel	142 / 4-axel	175 / 1-axel	144 / 1-axel	160 / 2-axel

Note: ν = Poisson's ratio, E = Young's Modulus, s = spacing, t = thickness, w = width, l = length, C = Concrete, W = Wood, MC = Mohr Coulomb

CFIRE

University of Wisconsin-Madison
Department of Civil and Environmental Engineering
1410 Engineering Drive, Room 270
Madison, WI 53706
Phone: 608-263-3175
Fax: 608-263-2512
cfire.wistrans.org